



VNIVERSITAT  
DE VALÈNCIA

1

2     **Search for associated production of a Higgs**  
3     **boson and a single top quark in the  $2\ell + \tau_{had}$**   
4     **final state using proton-proton collisions**  
5     **at  $\sqrt{s} = 13$  TeV with the ATLAS detector**

6

PhD Thesis

7

**Pablo Martínez Agulló**

8

Instituto de Física Corpuscular (IFIC)  
Departament de Física Atòmica, Molecular i Nuclear  
Programa de Doctorat en Física

9

10

Under the supervision of

11

**Carlos Escobar Ibáñez**  
and  
**Susana Cabrera Urbán**

12

13

14

15

València, 14th February 2023



<sup>16</sup> **Carlos Escobar Ibáñez,**  
<sup>17</sup> investigador científico del Consejo Superior de Investigaciones Científicas, y  
<sup>18</sup>

<sup>19</sup> **Susana Cabrera Urbán,**  
<sup>20</sup> científica titular del Consejo Superior de Investigaciones Científicas,

<sup>21</sup> **Certifican:**

<sup>22</sup> Que la presente memoria, **Search for associated production of a**  
**Higgs boson and a single top quark in the  $2\ell + \tau_{had}$  final state**  
**using proton-proton collisions at  $\sqrt{s} = 13$  TeV with the ATLAS**  
**detector**, ha sido realizada bajo su dirección en el Instituto de Física  
Corpuscular, centro mixto de la Universitat de València y del CSIC, por  
**Pablo Martínez Agulló**, y constituye su Tesis para optar al grado de  
Doctor en Física.

<sup>29</sup> Y para que así conste, en cumplimiento de la legislación vigente, presenta  
<sup>30</sup> en el Departamento de Física Atómica, Molecular y Nuclear de la Univer-  
<sup>31</sup> sidad de Valencia la referida Tesis Doctoral, y firman el presente certificado.

<sup>32</sup>

<sup>33</sup> València, a DD de MES de 2023,

<sup>34</sup>

<sup>35</sup> Carlos Escobar Ibáñez

Susana Cabrera Urbán



36  
37  
38  
39  
40

*Ja que no s'entén el que dius,  
que s'entenga la lletra.*

—ROSITA CANDELA-ESCLAPEZ (1947)



# <sup>41</sup> Preface

<sup>42</sup> The Standard Model of particle physics is both incredibly successful and  
<sup>43</sup> glaringly incomplete theory. It brings together all elementary particles that  
<sup>44</sup> make up the known universe in a single theory. Among these, the top quark  
<sup>45</sup> and the Higgs boson are of special interest because they can help to answer  
<sup>46</sup> some of the open questions. The object of study of this thesis focusses in  
<sup>47</sup> these two singular particles and its interplay.

<sup>48</sup> The studies presented at this dissertation have been carried using an  
<sup>49</sup> integrated luminosity of  $139 \text{ fb}^{-1}$  of proton-proton collision data at center-  
<sup>50</sup> of-mass energy of  $13 \text{ TeV}$  collected by the ATLAS detector during the Large  
<sup>51</sup> Hadron Collider (LHC) Run 2. Located at the European Organization  
<sup>52</sup> for Nuclear Research, the LHC is the most powerful particle accelerator  
<sup>53</sup> in the world and ATLAS one of its largest detectors. The experimental  
<sup>54</sup> setup in which this work is contextualised is described in Chapter 3. The  
<sup>55</sup> data and generation of Monte Carlo simulations within ATLAS is described  
<sup>56</sup> in Chapter 4. The reconstruction and identification of physical objects is  
<sup>57</sup> explained in Chapter 5.

<sup>58</sup> The discovery of a Higgs boson by the ATLAS [1] and CMS [2] exper-  
<sup>59</sup> iments in 2012 opened a new field for exploration in the realm of particle  
<sup>60</sup> physics. In order to better understand Standard Model, it is of promi-  
<sup>61</sup> nent interest to determine the Yukawa coupling of the Higgs boson to the  
<sup>62</sup> top quark ( $y_t$ ), being the latter the most massive fundamental particle and,  
<sup>63</sup> consequently, the one with the largest coupling to the Higgs boson.

<sup>64</sup> The direct measurement of  $y_t$  is only possible at the LHC via two asso-  
<sup>65</sup> ciated Higgs productions: with a top-quark-antiquark pair ( $t\bar{t}H$ ) and with  
<sup>66</sup> a single-top quark with an additional parton ( $tHq$ ). While the  $t\bar{t}H$  just  
<sup>67</sup> permits the determination of the magnitude of  $y_t$ , the only way of simultan-  
<sup>68</sup> eously measuring its sign and magnitude is through the  $tH$  production [3].  
<sup>69</sup> The possible observation of an excess of signal events with respect to the  
<sup>70</sup> Standard Model prediction, would be an evidence of new physics in terms  
<sup>71</sup> of CP-violating  $y_t$  coupling.

72 In this work it is presented a search for the  $tHq$  production in a final  
73 state with two light-flavoured-charged leptons (electrons or muons) and one  
74 hadronically-decaying  $\tau$  lepton (named  $2\ell + 1\tau_{\text{had}}$  channel). This search is  
75 exceptionally challenging due to the extremely small cross-section of the  $tHq$   
76 process ( $70 \text{ fb}$  [4]), and of the  $2\ell + 1\tau_{\text{had}}$  final-state channel, in particular,  
77 which only accounts for a 3.5% of the total  $tHq$  production.

78 Therefore, to distinguish the  $tHq$  signal events from background events,  
79 machine-learning techniques are used. Particularly, boosted-decision trees  
80 are employed to define signal-enriched regions as well as control regions  
81 that constrain the most important background processes. The most relev-  
82 ant backgrounds are those related to top-quark-antiquark-pair production  
83 without and with and additional boson ( $t\bar{t}$ ,  $t\bar{t}H$ ,  $t\bar{t}W$  and  $t\bar{t}Z$ ) and  $Z$  boson  
84 plus jets.

85 Additionally, to help identifying signal events within the data, the re-  
86 construction of the event plays an important role. Different tools are used  
87 to retrieve the four momentum of the top quark and Higgs boson from the  
88 reconstructed objects. This information can be later used to build variables  
89 that help separating the signal events from the processes that mimic the  
90  $2\ell + 1\tau_{\text{had}}$  signature. The reconstruction of the events is also enhanced by  
91 similar machine-learning methods since in the scenario in which the light-  
92 flavour leptons have the same sign, a priori, it is not possible to determine  
93 which lepton is originated from the Higgs boson and which from the top  
94 quark.

95 Significant suppression of the background events with jets wrongly selec-  
96 ted as leptons or non-prompt leptons originating from heavy-flavour decays  
97 is achieved by demanding electrons and muons to pass strict identification  
98 and isolation requirements. Simultaneously, hadronic- $\tau$  leptons are deman-  
99 ded to pass the requirement of a recurrent-neural-network-based discrimin-  
100 ator to reduce misidentifications from jets.

101 The tools and methods developed for the associated  $tHq$  production  
102 search are described in Chapter 6.

# <sup>103</sup> Acknowledgements

<sup>104</sup> This work would not have been possible without the invaluable assist-  
<sup>105</sup> ance of a large number of people, whom I have been fortunate to meet. I  
<sup>106</sup> would like to thank them all and dedicate this thesis to them.

<sup>107</sup> Special mention to Stack Overflow, this thesis is as much yours as it is  
<sup>108</sup> mine. Thanks.

<sup>109</sup> Gracias gracias



# <sup>110</sup> Contents

<sup>111</sup>	Preface	v
<sup>112</sup>	Acknowledgements	vii
<sup>113</sup>	<b>1 Theoretical Framework</b>	1
<sup>114</sup>	1.1 The Standard Model of particle physics . . . . .	1
<sup>115</sup>	1.1.1 Introduction to the SM and its elementary particles .	2
<sup>116</sup>	1.1.2 Quantum electrodynamics . . . . .	6
<sup>117</sup>	1.1.3 Electroweak interactions . . . . .	8
<sup>118</sup>	1.1.4 Quantum chromodynamics . . . . .	15
<sup>119</sup>	1.1.5 Particle masses . . . . .	18
<sup>120</sup>	1.1.6 Wrap up . . . . .	25
<sup>121</sup>	1.1.7 Cross-section . . . . .	31
<sup>122</sup>	<b>2 Top quark and Higgs boson physics</b>	33
<sup>123</sup>	2.1 Top quark . . . . .	33
<sup>124</sup>	2.1.1 Top-quark discovery . . . . .	34
<sup>125</sup>	2.1.2 Top quark production at LHC . . . . .	36
<sup>126</sup>	2.1.3 Top-quark decay . . . . .	44
<sup>127</sup>	2.1.4 Top quark polarisation . . . . .	45
<sup>128</sup>	2.2 Higgs boson . . . . .	47
<sup>129</sup>	2.2.1 Higgs-boson discovery . . . . .	48
<sup>130</sup>	2.2.2 Higgs boson production at LHC . . . . .	48

131	2.2.3 Higgs-boson decay . . . . .	51
132	2.3 Top quark and Higgs boson interplay . . . . .	52
133	2.3.1 $\mathcal{CP}$ properties in top-Higgs interactions . . . . .	53
134	2.3.2 $t\bar{t}H$ . . . . .	55
135	2.3.3 $tH$ . . . . .	56
136	<b>3 The ATLAS experiment at CERN’s Large Hadron Collider</b>	<b>63</b>
137	3.1 CERN . . . . .	64
138	3.2 Large Hadron Collider . . . . .	65
139	3.2.1 Machine design . . . . .	68
140	3.2.2 Accelerator complex . . . . .	71
141	3.2.3 LHC Experiments . . . . .	71
142	3.2.4 LHC Computing grid . . . . .	73
143	3.2.5 Phenomenology of proton-proton collisions . . . . .	75
144	3.3 ATLAS . . . . .	80
145	3.3.1 Coordinate system . . . . .	82
146	3.3.2 Inner Detector . . . . .	83
147	3.3.3 Calorimeters . . . . .	88
148	3.3.4 Muon Spectrometer . . . . .	93
149	3.3.5 Magnet system . . . . .	95
150	3.3.6 Trigger and Data Acquisition System . . . . .	97
151	3.4 Alignment of the inner detector . . . . .	99
152	3.4.1 Track based alignment . . . . .	101
153	3.4.2 Web-based display for alignment monitoring . . . . .	104
154	3.4.3 Alignment results during Run-2 . . . . .	106
155	<b>4 Recording data and simulating events in ATLAS</b>	<b>109</b>
156	4.1 Data . . . . .	110
157	4.1.1 The Pile-up effect . . . . .	111
158	4.2 Monte Carlo . . . . .	112

159	4.2.1 MC simulations . . . . .	113
160	4.2.2 MC generators . . . . .	115
161	<b>5 Object reconstruction and identification</b>	<b>117</b>
162	5.1 Tracks and vertices . . . . .	117
163	5.2 Electrons and photons . . . . .	120
164	5.3 Muons . . . . .	122
165	5.4 Jets . . . . .	122
166	5.4.1 Jet energy calibration and resolution . . . . .	123
167	5.4.2 Bottom quark induced jets . . . . .	124
168	5.5 Missing transverse energy . . . . .	124
169	<b>6 Search for rare associate <math>tHq</math> production</b>	<b>125</b>
170	6.1 Introduction . . . . .	125
171	6.2 Data and simulated events . . . . .	126
172	6.2.1 Data event samples . . . . .	127
173	6.2.2 Simulated event samples . . . . .	127
174	6.2.3 Single lepton triggers . . . . .	129
175	6.3 Object definition . . . . .	129
176	6.3.1 Triggers . . . . .	129
177	6.3.2 Electrons . . . . .	129
178	6.3.3 Muons . . . . .	129
179	6.3.4 Taus . . . . .	129
180	6.3.5 Jets . . . . .	129
181	6.3.6 $b$ -tagged jet identification . . . . .	129
182	6.3.7 Missing transverse momentum . . . . .	129
183	6.3.8 Overlap removal . . . . .	129
184	6.4 Signal . . . . .	129
185	6.4.1 Signal generation and validation . . . . .	130
186	6.4.2 Parton-level truth validation . . . . .	130

187	6.4.3 Lepton assignment . . . . .	130
188	6.4.4 Top quark and Higgs boson reconstruction . . . . .	135
189	6.5 Background estimation . . . . .	136
190	6.5.1 Fakes estimation . . . . .	136
191	6.5.2 Reducible backgrounds . . . . .	137
192	6.6 Event selection . . . . .	138
193	6.6.1 Preselection . . . . .	139
194	6.6.2 Discriminant variables . . . . .	140
195	6.6.3 BDT . . . . .	140
196	6.6.4 Signal Region . . . . .	141
197	6.6.5 Control Regions . . . . .	141
198	6.7 Systematic uncertainties . . . . .	142
199	6.7.1 Theoretical uncertainties . . . . .	142
200	6.7.2 Modelling uncertainties . . . . .	142
201	6.7.3 Experimental uncertainties . . . . .	142
202	6.8 Fit results . . . . .	142
203	6.8.1 Likelihood fit . . . . .	142
204	6.8.2 Strategy . . . . .	144
205	6.8.3 Fit with Asimov data . . . . .	144
206	6.8.4 Fit to data . . . . .	144
207	6.8.5 Results . . . . .	144
208	6.8.6 Data fit . . . . .	145
209	6.9 Combination results . . . . .	145
210	6.10 Conclusions . . . . .	145
211	<b>7 Conclusion</b>	<b>147</b>
212	<b>Appendices</b>	<b>149</b>
213	<b>A Effect of negative weights</b>	<b>149</b>

214	A.1 Negative weights uncertainties . . . . .	149
215	A.2 Statistical uncertainty of negative weights . . . . .	149
216	A.2.1 Errors in binned histograms . . . . .	151
217	A.3 Negative weights in MVA methods . . . . .	152
218	<b>B Boosted Decision Trees</b>	<b>153</b>
219	B.1 How does a BDT work? . . . . .	153
220	B.1.1 Training . . . . .	155
221	B.1.2 Evaluation / Validation . . . . .	159
222	B.1.3 Application . . . . .	159
223	B.2 Treatment of negative weights . . . . .	159
224	B.2.1 BDT for Lepton origin assignment . . . . .	159
225	B.3 Cross validation and $k$ -folding . . . . .	159
226	B.4 Other considerations about BDTs . . . . .	161
227	B.4.1 Hyperparameters . . . . .	164
228	<b>Abbreviations</b>	<b>170</b>
229	<b>Bibliography</b>	<b>173</b>
230	<b>Summary of the results</b>	<b>187</b>
231	<b>Resumen de la tesis</b>	<b>189</b>
232	1 Marco teórico . . . . .	189
233	1.1 El Model Estándar . . . . .	189
234	1.2 La física del quark top . . . . .	191
235	1.3 La física del bosón de Higgs . . . . .	191
236	2 Dispositivo experimental . . . . .	191
237	2.1 El gran colisionador de hadrones . . . . .	191
238	2.2 El detector ATLAS . . . . .	191
239	3 Búsqueda de procesos $tH$ con un con final $2\ell + 1\tau_{\text{had}}$ . . . . .	192

---

240	3.1	Selección de eventos . . . . .	192
241	3.2	Estimación del fondo . . . . .	192
242	3.3	Fontes de incertidumbre . . . . .	192
243	3.4	Resultados . . . . .	192
244	4	Conclusiones . . . . .	192

<sup>245</sup> **Chapter 1**

<sup>246</sup> **Theoretical Framework**

247  
248  
249  
250  
251

*L'essentiel est invisible pour les yeux.*  
—ANTOINE DE SAINT-EXUPÉRY,  
LE PETIT PRINCE (1943)

<sup>252</sup> **1.1 The Standard Model of particle physics**

<sup>253</sup> Since the very first moment of our history, the humankind has pursued  
<sup>254</sup> the knowledge of nature, has tried to understand and describe how the  
<sup>255</sup> universe works at a fundamental level. In fact, the word physics comes  
<sup>256</sup> from the Greek “ $\varphi\nu\sigma\iota\kappa\eta$ ” which means “nature” [5][6]. Most of the enquires  
<sup>257</sup> regarding this, can be boiled down to two basic questions: What are the  
<sup>258</sup> ultimate building blocks of reality? and which are the rules that govern  
<sup>259</sup> them?

<sup>260</sup> In the 7<sup>th</sup> century BCE, the pre-Socratic philosopher Thales of Miletus  
<sup>261</sup> already proclaimed that every event had a natural cause [7]. Later, to un-  
<sup>262</sup> derstand how the basic components of the matter were formed, the ancient  
<sup>263</sup> Indian philosophers such as Kanada and Dignaga on the 6<sup>th</sup> century BCE  
<sup>264</sup> and Greeks Democritus and Leucippus on the 5<sup>th</sup> century BCE, developed  
<sup>265</sup> the atomism, which comes from “ $\alpha\tau\omega\mu\omega\nu$ ” meaning uncuttable or indivisible  
<sup>266</sup> [8][9].

From then to our days, the search for the minute fragments that comprise the matter and its interactions has led us to the Standard Model (SM) of particle physics, one of the most successful scientific theories cultivated so far. This understanding of the universe can explain phenomena from behaviour of atoms to how stars burn.

### 1.1.1 Introduction to the SM and its elementary particles

Based on Quantum Field Theory (QFT), the SM of particle physics provides the theoretical framework that constitutes what is currently accepted as the best description of particles physics. It aims to explain both all particles of matter and their interactions. The completion of the SM was a collaborative effort of several scientists during the second half of the 20<sup>th</sup>, being the current formulation finalised in the decade of 1970. A representation of the fundamental particles, i.e. particles that are not made of anything else, that compose the SM is presented in Figure 1.1. Most of these particles are unstable and decay to lighter particles within fractions of a second. As the scheme in Figure 1.1 indicates, the 12 fermions have their corresponding 12 anti-fermions and the quarks and gluons carry colour charge.

The SM is a gauge theory based on the symmetry group  $SU(3)_C \otimes SU(2)_L \otimes U(1)_Y$ , which describes all fundamental interactions except from the gravitational force<sup>1</sup>. This theory provides an explanation to strong, weak and electromagnetic interactions via the exchange of the corresponding vector<sup>2</sup> bosons (spin-1 gauge fields). The mediation for the electromagnetic interaction (explicated in 1.1.2) is done by one massless photon ( $\gamma$ ), this force is invariant under the  $U(1)$  symmetry group. While for the weak interactions, guided by  $SU(2)$ , three massive bosons,  $W^+$ ,  $W^-$  and  $Z$ , act as mediators ( $m_{W^\pm} = 80.385 \pm 0.015$  GeV [12] and  $m_Z = 91.1876 \pm 0.02$  GeV [13]). Although the electromagnetic and weak interactions seem completely different at low energies, they are two aspects of the same force and can be described simultaneously by the  $SU(2)_L \otimes U(1)_Y$  symmetry group, which represents the so called Electro-Weak (EW) sector (detailed in Section 1.1.3). The strong force, with its eight massless gluons ( $g$ ), is described by the  $SU(3)_C$  colour group (see Section 1.1.4). All these interactions differ in their magnitude, range and the physical phenomena

---

<sup>1</sup>The gravitational interaction is described by Einstein’s General Relativity (GR) [11].

<sup>2</sup>“Vector bosons” refer to all particles that have spin 1 in contrast to the “scalar boson’s” which have spin 0.

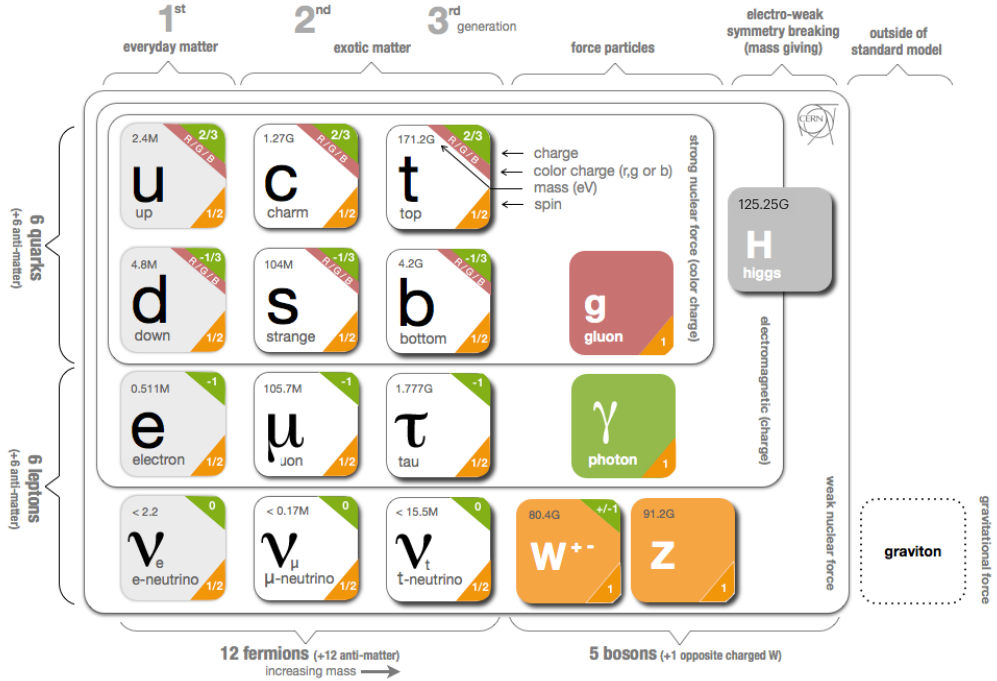


**Figure 1.1:** Fundamental particles of the Standard Model (image modified from [10]).

that describe. These features are summarised in Table 1.1, where not only the interactions of the SM are included but the gravitation is as well.

Apart from the vector bosons, there is one massive scalar boson, the Higgs boson ( $m_H = 125.25 \pm 0.17$  GeV). Through the interaction with this particle, all massive particles of Figure 1.1 gain their mass via the EW spontaneous symmetry breaking. This mechanism was first described by Englert, Brout [14] and Higgs [15], and its summarised in Section 1.1.5.1.

Interaction	Theory	Mediator	Relative strength	Range (m)
Strong	QCD	$g$	1	$10^{-15}$
Electromagnetic	QED/EW	$\gamma$	$1/137$	$\infty$
Weak	EW	$W^\pm, Z$	$10^{-6}$	$10^{18}$
Gravitational	GR	-	$6 \times 10^{-39}$	$\infty$

**Table 1.1:** Typical strength of the fundamental interactions with respect to the strong interaction. Here the strength is understood as the coupling constant or gauge coupling parameter. In GR the gravitational interaction is not a force but the effect of the four-dimensional spacetime curvature and, hence, it has no mediator in this formalism.

309 Before describing the fundamental interactions of the SM in the QFT  
 310 formalism, let's introduce the main two types of particles according to their  
 311 spin, i.e. intrinsic angular momentum: fermions and bosons.

312 **Fermions**

313 The fermions are the particles that follow the Fermi-Dirac statistics, i.e.  
 314 obey the Pauli exclusion principle [16], resulting in a distribution of particles  
 315 over energy levels in which two elements with the same quantum numbers  
 316 cannot occupy the same states. The fermions include all particles with half-  
 317 integer spin: quarks, leptons and baryons. A baryon is a non-fundamental  
 318 particle composed of an odd number of valence quarks may be encountered  
 319 or experienced in everyday life is baryonic matter. Some examples of bary-  
 320 ons are<sup>3</sup> the proton ( $u u d$ ), the neutron ( $d d u$ ),  $\Lambda$  ( $u d s$ ),  $\Lambda_c^+$  ( $u d c$ ) and  
 321  $\Sigma^+$  ( $u u s$ ). Apart from the 3-quark baryons, an exotic pentaquark state  
 322 has been observed at LHCb experiment of the LHC [17].

323 The fundamental fermionic matter (Table 1.2) is organised in the three  
 324 families of leptons and quarks:

$$325 \quad \begin{bmatrix} \nu_e & u \\ e^- & d \end{bmatrix}, \begin{bmatrix} \nu_\mu & c \\ \mu^- & s \end{bmatrix}, \begin{bmatrix} \nu_\tau & t \\ \tau^- & b \end{bmatrix}$$

326 .

327 These three generations, which are defined as the columns in Figure 1.1,  
 328 exhibit the same kind of gauge interactions and they only differ in their  
 329 mass [18]. According to the EW symmetry, each family can be classified as:

$$330 \quad \begin{bmatrix} \nu_\ell & q_u \\ \ell^- & q_d \end{bmatrix} \equiv \begin{pmatrix} \nu_\ell \\ \ell^- \end{pmatrix}_L, \begin{pmatrix} q_u \\ q_d \end{pmatrix}_L, \ell^-_R, q_{uR}, q_{dR}$$

331 (plus the corresponding antiparticles) where the subindices  $L$  and  $R$  stand  
 332 from left and right handed particles respectively. This structure responds to  
 333 the fact that left-handed particles convert different than right-handed ones  
 334 under  $SU(2)$  transformations. The left-handed fields are  $SU(2)_L$  doublets  
 335 and the right-handed ones  $SU(2)_L$  singlets. This difference is explained  
 336 with more detail in Section 1.1.3.

337 The fundamental representation of  $SU(3)$  is a triplet, this is why each  
 338 quark can appear in three different colours, whereas each antiquark can  
 339 exhibit one of the corresponding “anticolours”.

---

<sup>3</sup>Between round brackets, the valence quarks are shown.

Family	Name	Mass	Q
Quarks	Up ( $u$ )	$2.16^{+0.49}_{-0.26}$ MeV	$2/3$
	Down ( $d$ )	$4.67^{+0.48}_{-0.17}$ MeV	$-1/3$
	Charm ( $c$ )	$1.27 \pm 0.02$ GeV	$2/3$
	Strange ( $s$ )	$93^{+11}_{-5}$ MeV	$-1/3$
	Top ( $t$ )	$172.76 \pm 0.30$ GeV	$2/3$
	Bottom ( $b$ )	$4.18^{+0.03}_{-0.02}$ GeV	$-1/3$
Leptons	Electron ( $e^-$ )	$0.5109989461 \pm 0.0000000031$ MeV	$-1$
	Muon ( $\mu$ )	$105.6583745 \pm 0.0000024$ MeV	$-1$
	Tau ( $\tau$ )	$776.86 \pm 0.12$ MeV	$-1$
	Electron neutrino ( $\nu_e$ )	$\nu_e, \nu_\mu, \nu_e$	0
	Muon neutrino ( $\nu_\mu$ )	$\neq$	0
	Tau neutrino ( $\nu_\tau$ )	$\nu_1, \nu_2, \nu_3$	0

**Table 1.2:** Properties of the quarks and leptons. The electric charge, represented by Q, is presented in units of elementary charge ( $1.602 \times 10^{-19}$  C). The  $\nu_1, \nu_2, \nu_3$  are the neutrino mass eigenstates.

340 The SM fermions properties are summarised in Table 1.2. As can be seen  
 341 in its last rows, the neutrino flavour states do no correspond to the mass  
 342 states ( $\nu_1, \nu_2, \nu_3$ ). What happens is that each flavour state is a quantum  
 343 mechanical combination of neutrinos of different masses and viceversa. More  
 344 details about the neutrino masses can be found in a dedicated text in Section  
 345 1.1.6.2

346 The fundamental fermions are usually understood as the fundamental  
 347 building blocks of matter. However, while the building blocks are important,  
 348 there is a point that also has to be taken into account, the force. Without  
 349 force these fermions would not interact which each other. The particles that  
 350 mediate these interactions are the gauge bosons.

### 351 **Bosons**

352 Bosons differ from fermions by obeying the Bose-Einstein statistics, thus,  
 353 bosons are not limited to single occupancy for a determined state. In other  
 354 words, the Pauli exclusion principle is not applied. All particles with integer  
 355 spin are bosons; from the particles shown on the right columns of Figure 1.1  
 356 to the mesons. Mesons, along with baryons, are part of the hadron family,  
 357 i.e. particles composed of quarks (see Section 1.1.4). The particularity  
 358 of mesons is that they are formed from an equal number of quarks and  
 359 antiquarks (usually one of each) bound together by strong interactions.  
 360 Some examples of mesons are  $\pi^+$  ( $u \bar{d}$ ),  $\pi^0$  ( $\frac{u\bar{u}-d\bar{d}}{\sqrt{2}}$ ),  $K^+$  ( $u \bar{s}$ ) and  $J/\psi$   
 361 ( $c \bar{c}$ ).

362 The elementary vector bosons are the force carriers and presented in  
363 Table 1.1 while the Higgs boson is a fundamental particle as well.

364 **Gauge Invariance**

365 Constituting one of the most successful theories of Physics, the SM is able  
366 to provide an elegant mathematical framework to describe the experimental  
367 physics results with great precision. Another key element to understand the  
368 SM is the concept of gauge invariance. As it is illustrated during the rest  
369 of the Section 1.1, by demanding that the Lagrange density (also denoted  
370 as Lagrangian) invariant under local gauge transformations, the existence  
371 of the SM force-carrier bosons ( $\gamma$ ,  $W^+$ ,  $W^-$ ,  $Z$  and  $g$ ).

372 **1.1.2 Quantum electrodynamics**

373 The gauge invariance refers to the invariance of a theory under trans-  
374 formations which the theory is said to posses internal symmetry. The trans-  
375 formations which are applied in all space-time locations simultaneously are  
376 known as “global” transformations while the ones that vary from one point  
377 to another are “local”. Each local symmetry is the basis of a gauge theory  
378 and requires the introduction of its own gauge bosons as it is discussed in  
379 the following pages.

In QFT, particles are described as excitations of quantum fields that satisfy the corresponding mechanical field equations. The Lagrangians in QFT are used analogous to those of classical mechanics, where the equation of motion can be derived from the Lagrangian density function ( $\mathcal{L}$ ) and the Euler-Lagrange equations for fields:

$$\frac{\partial \mathcal{L}}{\partial \phi} - \partial_\mu \frac{\partial \mathcal{L}}{\partial (\partial_\mu \phi)} = 0,$$

380 where  $\partial_\mu = \frac{\partial}{\partial x^\mu}$  denotes the partial derivatives with respect to the four-  
381 vector  $x^\mu$  and  $\phi = \phi(\vec{x}, t)$  is the quantum field of a fermion or boson. The  
382 Lagrangian is used to express the dynamics of the quantum field. In QFT,  
383 Noether’s theorem [19] relates a symmetry in the  $\mathcal{L}$  to a conserved current.

384 The Dirac equation,  $(i\gamma^\mu \partial_\mu - m)\Psi(x) = 0$ , is one of the simplest relativ-  
385istic field equations. Its Lagrangian describes a free Dirac fermion:

$$\mathcal{L}_0 = i\bar{\Psi}(x)\gamma^\mu \partial_\mu \Psi(x) - m\bar{\Psi}(x)\Psi(x), \quad (1.1)$$

386 being  $\Psi$  the wave function (spinor represented by four complex-valued  
387 components) of the particle,  $\gamma^\mu$  are the Dirac or gamma matrices,

<sup>388</sup>  $\{\gamma^0, \gamma^1, \gamma^2, \gamma^3\}$ ,  $m$  the rest-mass of the fermion and  $\bar{\Psi} = \Psi^\dagger \gamma^0$ , the hermitic conjugate of the wave function. The gamma matrices build a set of  
<sup>389</sup> orthogonal basis vectors for covariant vectors in a Minkowski space. The first term of  $\mathcal{L}_0$  is the kinetic term while the second is the mass term.  
<sup>390</sup>  
<sup>391</sup>

This Lagrangian is invariant under  $U(1)$  global transformations such as:

$$\Psi(x) \xrightarrow{U(1)} \Psi'(x) \equiv \exp\{iQ\theta\}\Psi(x), \quad (1.2)$$

<sup>392</sup> where  $Q\theta$  is a real constant. The phase of  $\Psi(x)$  is a pure convention-  
<sup>393</sup> dependent quantity without a physical meaning since the observables de-  
<sup>394</sup> pend on  $|\Psi(x)|^2$ .

However, if  $\theta$  was  $x$  dependent, the transformation 1.2 would be:

$$\Psi(x) \xrightarrow{U(1)} \Psi'(x) \equiv \exp\{iQ\theta(x)\}\Psi(x), \quad (1.3)$$

which is not longer a global transformation but a local transformation instead. The transformation in 1.3 would not let the  $\mathcal{L}_0$  in 1.1 invariant because the derivative in the kinetic term would go as:

$$\partial_\mu \Psi(x) \xrightarrow{U(1)} \exp\{iQ\theta\}(\partial_\mu + iQ\partial_\mu\theta)\Psi(x). \quad (1.4)$$

The gauge principle is the requirement that the  $U(1)$  phase invariance should hold locally. In order to do so, it is necessary to introduce an additional term to the Lagrangian so that when one applies  $\Psi'(x) \equiv \exp\{iQ\theta(x)\}\Psi(x)$ , the  $\partial_\mu\theta$  term is canceled in 1.4. To achieve this invariance, a term with the vector gauge field  $A_\mu$  is inserted. This field transforms as

$$A_\mu(x) \xrightarrow{U(1)} A'_\mu(x) \equiv A_\mu(x) + \frac{1}{e}\partial_\mu\theta \quad (1.5)$$

with a new  $D_\mu$ , which acts as follows:

$$D_\mu\Psi(x) \equiv [\partial_\mu + ieQA_\mu(x)]\Psi(x) \quad (1.6)$$

which transforms like the field:

$$D_\mu\Psi(x) \xrightarrow{U(1)} (D_\mu\Psi)'(x) \equiv \exp\{iQ\theta\}D_\mu\Psi(x).$$

The Lagrangian density can be defined by replacing the partial derivatives in  $\mathcal{L}_0$  (1.1) by the covariant derivative in 1.6:

$$\begin{aligned} \mathcal{L}_{QED} &\equiv i\bar{\Psi}(x)\gamma^\mu D_\mu\Psi(x) - m\bar{\Psi}(x)\Psi(x) \\ &= i\bar{\Psi}(x)\gamma^\mu[\partial_\mu + ieQA_\mu(x)]\Psi(x) - m\bar{\Psi}(x)\Psi(x) \\ &= i\bar{\Psi}(x)\gamma^\mu\partial_\mu\Psi(x) - \bar{\Psi}(x)\gamma^\mu eQA_\mu\Psi(x) - m\bar{\Psi}(x)\Psi(x) \\ &= \mathcal{L}_0 - eQA_\mu\bar{\Psi}(x)\gamma^\mu\Psi(x). \end{aligned} \quad (1.7)$$

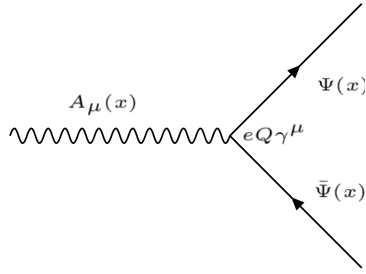


**Figure 1.2:** Three-point interaction vertex of QED.

The resulting Lagrangian is invariant under  $U(1)$  local transformation. When the conversions 1.3 and 1.5 take place, the effects of the transformation are canceled out. Along with the original Lagrangian ( $\mathcal{L}_0$ ), the  $\mathcal{L}_{QED}$  has an additional term describing the interaction between the fermion  $\Psi$  and the gauge field  $A_\mu$  with a strength proportional to the charge  $eQ$ . This term,  $eQA_\mu\bar{\Psi}\gamma^\mu\Psi$ , that has been generated only by demanding the gauge invariance under  $U(1)$ , is not other than the vertex of QED (Figure 1.2).

This new  $A_\mu$  term is the electromagnetic field and its quanta is the photon. A mass term containing  $A^\mu A_\mu$  is forbidden because it would violate the  $U(1)$  local invariance. In consequence, the mediator of the new  $A_\mu$  field, the photon, is predicted to be a massless particle. To make  $A_\mu$  a propagating field it is necessary to add the kinetic term of the field  $A_\mu$ :

$$\mathcal{L}_{kin} \equiv -\frac{1}{4}F_{\mu\nu}(x)F^{\mu\nu}(x), \quad (1.8)$$

where  $F^{\mu\nu} \equiv \partial_\mu A_\nu - \partial_\nu A_\mu$ . The kinetic term  $F_{\mu\nu}F_{\mu\nu}F^{\mu\nu}$  is already invariant under local  $U(1)$  phase transformations. From the QED Lagrangian in 1.7 and the kinetic term in 1.8, the Maxwell equations can be derived to describe electromagnetism, the infinite range<sup>4</sup> interaction that occurs between particles with electrical charge. The  $\mathcal{L}_{QED}$  with this kinetic term is written as:

$$\mathcal{L}_{QED} = \bar{\Psi}(x)(i\gamma^\mu\partial_\mu - m)\Psi(x) - eQ\bar{\Psi}(x)\gamma^\mu A_\mu\Psi(x) - \frac{1}{4}F_{\mu\nu}(x)F^{\mu\nu}(x). \quad (1.9)$$

### 402 1.1.3 Electroweak interactions

#### 403 1.1.3.1 Weak interactions and Symmetries

The weak interaction is mediated by the  $W^+$ ,  $W^-$  and  $Z$  massive gauge bosons. Due their large mass, the range of the interactions is within a scale

<sup>4</sup>Since the photon is (predicted to be) massless, the electromagnetic interaction has an infinite range.

<sup>406</sup> of  $\sim 10^{-18}$  m. It is responsible for radioactive decays and flavour changing<sup>5</sup>  
<sup>407</sup> decays of fermions such as the decay of the muon ( $\mu^- \rightarrow e^- \bar{\nu}_e \nu_\mu$ ).

<sup>408</sup> Another particularity of this interaction is that it is the only interaction  
<sup>409</sup> that violates several fundamental symmetries. There is a relation between  
<sup>410</sup> symmetries and conservations laws which is known as Noether's theorem.  
<sup>411</sup> Classical physics examples of how the symmetries leads to conserved quanti-  
<sup>412</sup> ties are:

- <sup>413</sup> • Invariance under change of time  $\rightarrow$  Conservation of energy
- <sup>414</sup> • Invariance under translation in space  $\rightarrow$  Conservation of momentum
- <sup>415</sup> • Invariance under rotation  $\rightarrow$  Conservation of angular momentum

<sup>416</sup> The three discrete symmetries that are fundamental for the SM formu-  
<sup>417</sup> lation and are always hold for electromagnetic and strong interactions are:

- **Charge conjugation ( $\mathcal{C}$ ):** Replace positive quantum charges by neg-  
 ative charges and vice versa. It does not affect mass, energy, mo-  
 mentum or spin. Essentially, it is a transformation that switches all  
 particles with their corresponding antiparticles.

$$\mathcal{C}\Psi(\vec{r}, t) = \bar{\Psi}(\vec{r}, t)$$

- **Parity ( $\mathcal{P}$ ):** Parity involves a transformation that changes the alge-  
 braic sign of the spatial coordinate system. It does not reverse time,  
 mass, energy or other scalar quantities.

$$\mathcal{P} : \begin{pmatrix} x \\ y \\ z \end{pmatrix} \rightarrow \begin{pmatrix} -x \\ -y \\ -z \end{pmatrix} \quad \mathcal{P}\Psi(\vec{r}, t) = \Psi(-\vec{r}, t)$$

- **Time reversal ( $\mathcal{T}$ ):** Consists in flipping the sign of the time

$$\mathcal{T} : t \rightarrow -t \quad \mathcal{T}\Psi(\vec{r}, t) = \Psi(\vec{r}, -t)$$

<sup>418</sup> The simultaneous combination of this three symmetries mentioned above  
<sup>419</sup> results in the  $\mathcal{CPT}$  symmetry, a profound symmetry of QFT which is  
<sup>420</sup> consistent through all experimental observations [20]. Meanwhile, the  $\mathcal{P}$ -  
<sup>421</sup> symmetry and the  $\mathcal{C}$ -symmetry can be combined to create the  $\mathcal{CP}$ -symmetry,  
<sup>422</sup> the product of the two transformations. The weak interaction violates  $\mathcal{P}$   
<sup>423</sup> and  $\mathcal{C}$  symmetries. It also violates the combined  $\mathcal{CP}$ -symmetry. Therefore,  
<sup>424</sup> through the CPT theorem [21], if the  $\mathcal{CP}$  is violated,  $\mathcal{T}$  is violated as well  
<sup>425</sup> to preserve the  $\mathcal{CPT}$  invariance [22].

---

<sup>5</sup>The leptonic charges are conserved.

426 **Parity violation**

427 Previously theorised by Lee and Yang [23], the confirmation of the non-  
 428 conservation of  $\mathcal{P}$  in weak interactions arrived with the Wu experiment in  
 429 1957 [24]. Studying the beta decay of the Cobalt-60, Wu and collaborators  
 430 found that the neutrino and the antineutrino have the relative orientations  
 431 of spin and linear momentum fixed. The neutrino spin is always opposite  
 432 to the linear momentum, this is called left-handed particles. Meanwhile, for  
 433 the antineutrinos, the momentum is always aligned in the same direction as  
 434 the spin (right-handed particles). This causes the weak interactions which  
 435 emit neutrinos or antineutrinos to violate the conservation of parity.

Only left-handed particles and right-handed antiparticles are sensitive to the weak force. Dirac fermion fields,  $\psi$ , exhibit chiral symmetry and the right and left handed chiral states can be expressed as:

$$\psi_L(x) = \frac{1}{2}(1 - \gamma_5)\psi(x) \equiv P_L\psi(x) \quad (1.10)$$

$$\psi_R(x) = \frac{1}{2}(1 + \gamma_5)\psi(x) \equiv P_R\psi(x) \quad (1.11)$$

with

$$\gamma^5 \equiv \gamma_5 \equiv \gamma^0\gamma^1\gamma^2\gamma^3 = \begin{pmatrix} 1 & 0 \\ 0 & 1 \end{pmatrix}$$

436 where  $P_L$  and  $P_R$  are known as projection operators. The last equality is  
 437 valid in the Dirac representation.

438  **$\mathcal{CP}$  violation**

439 While  $\mathcal{P}$  and  $\mathcal{C}$  are violated in a maximal way by the weak interactions,  
 440 the product of these two discrete transformations,  $\mathcal{CP}$ , is still a good sym-  
 441 metry (left-handed fermions  $\leftrightarrow$  right-handed fermions). Experiences such  
 442 as the Wu experiment respect the  $\mathcal{CP}$  symmetry and, in fact, in the  $\mathcal{CP}$  is a  
 443 symmetry of nearly all the observed phenomena. However, in 1964 Cronin  
 444 and Fitch discovered a slight (2%) violation of the  $\mathcal{CP}$  symmetry in the  
 445 decays of neutral kaons [25]. The  $\mathcal{CP}$  violation plays a fundamental role to  
 446 explain the dominance of matter over antimatter in the present universe.  
 447 More information about the matter-antimatter asymmetry can be found in  
 448 the dedicated text in Section 1.1.6.2.

449 Direct  $\mathcal{CP}$  violation is allowed in the SM if a complex phase is present  
 450 in the CKM matrix (described below). The “direct”  $\mathcal{CP}$  violation is a phe-  
 451 nomenon where the same decay process has a different probability for a  
 452 particle than for an antiparticle. An example of strong global  $\mathcal{CP}$  asym-  
 453 metry observed corresponds to the decay into two kaons and one pion. The  
 454 probability of  $B^+ \rightarrow \pi^+ K^+ K^-$  is 20% higher than for  $B^- \rightarrow \pi^- K^+ K^-$ .

## CKM matrix

The eigenstates that interact through weak interactions, known as “weak eigenstates” ( $d'$ ,  $s'$ ,  $u'$ ), are different from the physically observed mass eigenstates ( $d$ ,  $s$ ,  $u$ ). This make possible the charged-flavour-changing-weak decays trough the Cabibbo-Kobayashi-Maskawa (CKM) matrix. The CKM matrix,  $V_{CKM}$ , describes the mixing between the three generations of quarks in the SM. The coupling of two quarks  $i$  and  $j$  to a  $W$  boson is proportional to the CKM matrix element  $V_{ij}$ .

$$\begin{pmatrix} d' \\ s' \\ u' \end{pmatrix} = \begin{pmatrix} V_{ud} & V_{us} & V_{ub} \\ V_{cd} & V_{cs} & V_{cb} \\ V_{td} & V_{ts} & V_{tb} \end{pmatrix} \begin{pmatrix} d \\ s \\ u \end{pmatrix} \quad (1.12)$$

It is a  $3 \times 3$  unitary matrix described by four independent parameters: three angles ( $\theta_{ij}$ ) and one phase ( $\delta_{13}$ ). Different equivalent representations of the CKM matrix can be found in literature but the Particle Data Group recommends the standard CKM parameterisation:

$$V_{CKM} = \begin{pmatrix} c_{12}c_{13} & -s_{12}c_{13} & s_{13}e^{-i\delta_{13}} \\ -s_{12}c_{23} - c_{12}s_{23}s_{13}e^{i\delta_{13}} & -c_{12}c_{23} - s_{12}s_{23}s_{13}e^{i\delta_{13}} & s_{23}c_{13} \\ s_{12}s_{23} - c_{12}c_{23}s_{13}e^{i\delta_{13}} & -c_{12}s_{23} - s_{12}c_{23}s_{13}e^{i\delta_{13}} & c_{23}c_{13} \end{pmatrix} \quad (1.13)$$

where  $c_{ij} \equiv \cos \theta_{ij}$  and  $s_{ij} \equiv \sin \theta_{ij}$ , with  $i$  and  $j$  labelling the generations ( $i, j \in \{1, 2, 3\}$ ). The angles  $\theta_{12}$ ,  $\theta_{23}$  and  $\theta_{13}$  are known as Euler angles. The complex phase  $\delta_{13}$  allows the  $\mathcal{CP}$  violation [26].

The different elements of the CKM matrix are determined experimentally and are summarised in Table 1.3. As can be seen in this table, the largest values correspond to the diagonal elements of the CKM matrix. This implies that the processes that do not change the flavour are strongly preferred over the family-changing charged currents. For instance, for the top quark, the decay to any of the three down-type quarks is allowed but only  $|V_{td}|^2 \times 100\% = 0.0064\%$  of times will decay to a down quark and  $|V_{ts}|^2 \times 100\% = 0.14\%$  to a strange quark.

### 1.1.3.2 Electroweak unification

At energies above the scale of the mass of the weak vector bosons ( $E_{EW} \sim m_Z \sim m_W \sim 100 \text{ GeV}$ ), the electromagnetic and weak interactions are unified into the Electroweak (EW) force. In other words, electromagnetism and weak interactions are simultaneously described by the symmetry group  $SU(2)_L \otimes U(1)_Y$ . The subindex  $L$  refers to left-handed fields and  $Y$

CKM element	Value
$V_{ud}$	$0.9740 \pm 0.00011$
$V_{us}$	$0.22650 \pm 0.00048$
$V_{cd}$	$0.22636 \pm 0.0048$
$V_{cs}$	$0.97340 \pm 0.011$
$V_{cb}$	$0.04053^{+0.00083}_{-0.00061}$
$V_{ub}$	$0.00361^{+0.00011}_{-0.00009}$
$V_{td}$	$0.00854^{+0.00023}_{-0.00016}$
$V_{ts}$	$0.03978^{+0.00082}_{-0.00060}$
$V_{tb}$	$0.999172^{+0.000024}_{-0.000035}$

**Table 1.3:** Magnitude of the nine elements of the CKM matrix. The mean for the different measurements has been done by [27]. Note how the elements that refer to quarks of the same generation are favoured over the flavour-changing currents.

476 to the weak hypercharge. In contrast, at low energies, this interactions are  
 477 treated as independent phenomena, the electromagnetism is described QED  
 478 and the weak interaction by Fermi's theory.

In the EW model (Glashow-Salam-Weinberg model), two new quantum numbers are assigned to the particles of the SM: the weak isospin ( $\vec{T}$ ) and  $Y$ . Here, the left-handed chiral states of fermions form isospin doublets ( $\chi_L$ ) with  $T_3 = \pm 1/2$  and the right-handed form chiral states are composed of isospin singlets ( $\chi_R$ ) with  $T_3 = 0$ . For a particle,  $T_3$  is the third component of the  $\vec{T}$ , which is related to the electric charge ( $Q$ ) and the  $U(1)$  hypercharge by Gell-Mann-Nishijima relation:

$$Q = T_3 + \frac{1}{2}Y \quad (1.14)$$

479 With this expression, the electromagnetic coupling and the electroweak  
 480 couplings are connected. Having  $\chi_L$  with  $T_3 = \pm 1/2$  and  $\chi_R$  with  $T_3 = 0$   
 481 implies that a  $SU(2)$  weak interaction can rotate left-handed particles (i.e.  
 482 convert a left-handed  $e^-$  into a left-handed  $\nu_e$  emitting a  $W^-$ ) but cannot  
 483 do the same with right-handed.

484 Using the gauge invariance principle it is possible to find the QED and  
 485 QCD Lagrangians, as it is described in Sections 1.1.2 and 1.1.4 respectively.

The free Lagrangian, as in the case of QED and QCD is:

$$\begin{aligned} \mathcal{L} &= i \sum_{j=1}^3 \bar{\Psi}(x) \gamma^\mu \partial_\mu \Psi(x) \\ &= i \sum_{j=1}^3 \bar{\chi}_L(x) \gamma^\mu \partial_\mu \chi_L(x) + i \sum_{k=1}^3 \bar{\chi}_R(x) \gamma^\mu \partial_\mu \chi_R(x) \end{aligned} \quad (1.15)$$

where the wave function  $\Psi$  has been spited into the left isospin doublets  $\chi_L$  and right isospin singlets  $\chi_R$ . The indices  $j$  and  $k$  run over the three generations of the SM. This Lagrangian should be invariant when a gauge transformation under the  $SU(2)_L \times U(1)_Y$  symmetry group in the flavour space is applied:

$$\chi_L(x) \xrightarrow{SU(2)_L \times U(1)_Y} \chi'_L(x) = \exp\{i\alpha^n \tau_n\} \exp\{i\beta y\} \chi_L(x) \quad (1.16)$$

$$\chi_R(x) \xrightarrow{SU(2)_L \times U(1)_Y} \chi'_R(x) = \exp\{i\beta y\} \chi_R(x) \quad (1.17)$$

with  $\alpha, \beta \in \mathbb{R}$  and  $n \in \{1, 2, 3\}$ . This transformation is given by the generators of  $SU(2)_L \times U(1)_Y$ , i.e. the Pauli matrices  $(\tau_n)$  and the weak hypercharge  $y$ . Note that  $SU(2)_L$  transformation,  $\exp\{i\alpha^n \tau_{nu}\}$ , only acts on the doublet fields. This term containing the Pauli matrices is non-abelian like in QCD and, like in QCD, this leads to self-interacting terms.

To ensure invariance under  $SU(2)_L \times U(1)_Y$ , four different gauge fields have to be added (three from  $SU(2)$  and one from  $U(1)$ ). Four is also the correct number of gauge bosons needed to describe EW interactions:  $W^+$ ,  $W^-$ ,  $Z$  and  $\gamma$ . While the three weak isospin currents couple to the triplet of vector bosons  $W_\mu^n$  with  $n \in \{1, 2, 3\}$ , the weak hypercharge couples to an isosinglet  $B_\mu$ . The fields  $W_\mu^1$  and  $W_\mu^2$  are electrically charged whereas  $W_\mu^3$  and  $B_\mu$  are neutral fields. The EW covariant derivative is defined as:

$$D^\mu \chi_{L_j}(x) = [\partial_\mu - ig \frac{\tau_i}{2} W_\mu^i(x) - ig' \frac{y_j}{2} B_\mu(x)] \chi_{L_j}(x) \quad i \in [1, 2, 3] \quad (1.18)$$

$$D^\mu \chi_{R_j}(x) = [\partial_\mu - ig' \frac{y_j}{2} B_\mu(x)] \chi_{R_j}(x), \quad (1.19)$$

where  $g$  and  $g'$  are the interaction couplings to  $W_\mu^i$  isotriplet and the  $B_\mu$  isosinglet.

Using the derivatives in Equations 1.18 and 1.19, the Lagrangian in 1.20 is already invariant under local  $SU(2)_L \times U(1)_Y$  transformations:

$$\mathcal{L} = i \sum_{j=1}^3 \bar{\chi}_L^j(x) \gamma^\mu D_\mu \chi_L^j(x) + i \sum_{k=1}^3 \bar{\chi}_R^k(x) \gamma^\mu D_\mu \chi_R^k(x) \quad (1.20)$$

Finally, if kinetic terms for the gauge bosons are included in 1.20, the EW SM Lagrangian is obtained:

$$\begin{aligned} \mathcal{L}_{EW} = & i \sum_{j=1}^3 \bar{\chi}_L^j(x) \gamma^\mu D_\mu \chi_L^j(x) + i \sum_{k=1}^3 \bar{\chi}_R^k(x) \gamma^\mu D_\mu \chi_R^k(x) \\ & - \frac{1}{4} W_{\mu\nu}^n(x) W_n^{\mu\nu}(x) - \frac{1}{4} B_{\mu\nu}(x) B^{\mu\nu}(x) \end{aligned} \quad (1.21)$$

493 Where the addition of kinetic terms gives rise to cubic and quadratic self-  
 494 interactions among the gauge fields. Note that the mass terms of the fields  
 495 are forbidden in order to ensure local gauge invariance and since the ob-  
 496 served  $W^+$ ,  $W^-$  and  $Z$  bosons have masses different from zero, for the  
 497 moment let's assume that something breaks the symmetry generating the  
 498 observed masses.

499 The in  $\mathcal{L}_{EW}$  in 1.21 can be divided in two different parts according to  
 500 the charge of the bosons: charged currents and neutral currents. Relating  
 501 the charged currents ( $W_\mu^1$  and  $W_\mu^2$ ) to the  $W^+$  and  $W^-$  bosons of the SM  
 502 and the neutral ( $W_\mu^3$  and  $B_\mu$ ) ones with the  $Z$  and  $\gamma$ , it is possible to build  
 503 linear combinations fo the original gauge fields that define the SM bosons.

Therefore, from the charged-current interactions, the  $W^+$  and  $W^-$  bosons are:

$$W^\pm \equiv \frac{1}{\sqrt{2}}(W_\mu^1 \mp i W_\mu^2). \quad (1.22)$$

While for the neutral-current these combinations can be defined as a rotation of the so called Weinberg (or weak mixing) angle  $\theta_W$ :

$$\begin{pmatrix} W_\mu^3 \\ B_\mu \end{pmatrix} \equiv \begin{pmatrix} \cos \theta_W & \sin \theta_W \\ -\sin \theta_W & \cos \theta_W \end{pmatrix} \begin{pmatrix} Z_\mu \\ A_\mu \end{pmatrix}.$$

Rewriting this equation, the photon and  $Z$ -boson fields are

$$A_\mu = B_\mu \cos \theta_W + W_\mu^3 \sin \theta_W Z_\mu = -B_\mu \cos \theta_W + W_\mu^3 \sin \theta_W. \quad (1.23)$$

In order to ensure that this  $A_\mu$  is the one of QED, apart from the Gell-Mann-Nishijima relation (Equation 1.14), it is requiered that the couplings of the  $\gamma$ ,  $W^\pm$  and  $Z$  satisfy the relation:

$$g \sin \theta_W = g' \cos \theta_W = e. \quad (1.24)$$

504 Within the unified EW model, once  $\theta_W$  is known, the mass of  $Z$  is  
 505 specified. Current measurements of  $\theta_W$  give a value of  $\sin^2 \theta_W = 0.2310 \pm$   
 506 0.0005 [28].

507 There is no mass term for the bosons in the EW Lagrangian that has  
 508 been obtained in 1.21 by demanding the  $SU(2)_L \times U(1)_Y$  local invariance,  
 509 which enters in contradiction with the experimental observations for the  
 510  $W$  and  $Z$  bosons ( $m_{Z,W} \sim 80$  GeV). The introduction of such a mass term  
 511 would break the symmetry, however, the it is possible to add the mass for  
 512 the  $W$  and  $Z$  bosons without loosing the properties of the symmetry. The  
 513 method to do so is known as Englert–Brout–Higgs–Guralnik–Hagen–Kibble  
 514 mechanism or, more commonly, just as Higgs mechanism. This mechanism  
 515 is described in Section 1.1.5.



(a) Quark colours combine to be colourless. (b) Antiquark colours also combine to be colourless.

**Figure 1.3:** Colour charge combinations for quarks and antiquarks. Due to the confinement, the hadrons are colourless.

### 516 1.1.4 Quantum chromodynamics

#### 517 1.1.4.1 Quarks and colour

518 QCD is QFT-based theory for describing the strong interactions between  
519 quarks and gluons (partons). This type of interaction is the responsible  
520 of the nuclear force, the one that acts between the protons and neutrons  
521 of atoms binding them together. Without the strong force, the protons  
522 inside the nucleus would push each other apart due to the electromagnetic  
523 repulsion. It also holds the quarks within a hadron together.

QCD is based in the  $SU(3)$  symmetry group and its name derives from the “colour” charge, an analogous to the electric charge of QED but for strong interactions. The colour charge was introduced in 1964 [29] to explain how quarks could coexist within some hadrons apparently having the same quantum state without violating the Pauli exclusion principle. To satisfy the Fermi-Dirac statistics it is necessary to add an additional quantum number, the colour, to the theory. Each species of quark ( $q$ ) may have three different colours ( $q^\alpha$ ,  $\alpha = 1, 2, 3$ ): red, green, blue. Baryons and mesons are described then by the colour singlet combinations:

$$B = \frac{1}{\sqrt{6}} \epsilon^{\alpha\beta\gamma} |q_\alpha q_\beta q_\gamma\rangle \quad M = \frac{1}{\sqrt{3}} \epsilon^{\alpha\beta} |q_\alpha \bar{q}_\beta\rangle .$$

524 Additionally, it is postulated that all hadrons must have a global neutral  
525 colour charge, i.e. the hadrons must be “colourless”. This assumption  
526 is known as confinement hypothesis and it is made to avoid the existence  
527 of non-observed extra states with non-zero colour. It is called colour con-  
528 finement because it implies that it is not possible to observe free quarks  
529 since they carry colour charge and, hence, they have to be confined within  
530 colour-singlet combinations. Figure 1.3 depicts how different colours and  
531 anticolours combine to create the “colourless” state.

532 **1.1.4.2 Gauge invariance for  $SU(3)$**

The dynamics of the quarks and gluons are controlled by the QCD Lagrangian. Using the power of the gauge invariance principle it is possible to deduce  $\mathcal{L}_{QCD}$  similarly to the reasoning developed in Section 1.1.2. Firstly, let's denote a quark field of colour  $\alpha$  and flavour  $f$  by  $q_f^\alpha$ . The vector  $q_f^T \equiv (q_f^1, q_f^2, q_f^3)$  is defined under the  $SU(3)$  colour space, meaning that each dimension corresponds to a colour. The Lagrangian

$$\mathcal{L}_0 = \sum_f \bar{q}_f (i\gamma^\mu \partial_\mu - m_f) q_f \quad (1.25)$$

is invariant under global  $SU(3)$  transformation in the colour space,

$$q_f^\alpha \rightarrow (q_f^\alpha)' = U_\beta^\alpha q_\beta^\beta, \quad UU^\dagger = U^\dagger U = 1, \quad \det U = 1. \quad (1.26)$$

In the  $SU(N)$  algebra,  $SU(N)$  is the group of  $N \times N$  unitary matrices ( $U$ ) which can be written in the form  $U = \exp\{i(\lambda^a/2)\theta_a\}$  with  $a = 1, 2, \dots, N^2 - 1$ . Therefore, the  $SU(3)$  matrices can be written as

$$U = \exp\left\{i\frac{\lambda^a}{2}\theta_a\right\}, \quad (1.27)$$

where the index  $a$  goes from 1 to 8 for the arbitrary parameter  $\theta_a$  and  $\frac{\lambda^a}{2}$ , which denotes the fundamental representation of the  $SU(3)$  algebra. The Einstein notation for summation over repeated indices is implied. The matrices  $\lambda^a$  are traceless and satisfy the commutation relations [18]:

$$\left[\frac{\lambda^a}{2}, \frac{\lambda^b}{2}\right] = if^{abc} \frac{\lambda^c}{2}, \quad (1.28)$$

533 being  $f^{abc}$  the  $SU(3)_C$  structure constants, which are real and totally anti-symmetric.

To satisfy the gauge invariance requirement, the Lagrangian has to be invariant under  $SU(3)$  local transformations, i.e, transformations in which the phase is dependent of the space-time location,  $\theta_a = \theta_a(x)$ . To fulfil the condition, the quark derivatives in the Lagrangian in 1.25 have to be substituted by covariant objects. Since there are eight independent gauge parameters, eight different gauge bosons  $G_a^\mu(x)$  are needed<sup>6</sup>. This bosons are the eight gluons and the new covariant objects are:

$$D^\mu q_f \equiv \left[ \partial_\mu + ig_s \frac{\lambda^a}{2} G_a^\mu(x) \right] q_f \equiv [\partial_\mu + ig_s G^\mu(x)] q_f.$$

---

<sup>6</sup>The eightfold multiplicity of gluons is labeled by a combination of color and anticolor charge (e.g. red–antigreen)

- 535 The compact matrix notation is used  $[G^\mu(x)]_{\alpha\beta} \equiv \left(\frac{\lambda^a}{2}\right)_{\alpha\beta} G_a^\mu(x)$ .

To ensure that the covariant derivative ( $D^\mu q_f$ ) transforms like the  $q_f$ , the transformation of the gauge fields are:

$$D^\mu \rightarrow (D^\mu)' = UD^\mu U^\dagger \quad G^\mu \rightarrow (G^\mu)' = UG^\mu U^\dagger + \frac{i}{g_s}(\partial_\mu U)U^\dagger. \quad (1.29)$$

The quark and gluon fields transform under an infinitesimal local transformation, i.e.  $\theta_a(x) = \delta\theta_a(x) \approx 0$ , the  $SU(3)_C$  unitary matrices (eq. 1.27) can be expressed as their first order expansion:

$$U = \exp\left\{i\frac{\lambda^a}{2}\theta_a(x)\right\} \approx 1 + i\left(\frac{\lambda^a}{2}\right)\delta\theta_a(x)$$

and, consequently, the transformations for the colour-vector field (eq. 1.26) and gluon field (eq. 1.29) become:

$$\begin{aligned} q_f^\alpha \rightarrow (q_f^\alpha)' &= q_f^\alpha + \left(\frac{\lambda^a}{2}\right)_{\alpha\beta}\delta\theta_a q_f^\beta \\ G_a^\mu \rightarrow (G_a^\mu)' &= G_a^\mu - i\frac{i}{g_s}\partial_\mu(\delta\theta_a) - f^{abc}\delta\theta_b G_c^\mu. \end{aligned}$$

- 536 In contrast to the transformation for the photon field in QED (Equation 1.5), the non-commutativity<sup>7</sup> of the  $SU(3)_C$  matrices give rise to an  
 537 additional term involving the gluon fields themselves ( $-f^{abc}\delta\theta_b G_c^\mu$ ), as the  
 538 relation 1.28 expresses. For constant  $\delta\theta_a$ , the transformation rule for the  
 539 gauge fields is expressed in terms of the structure constants  $f^{abc}$ ; thus, the  
 540 gluon fields belong to the adjoint representation for the colour group. There  
 541 is a unique coupling at  $SU(3)_C$ ,  $g_s$ . All the colour-triplet flavours couple to  
 542 the gluon fields with exactly the same interaction strength.

It is necessary to introduce the corresponding fields strengths to build a gauge-invariant kinetic terms for the gluon fields.

$$\begin{aligned} G^{\mu\nu} &\equiv -i\frac{-i}{g_s}[D^\mu, D^\nu] = \partial_\mu G^\nu - \partial_\nu G^\mu + ig_s[G^\mu, G^\nu] \equiv \frac{\lambda^a}{2}G_a^{\mu\nu}(x) \\ G_a^{\mu\nu} &\equiv \partial_\mu G_a^\nu - \partial_\nu G_a^\mu - g_s f^{abc}G_b^\mu G_c^\nu. \end{aligned}$$

Under a  $SU(3)_C$  transformation,

$$G^{\mu\nu} \rightarrow (G^{\mu\nu})' = UG^{\mu\nu}U^\dagger \quad (1.30)$$

---

<sup>7</sup>Because the generators of  $SU(3)$  do not commute, QCD is known as non-Abelian gauge theory.

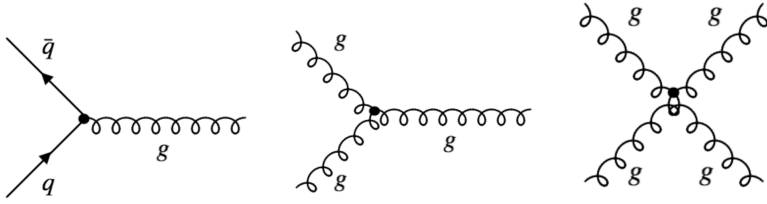


**Figure 1.4:** The predicted QCD interaction vertices arising from the requirement of  $SU(3)_C$  local gauge invariance. The presence of the triples and quadruple gluon vertices is possible to the Non-Abelian nature of  $SU(3)_C$ .

and the colour trace  $\text{Tr}(G^{\mu\nu}G_{\mu\nu}) = \frac{1}{2}G^{\mu\nu}G_{\mu\nu}$  remains invariant. Normalising the gluon kinetic term, the  $SU(3)_C$  invariant QCD Lagrangian is obtained:

$$\mathcal{L}_{QCD} \equiv -\frac{1}{4}G_a^{\mu\nu}G_{\mu\nu}^a + \sum_f \bar{q}_f(i\gamma^\mu D_\mu - m_f)q_f. \quad (1.31)$$

544 Note how the gluon-gluon vertex is find by demanding the gauge invari-  
 545 ance under local  $SU(3)_C$  transformation. A mass term is forbidden for the  
 546 gluon fields by the  $SU(3)_C$  gauge symmetry because a something of the form  
 547  $\frac{1}{2}m_G^2 G_a^\mu G_\mu^a$  would not be invariant under the transformation in 1.29. The  
 548 gluons are, then, predicted by the theory to be spin-1 massless particles.

549 Thanks to the colour symmetry properties, this Lagrangian looks very  
 550 simple and all its interactions depend on the strong coupling constant,  $g_s$ .  
 551 In contrast to the Lagrangian derived for QED (eq 1.7), in  $\mathcal{L}_{QCD}$  the boson  
 552 field have a self-interacting term. This gluon self-interactions give rise to the  
 553 triple and quadratic gluon vertex (center and right diagrams in Figure 1.4).  
 554 This self-interactions among the gluon fields can explain features the asymp-  
 555 totic freedom and confinement, properties that were not present in QED.  
 556 The asymptotic freedom causes interactions between particles to become  
 557 asymptotically weaker as the energy scale increases and the corresponding  
 558 length scale decreases. The confinement implies that the strong forces in-  
 559 crease with the distance, therefore, as two colour charges are separated,  
 560 at some point it becomes energetically favorable for a new quark-antiquark  
 561 pair to appear rather than keep getting further. This new quarks bond with  
 562 the previous two, preventing single quarks to be isolated. This mechanism,  
 563 depicted in Figure 1.5, explains why the strong interaction is responsable  
 564 for keeping the quarks together forming hadrons.

### 565 1.1.5 Particle masses

For the QED Lagrangian,  $\mathcal{L}_{QED}$  (eq. 1.9), it is clear how the mass of the photon must be zero in order to satisfy the  $U(1)$  local gauge symmetry



**Figure 1.5:** The QCD colour confinement explains the inseparability of quarks inside a hadron in spite of investing ever more energy. In this example, the mechanism is shown for a meson.

because, if a mass term for the vector gauge field  $A_\mu$  is included, the  $\mathcal{L}_{QED}$  would be:

$$\mathcal{L}_{QED} = \bar{\Psi}(x)(i\gamma^\mu \partial_\mu - m)\Psi(x) - eQ\bar{\Psi}(x)\gamma^\mu A_\mu\Psi(x) - \frac{1}{4}F_{\mu\nu}(x)F^{\mu\nu}(x) + \frac{1}{2}m_\gamma^2 A_\mu A^\mu$$

and, with the  $U(1)$  transformation in Equation 1.5, the new mass term becomes:

$$\frac{1}{2}m_\gamma^2 A_\mu A^\mu \rightarrow \frac{1}{2}m_\gamma^2 (A_\mu + \frac{1}{e}\partial_\mu \theta)(A^\mu + \frac{1}{e}\partial^\mu \theta) \neq \frac{1}{2}m_\gamma^2 A_\mu A^\mu.$$

566 Confirming that the photon mass term is not invariant under local  $U(1)$   
 567 and, consequently, that the photon must be massless to satisfy the gauge  
 568 invariance. Experimental efforts to measure the mass of the photon have  
 569 set an upper limit of  $m_\gamma \leq 1 \times 10^{-18}$  eV [30].

570 With the Lagrangian of QCD in Equation 1.31 happens the same, the  
 571 mass term for the gluon fields are forbidden by the  $SU(3)_C$  gauge symmetry.  
 572 Therefore, the mediating bosons for the strong interactions are massless as  
 573 well (experimentally, a mass as large as upper limits of a few MeV have  
 574 been set, see [31]).

575 While the prohibition of mass terms for the bosons of QED and QCD is  
 576 not a problem, this requirement also applies to the  $SU(2)_L$ . This condition  
 577 enters into open contradiction with the measurements of large masses for  
 578 the  $W$  and  $Z$  bosons of weak interactions.

579 For weak interactions, the problem of massless particles do not only  
 580 affect the bosons. Since under the  $SU(2)_L$  transformations left-handed  
 581 particles transform as weak isospin doubles and right-handed particles as  
 582 isospin singlets, the mass term of a spinor field  $\Psi$  written as chiral states  
 583 also breaks the required gauge invariance:  $-m\bar{\Psi}(x)\Psi(x) = -m\bar{\Psi}(x)(P_R +$   
 584  $P_L)\Psi(x) = -m(\bar{\Psi}_R(x)\Psi_L(x) + \bar{\Psi}_L(x)\Psi_R(x))$

585 The Higgs mechanism describes how both the  $W$  and  $Z$  bosons and the  
 586 fermions acquire mass without breaking the local gauge symmetry of the  
 587 SM.

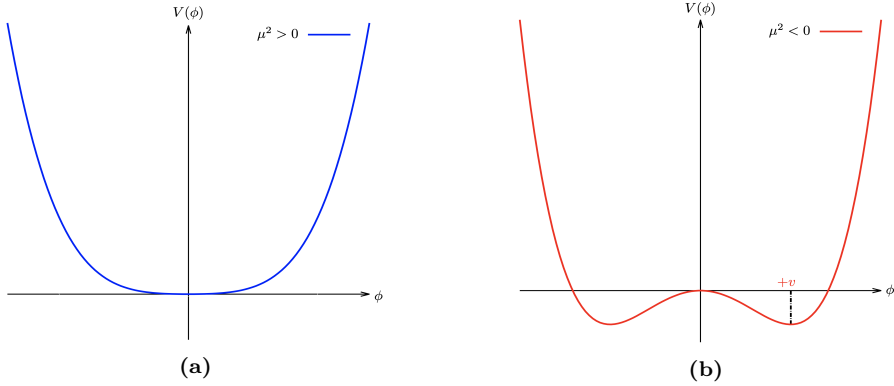


**Figure 1.6:** The potential  $V(\phi)$  of Lagrangian 1.32 for (a)  $\mu^2$  positive and (b) negative.

### 588 1.1.5.1 The Higgs mechanism

#### Goldstone theorem and spontaneous symmetry breaking

For a scalar field  $\phi$  with a Lagrangian of the form:

$$\mathcal{L} = \frac{1}{2}\partial_\mu\phi_i\partial^\mu\phi_i - V(\phi) \text{ where } V(\phi) = \frac{1}{2}\mu^2\phi_i\phi_i + \frac{1}{4}\lambda(\phi_i\phi_i)^2. \quad (1.32)$$

This Lagrangian is invariant under  $\phi_i \rightarrow \phi'_i = R_{ij}\phi_j$ , where  $R_{ij}$  are rotational matrices in 4-dimensions. The mass term is the one with  $\phi_i\phi_i$  and the parameter  $\lambda$  has to be positive for  $\mathcal{L}$  to describe a physical system, if  $\lambda < 0$  the potential is unbounded from below. Contrary, the parameter  $\mu^2$  can be either positive or negative. As depicted in Figure 1.6a, if  $\mu^2 > 0$ , the vacuum expectation value (i.e. minimum of potential) is located at the origin  $\phi_0$  and this  $\mathcal{L}$  would describe a spin-0 particle of mass  $\mu$ . However, if  $\mu^2 < 0$ , the potential  $V(\phi)$  has the form of Figure 1.6a and  $\mathcal{L}$  would not represent anymore the Lagrangian of a particle of mass  $\mu$ . The vacuum expectation value is now multivalued:

$$\phi_0 = \pm\sqrt{-\frac{\mu^2}{\lambda}} \equiv \pm v.$$

Expanding the field around the minima at  $\phi_i = (0, 0, 0, v)$ , the  $\mathcal{L}$  becomes:

$$\begin{aligned} \mathcal{L} = & \frac{1}{2}\partial_\mu\sigma\partial^\mu\sigma + \mu^2\sigma^2 - \sqrt{\mu^2\lambda}\sigma^3 - \frac{1}{4}\lambda^4 \\ & + \frac{1}{2}\partial_\mu\pi_i\partial^\mu\pi_i - \frac{1}{4}\lambda(\pi_i\pi_i)^4 - \lambda v\pi_i\pi_i\sigma - \frac{1}{2}\pi_i\pi_i\sigma^2, \end{aligned} \quad (1.33)$$

589 where  $i$  runs from 1 to 3. Here  $\sigma = \phi_4 - v$  and  $\pi_i = \phi_i$  are new boson fields,  
590 being the latter massless and the former with a mass of  $m_\sigma^2 = -2\mu^2$ . The

591 new terms break the original symmetry because the symmetry of the Lag-  
 592 rangian is not longer a symmetry of the vacuum, it has been spontaneously  
 593 broken. One massive  $\sigma$  boson and three massless  $\pi_i$  bosons with a residual  
 594  $O(3)$  symmetry have appeared. This is a consequence of the Goldstone the-  
 595 oreom which states that “for a continuous symmetry group  $\mathcal{G}$  spontaneously  
 596 broken down to a subgroup  $\mathcal{H}$ , the number of broken generators is equal  
 597 to the number of massless scalars that appear in the theory” [32]. There-  
 598 fore, since the  $O(N)$  group has  $N(N - 1)/2$  generators, the  $O(N - 1)$  has  
 599  $(N - 1)(N - 2)/2$  and, hence,  $N - 1$  Goldstone bosons appear. The example  
 600 shown is for  $N = 4$ .

### The Higgs mechanism in the SM - Bosons

To apply this mechanism to the SM, it is necessary to generate mass for the  $W^+$ ,  $W^-$  and  $Z$  bosons while keeping the photon massless. In order to do so, the EW symmetry group  $SU(2)_L \times U(1)_Y$  has to be broken into a  $U(1)$  subgroup describing electromagnetism. A gauge-invariant interaction that gives masses to fermions without mixing chiral components is introduced by defining a  $SU(2)$  isospin doublet of complex scalar field with hypercharge  $Y = 1$ :

$$\Phi = \begin{pmatrix} \phi^+ \\ \phi_0 \end{pmatrix}.$$

Being  $\phi^+$  positively charged and  $\phi^0$  neutral. The Lagrangian  $\mathcal{L}_{Higgs}$  has to be added to the  $\mathcal{L}_{EW}$  in 1.21.

$$\mathcal{L}_{Higgs} = (D_\mu \Phi)^\dagger (D^\mu \Phi) - V(\Phi) \text{ where } V(\Phi) = \mu^2 \Phi^\dagger \Phi + \lambda (\Phi^\dagger \Phi)^2,$$

with  $\lambda > 0$  required for vacuum stability. When  $\mu^2 > 0$ , the minimum of the potential occurs when both fields ( $\phi^+$  and  $\phi^0$ ) are at zero. If  $\mu^2 < 0$ , the minimum of the potential has an infinite number of degenerate states that satisfy  $\Phi^\dagger \Phi = \mu^2/2\lambda$  and the physical vacuum state will correspond to any particular point on the circle of Figure 1.7. Having to chose a particular point breaks the global  $U(1)$  symmetry of the Lagrangian. Without loss of generality, in this scenario, the ground state  $\Phi_0$  can be chosen to be:

$$\Phi_0 = \frac{1}{\sqrt{2}} \begin{pmatrix} 0 \\ v \end{pmatrix} \text{ where } v = 2\sqrt{\frac{\mu^2}{\lambda}}.$$

601 being  $v$  the vacuum expectation value. This defines the already mentioned  
 602 circle in the minimum of  $V(\Phi)$  in the  $\mu^2 < 0$  scenario.

The Lagrangian density must be formulated in terms of deviations from one of these ground states. This can be done by introducing an excitation,  $h(x)$ , that can be understood as a small deviation of the field from the

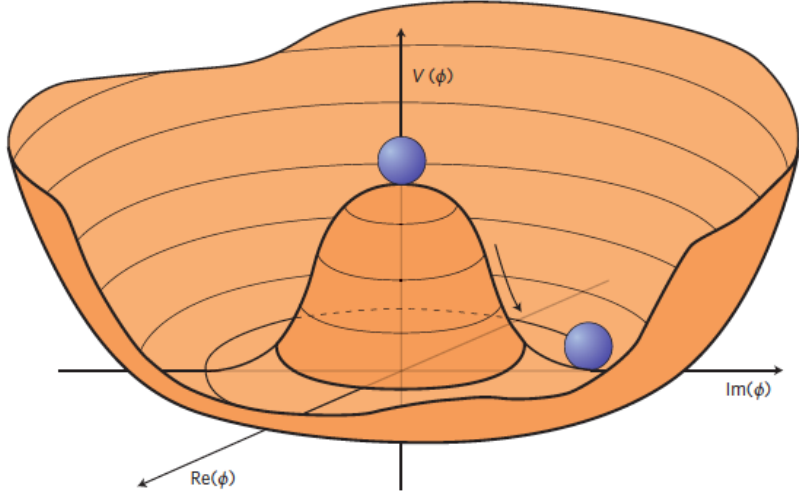


**Figure 1.7:** An illustration of the Higgs potential  $V(\Phi)$  in the case of  $\mu^2 < 0$ . Choosing any particular point in the circle defined by  $v$  spontaneously breaks the  $U(1)$  rotational symmetry. This type of potential is frequently called “Mexican hat”.

ground state. Accordingly, the fields can be expanded around the minimum as:

$$\Phi = \frac{1}{\sqrt{2}} \begin{pmatrix} 0 \\ v + h(x) \end{pmatrix} \exp\{i\chi(x)\}.$$

The new field  $\chi(x)$  can be set to zero in the so called “unitary gauge”.

$$\Phi = \frac{1}{\sqrt{2}} \begin{pmatrix} 0 \\ v + h(x) \end{pmatrix}. \quad (1.34)$$

Expanding the covariant derivative of the  $\mathcal{L}_{Higgs}$ :

$$\begin{aligned} (D_\mu \Phi)^\dagger (D^\mu \Phi) &= \left| \left( \partial_\mu + ig \frac{\tau^k}{2} W_\mu^k(x) + ig' \frac{y}{2} B_\mu \right) \right|^2 \\ &= \frac{1}{2} \left| \begin{pmatrix} \partial_\mu + i\frac{1}{2}(gW_\mu^3 + g'\frac{y}{2}B_\mu) & i\frac{g}{2}(W_\mu^1 - iW_\mu^2) \\ i\frac{g}{2}(W_\mu^1 - iW_\mu^2) & \partial_\mu - i\frac{1}{2}(gW_\mu^3 - g'\frac{y}{2}B_\mu) \end{pmatrix} \begin{pmatrix} 0 \\ v + h \end{pmatrix} \right|^2 \\ &= \frac{1}{2} (\partial_\mu h)^2 + \frac{1}{8} (v + h)^2 |W_\mu^1 - iW_\mu^2|^2 \\ &\quad + \frac{1}{8} (v + h)^2 |gW_\mu^3 - g'B_\mu| + (\text{interaction terms}), \end{aligned}$$

where the  $\tau_k$  with  $k = 1, 2, 3$  are the Pauli Matrices. In this equation there are terms mixing the  $W^3$  and the  $B_\mu$  fields that, by using the physical fields defined in Equation 1.1.3.2, should disappear since the physical bosons do not mix. Applying the Relation 1.1.3.2 into the covariant derivative,

$$(D_\mu \Phi)^\dagger (D^\mu \Phi) = \frac{1}{2} + \frac{g^2 v^2}{4} W_\mu^+ W^{-\mu} + \frac{g^2 v^2}{8 \cos^2 \theta_W} Z_\mu Z^\mu + 0 A_\mu A^\mu,$$

the  $W^+$ ,  $W^-$  and  $Z$  bosons have finally acquired mass. Through the Higgs mechanism, their masses within the SM are:

$$M_W = \frac{1}{2}gv \quad M_Z = \frac{1}{2} \frac{gv}{\cos \theta_W}$$

603 Additionally, a new scalar field  $h(x)$  has appeared with its correspondent  
 604 mass term, the Higgs field. Note that the  $h(x)$  was introduced as a perturba-  
 605 tion from the ground state of the Higgs potential  $V(\Phi)$ , so the Higgs boson  
 606 can be understood as an excitation of the Higgs potential. Apart from cou-  
 607 plings to the electroweak gauge fields, the Higgs field has also self-interaction  
 608 vertices. The mass of this boson is  $m_H = \sqrt{2}\mu$ .

With this covariant term, the Higgs Lagrangian density of the system is obtained:

$$\begin{aligned} \mathcal{L}_{Higgs} = & \frac{1}{2}(\partial_\mu h)(\partial^\mu h) + \frac{g}{4}(v+h)^4 W_\mu W^\mu + \frac{g^2}{8\cos^2 \theta_W} (v+h)^2 Z_\mu Z^\mu \\ & + \frac{\mu^2}{2}(v+h)^2 - \frac{\lambda}{16}(v+h)^4 \end{aligned}$$

and expressing it in terms of the boson masses and coupling parameters, it can be written as:

$$\begin{aligned} \mathcal{L}_{Higgs} = & \frac{1}{2}(\partial_\mu h)(\partial^\mu h) - \frac{1}{2}m_H^2 h^2 + \frac{1}{2}m_W W_\mu W^\mu + \frac{1}{2}m_Z Z_\mu Z^\mu + g m_W h W_\mu W^\mu \\ & + \frac{g^2}{4} W_\mu W^\mu + g \frac{m_Z}{2\cos \theta_W} h Z_\mu Z^\mu - g^2 \frac{1}{4\cos^2 \theta_W} h^2 Z_\mu Z^\mu - g \frac{m_H^2}{4m_W} h^3 \\ & - g^2 \frac{m_H^2}{32m_W^2} h^4 + \text{const.} \end{aligned} \tag{1.35}$$

609 As can be seen in the Lagrangian 1.35, the coupling strengths of the  $W$  and  
 610  $Z$  fields to the Higgs are proportional to  $m_W$  and  $m_Z$  respectively.

### The Higgs mechanism in the SM - Fermions

The Higgs mechanism for spontaneous symmetry breaking of the  $SU(2)_L \times U(1)_Y$  gauge group of the SM generates the masses of the  $W^\pm$  and  $Z$  bosons. For originating the mass of the fermions without violating the EW gauge symmetry a similar procedure is carried but taking into account that the left-handed particles transform different than the right-handed. To do so, additional terms including the Yukawa couplings are added into the Lagrangian. These terms are of the form:

$$-y_f (\bar{\chi}_L^f \Phi \chi_R^f + \bar{\chi}_R^f \Phi^\dagger \chi_L^f),$$

where the  $f$  superindex runs over all quarks and charged leptons. It is usual to express the second part of the sum just as “plus hermitic conjugate” (“+ h.c.”). Note that the hermitic conjugate part is necessary to ensure that expression fulfils the requirement for a hermitian operator to be self-adjoint in a complex Hilbert space. The different  $y_f$  constants are known as Yukawa couplings of the particle  $f$  to the Higgs field. The Higgs doublet is denoted by  $\Phi$ . For the electron  $SU(2)$  doublet, the element with this coupling can be written as:

$$\mathcal{L}_e = -y_e \left[ (\bar{\nu}_e \bar{e})_L \begin{pmatrix} \phi^+ \\ \phi^0 \end{pmatrix} e_R + \bar{e}_R (\phi^{+*} \phi^{0*}) \begin{pmatrix} \nu_e \\ e \end{pmatrix}_L \right]. \quad (1.36)$$

Here,  $y_e$  is the Yukawa coupling of the electron to the Higgs boson. After spontaneously breaking the symmetry as it is done in eq. 1.34, the Lagrangian in 1.36 becomes:

$$\mathcal{L}_e = \frac{-y_e}{\sqrt{2}} v (\bar{e}_L e_R + \bar{e}_R e_L) + \frac{-y_e}{\sqrt{2}} h (\bar{e}_L e_R + \bar{e}_R e_L) \quad (1.37)$$

The  $y_e$  is not predicted by the Higgs mechanism, but can be chosen to be consistent with the observed electron mass ( $m_e$ ) so that  $y_e = \sqrt{2} m_e / v$ . Using this relation, the Lagrangian in 1.37 becomes:

$$\mathcal{L}_e = -m_e \bar{e} e - \frac{m_e}{v} \bar{e} e h \quad (1.38)$$

611 The first element of the Lagrangian in 1.38 gives mass to the electron and  
 612 gives rise to the coupling of the electron to the Higgs fields in its non-  
 613 zero vacuum expectation. The second term represents the coupling of the  
 614 electron and the Higgs boson itself.

615 The non-zero vacuum expectation value occurs only in the neutral part  
 616 of the Higgs doublet (the lower in  $\Phi = \begin{pmatrix} \phi^+ \\ \phi^0 \end{pmatrix}$ ) due to the form in the  
 617 ground state in 1.34. This implies that the combination  $\bar{\chi}_L^f \Phi \chi_R^f + \bar{\chi}_R^f \Phi^\dagger \chi_L^f$   
 618 can only generate masses for the fermions in the lower component of an  
 619  $SU(2)$  doublet, i.e. the charged leptons and the down type quarks. Putting  
 620 aside the procedure to give mass to the up-type quarks, this explains why  
 621 the neutrinos do not get mass through the Higgs mechanism.

For the up-type quarks, a gauge invariant term can be constructed from  $\bar{\chi}_L^f \Phi_c \chi_R^f + \bar{\chi}_R^f \Phi_c^\dagger \chi_L^f$ :

$$\mathcal{L}_u = y_u (\bar{u} \bar{d})_L \begin{pmatrix} -\phi^{0*} \\ \phi^- \end{pmatrix} u_R + \text{h.c.}$$

Applying the symmetry breaking:

$$\mathcal{L}_u = \frac{-y_u}{\sqrt{2}} v (\bar{u}_L u_R + \bar{u}_R u_L) + \frac{-y_u}{\sqrt{2}} h (\bar{u}_L u_R + \bar{u}_R u_L)$$

with a Yukawa coupling between the up quark and the boson  $y_u = \sqrt{2} m_u/v$ , resulting in:

$$\mathcal{L}_u = -m_u \bar{u} u - \frac{m_u}{v} \bar{u} u h.$$

Therefore, for Dirac fermions, mass terms that let the Lagrangian invariant under local gauge transformations can be constructed from

$$\mathcal{L} = -y_f [\bar{\chi}_L^f \Phi \chi_R^f + (\bar{\chi}_R^f \Phi \chi_L^f)^\dagger] \quad \text{or} \quad \mathcal{L} = y_f [\bar{\chi}_L^f \Phi_c \chi_R^f + (\bar{\chi}_R^f \Phi_c \chi_L^f)^\dagger].$$

The left Lagrangian is used for the leptons and down-type quarks, while the right one is used for the up-type quarks. These elements give rise not only to the mass of the fermions but also to the interaction strengths between these fermions and the Higgs boson. The Yukawa coupling of the fermions to the Higgs field is given by:

$$y_f = \sqrt{2} \frac{m_f}{v}, \quad (1.39)$$

where the Higgs vacuum expectation value is fixed by the Fermi coupling  $G_F$  and is measured to be  $v = \sqrt{2} G_F \approx 246.22 \text{ GeV}$ . The  $G_F$  is measured from the  $\mu^+$  lifetime [33]. The  $G_F$  is also used to determine the magnitude of the elements in the CKM matrix.

The value of fermionic masses is not predicted by the SM but obtained through experimental observations. Given the  $m_{top} = 172.76 \pm 0.30 \text{ GeV}$ , it is of particular interest the Yukawa coupling of the top quark to the Higgs field,  $y_t$ , which is almost exactly equal to one. It is important to verify this because deviation of the measured  $y_t$  from the SM prediction would be a proof of new physics.

### 1.1.6 Wrap up

Perhaps the ultimate and definitive (if talking about definitive makes any sense) theory of particle physics is a simple equation with a small number of free parameters. Meanwhile, the SM is here, and while it is not the ultimate theory, it is unquestionably one of modern physics' greatest successes. Despite its achievements, many questions remain unsolved.

#### 1.1.6.1 The parameters of the Standard Model

The SM contains 25 free parameters that must be determined through observation and experimentation. These are the masses of the twelve fermions (assuming color variations and antiparticles are not viewed as separate

642 fermions) or, more precisely, the twelve Yukawa couplings to the Higgs field  
 643 ( $m_{\nu_1}, m_{\nu_2}, m_{\nu_3}, m_e, m_\mu, m_\tau, m_u, m_d, m_c, m_s, m_t$  and  $m_b$ )

644 The three coupling constants of describing the strength of the gauge  
 645 interactions ( $g, g'$  and  $g_s$ ) and the two parameters describing the Higgs potential  
 646 ( $\mu$  and  $\lambda$ ) or, equivalently, its vacuum expectation value  $v$  and the  
 647 Higgs mass  $m_h$ . The three mixing angles and the complex phase of the CKM  
 648 matrix and the four of the PMNS matrix ( $\theta_{12}, \theta_{13}, \theta_{23}, \rho_{13}, \theta'_a, \theta'_b, \theta'_c$  and  $\theta'_d$ ),  
 649 which mixing of neutrino-mass eigenstates with neutrino-flavour eigen-  
 650 states).

651 From the 25 free parameters of the SM, 14 are associated to the Higgs  
 652 field, eight with the flavour sector and only three with the gauge interac-  
 653 tions.

#### 654 1.1.6.2 Problems with the Standard Model

655 While the SM is very good theory that has passed rigorous testing, this  
 656 is not the ending of the story, there are several limitations of the SM and  
 657 a variety phenomena that it does not explain. The SM does not cover all  
 658 questions in the universe and, hence, physicist continue looking for better  
 659 theories to explain more. There is a long list of small and minor issues with  
 660 the SM in the following pages only the most relevant ones are described.

#### 661 Gravity

662 Gravity is the first force that any person learns about and the one known  
 663 by the humankind for the most time. The SM describes all the other funda-  
 664 mental interactions but this one. In the Table 1.1, the four forces are  
 665 presented along with the theories to describe them. While QCD, QED and  
 666 EW interactions are part of the SM, the GR is not. GR is a geometric the-  
 667 ory that currently describes the gravitation in modern physics. Some of the  
 668 suggested solutions to integrate gravitational interactions in the SM consist  
 669 in postulating a new force carrier particle, the “graviton”, that mediates  
 670 this interaction in a similar way to how the gauge bosons were proposed.  
 671 Other explanations state that the gravity can only be described by a deeper  
 672 theory in which the time-space structure is not flat like it is in the SM but  
 673 dynamic.

#### 674 Neutrino masses

675 According to the SM the neutrinos are massless, nevertheless, many ex-  
 676 periments confirm that this is not true [34]. This is due to a property of  
 677 neutrinos that allows them to change their flavour while traveling through

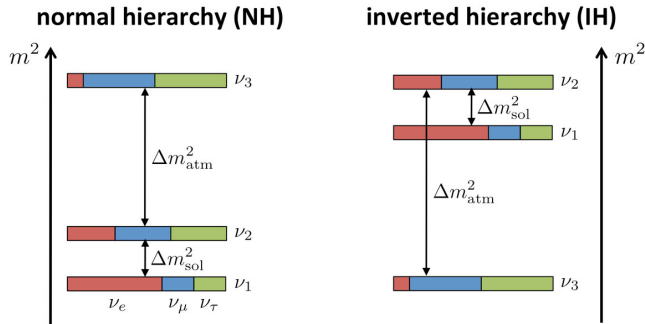


**Figure 1.8:** Two potential mass orderings of neutrinos are the normal ordering (normal hierarchy) and the inverted ordering (inverted hierarchy).

the space, this feature is known as “neutrino oscillations”. Each of the three neutrino flavours ( $\nu_e$ ,  $\nu_\mu$ ,  $\nu_\tau$ ) is a linear combination of three discrete neutrino-mass eigenstates ( $\nu_i$  with  $i \in \{1, 2, 3\}$ ) with mass eigenvalues ( $m_i$ ). While the neutrino oscillation experiments could probe the squared neutrino-mass eigenvalues ( $\Delta m_{ij}^2$ ), both the total scale of the masses and the sign of  $\Delta m_{ij}$  remains as some the most relevant open questions in particle physics. Regarding to the sign of  $\Delta m_{ij}$ , it is known that the mass of  $\nu_2$  is slightly higher than  $\nu_1$  ( $\Delta m_{21}^2 \equiv m_2^2 - m_1^2 \sim 10^{-4}$  eV) but for the third mass eigenstate it has not been measured yet whether it is greater (normal ordering) or lower (inverted ordering) than the other two, as it is depicted in Figure 1.8. Nevertheless, the absolute square difference is known ( $\Delta m_{31}^2 \equiv |m_3^2 - m_1^2| \sim 10^{-3}$  eV).

Non-zero neutrino masses opened an interesting portal on beyond SM physics and, even though neutrinos are very elusive when it comes to detect them, some next-generation experiments such as Dune are very promising when it comes to set competitive and model independent limits on neutrino masses.

Regarding to the nature of this mass, one could add mass terms to the SM as it is done in Section 1.1.5.1 for the up-type quarks but the origin of the neutrino masses is still not known. Also, if neutrinos gained mass through Yukawa interaction, it would imply the presence of right-handed neutrinos, which has not been observed.

## 700 Matter-antimatter asymmetry

In principle, the Big Bang should have produced an equal amount of matter and antimatter which would all have then annihilated, leaving behind an empty Universe filled with EM radiation. However, everything we see now is essentially totally constituted of matter, from the tiniest life forms on

705 Earth to the greatest celestial objects. In comparison, there isn't a lot of  
 706 antimatter around.

707 By looking at the CMB radiation, which contain the residual photons  
 708 of the Big Bang, researchers have determined that there was a symmetry  
 709 between the matter and antimatter content in the early universe. For every  
 710  $3 \times 10^9$  antimatter particles, there were  $3 \times 10^9$  and 1 matter particles. The  
 711 matter and antimatter annihilate and produced the CMB and the remaining  
 712 1 part turned into all the stars and galaxies that are seen. The field of  
 713 cosmology that studies the processes that produced an asymmetry between  
 714 leptons and antileptons in the very early universe is called leptogenesis.

715 Researches carried during the last few decades have revealed that the  
 716 laws of nature do not equally apply to matter and antimatter. So far, the  
 717 only non-trivial difference between matter and antimatter found is the  $\mathcal{CP}$   
 718 asymmetry (or  $\mathcal{CP}$  violation, which has been introduced in Section 1.1.3).  
 719 Alas, the quantity of  $\mathcal{CP}$  asymmetry included in the SM is insufficient to  
 720 explain the composition of the observable universe and, hence, extensive  
 721 searches of new sources of  $\mathcal{CP}$  violation are being carried.

722 In this context, the studies described in this thesis are part of the seek  
 723 of new  $\mathcal{CP}$ -violation sources. As Section 2.3.3 details, the observation of a  
 724 cross section<sup>8</sup> greater than the one predicted by the SM would imply that  
 725 Higgs-single-top-quark associated production does not conserve  $\mathcal{CP}$ .

## 726 Dark energy

727 According to cosmological observations, the matter described by the SM  
 728 only makes up around 5% of the universe. It turns out that roughly 68% of  
 729 the universe is dark energy, which is not considered by the SM.

730 Dark energy is an unknown type of energy postulated to explain the  
 731 observed accelerated expansion of the universe as Figure 1.9. This expansion  
 732 is dominated by a spatially smooth component with negative pressure  
 733 called dark energy. Modern cosmological measurements are based in super-  
 734 novae, cosmic microwave background fluctuations, galaxy clustering and  
 735 weak gravitational lensing, and methods agree with a spatially flat universe  
 736 with about 30% matter (visible and dark) and 70% dark energy [35].

## 737 Dark matter

738 The rest of the energy content in the universe is the matter. Dark matter  
 739 (DM) adds up for approximately 85% of all matter and 27% of all energy.  
 740 This matter is called dark because it does not interact with the electromag-

---

<sup>8</sup>The definition of cross section can be found in Section 3.2.0.1.

netic field, so maybe a name such us invisible matter would have been more appropriate since rather than being dark it just does not emit or reflect light. The only way to interact with DM is via gravitational interaction, which is bout 25 orders of magnitud weaker than the weak force (as Table 1.1 shows). This is why DM is so difficult to detect. The SM does not provide a proper explanation but searches are being carrie and candidates such as weakly interacting massive particles (WIMPs) or axions<sup>9</sup> have been proposed.

The existence of DM has been inferred through gravitational effects in astrophysical and cosmological observations. The rotational speed of the galaxies [38], the gravitational lensing [39] and the CMB angular spectrum [40] are some examples of phenomena that cannot be explained with general relativity unless there is more present matter what it is seen.

Although the vast majority of scientific community accepts dark matter existence, alternative explanations for the observed phenomena have suggested. Most of these model consists in modifications of GR. The search of DM at particle colliders, which is focussed on large missing transverse energy signatures, have not result in any observation. Nevertheless, the existence of a particle is never discarded, only its presence within the detector sensitivity limits.

## Others

(quizás, esto the "others" sobra ya) The different problems mentioned hitherto are just some of the most relevant open questions that fundamental physics has not being able to answer yet. Nonetheless, there are many other issues whose discussion would need many pages and are outside the scope of this work. Even so, it won't harm to list a few of them:

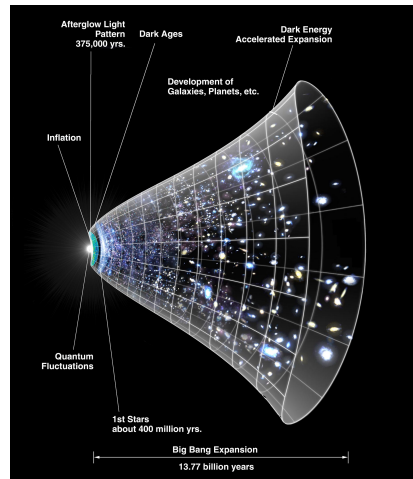


**Figure 1.9:** The universe's expansion over time. The dark-energy existence has been suggested to explain this expansion.

<sup>9</sup>An axion is a hypothetical elementary particle postulated to resolve the strong CP problem [36] [37].

- 777 • Hierarchy problem: It is caused by the enormous distance between  
778 two fundamental physics scales: the EW scale ( $\sim 10^2$  GeV) and the  
779 Planck scale ( $\sim 10^{19}$  GeV).
- 780 • Strong  $\mathcal{CP}$  problem: It refers to the fact that, while QCD does not  
781 explicitly prohibit  $\mathcal{CP}$  violation in strong interactions, it has yet to be  
782 observed in experiments.
- 783 • Naturalness: It is the property that the dimensionless ratios between  
784 free parameters or physical constants appearing in a physical theory  
785 should take values of order unity. By looking at the parameters of the  
786 SM described in Section 1.1.6.1, it can be seen that the naturalness  
787 principle is not satisfied. For instance, the masses of the first genera-  
788 tion of fermions are in the range of 1 MeV while the top quark has a  
789 mass of 172-173 GeV. Though this is not a flaw in the theory itself, it  
790 is frequently seen as a sign of undiscovered principles hidden behind  
791 a more comprehensive theory.
- 792 • Composite Higgs models:
- 793 • Majorana neutrinos: It is not clear yet if neutrinos are Majorana  
794 particles, i.e. they are their own antiparticles ( $\nu = \bar{\nu} = \nu_M$ ). Current  
795 experiments trying to solve this question are focused on neutrino-  
796 less double- $\beta$  decay, which can occur only if neutrinos are Majorana  
797 particles.

798 Most of theoretical concepts of the SM were in place by the end of the  
799 1960s. With the discovery of the  $W$  [41] and  $Z$  [42] bosons at CERN in the  
800 mid 1980s and the Higgs boson in 2012, the SM has established itself as one  
801 of the major pillars of modern physics. The understanding of the universe  
802 at the most fundamental level is based in this theory, which has been tried  
803 to be summarised through the entire Section 1.1.

804 Despite its brilliance and success, the SM is not the ending of the story.  
805 As exposed above, there are far too many unanswered questions and loose  
806 ends. The HL-LHC [43] and the next generation of experiments will look  
807 for evidence of physics outside the SM in the next years.

808 Among the open questions, unresolved concerns and measurements to be  
809 completed, this research is focused on the top quark<sup>10</sup>. On one hand, contrib-  
810 utions to the measurement of the polarisation of this quark are presented  
811 and, on the other hand, the study of the associated production of a single-  
812 top quark with a Higgs boson is present as well. Now that the basics of

---

<sup>10</sup>Here and in the following, the usage of the term top quark includes the top antiquark.

813 the SM have been settled, in the sections to come, the context of these two  
 814 topics is being discussed.

### 815 1.1.7 Cross-section

816 **No sé muy bien dónde meter esta sección. Quizás un apéndice**  
 817 **con Energy, Luminosity y Cross-section sea la mejor idea.**

818 The cross section ( $\sigma$ ) is a metric of the likely is a particular reaction to  
 819 occur. It is formally defined as the effective area that characterises the  
 820 interaction probability between two particles. Mathematically, it is expressed  
 821 as  $\sigma = \frac{\text{number of interactions}}{\text{number of incident particles}\cdot\text{solid angle}}$

822 The higher the cross section is for a process, the more probable is for it  
 823 to take place. Denoted by  $\sigma$ , it is measured in units of area named barns:  
 824 1 barn = b =  $10^{-24}$  cm<sup>2</sup>. For instance, for the LHC energy:

- 825 •  $\sigma(pp \rightarrow X) \approx 0.1$  b
- 826 •  $\sigma(pp \rightarrow X + H) \approx 1 \times 10^{-11}$  b
- 827 •  $\sigma(pp \rightarrow X + H; H \rightarrow \gamma\gamma) \approx 50 \times 10^{-15}$  b

828 It is usual to define the differential cross-section ( $\frac{d\sigma}{d\Omega}$ ) as the cross-section  
 829 per solid angle. If the differential cross-section is integrated over correspond-  
 830 ing the angular range, the cross section for a specific region ( $\sigma_\vartheta$ ) is obtained:

$$831 \quad \sigma_\vartheta = \int_0^\vartheta \int_0^{2\pi} \frac{d\sigma}{d\Omega} \sin(\vartheta) d\phi d\vartheta$$

with  $\vartheta \in [0, \pi]$  is the coverage of the scattering angle.

**this paragraph may be removed** The total cross-section is determined by the amplitude of the scattering matrix  $\mathcal{M}$ , which is independent of the experimental setup. The  $\mathcal{M}$ , also known as scattering amplitude, relates the initial state and the final state of a physical system undergoing a scattering process. Using  $\mathcal{M}$ , the total cross-section for a process is

determined by:

$$\sigma_{tot} = \int \frac{d\sigma}{d\Omega} d\Omega = \int \frac{1}{\Phi} |\mathcal{M}|^2 dQ$$

832 being  $\Phi$  the incident particle flux in the process and the parameter  $dQ$   
833 describes the kinematic phase space.

834 **Chapter 2**

835 **Top quark and Higgs boson  
836 physics**

837 **2.1 Top quark**

838 The top quark ( $t$ ) or, for simplicity, just top is the up-type quark of  
839 the third generation of fermions. Its most distinctive feature is its huge  
840 mass, which is the largest among all fundamental particle particles. The  
841 left-handed top is the  $Q = 2/3$  and  $T_3 = +1/2$  member of the weak isospin  
842 doublet that also contains the bottom quark. The right-handed top quark is  
843 the  $SU(2)_L$  weak isospin singlet ( $Q = 2/3$  and  $T_3 = 0$ ). Its phenomenology  
844 is driven by its large mass. The top quark is often regarded as a window  
845 for new physics since it provides a unique laboratory where to test the  
846 understanding of the SM.

847 Due to being so massive, its life time is very short ( $\tau_t = 5 \times 10^{-25}$  s [39]).  
848 Actually, it is shorter than the hadronisation timescale ( $1/\Lambda_{QCD} \sim 10^{-24}$  s),  
849 this represents a exceptional opportunity to study quarks in free state, some-  
850 thing that is quite exceptional due to colour confinement, as explained in  
851 Section 1.1.4. In fact, the top quark is the only quark that can be investi-  
852 gated unbonded. Its lifetime also is smaller than the spin decorrelation  
853 timescale ( $m_{top}/\Lambda_{QCD}^2 \sim 10^{-21}$  s [44]), implying that the top-quark states  
854 conserve their spin state from its production to its decay. Thanks to this,  
855 the top-quark properties, such as the spin information, can be accessed  
856 through its decay products and, consequently, be measured.

857 Another consequence of its large mass is that the top quark is the only  
858 quark with a Yukawa coupling ( $y_t$ ) to the Higgs boson of the order of one;  
859 hence, a thorough understanding of its properties (mass, couplings, decay  
860 branching ratios, production cross-section, etc.) can reveal crucial inform-

ation on basic interactions at the electroweak symmetry-breaking scale and beyond. The main objective of this thesis is, precisely, the study of the top quark and Higgs boson interplay to, ultimately, help to determine if the  $y_t$  is that predicted by the SM or there is some  $\mathcal{CP}$ -violating phase that would affect the sign of the Higgs-top Yukawa coupling. The theoretical base for the understanding the associated production of a top quark and a Higgs boson given in Section 2.3 and the analysis investigating this matter is presented through the rest of the thesis.

### 2.1.1 Top-quark discovery

In 1973, Kobayashi and Maskawa postulated the possibility of a third generation of quarks to explain  $\mathcal{CP}$  violations in kaon decays [45]. To match the names of the up and down quarks, the new generation's quarks were given the names top and bottom. The GIM<sup>1</sup> mechanism[46], which predicted the existence of the yet-to-be-discovered charm quark, was used to make this prediction. When the charm was observed [47], the GIM was integrated into the SM and the postulation of the third family, and thus the top quark, gained acceptance. Shortly after the charm, the bottom quark was discovered in the E288 experiment at Fermilab [48], reinforcing the idea of the existence of the top quark. However, due to its large mass, it took 18 years to confirm the existence of the top.

The top quark was observed for the first time at Tevatron with the CDF [49] and D $\emptyset$  [50] detectors via flavour-conservating strong interaction in 1995. Back then and until the start of LHC Run 1, Tevatron was the only accelerator powerful enough to produce top quarks.

### Top quark mass

As discussed in Section 1.1.6.1,  $m_{top}$  is a free parameter of the SM. The theory does not predict its value, hence it must be determined experimentally. To derive the  $m_{top}$  from hadron collision data, two approaches are explored:

- Direct measurements (also known as template methods) [51]: The  $m_{top}$  is determined by reconstructing (fully or partially) the decay products of one or more top quarks in a  $t\bar{t}$  or single-top event<sup>2</sup>. A comparison of the detector-level<sup>3</sup> distributions with templates created with a MC

---

<sup>1</sup>Standing for Glashow–Iliopoulos–Maiani, it is the mechanism to describe the flavour-changing neutral currents.

<sup>2</sup>In particle physics, an event is the result of a collision.

<sup>3</sup>Detector level is the event information as it is registered by the detector systems.

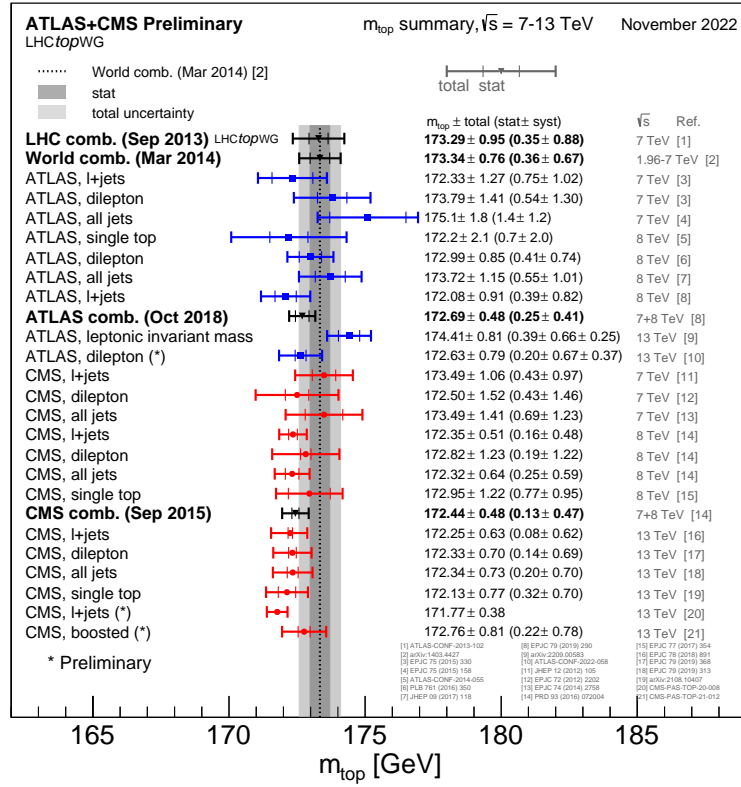


**Figure 2.1:** Summary of the ATLAS and CMS  $m_{top}$  measurements from top-quark decay. Results compared to LHC  $m_{top}$  combination [52]. The most precisely studied property of the top quark is its mass.

generator is used to determine the mass. Analysing  $t\bar{t}$  events with lepton-plus-jets and dilepton topologies provides the most precise results. Figure 2.1 summarises the measurements of ATLAS and CMS for  $m_{top}$  from direct-top-quark decay.

- Indirect measurements [51]: Performed from measurements of the cross section. These methods rely on the dependence on the value of the  $m_{top}$  for the total or differential production cross-sections for processes involving top quarks.

Among the top quark's properties, its mass is the one that has received the most attention so far. The most recent studies for the top quark mass measurements result in  $m_{top} = 172.76 \pm 0.30$  GeV [53]. This number is an average of the measurements at LHC with ATLAS ( $172.69 \pm 66$  GeV [54]) and CMS ( $172.6 \pm 3.5$  GeV at CMS [55]) and at Tevatron with CDF and D $\emptyset$

907 (combined result:  $174.30 \pm 0.89$  GeV [56]). These values are measured from  
908 the kinematics of  $t\bar{t}$  events<sup>4</sup>.

### 909 2.1.2 Top quark production at LHC

910 The LHC is sometimes referred as a top quark factory due to its ability  
911 to produce such particles. In this collider, at  $pp$  collisions, the top quark  
912 is mainly produced via two mechanisms: through QCD in top and anti-top  
913 pairs ( $t\bar{t}$ ), and by means of the  $Wtb$  vertex of EW in single-top quarks  
914 associated with other particles. Apart from the  $t\bar{t}$  (Section 2.1.2.1) and  
915 single-top (Section 2.1.2.2) productions, the associated  $t\bar{t} + X$  and four-top-  
916 quark productions (Sections 2.1.2.4 and 2.1.2.3 respectively) are presented  
917 as well.

918 Since the top quarks often constitute a main background in other physics  
919 analysis, a better understanding of this particle's properties will directly  
920 translate into improvements in those searches.

#### 921 2.1.2.1 Top pairs

922 The production top and anti-top pair of quarks is the largest source of  
923 production of top quarks in hadron collisions. This process is one of the  
924 most important at LHC because it allows to precisely study the properties  
925 of the top quark. Additionally, due to the dominance of this production  
926 mode, the top-quark-pair production is also a major background in many  
927 searches for rare processes. Including the one carried in this thesis, where  
928  $t\bar{t}$  is the main background in the both of the analysed decay channels (see  
929 Section 6.5).

930 For the  $p\bar{p}$  collisions at Tevatron or  $pp$  at LHC, the  $t\bar{t}$  production is  
931 described by perturbative QCD. In this approach, a hard scattering process  
932 between the two hadrons is the result of an interaction between the quarks  
933 and gluons that constitute these hadrons. This model is described with  
934 detail in Section 3.2.5.

935 At LHC, the gluon fusion (Figures ??, ??, ??) dominates with a 90% of  
936 the  $t\bar{t}$  production. It is followed by the quark and antiquark annihilation  
937 (Figure 2.2d), which accounts for a 10% of the total top-quark-pair pro-  
938 duction. The theoretical calculations for the  $t\bar{t}$  production are done to an  
939 accuracy of next-to-next-to-leading order (NNLO) in QCD [57] and meas-  
940 ured by ATLAS and CMS. Figure 2.3 shows the measurements for the  $t\bar{t}$

---

<sup>4</sup>This  $m_{top}$  results are sensitive to the top quark mass used in the MC generator that is usually interpreted as the pole mass.

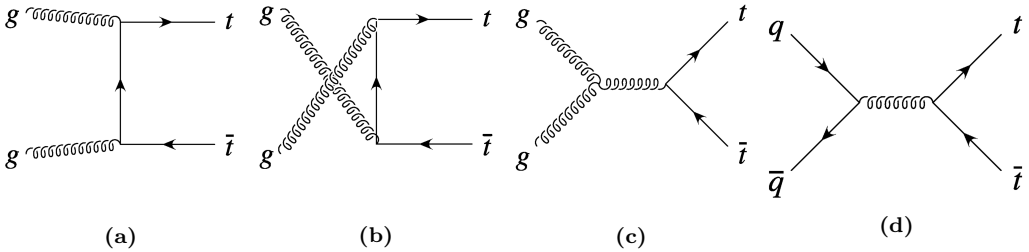


**Figure 2.2:** Representative Feynman diagrams of the LO processes contributing to the  $t\bar{t}$  production. Subfigures (a), (b) and (c) correspond to the production through gluon fusion and Subfigure (d) to the production via quark and antiquark annihilation.

941 production cross-section ( $\sigma_{t\bar{t}}$ ) at  $\sqrt{s} = 13$  TeV. The measurements and the  
 942 theory calculations are quoted at  $m_{top} = 172.5$  GeV.

### 943 2.1.2.2 Single top

944 In addition to the top-quark-antiquark-pair production, the single-top-  
 945 quark processes are of great importance to the study of the top quark prop-  
 946 erties at the LHC. This mechanism has a cross section three times smaller  
 947 than that of  $t\bar{t}$  and it's almost exclusively produced through the EW  $Wtb$   
 948 vertex. This is precisely the reason why single-top-quark production is es-  
 949 sential to gather information the  $Wtb$  interaction and to directly measure  
 950  $|V_{tb}|$  at hadron colliders. The reason why the single-top quark is produced  
 951 and decays via a  $b$ -quark and not from strange or down quarks is because  
 952 the CKM elements  $V_{ts}$  and  $V_{td}$  are smaller than  $V_{tb}$  by several orders of  
 953 magnitude as Table 1.3 shows.

954 At LO, there are three production modes for single top, being the  $t$ -  
 955 channel the dominant mechanism at the LHC with, approximately 70% of  
 956 the single top quark cross-section at a  $\sqrt{s} = 13$  TeV. The other processes  
 957 are the  $s$ -channel and the associated production  $tW$  production. Only  $t$ -  
 958 channel and  $tW$  productions are relevant to the EW single-top production  
 959 at LHC.

#### 960 **$t$ -channel**

961 This production mode involves the scattering of a light quark and a gluon  
 962 from the proton sea as shown in Figure 2.4. Note that additional diagrams  
 963 to those in Figure 2.4 are obtained by either replacing the  $u$  and  $d$  by a  $c$  and  
 964  $s$  quarks or by switching the light quarks in the fermion line. The diagrams  
 965 for antitop production are the charge conjugate of the ones presented.

The measurements cross-sections at 13 TeV for single-top ( $\sigma_{t-channel,t}$ ) and single-anti-top ( $\sigma_{t-channel,\bar{t}}$ ) quarks in the  $t$ -channel production are

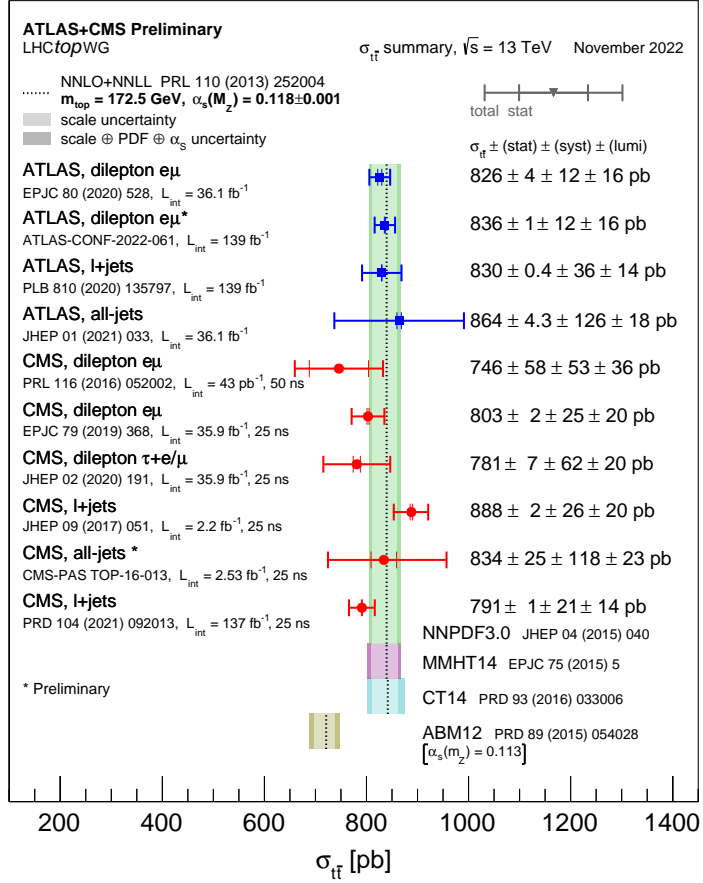


**Figure 2.3:** Summary of measurements  $\sigma_{t\bar{t}}$  at  $\sqrt{s} = 13 \text{ TeV}$  compared to the exact NNLO QCD calculation complemented with next-to-next-to-leading logarithmic resummation [58].

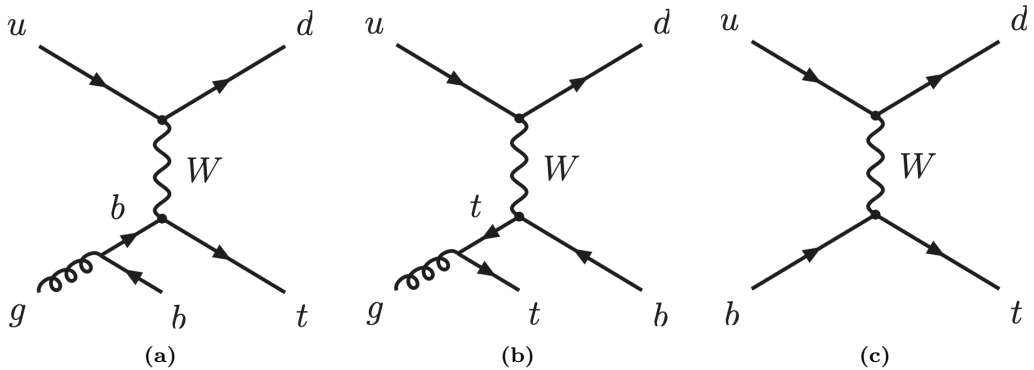


**Figure 2.4:** Representative Feynman diagrams for the single-top-quark production in the  $t$ -channel process. Observe that the  $u$  and  $d$  quarks could be substituted by  $c$  and  $s$  quarks.

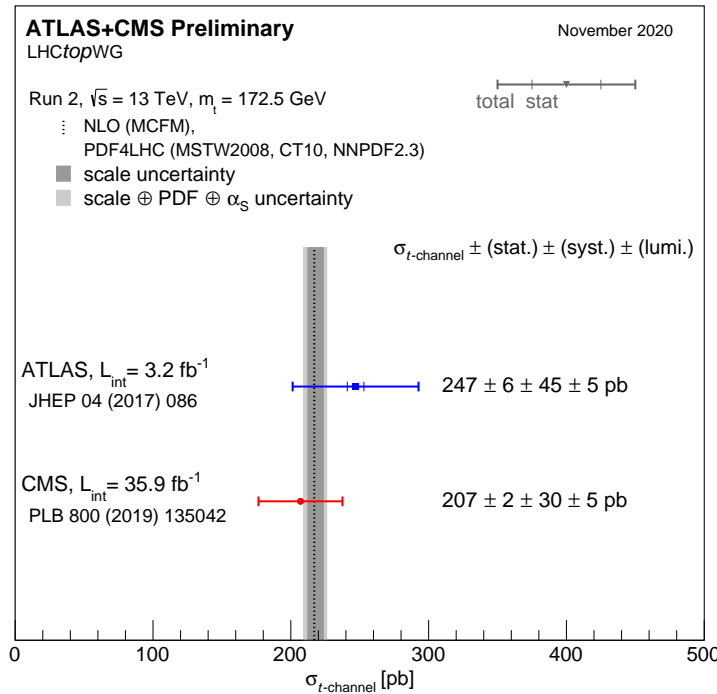


**Figure 2.5:** Summary of the ATLAS and CMS measurements of the single top production cross-sections in the  $t$ -channel at 13 TeV. The measurements are compared to NLO calculations [58].

shown in Figure 2.5. The theoretical calculations at next-to-leading order (NLO) for  $\sigma_{t\text{-channel}, t+\bar{t}}$  at 13 TeV are [59]:

$$\begin{aligned}\sigma_{t\text{-channel}, t} &= 136^{+7.6}_{-6.4} \text{ pb}, \\ \sigma_{t\text{-channel}, \bar{t}} &= 81.0^{+5.7}_{-4.9} \text{ pb}, \\ \sigma_{t\text{-channel}, t+\bar{t}} &= 217.0^{+13.1}_{-11.1} \text{ pb}.\end{aligned}$$

966 These numbers have been obtained using HATHOR 2.1 [60][61] and a  $m_{top}$   
967 of 172.5 GeV.

968 The dominant process in the SM is the one in diagram 2.4a, while the one  
969 in 2.4b is included in order to form a gauge invariant set but its contribution  
970 is not very significative since for the gluon is easier to decay to  $b\bar{b}$  pair than  
971 to a  $t\bar{t}$  pair. These two  $2 \rightarrow 3$  production modes are known as 4 Flavour  
972 Scheme (FS) because the proton is considered to be composed by four quark  
973 flavours ( $u, d, c$  and  $s$ ). It is characterised by having a  $b$  quark in the final  
974 state. This final-state  $b$ -quark is sometimes referred as second<sup>5</sup>  $b$  and it has

<sup>5</sup>The first would be the one from the top quark decay.

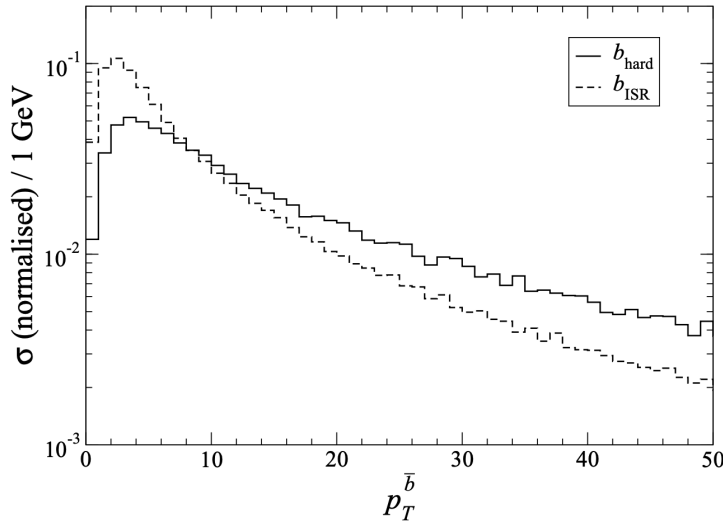


**Figure 2.6:** Normalised  $p_T$  distribution of the second  $b$  quark in the  $t$ -channel process, generated by MC simulation [62]. As can be seen, in most of cases this quark is produced with very low  $p_T$  and, consequently, it does not pass the trigger requirements and it is not detected at ATLAS.

975 a transverse momentum ( $p_T$ ) distribution peaking around 2 or 3 GeV as can  
 976 be seen in Figure 2.6. This is the reason why the final  $b$  quark from the  
 977 gluon splitting frequently goes undetected, because it does not pass the  $p_T$   
 978 threshold of the detector. This is why, at detector level, whenever only jet  
 979 is identified as originated from a  $b$  quark, it is assumed to be the  $b$  from the  
 980 top-quark decay. This particularity becomes more important in Chapter 6,  
 981 where the number of detected  $b$ -tagged jets is a relevant variable for the  
 982 definition of the preselection region.

983 The  $2 \rightarrow 2$  process in 2.4c is known as 5FS because the proton has  
 984 four flavours of quarks and since the process has a  $b$  quark in the initial  
 985 state, there are the five flavours. The simulations for the 4FS and 5FS  
 986 diagrams are produced separately and merged afterwards. When adding  
 987 the two contributions, some double-counting may appear due to the overlap  
 988 in the phase space so one has to be careful. The naming 4FS and 5FS is  
 989 later used again for the associated  $tH$  production.

### 990 **s-channel**

991 The  $s$ -channel process for single-top is the one with less impact among  
 992 single-top production channels. It is depicted in Figure 2.7a. This produc-  
 993 tion mode is also referred as the quark-antiquark annihilation or  $W^*$  process  
 994 and it is very similar to the Drell-Yann.

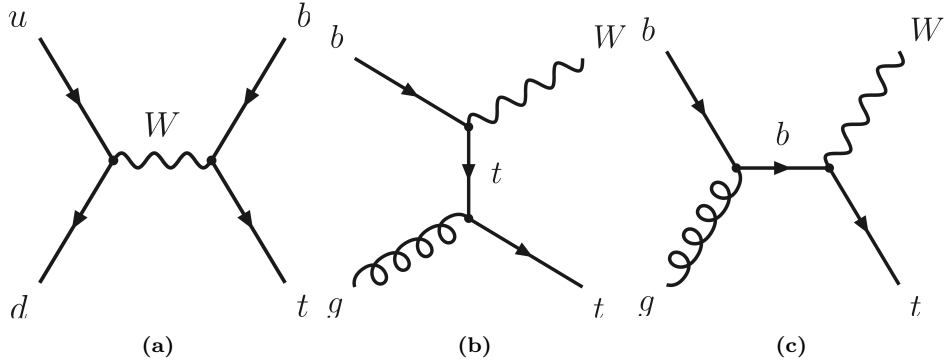


**Figure 2.7:** Representative Feynman diagrams for the single-top-quark production in (a) the  $s$ -channel and with (b, c) an associated  $W$  boson. While the first one is not observed, the  $tW$  is one the backgrounds in the  $tHq$  analysis.

According to the LHC cross-section group, at  $\sqrt{s} = 13$  TeV, the combined cross-section for the single top and single anti-top production in the  $s$ -channel ( $\sigma_{s\text{-channel}}$ ) is [60]:

$$\sigma_{s\text{-channel}, t+\bar{t}} = 10.32^{+0.56}_{-0.61} \text{ pb.}$$

995 Note that while at LHC the  $s$ -channel production has not been observed  
996 at LHC, for Tevatron it was a significant part of the total single-top cross-  
997 section.

### 998 Associated $tW$

999 Finally, the associated production of  
a single top quark with a  $W$  boson  
(sometimes referred as  $tW$ -channel) is  
represented by two the Feynman dia-  
grams in Figures 2.7b and 2.7c. To  
these two diagrams, the charge con-  
jugate processes could be added to  
complete the  $tW$  mechanisms. The  
predicted cross-section for the associ-  
ated  $tW$  is:

$$\sigma_{tW, t+\bar{t}} = 71.7 \pm 5.2 \text{ pb.}$$

This and all  $\sigma$  in this section are cal-  
culated for a top mass of  $m_{top} =$   
172.5 GeV. The measurements for the  
associated  $tW$  are shown in Figure  
2.8.

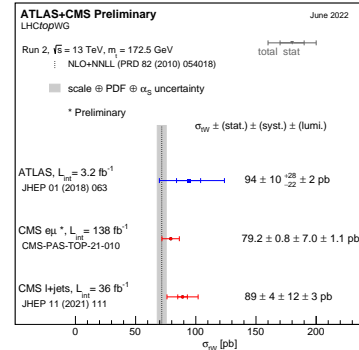


**Figure 2.8:** Cross-section mea-  
surements for the associated  $tW$   
production boson performed by  
ATLAS and CMS at 13 TeV, and  
combined result compared with the  
NLO + next-to-next-to-leading log-  
arithmic (NNLL) prediction.

### 2.1.2.3 Four tops

The production of four top quarks ( $t\bar{t}t\bar{t}$ ) is a rare SM process that takes place at LHC with a predicted cross section of  $\sigma_{t\bar{t}t\bar{t}} = 12.0^{+2.2}_{-2.5} \text{ fb}$  for  $p\ p$  collisions at  $\sqrt{s} = 13 \text{ TeV}$  (calculations at NLO for QCD and EW [63]). Figure 2.9 presents the  $\sigma_{t\bar{t}t\bar{t}}$  measurements by ATLAS and CMS compared to the quoted theoretical calculation. The representative Feynman diagrams are presented in Figure 2.10, where of particular interest is the production by the exchange of a Higgs boson. This indicates a strong dependence of this type of production with the top-quark-Yukawa coupling.

1009

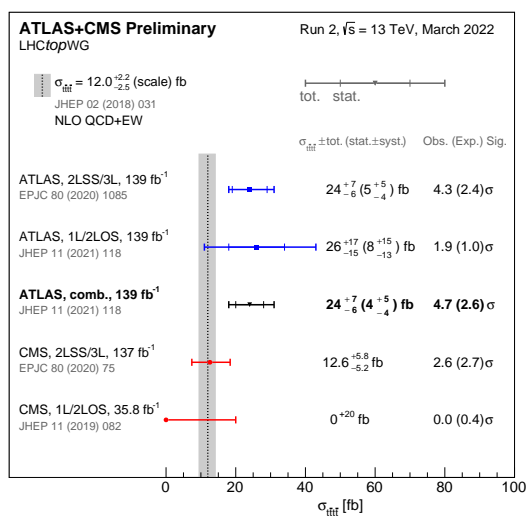


**Figure 2.9:** Summary of the ATLAS and CMS measurements of the  $t\bar{t}t\bar{t}$  production cross-sections at 13 TeV in various channels.

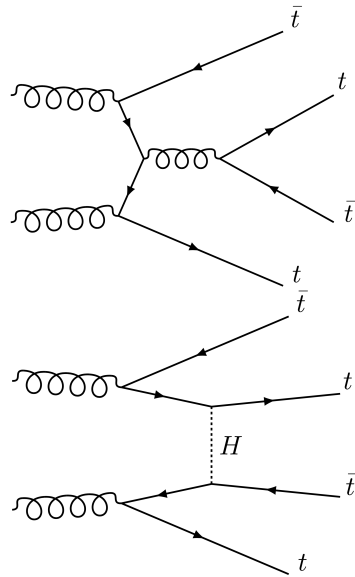


**Figure 2.10:** Representative Feynman diagrams for the  $gg \rightarrow t\bar{t}t\bar{t}$  production.

### 2.1.2.4 Associated $t\bar{t} + X$ production

The associated top productions are important processes to measure the coupling of the top to the other particles of the SM. When a pair of tops is produced along other particle it is referred as  $t\bar{t}X$ . The most relevant  $t\bar{t}X$  productions are those in which the pair is created with  $W$ ,  $Z$  or  $\gamma$  boson. From these,  $t\bar{t}W$  and  $t\bar{t}Z$  play a role in this thesis's analysis. This two processes are backgrounds in the  $2\ell \text{ OS} + 1\tau_{\text{had}}$  channel of the  $tHq$  production, being the second and third most important after  $t\bar{t}$ . The different production diagrams for  $t\bar{t}W$  are shown in Figure 2.11.

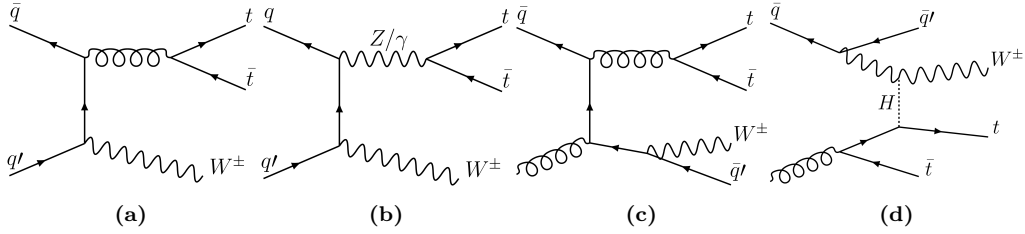


**Figure 2.11:** Representative Feynman diagrams for  $t\bar{t}W$  production. Left diagrams show the  $\bar{q}q' \rightarrow t\bar{t}W$  processes and right ones the  $\bar{q}g \rightarrow t\bar{t}Wq'$  production. **igual tampoco hace falta enseñar estos diagramas**

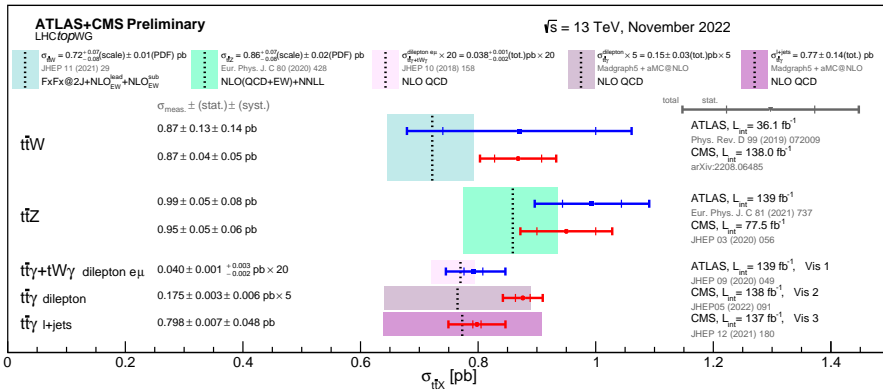


**Figure 2.12:** Summary of the ATLAS and CMS measurements of the  $t\bar{t}X$  production cross-sections at 13 TeV. Here  $X = W, Z$  and  $\gamma$ .

1019     The cross sections for the  $t\bar{t}W$ ,  $t\bar{t}\gamma$  and  $t\bar{t}Z$  productions are presented  
1020     in Figure 2.12. The associated production of a  $t\bar{t}$  pair with a Higgs boson  
1021     is described in Section 2.3.2.

### 1022     2.1.2.5 Associated $t + X$ production

1023     Not only the top pairs but also the single-top quark can be produced  
1024     in association with other particles ( $tX$ ). This type of production play  
1025     an important role in the  $tHq$  searches since the  $tZq$  process is one of the  
1026     backgrounds in the more difficult to separate in the  $2\ell$  OS +  $1\tau_{had}$  channel.  
1027     The other EW  $tX$  is the  $tq\gamma$ , in which the top quark is produced along  
1028     with a photon. Both  $tZq$  and  $tq\gamma$  are sensitive to BSM physics like flavour-  
1029     changing neutral currents or vector-like quarks. ATLAS and CMS have  
1030     measured both processes and while for  $tZq$  a good SM agreement is found,  
1031     this is not the case for the  $tq\gamma$  as can be seen in Figure 2.13

1032     In this work, the most relevant  $tX$  mode is the single-top-quark produc-  
1033     tion in association with a Higgs boson. This is the main process to search

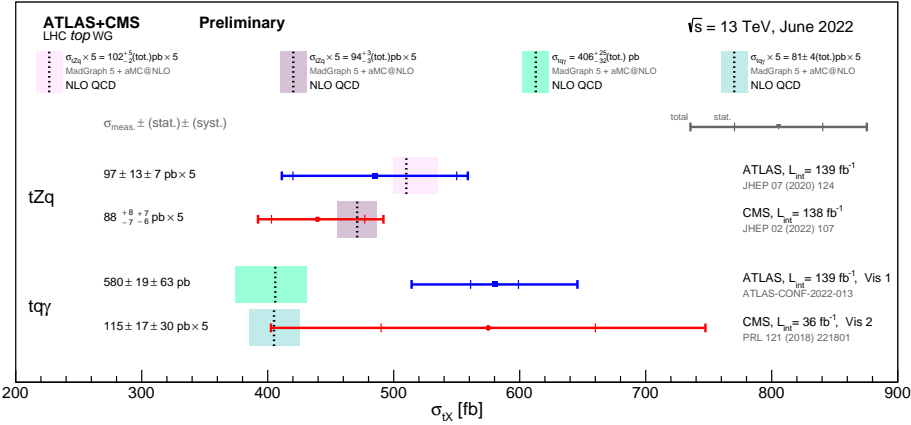


**Figure 2.13:** Summary of the ATLAS and CMS measurements of the  $tX$  production cross-sections at 13 TeV. Here  $X = Z$  and  $\gamma$ . The  $tHq$  process is not included in this plot but the work developed in this document aims to help to provide better limits on its cross-section.

for in the thesis and its features are discussed with more detail in Section 2.3.3.

### 2.1.3 Top-quark decay

As advanced in the Section 2.1.2.2, due to the large  $V_{tb}$  element of the CKM matrix, the top quark decays almost entirely ( $\sim 99.8\%$ ) through the medium of the  $Wtb$  vertex to a  $b$  quark and a  $W$  boson. This vertex and the decay chain of the top quark is represented in Figure 2.14. The final state decay is classified according to the subsequent decay of the  $W$  boson. Since the  $W$  are massive vector bosons, its lifetime is very short ( $\tau_W \approx 3 \times 10^{-25} \text{ s}$ ). For the  $W^+$ , the BRs for the different decay modes are:

$$\begin{aligned}
 W^+ &\rightarrow e^+ \nu_e & (10.71 \pm 0.16)\% \\
 W^+ &\rightarrow \mu^+ \nu_\mu & (10.63 \pm 0.15)\% \\
 W^+ &\rightarrow \tau^+ \nu_\tau & (11.38 \pm 0.21)\% \\
 W^+ &\rightarrow q\bar{q} \text{ (hadrons)} & (67.41 \pm 0.27)\% \\
 W^+ &\rightarrow \text{invisible} & (1.4 \pm 2.9)\%
 \end{aligned}$$

For the conjugate processes involving the  $W^-$ , the BR are the same. Therefore, the  $W$  decay and consequently the top-quark decay can be classified either as leptonic or hadronic. Due to its large mass, the  $W$  can decay to any quark except the top quark. For a certain decay mode, the BR is defined as the fraction times that the particle decays in that particular mode with respect to total possible decays.

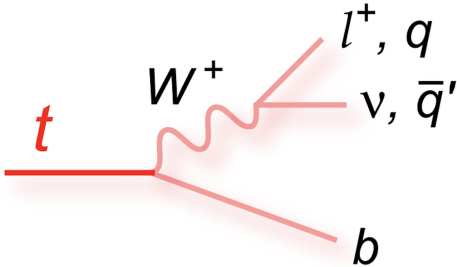


**Figure 2.14:** Decay of a top quark to a  $b$  quark and a  $W$  boson. The  $W$  boson can decay either leptonically to a neutrino and a lepton or hadronically to a pair of light-flavour quarks. In the hadronic  $W$  decay, a jet triplet is formed along with the  $b$  quark.

#### 1043 2.1.4 Top quark polarisation

1044 As mentioned previously, the lifetime of the top quark is shorter than  
 1045 the depolarisation scale and, hence, the top-quark spin information can be  
 1046 transferred into its decay products. This allows to measure the top-quark  
 1047 polarisation from its child particles. The polarisation refers to the alignment  
 1048 between the momentum and the spin of the top quark and antiquarks. The  
 1049 polarisation of  $t$  and  $\bar{t}$  are important quantities because they are sensitive to  
 1050 many BSM effects and can also provide useful input for the MC generators  
 1051 which are described in Section 4.2.

1052 At LHC, the single-top-quark production is the only source of highly  
 1053 polarised top quarks. Specifically, in the  $t$ -channel (see Section 2.1.2.2) the  
 1054 top quark is created with a high degree of polarisation in the direction of the  
 1055 spectator quark momentum [64]. As a consequence of the vector and axial-  
 1056 vector form of the coupling of the top quark to the  $W$  boson and bottom  
 1057 quark in the  $t$ -channel ( $t \rightarrow Wb$  vertex), specific values of the polarisation  
 1058 vectors  $\{P'_x, P'_y, P'_z\}$  of top quarks/antiquarks are expected in the SM.

1059 Even though it is not described with detail in this manuscript, during the  
 1060 development of my thesis I have also been involved in the first measurement  
 1061 of the top-(anti)quark-polarisation vectors. My contribution is an extension  
 1062 of the work done in reference [65] and the results of these measurements are  
 1063 published in reference [66]. In this work, the three components of the polar-  
 1064 isation vector for the top quark and antiquark have been measured in the  
 1065 single-top  $t$ -channel production. Using the entire Run 2 dataset recorded by  
 1066 ATLAS and demanding events with exactly one light lepton, I defined a set  
 1067 of stringent selection requirements to discriminate the  $t$ -channel signal from  
 1068 the background contributions. This signal-region<sup>6</sup> definition used specific  
 1069 cuts in several variables such as the lepton  $p_T$  or the invariant masses of

<sup>6</sup>The signal region is a region of the phase space enriched with events of the signal process.

several particles. I have also developed the so called trapezoidal cut, which is described in the published paper.

The polarisation vectors are later obtained from the distributions of the direction cosines of the charged-lepton momentum in the top-quark rest frame:  $\cos(\theta_{lx'})$ ,  $\cos(\theta_{ly'})$  and  $\cos(\theta_{lz'})$ . Figure 2.15 shows the distributions for this angular variables.

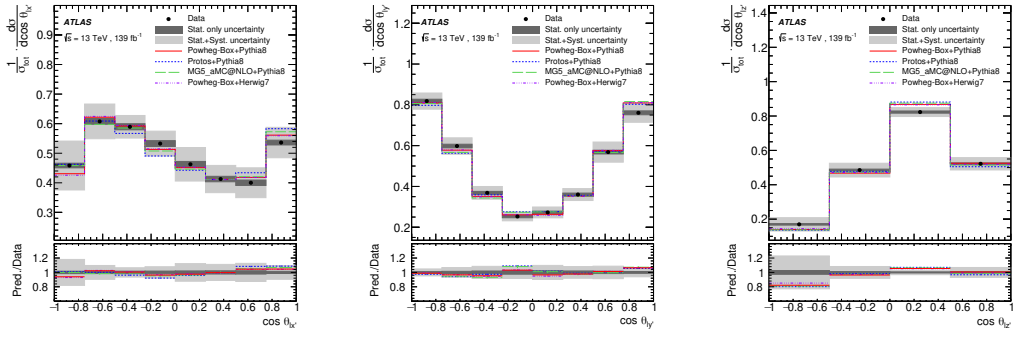


**Figure 2.15:** Normalised differential cross-sections as a function of  $\cos(\theta_{lx'})$ ,  $\cos(\theta_{ly'})$  and  $\cos(\theta_{lz'})$ . The data is shown as black points with statistical uncertainties compared to the predictions of the MC generators, which are shown as lines. The ratio between the predictions and data is shown on the lower panel. These plots are inclusive for top quark and top antiquark.

Limits on the two of the components of the polarisation vector of the top quark and antiquark have been set and Figure 2.16 presents the observed best-fit polarisation measurements for  $P_x'$  and  $P_z'$  in the two dimensional parameter space. The components of polarisation are measured to be:

For top quarks

- $P_x' = 0.01 \pm 0.18$
- $P_y' = -0.029 \pm 0.027$
- $P_z' = 0.91 \pm 0.10$
- $P_x^{\bar{t}} = -0.02 \pm 0.20$
- $P_y^{\bar{t}} = -0.007 \pm 0.051$
- $P_z^{\bar{t}} = -0.79 \pm 0.16$

For top antiquarks

Data measurements of the polarisation-vector components and differential cross-sections show good agreement with SM predictions. The results are consistent with NNLO QCD predictions and expectation of  $P_y' = P_y^{\bar{t}} = 0$  from the hypothesis of  $\mathcal{CP}$  symmetry in the top-quark and top-antiquark decay.

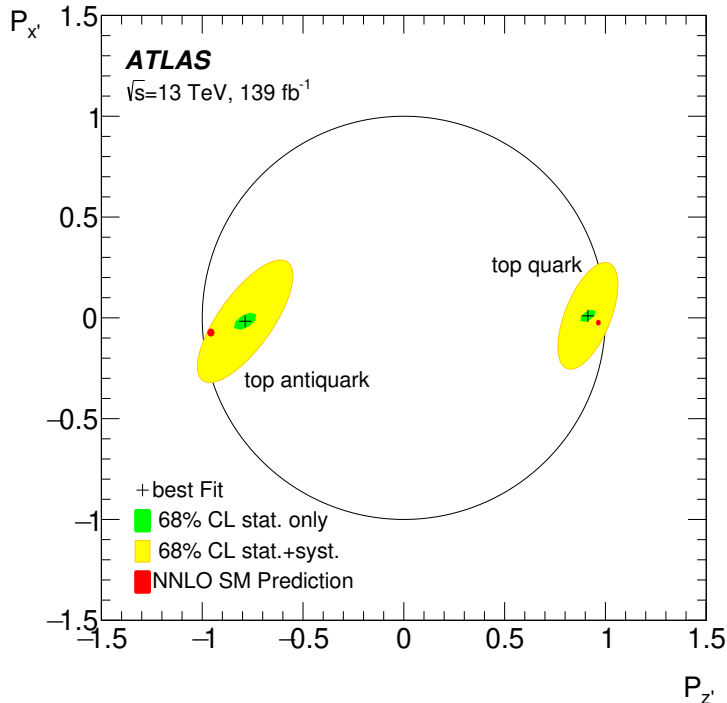


**Figure 2.16:** Observed best-fit limit on two-dimensional top quark polarisation parameter space  $\{P_{z'}, P_{x'}\}$ . The statistical-only (green) and the statistical+systematic uncertainty contours have a 68% CL. The physically allowed values for  $P_{z'}$  and  $P_{x'}$  are lay inside the black circle. The red point indicates the parton-level prediction at NNLO.

## 1086 2.2 Higgs boson

1087 Following the top quark, the Englert-Brout-Higgs-Guralnik-Hagen-  
 1088 Kibble-Higgs boson or, for simplicity, Higgs boson ( $H$ ) or just Higgs is  
 1089 the most massive particle in the SM with a mass of  $m_H = 125.25 \pm 0.17$   
 1090 GeV [67]. The value provided by [67] is an average of the ATLAS com-  
 1091 bined measurement ( $m_H = 124.86 \pm 0.27$  GeV [68]) and the CMS results  
 1092 ( $m_H = 125.46 \pm 0.16$  [69]).

1093 The Higgs boson existence was theorised in 1964 by three independent  
 1094 groups: Englert-Brout [70], Higgs [71] and Guralnik-Hagen-Kibble [72], and  
 1095 its discovery meant one of the greatest successes of the SM. This theory  
 1096 was not only able to calculate with great precision the observed physics  
 1097 phenomena but also predicted the existence of a particle that was found  
 1098 later (see 2.2.1).

1099 **2.2.1 Higgs-boson discovery**

1100 Any particle physicist enthusiast remembers July 4th of 2012 pretty  
1101 well, it was LHC experiments ATLAS [1] and CMS [2] who announced the  
1102 discovery of a massive state  $H$  with the properties expected for the Higgs  
1103 boson.

1104 Both the ATLAS and CMS Collaborations reported excesses of events  
1105 for 2011 ( $\sqrt{s} = 7$  TeV and  $\mathcal{L} = 4.8 \text{ fb}^{-1}$ ) and 2012 ( $\sqrt{s} = 8$  TeV and  $\mathcal{L} = 458$   
1106  $\text{fb}^{-1}$ ) datasets of proton-proton ( $pp$ ) collisions. This surplus of events was  
1107 compatible in its production and decay with the SM Higgs boson in the mass  
1108 region  $m_H \in [124, 135]$  GeV with significances of  $2.9\sigma$  for ATLAS and  $3.1\sigma$   
1109 for CMS. At Tevatron (circular proton-antiproton collider at Fermilab), the  
1110 experiments CDF [73] and D $\emptyset$  [74] also reported an excess in the mass region  
1111  $m_H \in [120, 135]$  GeV. The discovery was the result of the combination of  
1112 several individual searches.

1113 **2.2.2 Higgs boson production at LHC**

1114 One of the reasons why the Higgs boson was found the latest among  
1115 SM fundamental particles is because it is a fairly heavy particle and, hence,  
1116 it was necessary a lot of energy to produce it. Even though that colliders  
1117 such us SLAC or LEP had enough energy, they were colliding electrons and  
1118 positrons and, since the coupling of the Higgs to fermions is proportional to  
1119 the fermions mass, the process  $e^- e^+ \rightarrow H$  processes is highly suppressed<sup>7</sup>  
1120 and, for this reason, there were not enough statistics of events with a Higgs  
1121 boson. The most favoured way of producing a Higgs boson is trough the  
1122 mediation of the heaviest fundamental particles in the SM because these  
1123 have the strongest couplings with the Higgs and, consequently, the greater  
1124 cross section.

1125 The four most dominant processes for Higgs boson production at LHC  
1126 are summarised in Figure 2.17:

- 1127 • **Gluon-gluon Fusion ( $ggF$ ):** This channel is depicted in Figure 2.17a  
1128 and, as the diagram shows, the process  $gg \rightarrow H$  has to be mediated  
1129 by a massive fermion loop. This due to the fact that there is no  
1130 direct gluon-Higgs coupling within the SM. Although in principle all  
1131 quarks should be included in the loop, in practise it is the top quark

---

<sup>7</sup>The dominant Higgs production in  $e^- e^+$  annihilation is the so called Higgsstrahlung, an  $s$ -channel process in which the  $H$  is produced in association to a  $Z$  boson similarly to Figure 2.17c. Due to electrons small mass, the electron-Higgs coupling does not favour the  $e^- e^+ \rightarrow H$  process.

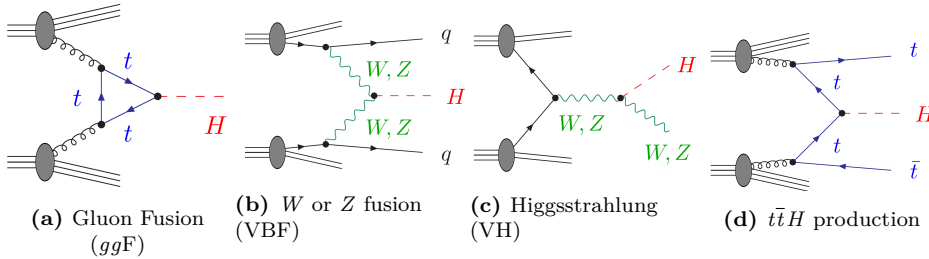


**Figure 2.17:** Lowest-order Feynman diagrams for the dominant production mechanisms of a Higgs boson at hadron colliders.

the one doing so because its coupling to the Higgs boson is 35 times stronger than the next-heaviest fermion, the bottom quark. Due to the abundance of gluons in  $pp$  collisions, the  $ggF$  is very favoured at LHC.

Another interesting property is that the  $ggF$  production rate is sensible to the  $\mathcal{CP}$ -mixing angle in the top Yukawa coupling. This is related to the one of the major aims of this thesis, the search of a presence of  $\mathcal{CP}$ -odd contributions in  $y_t$ .

- **Vector Boson Fusion (VBF):** The second most important mode is the radiation by the incoming quarks of a pair of  $W$  or  $Z$  vector bosons that fuse to form a Higgs as Figure 2.17b illustrates. The vector bosons of the process  $V\bar{V} \rightarrow H$  are originated from initial state quarks which scatter through the final state (changing its flavours in the case of  $W$  fusion) producing two forward jets.
- **Higgsstrahlung (VH):** There is another significant contribution involving the  $W$  or  $Z$  bosons, the Higgsstrahlung or associated  $WH$  or  $ZH$  production. Here, a off-shell  $W$  or  $Z$  (formed from the annihilation of two quarks) radiate a Higgs boson via  $V^* \rightarrow VH$ . Figure 2.17c depicts the VH associated production.
- **Quark-pair associated production ( $q\bar{q}H$ ):** In this mode, the Higgs is produced from a  $q\bar{q}$  pair via  $q\bar{q} \rightarrow H$  with a  $q\bar{q}H$  final state. Typically, the involved quark pair is either a  $b\bar{b}$  or  $t\bar{t}$ . In the case of  $t\bar{t}$  (Figure 2.17d), the top quarks decay before hadronising, leading to final states with a high number of physics objects.
- **Associated Higgs boson and single-top quark ( $tHX$ ):** This sub-dominant contribution can be either a  $tHq$  or a  $tWH$ . The former constitutes the central topic developed in this thesis, where this process is searched. Details about this production modes are further discussed in Section 2.3.3 .

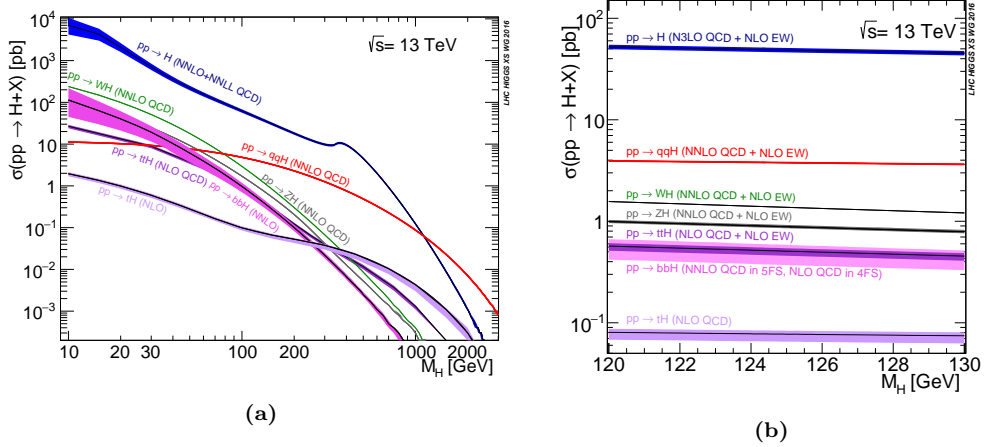
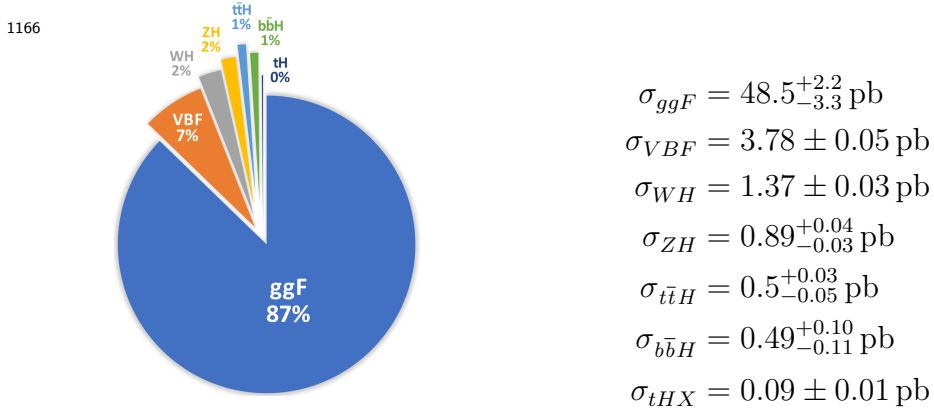


**Figure 2.18:** Higgs boson production cross-sections as function of  $m_H$  at  $\sqrt{s} = 13$  TeV [4]. A wide range of  $m_H$  values is showed in (a). In (b) is shown the result zooming around the measured Higgs mass value. Looking at (a) it can be seen that if the Higgs weighted just about 60 GeV more there would have been only two relevant decay modes,  $H \rightarrow WW$  and  $H \rightarrow ZZ$ . On the other hand, if had Higgs been just 30 GeV lighter, these two channels would have been very difficult to observe.

1161     The cross section of the different mechanisms for single-Higgs-boson<sup>8</sup>  
 1162     production at  $\sqrt{s} = 13$  TeV are shown in Figure 2.18 as a function of  $m_H$ .  
 1163     For Figure 2.18a, the  $\sigma_{tH}$  accounts for the  $t$ -channel and  $s$ -channel but not  
 1164     the  $tW$ -channel. Assuming a  $m_H = 125.2$  GeV, the cross sections for Higgs  
 1165     production are [4]:



<sup>8</sup>So far, the single Higgs production has been heavily studied at LHC but during Run 3 the interest in double-Higgs production is increasing.

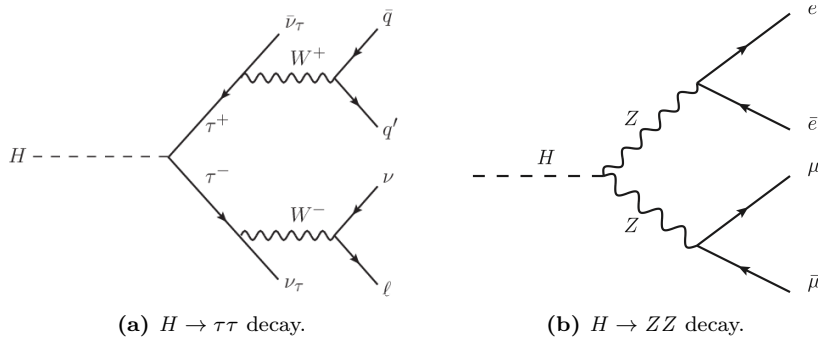


**Figure 2.19:** Feynman diagrams for the Higgs decay into a pair of (a) tau leptons and (b)  $Z$  bosons. Both decay modes are taken into account for the associated  $tHq$  production described in this thesis. In (a), the  $\tau^+$  is decaying to quarks which will form hadrons, therefore, it is referred as hadronic tau. In contrast, the  $\tau^-$  in (a) is a leptonic tau. In the diagram in (b) the Higgs decays into a four light-leptons final state.

### 1167 2.2.3 Higgs-boson decay

1168 The Higgs boson has a very short lifetime ( $\tau_H = 1.6 \times 10^{-22}$  s [4]) and,  
 1169 hence, is always detected through its decay products. Figure 2.20 shows the  
 1170 branching ratio<sup>9</sup> (BR) for the different Higgs-boson-decay-modes.

1171 Despite the expected large Yukawa coupling between the Higgs boson  
 1172 and the top quark, the  $H \rightarrow t\bar{t}$  is forbidden because the  $m_H < 2m_{top}$ .  
 1173 Consequently, the most prominent decay mode is the  $H \rightarrow b\bar{b}$  followed  
 1174 by the  $H \rightarrow W^+W^-$ . This is why for the  $tHq$  searches, the channel in  
 1175 which the Higgs decay to  $b\bar{b}$  is the one with higher statistics. For the rest  
 1176 fermionic decays, the decay rates are ordered by the fermion masses, being  
 1177 the  $\tau^-\tau^+$  decay mode (Figure 2.19a) the most relevant among the leptonic.  
 1178 Regardless of the expected large coupling between the weak force bosons  
 1179 and the Higgs, the  $H \rightarrow VV^*$  is suppressed due to the requirement that one  
 1180 vector boson has to be produced off-shell<sup>10</sup>. In the context of determining  
 1181 possible non-SM  $\mathcal{CP}$  contributions in the top-Higgs coupling, the  $H \rightarrow \gamma\gamma$  is  
 1182 also a relevant process because this decay rate is sensible to the top Yukawa  
 1183 coupling.

1184 For the analysis carried in this thesis, are of particular the decays  $H \rightarrow$   
 1185  $W^+W^-$ ,  $H \rightarrow ZZ$  and  $H \rightarrow \tau^-\tau^+$ . Sorted by its importance and assuming  
 1186 a  $m_H = 125.2$  GeV, the BR for the Higgs are [75]:

<sup>9</sup>The fraction of particles which decay by an individual decay mode with respect to the total number of particles which decay.

<sup>10</sup>Off-shell means that the particle is produced virtually and it does not satisfy the energy-momentum relation.

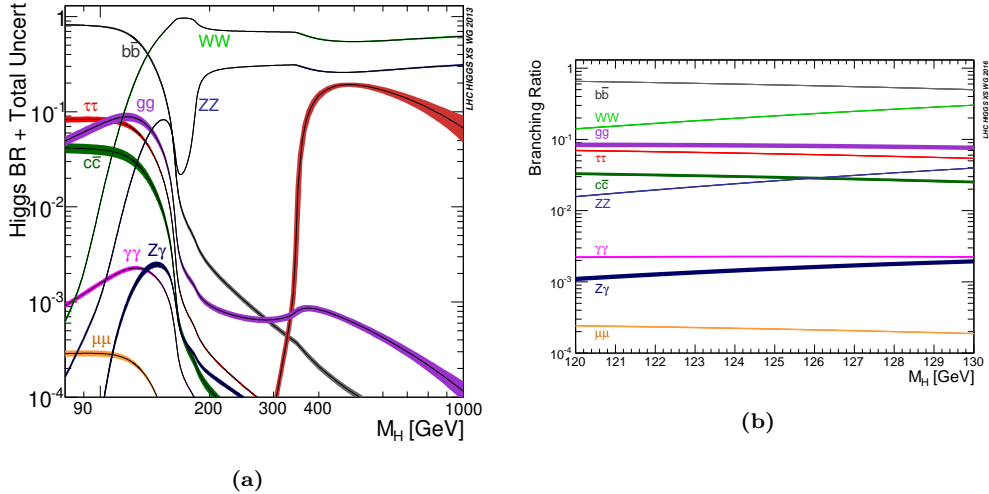
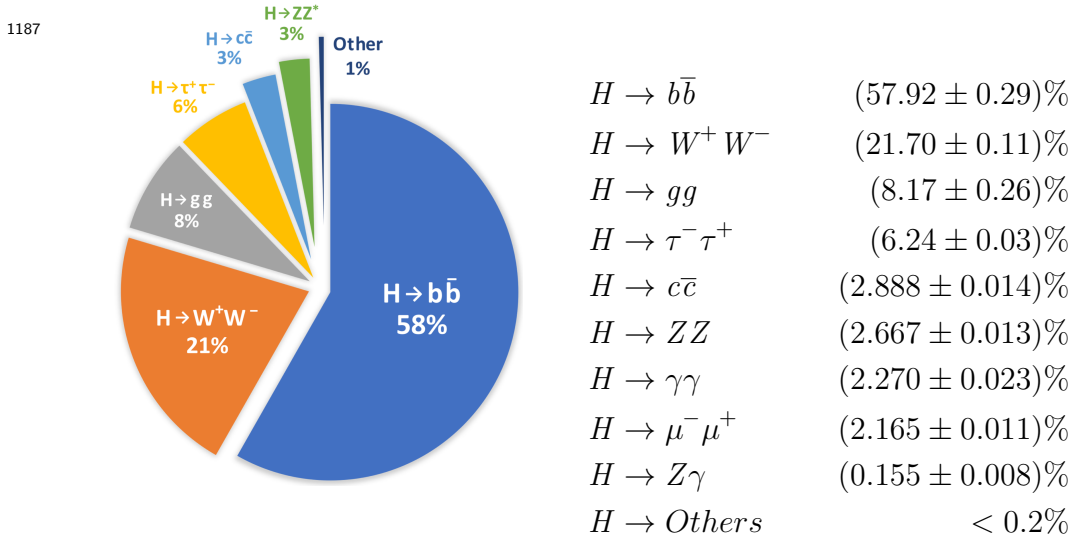


**Figure 2.20:** Standard Model Higgs-boson-decay branching ratios as function of  $m_H$  at  $\sqrt{s} = 13$  TeV [4]. In (a) the BR are shown in a Higgs mass range  $m_H \in (90, 10^3)$  GeV. In (b) only values of  $m_H$  around the measured one are shown. Looking at (a) it can be seen that if the Higgs weighed just about 50 GeV more there would have been only two relevant decay modes,  $H \rightarrow WW$  and  $H \rightarrow ZZ$ . On the other hand, if had Higgs been just 10 GeV lighter, these two channels would have been very difficult to observe.



## 1188 2.3 Top quark and Higgs boson interplay

So far, the couplings of the Higgs boson to the SM particles have been found to be proportional and uniquely determined by the masses of these particles. Since the top quark is the most massive particle, the Yukawa coupling between the top quark and the Higgs boson ( $y_t$ ) is expected to be the strongest among all fermions and, hence, its study is of crucial import-

ance, as it is discussed in references [76][77] and developed in the succeeding sections. The Yukawa coupling is expected to be of the order of the unity:

$$y_t = \frac{\sqrt{2}m_{top}}{v} = 2^{3/4}G_F^{1/2}m_{top} = 0.995 \simeq 1.$$

This value is quite larger than the couplings of the other quarks. For comparison  $y_b \simeq 0.025$  and  $y_c \simeq 0.007 >> y_{s,d,u}$ .

The production of a pair of top quarks along with a Higgs boson ( $t\bar{t}H$ ) allows possible to measure the absolute value of  $y_t$ . This process has the advantage of being the leading mechanism to produce the Higgs together with the quark top. At  $\sqrt{s} = 13$  TeV it has a cross section of **poner cálculos del SM para  $\sigma_{t\bar{t}H}$** .

Having a very much lower cross section than  $t\bar{t}H$  (**poner  $\sigma_{t\bar{t}H}$** ), the Higgs boson production alongside a single top quark ( $tH$ ) brings valuable information, specially regarding the sign of the Yukawa coupling. Note that the sign of  $y_t$  is not a well-defined physical property by itself but the relative sign compared to the coupling of the Higgs to weak<sup>11</sup> boson is indeed physical [76]. This is explored with more detail in 2.3.3.

A change in the Yukawa sign and/or absolute value with respect to its SM value would signal an origin of the fermion masses different from the described by the EWSB because the relative sign of the Higgs coupling to fermions and gauge vector bosons is crucial for recovering the unitarity and renormalisability of the theory [78].

### 2.3.1 $\mathcal{CP}$ properties in top-Higgs interactions

The  $\mathcal{CP}$  properties of the Yukawa coupling of the Higgs boson to the top quark can be probed through the associated production of these two particles. While SM predicts the Higgs to be a scalar boson ( $J^{\mathcal{CP}} = 0^{++}$ ), the presence of a  $J^{\mathcal{CP}} = 0^{+-}$  pseudoscalar admixture has not been excluded yet. This pseudoscalar would introduce a second coupling to the top quark. Finding a  $\mathcal{CP}$ -odd contribution would be a sign of physics beyond the SM and could account for the imbalance between matter antimatter in the universe.

The production rates of  $t\bar{t}H$  and  $tH$  depend on the  $y_t$  coupling. The former is specially sensible to  $y_t$  deviations from the SM as it is described in Section 2.3.3. As already mentioned, the presence of a  $\mathcal{CP}$ -mixing in  $y_t$  would also affect the  $ggF$  production and  $H \rightarrow \gamma\gamma$  decay rates.

---

<sup>11</sup>The coupling of the Higgs to the gauge bosons is taken as positive.

### Higgs characterisation in $tH$

The Higgs characterisation model used in the thesis is the one described in reference [3]. Let's consider a spin-0 particle with a  $\mathcal{CP}$ -violating Yukawa interaction with the top quark,  $X_0$ . This  $X_0$  particle couples to both scalar and pseudoscalar fermionic densities, and its interaction with the  $W$  boson is the one described by the SM. The reason to call this particle  $X_0$  instead of  $H$  is because its description does not correspond to the typical realisation of the Higgs but, in practise, we are referring to the Higgs. Within this model, the term in the effective Lagrangian that describes the Higgs-top Yukawa coupling below the EWSB scale is:

$$\mathcal{L} = -\bar{\psi}_t[\cos(\alpha)\kappa_{Htt}g_{Htt} + i\sin(\alpha)\kappa_{Att}g_{Att}\gamma^5]\psi_tX_0, \quad (2.1)$$

where  $\psi_t$  and  $X_0$  represent the top quark and the Higgs boson respectively and  $\alpha$  is the  $\mathcal{CP}$  mixing phase. The  $\kappa_{Htt}$  and  $\kappa_{Att}$  are real-dimensionless rescaling parameters. Finally,  $g_{Htt} = g_{Att} = \frac{m_{top}}{v} = \frac{y_t}{\sqrt{2}}$ . The Lagrangian 2.1 can be rewritten as:

$$\mathcal{L} = -\frac{y_t}{\sqrt{2}}\bar{\psi}_t[\cos(\alpha)\kappa_{Htt} + i\sin(\alpha)\kappa_{Att}\gamma^5]\psi_tX_0. \quad (2.2)$$

1220 The advantage of this top-Higgs parametrisation is that is simple to inter-  
 1221 polate between the  $\mathcal{CP}$ -even ( $\cos(\alpha) = 1$  and  $\sin(\alpha) = 0$ ) and the  $\mathcal{CP}$ -odd  
 1222 ( $\cos(\alpha) = 0$  and  $\sin(\alpha) = 1$ ) scenarios. The SM coupling corresponds to  
 1223 the  $\mathcal{CP}$ -even:  $\mathcal{L} = -\frac{y_t}{\sqrt{2}}\bar{\psi}_t\psi_tX_0$ .

1224 The proposed Lagrangian for the interaction of the Higgs with a top  
 1225 quark is based on considering the SM an effective field theory (EFT) ap-  
 1226 plicable only up to energies no exceeding certain scale  $\Lambda$  [79].

1227 Figure 2.21 shows the cross section for the  $tX_0$  production in the  $t$ -  
 1228 channel as function of the  $\mathcal{CP}$ -mixing angle. For comparison, the  $t\bar{t}X_0$  is  
 1229 also included. In the same way that  $tX_0$  models the  $tHq$  process,  $t\bar{t}X_0$   
 1230 models the  $t\bar{t}H$ . The uncertainty band is derived from the choice of scale  
 1231 ( $\mu$ ) and the FS dependence. The values of  $\kappa_{Htt}$  and  $\kappa_{Att}$  in Figure 2.21 are  
 1232 set to reproduce the SM expectation for the gluon fusion cross-section.

1233 The first relevant appreciation by looking at Figure 2.21 is that the  $t\bar{t}H$   
 1234 cross-section is symmetric around a  $\mathcal{CP}$  angle of  $\alpha = \pi/2$ . This implies  
 1235 that by measuring  $\sigma(t\bar{t}H)$  it would not be possible to discriminate between  
 1236 the the  $\mathcal{CP}$ -odd and  $\mathcal{CP}$ -even scenarios. However, for the  $tHq$  production,  
 1237 this degeneracy is removed by the interference of the LO diagrams as it is  
 1238 described in Section 2.3.3.2.

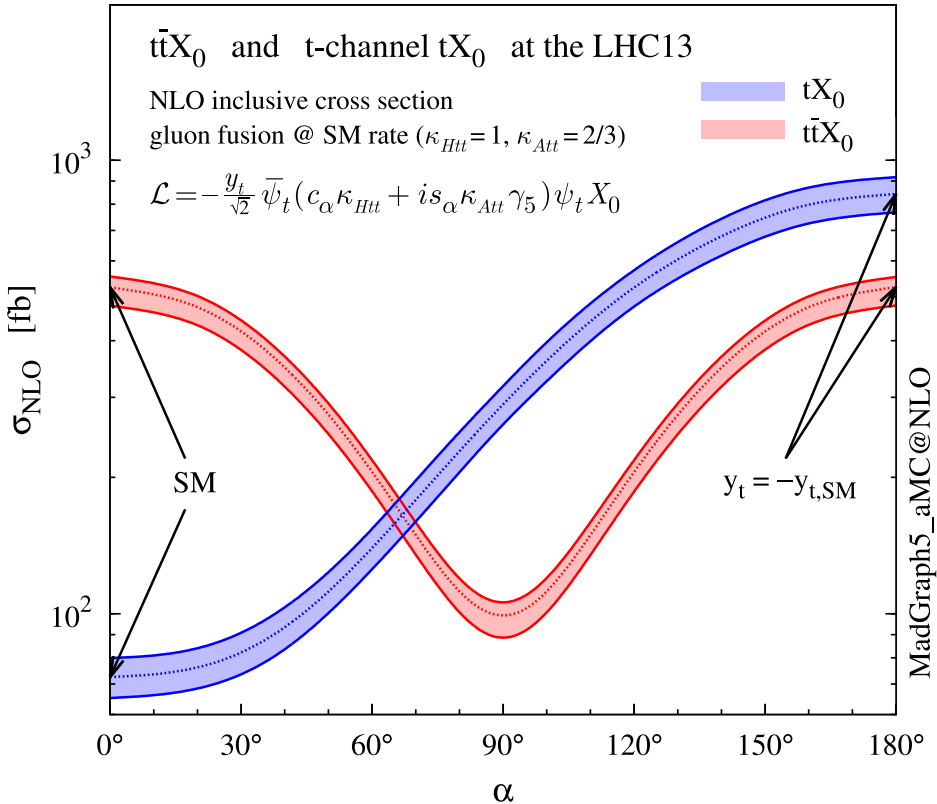


**Figure 2.21:** NLO cross-section as a function of the  $\mathcal{CP}$ -mixing angle for  $t$ -channel  $tX_0$  and  $t\bar{t}X_0$  at  $\sqrt{s} = 13$  TeV. The  $X_0$  is represents a general  $\mathcal{CP}$ -violating Higgs boson. Note that while the  $t\bar{t}H$  cross-section degenerate under the transformation  $y_t \rightarrow -y_t$ . This is not the case for  $\sigma(tHq)$ , which is sensible to  $\alpha$ .

### 2.3.2 $t\bar{t}H$

The production of a top-antitop pair in association with a Higgs boson is one of the most important process to measure the strength of the Yukawa coupling ( $|y_t|$ ), which is crucial to understand the origin of the fermion masses. Detecting a deviation from the SM prediction for  $\sigma(t\bar{t}H)$  could indicate the presence of new physics that violate the  $\mathcal{CP}$  symmetry. But, as Figure 2.21 illustrates, this process is not sensible to the sign of the Yukawa mixing angle.

From the phenomenology point of view, the calculations for the  $t\bar{t}H$  production cross-section at  $\sqrt{s} = 13$  TeV can be calculated at NLO+NNLL accuracy [80]:

$$\sigma_{NLO+NNLL}(t\bar{t}H) = 486^{+29.9}_{-24.5} \text{ fb.}$$

This calculation depends on the chosen scales for the soft and hard processes but it gives an idea of the order of magnitude for this process. The LO Feynman diagrams for the  $t\bar{t}H$  production are presented in Figure 2.22

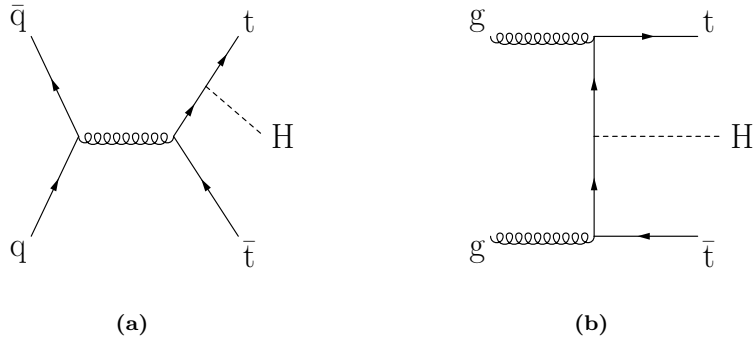


**Figure 2.22:** LO Feynman diagrams for  $t\bar{t}H$  production. Although this is the most relevant mechanism for the associated production of a Higgs boson with, at least, one top quark, the  $t\bar{t}H$  is still a rare process. It counts for roughly 1% of all Higgs productions

1250     The first associated production of a Higgs boson with a pair of top  
 1251     quarks was observed in 2008 by ATLAS [81] and CMS [82]. This process  
 1252     marked a significant milestone for the field of high-energy physics because  
 1253     it helped establishing the first direct measurement of the tree-level coupling  
 1254     of the Higgs boson to the top quark, which was in agreement with the SM  
 1255     expectation.

1256     The associated production of Higgs boson with top quark pair has been  
 1257     studied by ATLAS and CMS previously not only during Run 1 at  $\sqrt{s} =$   
 1258     7 TeV and 8 TeV [83] [84] but also at Run 2 [81], where the cross section was  
 1259     expected to be increased by a factor of four. The ATLAS Run 2 analyses use  
 1260     only an integrated luminosity up to  $79.8 \text{ fb}^{-1}$  and considers the following  
 1261     Higgs-decay channels:  $b\bar{b}$ ,  $W^+ W^-$ ,  $\tau^- \tau^+$ ,  $\gamma \gamma$  and  $Z Z$ . Assuming the SM  
 1262     BR, the total measured-cross-section by [81] is  $\sigma(t\bar{t}H) = 670^{+200}_{-190} \text{ fb}$ . This  
 1263     result, which is a combination of all the mentioned decay channels, is in  
 1264     agreement with the SM predictions and is shown in Figure 2.23. Meanwhile,  
 1265     CMS has found a strength of  $\mu_{t\bar{t}H} = 1.38^{+0.36}_{-0.29}$  for the  $\gamma \gamma$  Higgs decay  
 1266     channel and  $\mu_{t\bar{t}H} = 0.92^{+0.36}_{-0.29}$  for the multiplet channels [85].

### 1267     2.3.3 $tH$

1268     The associated  $tH$  production takes place via three different types of  
 1269     processes. Firstly, the  $t$ -channel, where the Higgs boson couples to a top  
 1270     quark or  $W$  boson (Figures 2.24a and 2.24b respectively). In this channel  
 1271     the top and Higgs are created along with an additional quark, giving rise  
 1272     to the so called  $tHq$  production. The other two production modes are the  
 1273      $tW$  process, in which the Higgs couples to the top quark (Figure 2.24c), and  
 1274     the  $s$ -channel. In Section 2.3.3.1, the details of the associated top-Higgs

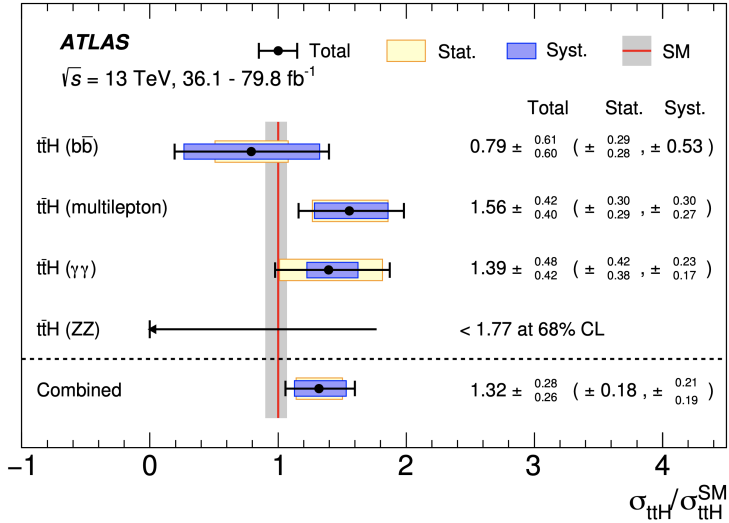


**Figure 2.23:** Comparison of the measured  $t\bar{t}H$  production cross-section to its SM theoretical expectation [81]. The red vertical line indicates the SM prediction.

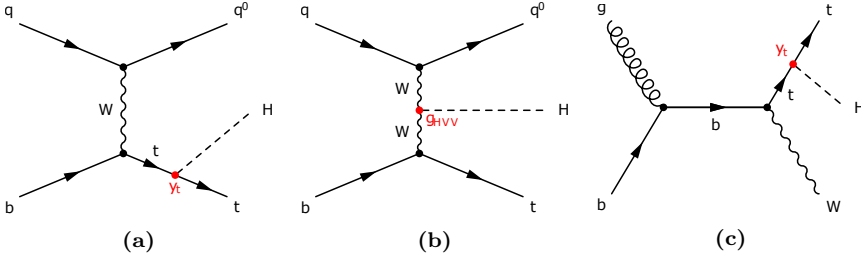


**Figure 2.24:** Representative LO Feynman diagrams for the  $t$ -channel  $tHq$  associated production, where the Higgs boson couples either to the top quark (a) or the  $W$  boson (b). Here  $g_{HVV}$  is the coupling of the Higgs boson to the vector bosons. On (c) an example of the  $tWH$  production is presented.

1275 production modes are given. All three processes have a much smaller cross  
 1276 section than the main Higgs production channels that were discussed in  
 1277 Section 2.2.2. However, the  $tH$  modes yield a unique feature that make them  
 1278 fascinating: they are simultaneously sensitive to the sign and magnitude of  
 1279 the Higgs coupling to both the top quark,  $y_t$ , and the weak bosons,  $g_{HVV}$ .

### 1280 2.3.3.1 $tH$ production modes

1281 At LO, the production of a Higgs boson in association with a single-  
 1282 top quark and additional parton ( $tHq$ ) in  $pp$  collisions is classified in three  
 1283 groups according to the virtuality of the  $W$  boson. These groups are:  $t$ -  
 1284 channel and  $s$ -channel productions, and associated production with an on-  
 1285 shell  $W$  boson. This categorisation is the same as for the single-top-quark  
 1286 (Section 2.1.2.2), which makes sense since the  $tHq$  production is, basically,

1287 a single-top-quark process in which a Higgs boson is radiated either from  
 1288 the  $W$  boson or the top quark. Note that this separation, while useful, is  
 1289 not physical and it only holds at LO and 5FS. At higher orders in QCD or  
 1290 in other flavour scheme, the classification becomes fuzzy.

### **$tH$ production in the $t$ -channel :: $tHq$**

The  $t$ -channel production modes resemble the ones described in Figure 2.4. These are classified in 4FS and 5FS as it is done for the single-top case. The 4FS and the 5FS modes are shown in Figures 2.25 and 2.25 respectively. For the 4FS modes, the diagrams in which the gluon decays to a top pair (2.25c, 2.25d and 2.25e) contribute less than the ones in which it does to a  $b\bar{b}$  (2.25a and 2.25b) because it is easier for the gluon to decay into  $b\bar{b}$  than into  $t\bar{t}$ . The NLO cross-section for the  $tHq$  process at  $\sqrt{s} = 13$  TeV is given by<sup>12</sup>:

$$\sigma_{NLO}^{t\text{-channel}}(tH) = 47.64 \pm 9.7^{+2.9\%}_{-3.1\%} \quad (2.3)$$

$$\sigma_{NLO}^{t\text{-channel}}(\bar{t}H) = 24.88 \pm 10.2^{+3.5\%}_{-2.6\%}. \quad (2.4)$$

Combining the  $tH$  and  $\bar{t}H$  contributions results in:

$$\sigma_{NLO}^{t\text{-channel}}(tH + \bar{t}H) = 72.55 \pm 10.1^{+3.1\%}_{-2.4\%}. \quad (2.5)$$

1291 For  $tHq$  and single-top-quark production at colliders, the 5FS calculations  
 1292 are easier than the 4FS due to the lesser final state-multiplicity and  
 1293 smaller phase space. This is why in the 5FS the single-top production is  
 1294 known at NNLO while the 4FS this is done only for NLO. Another advantage  
 1295 of the 5FS is that the  $t$ -channel,  $s$ -channel and associated  $tWH$  production  
 1296 do not interfere until NNLO. Contrary, the in 4FS, the  $t$ -channel at NLO  
 1297 and  $s$ -channel at NNLO can interfere. Nevertheless, these interferences are  
 1298 very small and can be neglected [3].

1299 Other feature of the 4FS is that it is assumed that the energy scale of the  
 1300 hard process ( $Q$ ) is not much higher than the bottom quark mass, which is  
 1301 also significantly larger than the QCD scale ( $\Lambda_{QCD}$ ). Therefore, the model  
 1302 is limited to  $Q \geq m_b \gg \Lambda_{QCD}$ . When  $Q \gg m_b$  inaccuracies appear. In  
 1303 contrast, the 5FS assumes  $Q \gg m_b$ . In practise, the bottom mass is set to  
 1304 zero in 5FS to simplify calculations [3].

1305 The work developed in this thesis is focussing on this production type.  
 1306 The associated production of a Higgs boson and top quark with an addi-  
 1307 tional light quark ( $q$ ) and  $b$  quark. This light quark is usually referred as

---

<sup>12</sup>The calculation of the  $\sigma_{NLO}^{t\text{-channel}}$  depends on the choice of scale. The numbers given here correspond to  $\mu = (m_H + m_{top})/4$ .

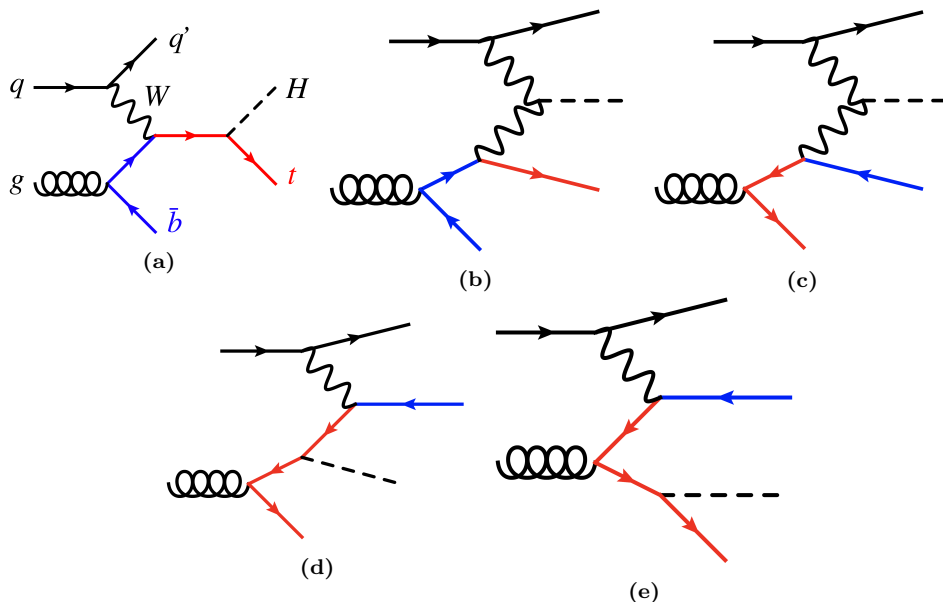


**Figure 2.25:** LO Feynman diagrams for  $t$ -channel  $tH$  production in the 4FS. The red line represents the top quark while the blue is the  $b$  quark. This model works for energy scales on the order on  $m_b$ .

1308 spectator quark and it is expected to produce a jet in the ATLAS calorimeters  
 1309 (in Chapter 3 the detector and its components are presented) with high  
 1310  $\eta$ . The reason here to have this large  $\eta(q)$  is because the  $q$  was contained  
 1311 within the initial parton and, therefore, it continues in the direction of the  
 1312 beam. The  $b$  quark is usually named spectator or second  $b$  and it is typi-  
 1313 cally not detected due to its small  $p_T$ , as Figure 2.6 depicts. The  $tWH$  is  
 1314 considered a background in this analysis because it does not have the same  
 1315 signature as the  $tHq$  process. **Bueno, ahora igual se pone  $tWH$  com  
 1316 señal también. Habrá que ver cómo queda esto.**

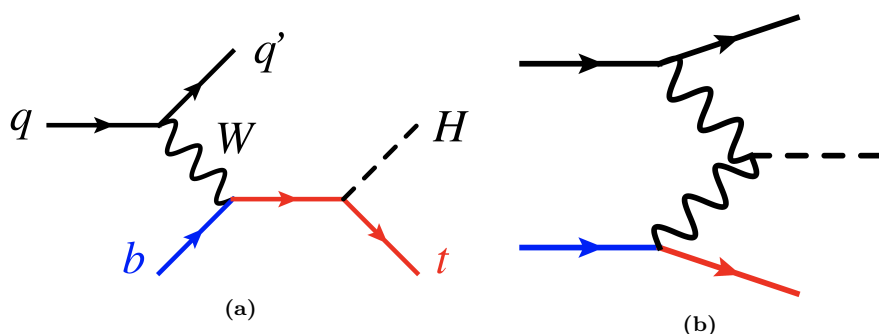


**Figure 2.26:** LO Feynman diagrams for  $t$ -channel  $tH$  production in the 5FS. Here, the  $b$  quarks are considered massless.

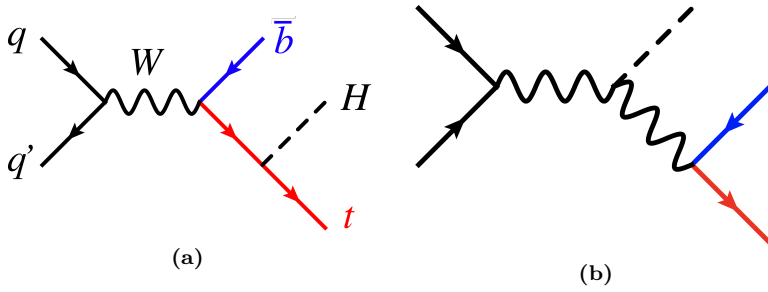


**Figure 2.27:** LO Feynman diagrams for  $s$ -channel  $tH$  production in the 5FS.

### **$tH$ production in the $s$ -channel**

The  $s$ -channel contribution to the total cross-section of the  $tH$  process is very small. Additionally, this channel contributes at low  $p_T$  and, since a  $p_T$  cut is applied in ATLAS, the  $s$ -channel events are suppressed. For these two reasons, this channel plays a less important role in the associated top-Higgs production. The NLO total cross-section for the  $tH$  process via the  $s$ -channel at  $\sqrt{s} = 13$  TeV is:

$$\sigma_{NLO}^{s\text{-channel}}(tH + \bar{t}H) = 2.812^{+3.3\%}_{-3.1\%}. \quad (2.6)$$

In reference [3] it is shown that the shapes of the distributions of most observables in the  $s$ -channel differ significantly from those of the  $t$ -channel. So, even though the total cross-section of the  $tH$  production with the  $s$ -channel is much smaller than the one for  $t$ -channel, one could think that including the  $s$ -channel in the analysis would increase the precision. This is not the case because the LHC is not sensible for the  $tH$  production via the  $s$ -channel for the reasons mentioned above. In fact, not even the  $s$ -channel-single-top production (without any associated Higgs boson) has been found at LHC.

### **$tH$ production in the $tW$**

The production of the Higgs boson in association with a top quark and  $W$  boson ( $tWH$ ) is a process that can be easily defined at LO accuracy in QCD and in the 5FS, i.e. through the partonic process  $gb \rightarrow tW(H)$  citeDemartin:2016axk. When NLO corrections are applied, the  $tWH$  interferes with the LO  $t\bar{t}H$  production. This arises from the  $gg \rightarrow tWb(H)$  with a resonant  $\bar{t}$  interfering with  $gg \rightarrow t\bar{t}(H)$ . This makes the  $tWH$  process difficult to distinguish from the  $t\bar{t}H$ , which has a cross section of one order of magnitude larger.

Regarding the possibility of finding this process in the LHC it is difficult to know if it is possible to observe it over the  $t\bar{t}H$  signal, which already is a rare process.

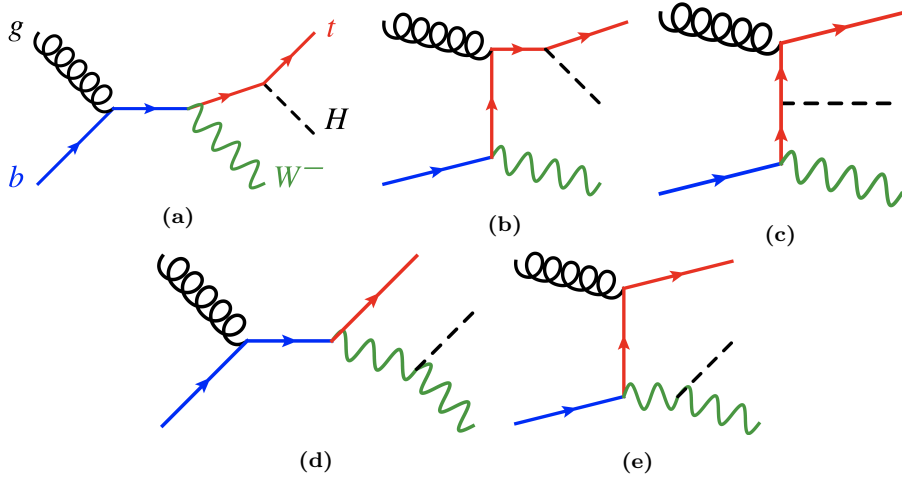


**Figure 2.28:** LO Feynman diagrams for  $tW^-H$  production in the 5FS. Diagrams extracted from reference [86].

1338 Anyways, the MC simulated  $tWH$  samples should be taken into account  
 1339 into account for the  $tHq$  search, where it is a background. Another option  
 1340 is to consider this process part of the signal in  $tHq$  searches so that we have  
 1341 a more comprehensive view of the associated top-Higgs production.

### 1342 2.3.3.2 $tHq$ sensibility to $y_t$

As already commented in the introduction of the Section 2.3, the main interest of the  $tHq$  process is that it is among the few processes in the LHC that are sensible to the relative size and phase between the couplings of the Higgs top and the Higgs to the gauge bosons. The other mechanisms to determine this relative sign are  $H \rightarrow \gamma\gamma$  and  $gg \rightarrow ZZ$ . This is due to the fact that in the SM the  $tHq$  production of the where the  $H$  couples to the  $W$  (Figure 2.24 right) interfere destructively with those in which the  $H$  is radiated from the top (Figure 2.24 left). As it is later explained in Section 3.2.0.1, the cross section is proportional to the square of the matrix element,  $\mathcal{M}$  and if there are several diagrams for a same process, the matrix elements have to be summed before squaring leading to interference terms. For the  $tHq$  production

$$\sigma_{tHq} \propto |\mathcal{M}_{qq \rightarrow tHq}|^2 = |\mathcal{M}_{qq \rightarrow tHq_{WH}} + \mathcal{M}_{qq \rightarrow tHq_{tH}}|^2 \quad (2.7)$$

1343 When squaring the scattering amplitude, the destructive interference<sup>13</sup> term  
 1344 decreases the  $\sigma_{tHq}$ . This behaviour makes the  $tHq$  cross-section exception-  
 1345 ally sensible to the departures of  $y_t$  from the SM predictions. Typically,

---

<sup>13</sup>By destructive interference is meant that the relative sign between  $\mathcal{M}_{qq \rightarrow tHq_{WH}}$  and  $\mathcal{M}_{qq \rightarrow tHq_{tH}}$  is negative.

the destructive interference yields a reduction in the rate as compared to the contribution from each individual diagram by about an order of magnitude [87]. Therefore, in the presence of non-SM new physics, a positive relative sign between the  $tH$  and the  $WH$  couplings would imply that the amount of  $tHq$  events recorded should increase a factor of  $\sim 13$  over the SM expectations, surpassing the number of events from  $t\bar{t}H$  production [88].

This can be clearly seen in Figure 2.21. In contrast to the cross-section for  $t\bar{t}H$ , which degenerates ( $\sigma(t\bar{t}H, y_t) = \sigma(t\bar{t}H, -y_t)$ ), the  $\sigma(tHq)$  increases with the  $\mathcal{CP}$ -mixing angle.

The  $tHq$  production has been studied at LHC Run 1 by CMS [89]

### 2.3.3.3 ATLAS and CMS results

In order to gather the necessary information, the widest campaign of measurements has to be undertaken, including as many possible decay modes. In this context, the scope of this thesis is the study of the production  $tH$  with a final state characterised by two light leptons ( $\ell$ ), i.e. electrons ( $e^\pm$ ) or muons ( $\mu^\pm$ ), and one hadronically decaying tau lepton ( $\tau_{\text{had}}$ ). This signature is usually referred as dileptau or lep-had channel and is denoted by  $2\ell + 1\tau_{\text{had}}$ .

<sup>1364</sup> **Chapter 3**

<sup>1365</sup> **The ATLAS experiment at  
<sup>1366</sup> CERN's Large Hadron Collider**

<sup>1367</sup> The work developed in this thesis is framed in the context of the AT-  
<sup>1368</sup> LAS detector [90], a general-purpose particle physics detector that records  
<sup>1369</sup> events arising from collisions within the Large Hadron Collider (LHC), the  
<sup>1370</sup> most powerful particle accelerator built to date. This experimental setup is  
<sup>1371</sup> located at CERN, one of the world's premier centres for scientific inquiry.

<sup>1372</sup> This chapter is devoted to the introduction of the CERN laboratory and  
<sup>1373</sup> a description of the technical design of LHC and ATLAS. The CERN or-  
<sup>1374</sup> ganisation is presented through an overview of its history, its achievements  
<sup>1375</sup> and some of the most relevant research projects carried out currently. The  
<sup>1376</sup> essential technical aspects of the LHC machine design are covered. The  
<sup>1377</sup> distribution and functioning of the accelerator complex and the main exper-  
<sup>1378</sup> iments conducted at LHC are summarised as well. Finally, a full overview  
<sup>1379</sup> of the different components of the ATLAS detector is provided, presenting  
<sup>1380</sup> the specific features of each part.

<sup>1381</sup> **If material had to be cut from 3, I may remove:**

- <sup>1382</sup> • **Section 3.1 CERN**
- <sup>1383</sup> • **Section 3.2.4, Grid**
- <sup>1384</sup> • **Section 3.2.0.1 (energy, lumi, cross section) should either be**  
<sup>1385</sup> **removed or moved to chapter 1.**

<sub>1386</sub> **3.1 CERN**

<sub>1387</sub> The European Organization for Nuclear Research, known as CERN, is  
<sub>1388</sub> the largest particle physics laboratory in the world. The convention estab-  
<sub>1389</sub> lishing CERN was ratified in 1954. Its name is derived from the French  
<sub>1390</sub> acronym *Conseil Européen pour la Recherche Nucléaire*, which was the pro-  
<sub>1391</sub> visionary body designated in 1952 to foster the fundamental physics research  
<sub>1392</sub> in Europe, and the acronym has been maintained until CERN’s foundation.  
<sub>1393</sub> Initially formed by 12 member states, now it has 23 member states and  
<sub>1394</sub> many non-European countries involved in different ways such as associate  
<sub>1395</sub> members, partners and observers [91].

<sub>1396</sub> The main site of the laboratory is located at Meyrin, a municipality of  
<sub>1397</sub> the Canton of Geneva (Switzerland), at the Franco–Swiss border. There  
<sub>1398</sub> are other sites in the vicinity of the Meyrin site, being the most relevant the  
<sub>1399</sub> Prévessin Site, the CERN’s second-largest site, straddling the communes of  
<sub>1400</sub> Prévessin-Moën (France).

<sub>1401</sub> Since its beginning, CERN’s objective has been helping to uncover what  
<sub>1402</sub> the universe is made of and how it works. CERN started its first accelerator,  
<sub>1403</sub> the Synchrocyclotron, on 1957 and rapidly observed the electron decay of  
<sub>1404</sub> the pion for the very first time [92]. Thereafter, the laboratory has con-  
<sub>1405</sub> tinued contributing to particle and nuclear physics and to more technical  
<sub>1406</sub> fields. For instance, one of the most significant achievements made through  
<sub>1407</sub> CERN experiments was the discovery in 1973 of neutral currents in the Gar-  
<sub>1408</sub> gamelle bubble chamber located in the Proton Synchrotron (PS) [93]. This  
<sub>1409</sub> was indirect evidence of the existence of the  $Z$  boson and, a decade later,  
<sub>1410</sub> in 1983, CERN announced the discovery of the  $Z$  and  $W$  bosons [94] at  
<sub>1411</sub> the UA1 and UA2 experiments within the Super Proton Synchrotron (SPS).  
<sub>1412</sub> This achievement earned CERN its first Nobel Prize in 1984. Other major  
<sub>1413</sub> successes of CERN were the determination of the number of light neutrino  
<sub>1414</sub> families at the Large Electron-Positron Collider (LEP) on 1995 [95] and the  
<sub>1415</sub> creation for the very first time of antihydrogen atoms in 1995 at the PS210  
<sub>1416</sub> experiment [96]. More crucial accomplishment followed such as the discov-  
<sub>1417</sub> ery during the 1990’s of  $\mathcal{CP}$  violation by NA31 [97] and NA48 experiments  
<sub>1418</sub> [98]. And, in 2012, the Higgs boson discovery by ATLAS and CMS[1] [2], a  
<sub>1419</sub> fundamental test for the robustness of the SM as described in Section 2.2.1.  
<sub>1420</sub> More recently, in 2015, a state consistent with a pentaquark was observed  
<sub>1421</sub> at LHCb [99].

<sub>1422</sub> Currently, a wide diversity of projects are carried at CERN being the  
<sub>1423</sub> most renowned of them the LHC and its experiments which are described in  
<sub>1424</sub> more detail in Section 3.2. In addition, fixed-target experiments, antimatter  
<sub>1425</sub> experiments and experimental facilities make use of the LHC injector chain.

Parameter	Design	Run-1	Run-2	Run-3	HL-LHC
Beam energy	7	3.5 - 4	6.5	7	7
Centre-of-mass energy ( $\sqrt{s}$ ) [TeV]	14	7 - 8	13	13.6	14
Bunch spacing [ns]	25	50	25	25	25
Bunch Intensity [ $10^{11}$ ppb]	1.15	1.6	1.2	up to 1.8	2.2
Number of bunches ( $n_b$ )	2800	1400	2500	2800	2800
Transverse emittance ( $\epsilon$ ) [ $\mu\text{m}$ ]	3.5	2.2	2.2	2.5	2.5
Amplitude function at the interaction point ( $\beta^*$ )[cm]	55	80	30→25	30→25	down to 15
Crossing angle [ $\mu\text{rad}$ ]	285	-	300→260	300→260	TBD
Peak Luminosity [ $10^{34} \text{ cm}^2 \text{ s}^{-1}$ ]	1.0	0.8	2.0	2.0	5.0
Peak pileup	25	45	60	55	150
Nominal magnetic field ( $B$ ) [T]	8.73	4.16 - 7.76	7.73	8.73	8.73
Injection energy [GeV]				450	
Circumference length [km]				26.7	
Radius [km]				4.24	
Number of dipole magnets				1232	
Length of dipole magnets [m]				14.3	
Number of quadrupole magnets				395	
Total mass [tons]				27.5	

**Table 3.1:** Summary of main accelerator parameters for the LHC, showing the design values, and those used during Run-1 and Run-2, as well as the expected parameters for Run-3 and the HL-LHC.

1426 The main fixed-target experiments at CERN are the Antiproton Decelerator  
 1427 (AD) [100] for slowing antiprotons for the antimatter factory [101] and the  
 1428 On-Line Isotope Mass Separator (ISOLDE) facility for short-lived ions [102].  
 1429 The world's first proton-driven plasma wakefield acceleration experiment is  
 1430 also at CERN, the Advanced Proton Driven Plasma Wakefield Acceleration  
 1431 Experiment (AWAKE) [103]. Even in the International Space Station ,  
 1432 CERN's Alpha Magnetic Spectrometer (AMS) tries to observe dark matter  
 1433 by studying cosmic rays [104]. The research programme at CERN covers  
 1434 topics from the basic structure of matter to cosmic rays, and from the SM  
 1435 to supersymmetry.

## 1436 3.2 Large Hadron Collider

1437 In 1991, the Large Hadron Collider (LHC) was proposed with the pur-  
 1438 pose of searching for the elusive Higgs boson[105][106]. Finally, after several  
 1439 years of planning and construction, on September 10 2008, a beam of pro-  
 1440 tons was successfully directed into the LHC pipes for the first time.

1441 A summary of the main parameters of LHC for  $pp$  collisions is presen-  
 1442 ted in Table 3.1. These parameters are shown for how the machine was  
 1443 designed, for Run-1 (2011-2012) and Run-2 (2015-2018) as well as the ex-  
 1444 pected parameters for Run-3 (2022-2025). The forecasted values for the  
 1445 High Luminosity (HL) LHC upgrade, scheduled post 2027, are provided too.

**1446 3.2.0.1 Energy and Luminosity**

**1447 this could be moved to an appendix of "concepts" along with**  
**1448 Cross Section.**

**1449 Energy**

**1450** Another name to refer to the field of Particle Physics is “high energy phys-  
**1451** ics”. Particles such as the Higgs boson or the top quark are more than 100  
**1452** times heavier than the proton so, in order to produce them, huge energies  
**1453** are required. The centre-of-mass energy,  $\sqrt{s}$ , allows the production of phys-  
**1454** ical effects. The greater the energy is, the larger is the range of the different  
**1455** processes that can be produced by the accelerator.

The four-vector,  $\mathbf{p} = (E, \vec{p})$ , of a particle of mass  $m$  describes its kinematics with its energy  $E$  and  $\vec{p}$ . The square of the four-vector,  $\mathbf{p}^2$ , corresponds to the particle mass:

$$\mathbf{p}^2 = E^2 - \vec{p}^2 = m^2 \quad (3.1)$$

When two particles of mass  $m_1$  and  $m_2$  and momenta  $\vec{p}_1$  and  $\vec{p}_2$  respectively collide, the centre-of-mass energy,  $\sqrt{s}$ , can be expressed as:

$$s = E_{CM}^2 = (\mathbf{p}_1 + \mathbf{p}_2)^2 = (E_1 + E_2)^2 - (\vec{p}_1 + \vec{p}_2)^2 \quad (3.2)$$

For symmetric colliding beams, such those of LHC, the collision point is at rest in the laboratory frame ( $\vec{p}_1 = -\vec{p}_2$ ) and, hence, the energy is

$$s = E_{CM}^2 = (E_1 + E_2)^2 \quad (3.3)$$

**1456** Since the energy of each beam is 6.5 TeV during Run-2, the centre-of-mass  
**1457** energy of LHC collisions is

$$\sqrt{s} = E_{CM} = (E_{beam1} + E_{beam2}) = 6.5 \text{ TeV} + 6.5 \text{ TeV} = 13 \text{ TeV} \quad (3.4)$$

**1458 Luminosity**

**1459** Besides  $\sqrt{s}$ , the luminosity is the most relevant parameter in an experiment,  
**1460** especially in searches for events with small cross-section. It measures the  
**1461** ability of the particle accelerator to produce enough events of the desired  
**1462** type.

The luminosity,  $\mathcal{L}(t)$ , is the ratio of events detected in a certain period of time for a given cross-section ( $\sigma$ ):

$$\mathcal{L} = \frac{1}{\sigma} \frac{dN}{dt} = \frac{1}{\sigma} R \quad (3.5)$$

where  $N$  is the number of the events and  $t$  the time.  $R = \frac{dN}{dt}$  is known as event rate. It can be understood as number of particle collision per unit area (typically expressed in  $\text{cm}^2$ ) and per second, therefore it is measured in  $\text{cm}^2 \text{s}^{-1}$  [107]. For instance, for LEP was  $\mathcal{L}_{LEP} = 1.0 \times 10^{32} \text{ cm}^2 \text{s}^{-1}$  and the LHC is designed to achieve  $\mathcal{L}_{LHC_{pp}} = 2.1 \times 10^{34} \text{ cm}^2 \text{s}^{-1}$  in  $pp$  collisions and  $\mathcal{L}_{LHC_{PbPb}} = 6.1 \times 10^{27} \text{ cm}^2 \text{s}^{-1}$  for heavy ion collisions.

For a circular collider, the instantaneous luminosity is proportional to the number of bunches per beam ( $n_1$  and  $n_2$ ), the revolution frequency ( $f$ ) with which the bunches are crossing and the number of proton bunches in the machine ( $n_b$ ), and it is and inversely proportional to the beams effective transverse area in which the collision takes places (Area =  $4\pi\sigma_x\sigma_y$ )

$$\mathcal{L} = f \cdot \frac{n_1 n_2 n_b}{4\pi\sigma_x\sigma_y} \cdot F(\theta_c, \sigma_x, \sigma_z) \quad (3.6)$$

where  $F(\theta_c, \sigma_x, \sigma_z)$  is a factor accounting for the luminosity reduction due to the beam crossing angle ( $\theta_c$ ). At the LHC, assuming that the particles travel at the speed of light, for its 27 km, the bunch crossing frequency is  $f = 11245.5 \text{ Hz}$ . The maximum number of proton bunches in the machine is <sup>1</sup> $n_b = 2808$ . In each bunch there are  $n_1 \approx n_2 \approx 1.15 \times 10^{11}$  particles. Finally, characterising the optics of the collision at the interaction point (IP), the RMS transverse beam width in the horizontal and vertical directions are  $\sigma_x \approx \sigma_y \approx 12, \dots, 50 \mu\text{m}$ . The expression 3.6 assumes that the particles in the beam are Gaussian distributed. According to equation 3.6 the instantaneous luminosity only depends on the machine and its beam parameters [108][109].

The integrated luminosity over time is given by

$$L = \int \mathcal{L} dt \quad (3.7)$$

and it is used to determine the number of events,  $N$ , that have taken place during that time:  $N = \sigma \times L$ . The number of observed events in then:

$$N_{events}^{obs} = \sigma_{process} \times \text{efficiency} \times L, \quad (3.8)$$

where the efficiency of the detection is to be optimised by the experimental physicist, the integrated luminosity ( $L$ ) is delivered by LHC and the cross-section of the process ( $\sigma_{process}$ ) is given by nature.

**I could remove everything about factors that minimise the luminosity and strategies to fix it.** Several factors can limit the maximum luminosity that can be achieved at LHC [107]:

<sup>1</sup>The theoretical maximum of 3564 bunches cannot be reached due to space needed between bunch trains and for the beam dump kicker magnets.

- 1485 • **Beam-beam effect:** The bunches of two beams or the particles in the  
1486 same bunch can interact electromagnetically, this leads to distortions  
1487 from the orbit and results in an increase of the emittance,  $\epsilon$ .
- 1488 • **Crossing angle:** Often used to avoid unwanted collisions in machines  
1489 with many bunches, due to the crossing angle  $\theta_c$ , the luminosity is  
1490 reduced by a factor  $F(\theta_c, \sigma_x, \sigma_z) = \sqrt{1 + (\theta_c \sigma_z / 2\sigma x)^2}$ .
- 1491 • **Beam offset:** Originated from the beam-beam effects or misalignments  
1492 in the quadrupole magnets, the beams can collide with small  
1493 transverse offset. Such beams' offsets induce a loss of  $\mathcal{L}$  at the inter-  
1494 action point.
- 1495 • **Hourglass effect:** Appears when beams collide in a point away from  
1496 the IP.

1497 On the other hand, there are diverse strategies to maximise the lumin-  
1498 osity delivered by a machine [108]:

- 1499 • **Maximise the total beam current:** Improvements in beam col-  
1500 limation, cryogenics vacuum and background protection could extend  
1501 the limit on the maximum beam current.
- 1502 • **Compensate reduction factor:** The hourglass effect may be re-  
1503 duced by shorter bunches at the expense of a higher longitudinal pileup  
1504 density (see Section 4.1.1).

### 1505 3.2.1 Machine design

1506 The LHC is a circular hadron accelerator with a circumference of 27 km.  
1507 Located within once was the LEP<sup>2</sup> collider tunnel. The LHC tunnels are  
1508 almost entirely outside the main site, being mainly on french territory.

1509 Circular accelerators are more space-efficient than linear ones due to  
1510 their ability to speed up particles with less physical space. They simultan-  
1511 eously ramp up opposite charge beams with a single magnetic field, with  
1512 bending power given by  $p[\text{GeV}] = 0.3qB[\text{T}]r[\text{m}]$ , where  $p$  is momentum,  $q$  is  
1513 particle charge ( $q = 1$  for protons),  $B$  is magnetic field, and  $r$  is accelerator  
1514 radius.

1515 The LHC has two rings with ultra-high vacuum (to prevent collisions  
1516 with gas molecules while moving through the accelerator) in which particle

---

<sup>2</sup>LEP is the accelerator used by CERN from 1999 to 2000 [110]

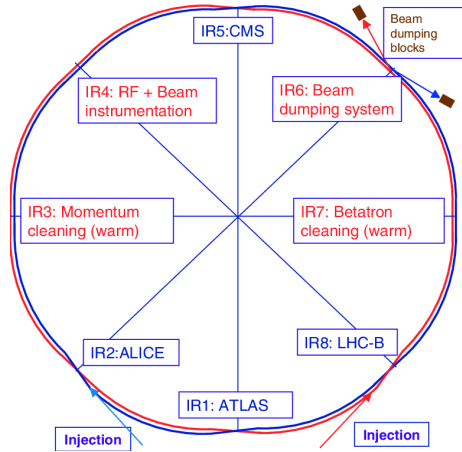


**Figure 3.1:** Schematic layout of the LHC (Beam 1 clockwise, Beam 2 anti-clockwise).

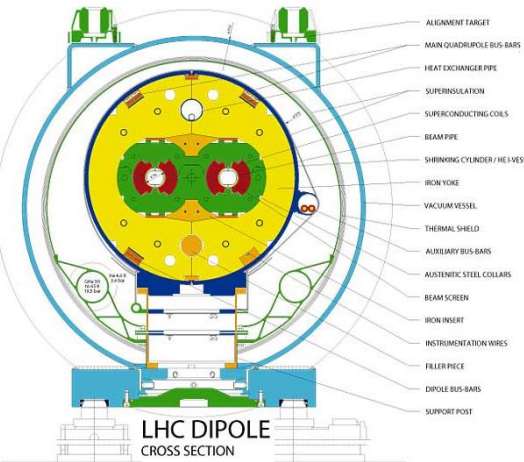


**Figure 3.2:** LHC dipole cross section.

beams travel in opposite directions. The design expected to collide proton beams at a centre-of-mass energy ( $\sqrt{s}$ ) up to 14 TeV at a luminosity ( $\mathcal{L}$ ) of  $10^{34} \text{ cm}^2 \text{ s}^{-1}$  (see Section 3.2.0.1 for details about luminosity). As well as protons, it can collide heavy ions, in particular lead nuclei, at  $\sqrt{s} = 2.3 \text{ TeV}$  per nucleon and a peak luminosity of  $\mathcal{L} = 10^{27} \text{ cm}^2 \text{ s}^{-1}$  [111]. These specifications make the LHC the accelerator with higher  $\sqrt{s}$  collision energy [112].

The beams in the LHC are made up of bunches of protons that are spaced 7 m apart and collide every 25 ns. Each bunch contains around  $1.1 \times 10^{11}$  hadrons, being 2556 the maximum possible number of bunches that can be reached with the beam preparation method currently used [113]. The size of each bunch is approximately 25 cm [114].

The LEP tunnel lies between 45 m and 170 m below the surface on a plane inclined at 1.4% sloping towards the Léman lake. The underground construction adds some shielding from outside interferences that could interact with the detectors and cause anomalous readings. Even 100 m underground, the cosmic rays can reach the detectors, so these are used to help to calibrate them. The tunnel has an internal diameter of 3.7 m, which makes it extremely difficult to install two completely separate proton rings [115] as in the Superconducting Super Collider (SSC). Therefore, the counter-rotating rings are built under the *two-in-one* twin-bore superconducting magnet design. These twin bore configurations have the disadvantage of having the rings magnetically coupled, which adversely affects flexibility [116]. Figure 3.2 shows an example of the LHC twin-bore dipole magnet.

1541 The LHC is not a perfect circle. Approximately 22 km of the LHC ring  
1542 consists of 8 curved sections. The remaining 5 km of the tunnel are made of 8  
1543 straight sections, denominated insertion regions (IR), that provide space for  
1544 the experiments. Figure 3.1 shows the distribution of IR and crossing points  
1545 for the LHC. This layout follows that of the LEP tunnel. The number of  
1546 crossing points where the beams pass from one ring to the other for colliding  
1547 was decreased from the original eight at LEP to four in the LHC in order to  
1548 reduce costs and optimise the utility insertions containing Radio Frequency  
1549 (RF), the collimation and the beam dump systems [106].

1550 The arcs contain the dipole bending magnets, which are shown in Section  
1551 3.2. The 1232 twin-bore magnets curve the trajectory of the particle beam  
1552 that would, otherwise, follow a straight line. Dipoles are also equipped with  
1553 additional multipole lattice magnets (sextupole, octupole and decapole),  
1554 which correct for small imperfections in the magnetic field at the extremities  
1555 of the dipoles.

1556 Each of the eight straight sections is approximately 528 m long. The RF  
1557 cavities delivering 2 MV (an accelerating field of 5 MV/m) at 400 MHz are  
1558 located in the IR4. The 16 RF cavities compensate the synchrotron radi-  
1559 ation losses (the electromagnetic radiation emitted when charged particles  
1560 travel in curved paths) that take place at the arcs of LHC. Since the protons  
1561 loose much less energy than electrons in a circular collider<sup>3</sup>, the LHC would  
1562 have profited from more circular sections. However, re-using LEP tunnels  
1563 was preferred in terms of cost. During the 20 minutes that are needed to  
1564 reach the beams maximum energy, the bunches have passed the RF cavities  
1565 more than 10 million times [106].

1566 The RF cavities (also known as resonators) are metallic chambers spaced  
1567 at intervals along the accelerator shaped to resonate at specific frequencies,  
1568 allowing radio waves to interact with passing particle bunches. The main  
1569 role of the RF cavities is to keep the proton bunches tightly packed to  
1570 ensure the required luminosity at the interaction point. They also transfer  
1571 RF power to the beam to accelerate it to the top energy [117].

1572 At the insertion of the arc and straight sections, quadrupole magnets  
1573 are installed to suppress the dispersion of particles. Acting as focal lenses,  
1574 quadrupole magnets gather the particles together. This system not only  
1575 cancels the horizontal dispersion arising in the arc but also adapts the LHC  
1576 reference orbit to the geometry of the LEP tunnel. Before entering the  
1577 detectors, the inner triplets (which are made mostly from quadrupoles)  
1578 tighten the beam, from  $0.2 \times 10^{-3}$  m down to  $16 \times 10^{-6}$  m. These are known  
1579 as insertion magnets.

---

<sup>3</sup>The energy radiated per particle by synchrotron radiation is proportional to the inverse of the mass of the particle:  $\Delta E \propto 1/m^4$ .

1580 In total there are more than 9000 magnets all over the LHC and more  
1581 than 50 types of magnets are needed to make the particles circulate in  
1582 their path without losing speed. The coils are made of niobium-titanium  
1583 (NbTi) which is cooled to less than 2 K with superfluid helium to reach  
1584 superconductivity.

### 1585 3.2.2 Accelerator complex

1586 To accelerate the proton beams, the existing CERN accelerator complex  
1587 is used. These accelerators were, back in the day, the state of the art  
1588 colliders and now they serve as injection system for the LHC. The path  
1589 followed by the particle beams is presented in Figure 3.3. The accelerator  
1590 complex consists in several machines interconnected to boost the beams  
1591 until these reach the LHC.

1592 The proton bunches are produced ionising a gas of hydrogen atoms and  
1593 then they are accelerated to a momentum of 50 MeV by the linear accelerator  
1594 (LINAC2). After being produced, the beams enter into the first circular  
1595 accelerator, the Proton Synchrotron Booster (PSB) which has 630 m radius  
1596 and increases the energy of the protons until 1.4 GeV.

1597 Right after the PSB, the Proton Synchrotron brings the particles 25 GeV.  
1598 It is followed by 6.9 km long SPS, which raises the energy to 450 GeV. Once  
1599 the protons have 450 GeV, the minimum energy at which the LHC can  
1600 maintain a stable beam, they are injected into the LHC by two different  
1601 2 km-long Transfer Injection (TI) lines [118]. Protons will circulate in the  
1602 LHC for 20 minutes until reaching the nominal beam energy [116].

1603 Heavy-ion collisions were included in the conceptual design of the LHC  
1604 from an early stage and follow the same to maximum acceleration as the  
1605 protons. Lead ions are extracted from a source of vaporised lead and initially  
1606 accelerated by the Low Energy Ion Ring (LEIR).

### 1607 3.2.3 LHC Experiments

1608 In the LHC four major experiments are carried, each of them with its  
1609 own detector (Figure 3.4) and physics programme. Distributed along the  
1610 collider as is shown in Figures 3.3, these highly sophisticated experiments  
1611 are:

- 1612 • **A Toroidal LHC ApparatuS (ATLAS)** [119]: Located in the IR1,  
1613 it is a generic multi-purpose experiment for high luminosity (up to  $\mathcal{L} = 10^{34} \text{ cm}^2 \text{ s}^{-1}$ ). It studies  $pp$  collisions and investigates a wide range
- 1614

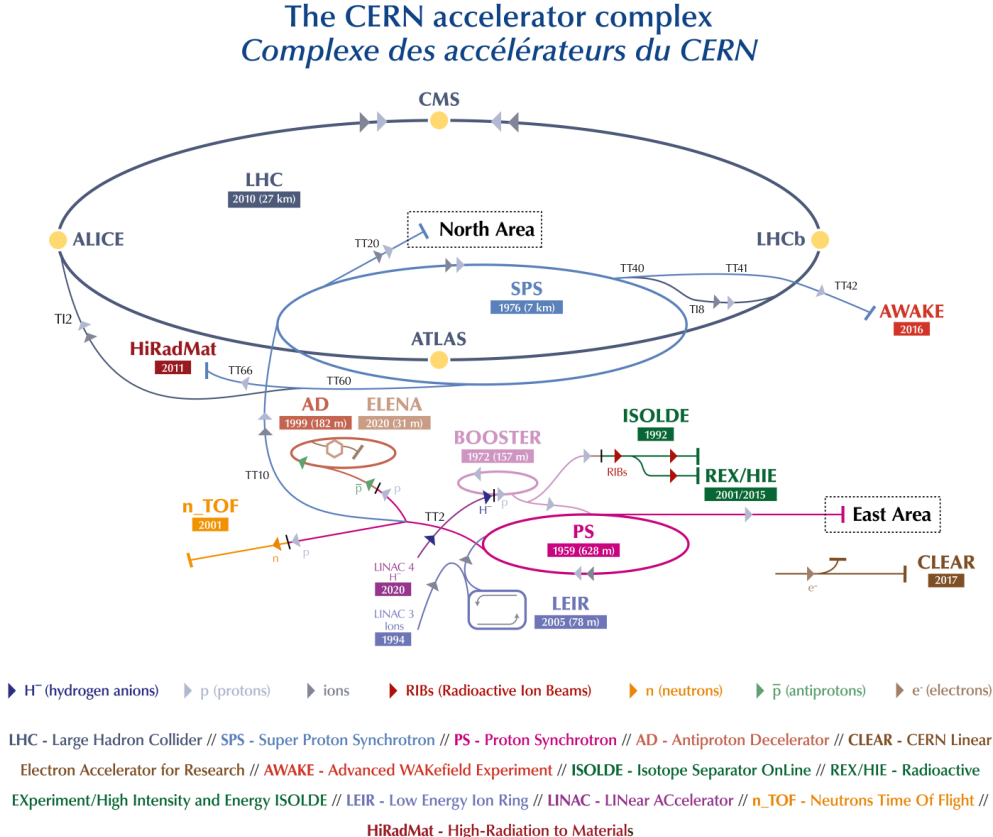


**Figure 3.3:** Scheme of CERN accelerator complex. Protons are injected from the LINAC2 into the PS Booster, then the PS, followed by the SPS, before finally reaching the LHC.

of physics, from the SM to the search for extra dimensions or dark matter. It has the dimensions of a cylinder, 46 m long, 25 m in diameter. The ATLAS detector weighs  $7 \times 10^3$  tonnes. The design of the ATLAS detector features excellent jet and  $E_T^{\text{miss}}$  resolution, particle identification and flavour tagging and standalone muon measurements. A scheme of this detector is shown in Figure 3.4a. ATLAS will be covered in detail in Section 3.3.

- **Compact Muon Solenoid (CMS)** [120]: Built inside the IR5, it's the other general-purpose experiment for high luminosity (same  $\mathcal{L}$  as ATLAS). CMS has the same objectives and goals as ATLAS but both its hardware and software designs are different. Even though CMS is smaller than ATLAS (21 m long, 15 m in diameter) it is much heavier, weighting  $14 \times 10^3$  tonnes. The bulk of its weight is the steel yoke that confines the 4 T magnetic field of its superconducting solenoid.

1629  
1630  
1631  
1632  
The design of CMS emphasises magnificent electron/photon energy  
and momentum resolution. Figure 3.4b illustrates this device. The  
role of coexistence of CMS and ATLAS is fundamental so that one  
can verify and confirm the experiments of the other independently.

- 1633  
1634  
1635  
1636  
1637  
1638  
1639  
1640  
• **Large Hadron Collider beauty (LHCb)** [121]: Hosted at IR2, it  
is a lower luminosity experiment designed to study the small asymmetries  
between matter and antimatter through  $\mathcal{CP}$  violation using rare decays of  $b$ -quark based hadrons. The detector is arranged as a  
succession of planar sub-detectors (as can be seen in Figure 3.4c) since  
most of the  $b$ -flavoured mesons follow the beam pipe direction when  
created in the  $pp$  collision. LHCb delivers remarkable low-momentum  
track reconstruction and particle identification.
- 1641  
1642  
1643  
1644  
1645  
1646  
1647  
1648  
1649  
• **A Large Ion Collider Experiment (ALICE)** [122]: It is a low  
luminosity experiment in IR8 that focuses on QCD. The main feature  
of ALICE is a general-purpose detector that it uses heavy-ion collisions  
to study matter interacting at extreme densities and temperatures,  
thus reproducing the quark-gluon plasma. This detector is shown in  
Figure 3.4d and it provides highly efficient track reconstruction in an  
environment full of heavy ions. Besides running with Pb ions, the  
physics programme includes collisions with lighter ions, lower energy  
collisions and a dedicated proton-nucleus run.

1650  
1651  
1652  
1653  
1654  
Along the LHC machine, there are other experiments much more smaller  
than ATLAS, CMS, LHCb and ALICE, typically sharing the cavern  
with the major projects. The most relevant among the minor experiments  
are LHCf [123], MATHUSLA [124], MilliQan [125], MoEDAL [126],  
TOTEM [127] and FASER [128].

### 1655 3.2.4 LHC Computing grid

1656  
1657  
1658  
1659  
1660  
1661  
1662  
1663  
1664  
The data collected by the different LHC experiments is stored, processed  
and, then, made available for all the researchers of each collaboration<sup>4</sup>. This  
is possible thanks to the last piece of the LHC, its computing model and  
infrastructure: the LHC Computing Grid (LCG). It consists of several computing farms distributed around the world and interconnected. Figure 3.5  
shows the geographical distribution of the different facilities that comprise the LCG. Just as the WWW enables access to information, the Grid enables access to computer resources. Employing a grid certificate, is possible for any user to run jobs on the grid and to access the data stored. The

---

<sup>4</sup>Within the grid context, each collaboration is known as Virtual Organisation (VO).

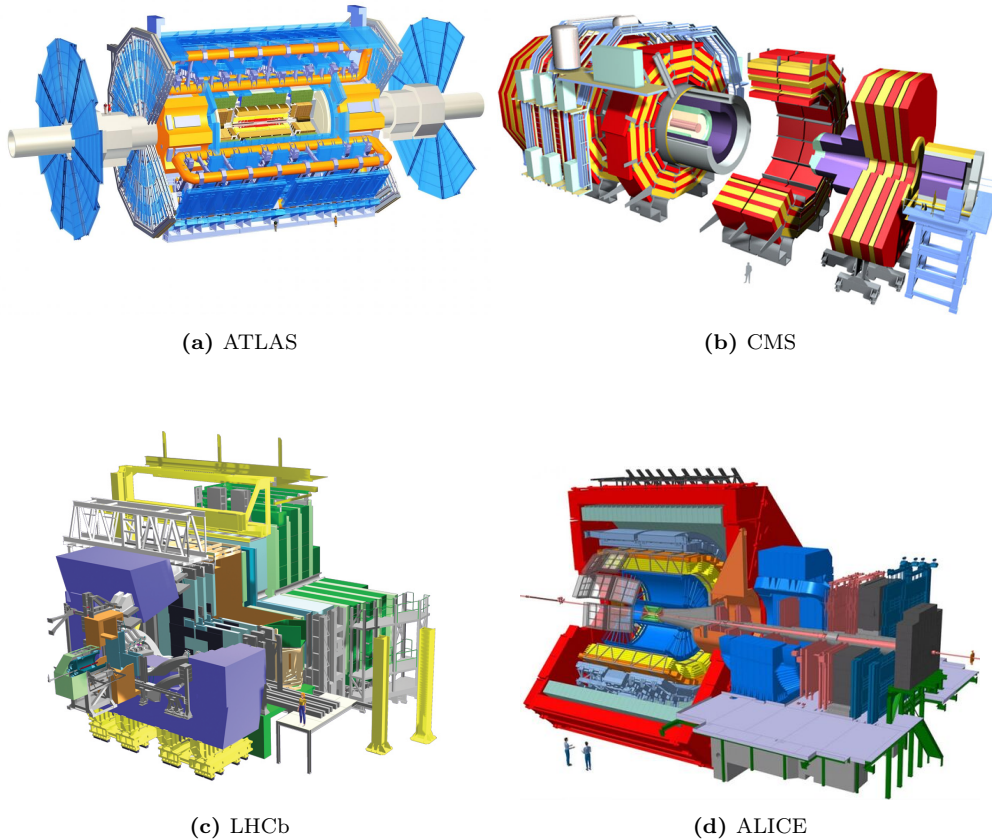


**Figure 3.4:** Scheme of LHC main experiments. Note that the images are not equally scaled.

1665 implementation of the grid model implies an effective coordination among  
 1666 all LHC collaboration centres [129].

1667 Different types of computing centres have been defined and classified in  
 1668 Tiers [131]:

- 1669     • **Tier-0:** This facility is located at CERN and it is responsible for  
 1670       archiving (first copy) and distributing the raw data received from the  
 1671       Event Filter, i.e., the data emerging from the Data Acquisition sys-  
 1672       tems (DAQ) after the trigger. It provides prompt reconstruction and  
 1673       distributes a copy of the raw data to the Tier-1 centres.
- 1674     • **Tier-1:** These facilities archive the raw data permanently and provide  
 1675       the computational capacity for reprocessing and for physical analysis.  
 1676       It also stores the simulated and reprocessed data. Currently, there  
 1677       are thirteen large computer centres serving as Tier-1 (see Figure 3.6).  
 1678       These make data available to their Tier-2 centres [132].

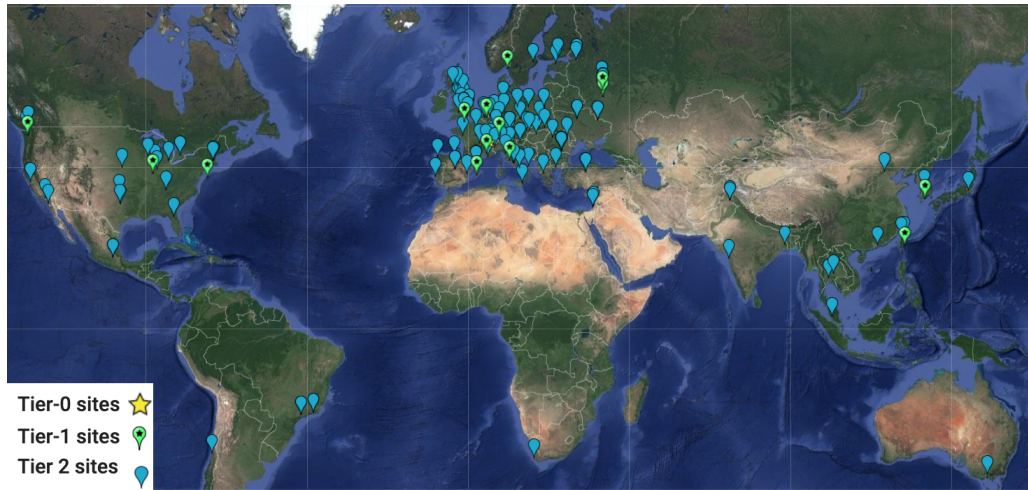


**Figure 3.5:** Worldwide LHC Computing Grid geolocalisation of sites [130].

- **Tier-2:** Typically located at universities and other scientific institutes, there are more than 150 Tier-2 sites. The derived datasets produced by the physics groups are copied to the Tier-2 facilities for further analysis. The MC simulations for event production are executed at this level.
- **Tier-3:** The local computing resources, from local clusters to even just an individual PC are referred to as Tier-3. There is no formal engagement between worldwide LCG and the Tier-3.

This system provides near real-time access to LHC data. The LCG collaboration spreads out over 42 countries with 170 computing centres and 1 million computer cores, being the world's largest computer grid. It deals with over two million tasks daily. These specifications make the LCG the most sophisticated system for data taking and analysis ever built for science.

### 3.2.5 Phenomenology of proton-proton collisions

**Either move to theory or to an appendix.** During the data tracking period of LHC Run-2, proton collisions took place with a centre-of-mass energy of 13 TeV. The total cross section for  $pp$  collisions at this energy was measured to be  $\sigma_{tot} = (110.6 \pm 3.4)$  mb according to [133]. The method used to measure  $\sigma_{tot}$  also made it possible to separate the cross section into the elastic cross-section  $\sigma_{el} = (31.9 \pm 1.7)$  mb and the inelastic cross-section  $\sigma_{inel} = (79.5 \pm 1.8)$  mb. However, only inelastic scattering generates particles with an sufficient angle with respect to the beam axis so that these particles enter into the geometrical acceptance of the detector. Figure 3.7 shows the

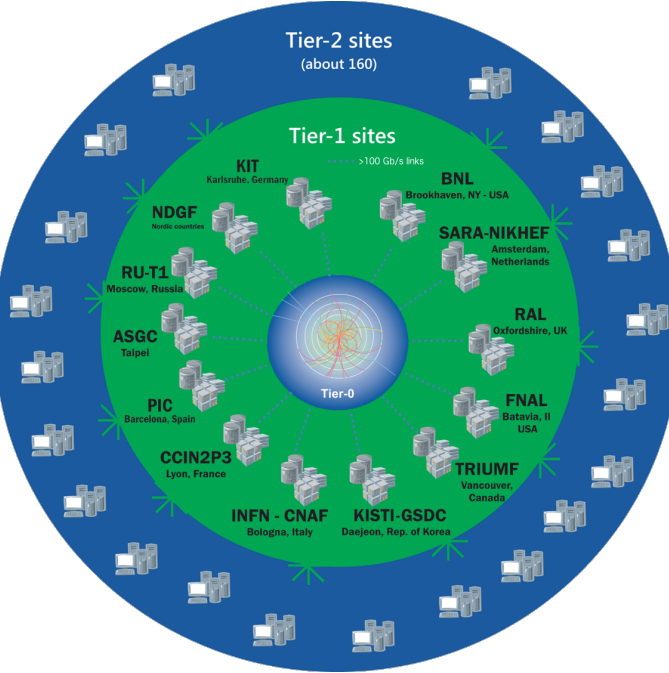


**Figure 3.6:** Distribution by Tiers of the LCG [132]. This project provides global computing resources to store, distribute and analyse the data recorded at the LHC.

1702 cross-section (elastic, inelastic and total) for  $pp$  collisions depending on  
 1703  $\sqrt{s}$ . The shown cross-section can be computed as the convolution of parton  
 1704 density functions (PDFs) with the parton scattering matrix element  $\mathcal{M}$ .

1705 At LHC energy regime, the  $pp$  collisions cannot be described as a point-  
 1706 like interactions, here is where the PDFs come into play. The PDFs are  
 1707 functions containing the long distance structure of the hadron in terms of  
 1708 valence and sea quarks and gluons. This description is known as “parton  
 1709 model”.

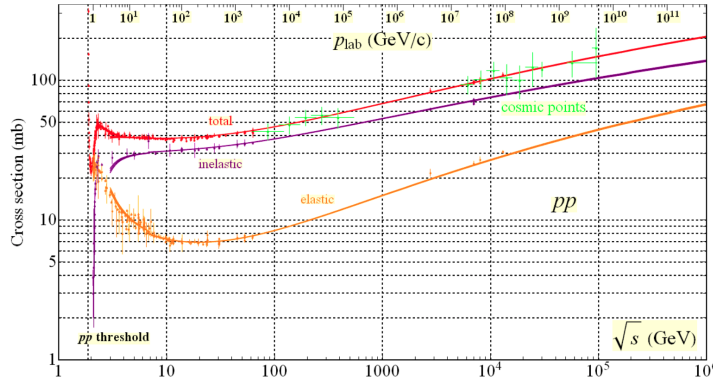
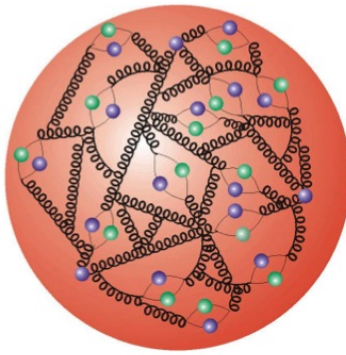


**Figure 3.7:** Total and elastic cross-section for  $pp$  collisions as a function of the laboratory momentum and the  $\sqrt{s}$  [134]. At  $\sqrt{s} = 13$  TeV,  $\sigma_{el} = (31.9 \pm 1.7)$  mb,  $\sigma_{inel} = (79.5 \pm 1.8)$  mb and  $\sigma_{tot} = (110.6 \pm 3.4)$  mb.

### 1710 3.2.5.1 Proton structure and parton model for collisions

1711



The parton model for hadrons describes these non-fundamental particles as a composite of a number of point-like constituents named partons. The proton is not only simply made of three quarks ( $uud$ , the so called “valence” quarks) but also, there is a “sea” of gluons and short-lived quark and anti-quark pairs. The partons in the sea are continuously interacting with each other and can have any flavour.

1712 The distribution of a hadron’s momentum among its constituents is de-  
 1713 scribed by its PDFs [135]. The momentum of the partons within a proton is  
 1714 determined through fits to several cross-section data points obtained from  
 1715 experiments such as deep inelastic scattering, Drell-Yan, and jet measure-  
 1716 ments. Several global fitting collaborations, including ABM, CT, MMHT,  
 1717 NNPDF, MSTW, and CTEQ, use different methods to perform these fits.  
 1718 The fits are then extrapolated to new energy scales.

1719 The PDF  $f_{a/A}(x, Q^2)$  is the probability of finding parton  $a$  in hadron  
 1720  $A$  carrying a fraction  $x = p_a/p_A$  of its momentum at the energy scale  $Q^2$ .  
 1721 At lower energies ( $Q \sim 1$  GeV), the momentum of a proton is primarily  
 1722 shared among its valence quarks, while at higher energies ( $1 < Q \lesssim 1$  GeV),  
 1723 the emission of gluons carrying some of the quark’s initial momentum is  
 1724 more likely. As an example, several PDFs at two different scale energies are  
 1725 presented in Figure 3.8 as a function of  $x$ . In QCD theory, these interactions  
 1726 can be divided into two categories: hard (large momentum transfer) and

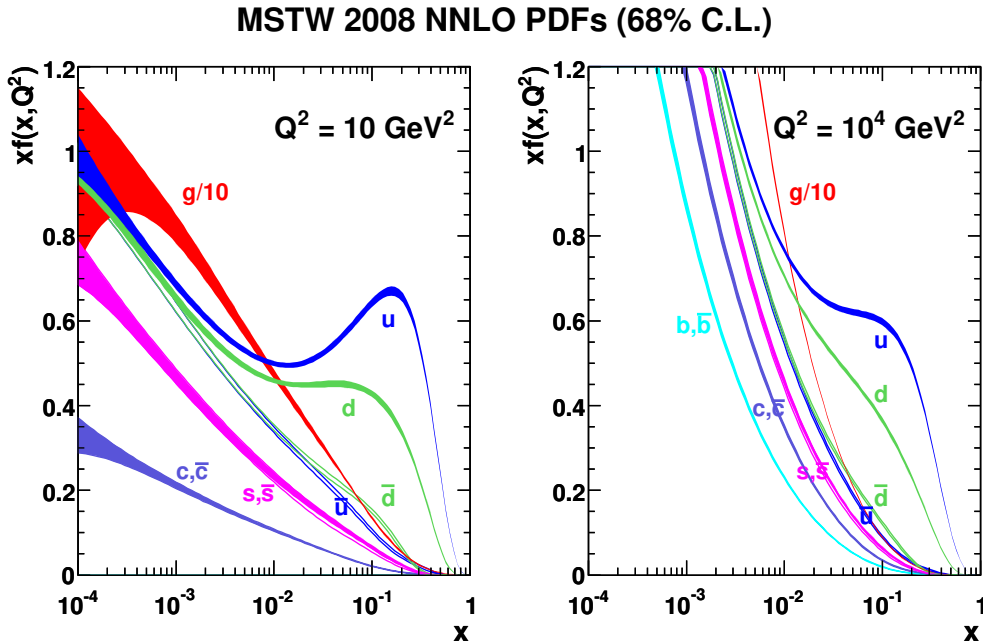


**Figure 3.8:** Parton distribution functions  $xf(x, q^2)$  plotted against  $x$  for gluons different quark flavours at  $Q^2 = 10 \text{ GeV}^2$  and  $Q^2 = 10^4 \text{ GeV}^2$  using MSTW 2008 NNLO [136].

1727 soft (low momentum transfer). Hard processes are well understood and  
 1728 can be predicted with good precision, while soft interactions have a much  
 1729 greater impact of non-perturbative QCD and are more difficult to calculate.

1730 When two protons ( $A$  and  $B$ ) collide, the partons of the two protons  
 1731 interact via a hard scattering process. Each of the interactions between the  
 1732 partons pairs is independent from the interactions of other partons. The  
 1733 remaining partons also contribute to the final state as “underlying events”.  
 1734 Figure 3.9 provides a simplified representation of a  $pp$  collision.

The total cross section in a hadron-hadron (where parton  $a$  from hadron  $A$  interacts with parton  $b$  from hadron  $B$ ) hard scattering process, such as a  $pp$  interaction, is:

$$\sigma_{AB \rightarrow X} = \sum_{a,b} \iint dx_a dx_b f_a(x_a, Q^2) f_b(x_b, Q^2) \times \hat{\sigma}_{ab \rightarrow X} \quad (3.9)$$

1735 where  $f_i(x_i, Q^2)$  is the PDF of  $A$  and  $B$ . Here, the  $Q$  is chosen to be the  
 1736 factorisation scale<sup>5</sup> The contribution of the individual partons  $a$  and  $b$  is  
 1737 denoted by  $\hat{\sigma}_{ab \rightarrow X}$ . With this equation, all process in  $pp$  collisions can be  
 1738 computed.

<sup>5</sup>The factorisation scale,  $\mu_F$ , determines the boundary between low and high energy and hence determines the scale at which perturbative calculation becomes valid.

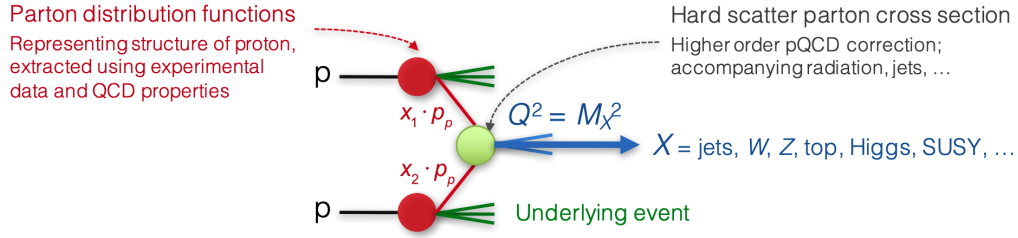


**Figure 3.9:** Simplified view of a  $pp$  collision [108].

Depending on the order achieved in perturbation theory (LO, NLO, NNLO, ...), the cross section of the individual partons to give the final state of interest ( $ab \rightarrow X$ ) is calculated as:

$$\begin{aligned}\hat{\sigma}_{ab \rightarrow X} &= \sum_{i=0}^{\infty} \alpha_s^i(\mu_R) \sigma_n(x_a, x_b, \mu_F^2) \\ &= [\sigma_{LO}(x_a, x_b, \mu_F^2) + \alpha_s(\mu_R) \sigma_{NLO}(x_a, x_b, \mu_F^2) \\ &\quad + \alpha_s(\mu_R)^2 \sigma_{NNLO}(x_a, x_b, \mu_F^2) + \dots]_{ab \rightarrow X}\end{aligned}$$

where  $\alpha_s^i(\mu_R)$  is the coupling constant derived for a specific renormalisation scale<sup>6</sup>. In theory, if the entire perturbation series could be computed, the need for  $\mu_F$  and  $\mu_R$  parameters would disappear. However, this is not feasible and the series must be truncated at a specific order. Hence, it becomes crucial to set the values of  $\mu_F$  and  $\mu_R$ . This results in uncertainties in the calculations which are often addressed by varying these parameters.

### 3.2.5.2 Underlying event

The Underlying Event (UE) encompasses all what is seen from a collision that not directly coming from the primary hard scattering process. This encompasses elements such as beam-beam remnants, multiple parton interactions (MPI) within a single collision, and initial and final state radiation (ISR/FSR). Typically, the UE have lower  $p_T$  than the main process. A precise modelling of the UE is crucial for conducting successful experimental studies because this soft interaction may affect the high- $p_T$  measurements. This is because it allows for a clear differentiation between the direct products from hard scattering and the rest of the event. **Maybe copy the Figure from Galo or Florencia thesis.**

<sup>6</sup>The renormalisation scale,  $\mu_R$ , is used to address the ultraviolet divergences in QCD that occur due to high momentum in the loops

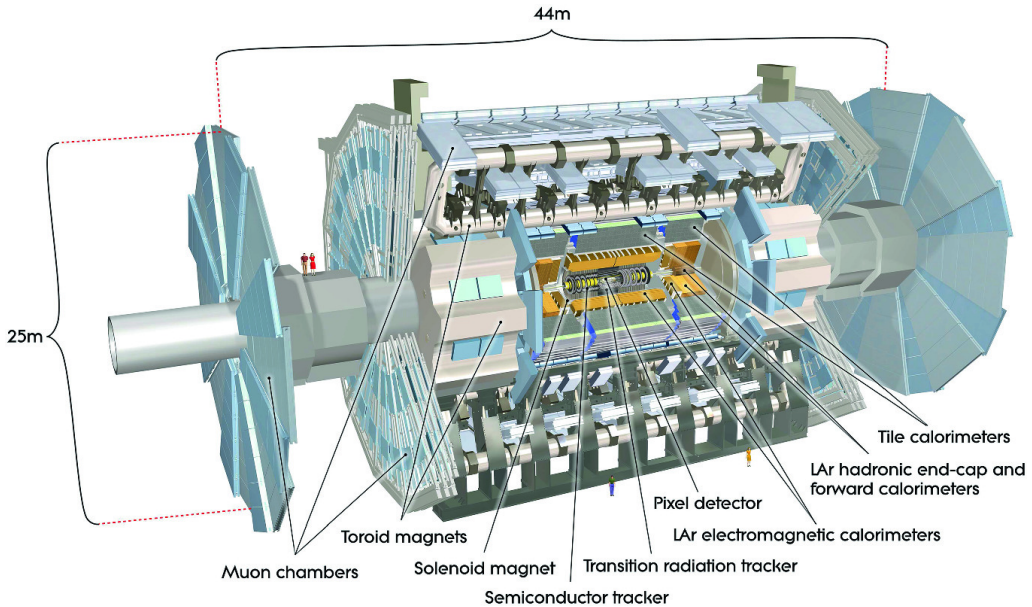


**Figure 3.10:** Simulated schematic view of the ATLAS detector.

### 1756 3.3 ATLAS

1757     Installed in its experimental cavern at point 1, ATLAS is the largest de-  
 1758     tector ever constructed for a particle collider with its 46 m long and 25 m in  
 1759     diameter. It is designed to record events of high-energy colliding particles at  
 1760     high luminosities. The thousands of millions of interactions that take place  
 1761     at the centre of the ATLAS detector are recorded and processed by the  
 1762     different sub-detectors, which are composed by more than 100 million sens-  
 1763     itive electronic channels. Each ATLAS sub-detector is sensible to a different  
 1764     type of particle and to different properties. Therefore, the layered structure  
 1765     allows for effective particle identification, as well as enables accurate mea-  
 1766     surements of energy and momentum. Figure 3.10 shows an overall layout of  
 1767     the ATLAS detector and identifies its different sub-detectors. In the picture  
 1768     can be appreciated that the cylindrical shape of ATLAS is divided into two  
 1769     parts: the “barrel” and the two “end-caps”. In the barrel region, the sub-  
 1770     detectors are built as coaxial layers around the beam pipe. As one moves  
 1771     away from the axis, it finds the Inner Detector (ID), the solenoid magnet,  
 1772     the Electromagnetic (ECAL) and Hadronic (HCAL) Calorimeters, and the  
 1773     Muon Spectrometer (MS) in the outermost layer. The technical details of  
 1774     these sub-detectors and the magnet system are presented in Sections 3.3.2,  
 1775     3.3.3, 3.3.4 and 3.3.5.

1776     ATLAS is able to explore a wide range of phenomena with high pre-  
 1777     cision, including new physics events. Even though it is a general-purpose  
 1778     experiment, it was designed taking into account the Higgs and BSM phe-

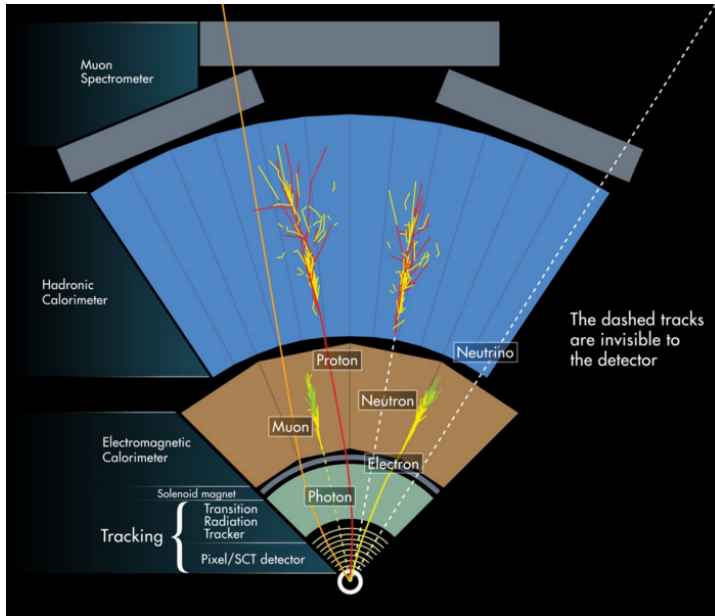


**Figure 3.11:** Fraction of the transversal plane of ATLAS. Each particle leaves a different signature in each layer. By signature is meant the particular distribution of energy deposition. This scheme is fundamental to understand the object reconstruction in the next chapter.

mena searches that were carried out at LHC. This is why, since the mass of the Higgs was not known at that time, its performance requirements cover a large mass range for the Higgs decay products.

One of the most important milestones for ATLAS (and for all science in the last decades) was the observation of a particle consistent with the Higgs boson in July 2012 (see 2.2.1). In 2016, the combination of ATLAS and CMS measurements for Higgs boson production on decay rates with Run-1 data was published [137]. After that, the physics programme at 13 TeV allowed precision studies of the Higgs boson and other SM particles, as well as the search for new particles with other masses.

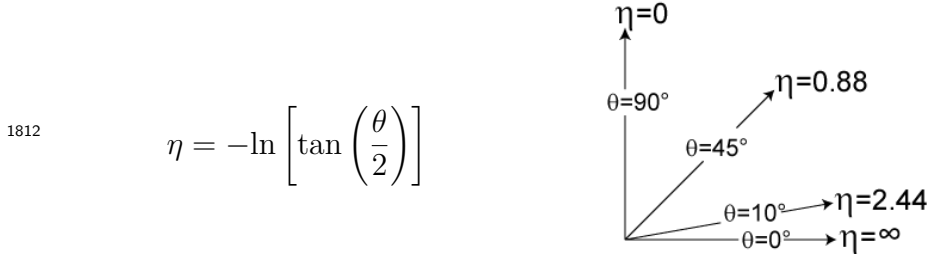
Other relevant items in ATLAS timeline are the observation and rate measurement of  $t\bar{t}$  events [138] or the evidence for rare electroweak  $W^\pm W^\pm$  production [139]. The first evidence of light-by-light scattering at high energy was also found with ATLAS [140]. The first  $t\bar{t}H$  associate production [141] and  $H \rightarrow b\bar{b}$  decays [142] were observed for first time by ATLAS too.

The physics programme of ATLAS include precise measurements of the SM [143], super-symmetry studies [144], sources of  $\mathcal{CP}$ -violation [145], large  $E_T^{\text{miss}}$  dark-matter searches [146], astroparticle physics [147], extra dimensions [148] and others.

ATLAS is not only a detector but also a collaboration of people composed of more than 5000 members including physicists, engineers, technicians, doctoral students and support staff. Working at CERN or at any of the 181 institutions that constitute ATLAS, the different teams work collaboratively to achieve success.

### 3.3.1 Coordinate system

Due to its cylindrical structure, ATLAS uses a right-handed system with its origin at the IP where the collisions take place. On one side, there are the ( $x, y, z$ ) Cartesian coordinates. The  $x$ -axis is pointing towards the centre of the ring circumference, the  $y$ -axis is perpendicular to the plane defined by the LHC ring and it points to the surface, and the  $z$ -axis is defined by the direction of the beam. On the other side, it is more frequent to employ the cylindrical coordinates ( $r, \phi, z$ ) or the system defined by the azimuthal angle ( $\phi$ ) and the pseudorapidity ( $\eta$ ):



where  $\theta$  is the polar angle<sup>7</sup>. As the polar angle approaches zero, pseudorapidity tends towards infinity. The change in pseudorapidity  $\Delta\eta$  is Lorentz invariant under boosts along the beam axis. The use of  $\eta$  is preferred over  $\theta$  because the distribution of events typically looks flat with respect to  $\eta$ . In terms of the momentum, the above equation can be expressed as:

$$\eta = -\ln \left( \frac{|\vec{p}| + p_z}{|\vec{p}| - p_z} \right)$$

being  $p_z$  the momentum along the beam direction. The rapidity is used when dealing with massive particles and it can be expressed as  $y = \frac{1}{2} \log[(E + p_z)(E - p_z)]$ , being  $E$  the energy projection of the momentum in the  $z$ -axis. Note that when the particles approach the speed of light, they are in the limit  $E \approx |\vec{p}|$  and the values for rapidity and pseudorapidity converge. The angular distance is measured in units of  $\Delta R = \sqrt{(\Delta\eta)^2 + (\Delta\phi)^2}$ , which is

<sup>7</sup>Defined as the angle between the particle three-momentum,  $\vec{p}$  and the positive direction of the beam axis.

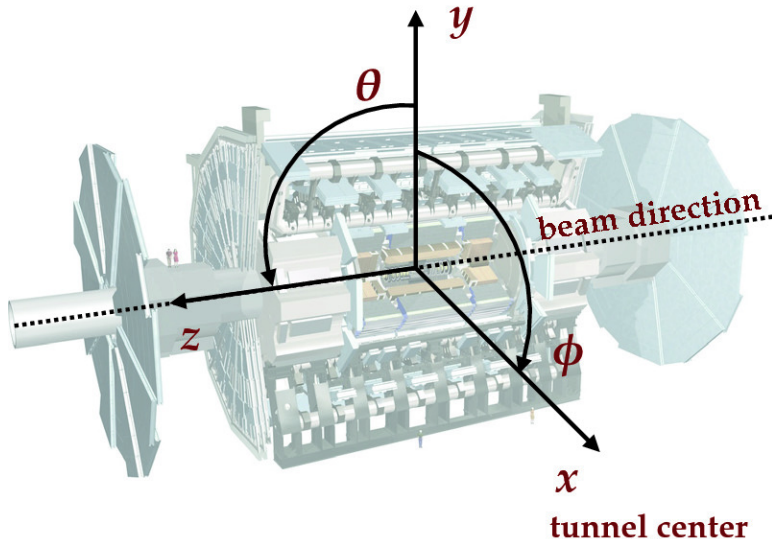


**Figure 3.12:** Coordinate system of the ATLAS detector.

invariant under a boost along the  $z$ -axis<sup>8</sup>. Figure 3.12 shows the coordinate system of ATLAS for both Cartesian and cylindrical coordinates.

The transverse magnitudes such as the transverse momentum ( $p_T$ ) and transverse energy ( $E_T$ ) are defined in the  $x$ - $y$  plane. Knowing the  $p_T$ , and the  $\eta$  and  $\phi$  angles, the cartesian momentum ( $p_x, p_y, p_z$ ) can be derived from:

$$\begin{aligned} p_x &= p_T \cos(\phi) & p_y &= p_T \sin(\phi) \\ p_z &= p_T \sinh(\phi) & |\vec{p}| &= p_T \cosh(\phi) \end{aligned}$$

### 3.3.2 Inner Detector

The ATLAS ID [149][150][119] is the closest sub-detector to the beam pipe. Its layout is shown in Figures 3.13 and 3.14. The charged particles follow a curved trajectory inside the ID due to the magnetic field of the ATLAS bending magnet (see 3.3.5). The different pieces that comprise the ID can reconstruct the traces of these particles with great accuracy allowing, thus, to measure its momentum (this is done using the sagitta method described in Section ??). For particles coming from the IP, the geometric acceptance of the ID is  $|\eta| < 2.5$  for pseudorapidity and full  $\phi$  coverage in the azimuthal angle. The ID provides  $p_T$  resolution of  $\sigma_{p_T}/p_T = 0.05\%$  GeV  $\oplus 1\%$  and a transverse impact parameter resolution<sup>9</sup> of 10  $\mu\text{m}$  for particles in

<sup>8</sup> $\Delta\eta = \eta_2 - \eta_1$  and  $\Delta\phi = \phi_2 - \phi_1$ .

<sup>9</sup>The impact parameter determine the distance of a reconstructed track from a charged particle to the perigee (the closest point of the track to the global  $z$ -axis)

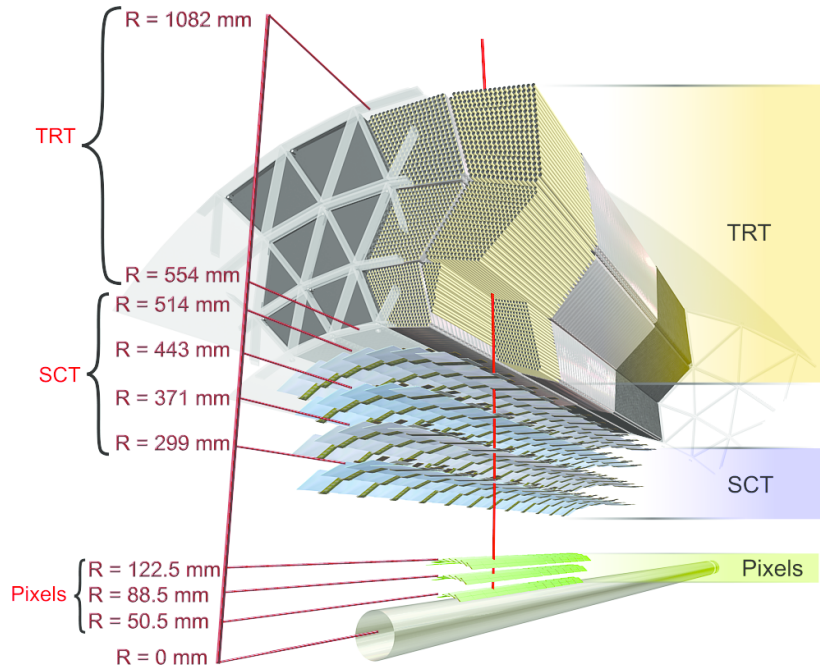


**Figure 3.13:** Barrel part of ID of the ATLAS experiment with the Pixel, SCT and TRT sub-detectors. The IBL is not shown here.

the central  $\eta$  region. It is designed to provide excellent momentum resolution, pattern recognition and measurements of both primary and secondary vertex for charged particles above the  $p_T$  threshold (nominally 0.5 GeV).

The ID is composed of four complementary sub-detectors: The Insertable B-Layer (IBL), the Pixel Detector, the Semiconductor Tracker (SCT) and the Transition Radiation Tracker (TRT). In the sections that follow, a description of each sub-system is provided.

Depending on the  $\eta$  that a particle has, it will interact with some elements of the detector. Figure 3.14 shows the end-cap elements transversed by two charged particles with  $\eta = 2.2$  and  $1.4$ . The track with  $\eta = 1.4$  traverses first the beryllium beam-pipe, then the three cylindrical silicon pixels and the four disks with double layers of the SCT. Finally, this particle travels across approximately 40 tubes in the TRT wheels. In contrast, the particle with  $\eta = 2.2$  encounter the first of the cylindrical silicon-pixel layers after leaving the beryllium pipe. Then, the two end-cap pixel disks and the four last disks of the end-cap SCT.

#### 1848    **Silicon semiconductors**

1849    When a charged particle traverses a doped silicon semiconductor, it creates  
1850    a pair electron-hole by ionisation. An electric field is applied to the active

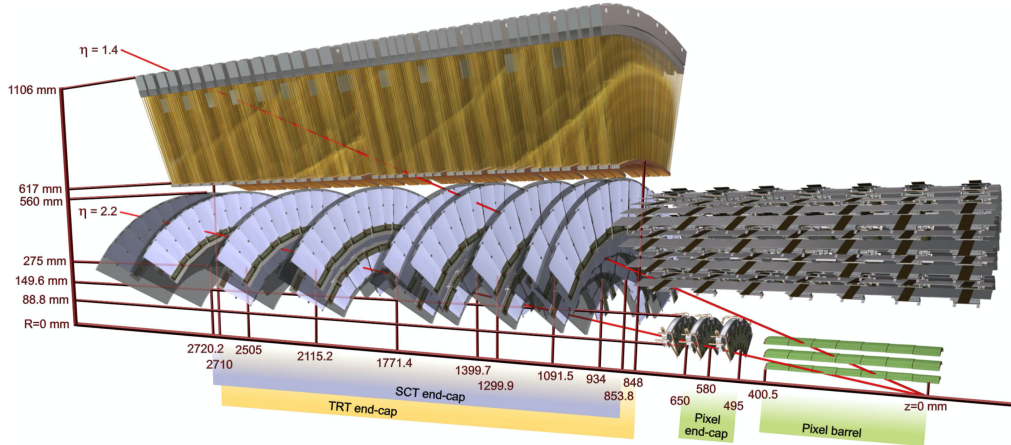


**Figure 3.14:** End-cap of the ID.

part of the detector module so that the electron drifts in oposite direction of the electric field and the hole in the field direction. Then, both charges are collected by the p-n junctions. The silicon sensors can be shaped either as pixels, providing precies 2D space point, or as strips, giving a single dimension positioning. On the order of  $10^5$  electron-hole pairs are liberated when a particle crosses the silicon wafer and, with appropriate electronics, a clear signal is obtained in the pixel or strip in which the charged was collected.

### 3.3.2.1 Insertable B-Layer

The IBL [151] is the innermost component of the ID. It is located between the beam pipe and the pixel detector. Added after Run-1, it provides the closest-to-IP measurements. This improves the robustness and performance of the ATLAS tracking system. It plays a fundamental role for  $b$ -tagging efficiency because this tagging relies on precise vertex reconstruction. The IBL provides redundancy in the measurements of tracks in order to control the fake rate arising from random combinations of clusters in events with a high pile-up background.

With a hit resolution of  $8 \mu\text{m}$  in  $r\phi$  and  $40 \mu\text{m}$  along  $z$ , the IBL covers the  $|\eta| < 2.7$  and the entire  $\phi$  range.

The barrel structure if the IBL has a radius of 3.2 cm and is composed by 14 carbon fibre staves as it is shown in Figure 3.15. Each stave has incorporated cooling  $\text{CO}_2$  circuits, has 32 or 16 modules and uses two types of photodetectors: ATLAS pixel planar sensors and 3D pixel sensors. The

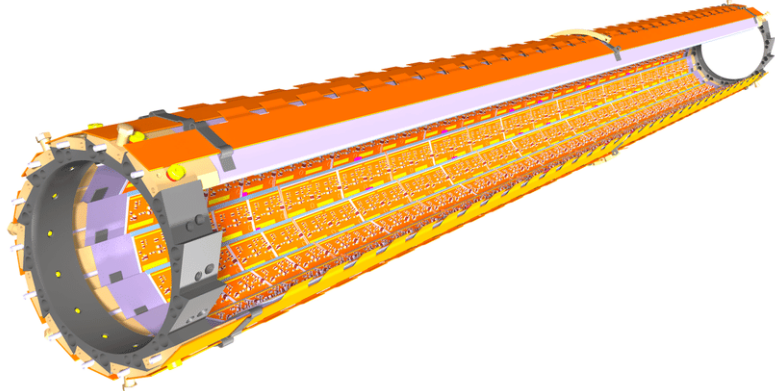


**Figure 3.15:** Schematic drawing of the ATLAS IBL Detector [151].

1874 used pixels have a size of  $50 \times 400 \mu\text{m}^2$ . Due to the high luminosity of the  
 1875 LHC, the IBL is built with radiation-tolerant sensors.

### 1876 3.3.2.2 Pixel Detector

1877 The ATLAS Pixel Detector [152] consists of a strip detector in the out-  
 1878 ermost layers and a pixel detector in the region which is closer to the IBL.  
 1879 Along with the IBL, it aims to reconstruct the trajectories of the particles  
 1880 traversing it. It provides a full coverage of the azimuthal angle  $\phi$  and a  
 1881 pseudorapidity range of  $|\eta| < 2.5$  as well as a resolution of  $10 \mu\text{m}$  in  $r\text{-}\phi$  and  
 1882  $115 \mu\text{m}$  in the  $z$ .

1883 The Pixel Detector and the IBL combined contain  $92 \times 10^6$  pixels with its  
 1884 respective electronic channels, which cover an area of approximately  $1.9 \text{ m}^2$   
 1885 of silicon consuming  $15 \text{ kW}$ . The barrel region consists of four concentric  
 1886 layers equipped with 1736 sensor modules and each of the two end-caps  
 1887 has three disks with 2888 modules [153]. Figure 3.17 shows the assembly  
 1888 view and cross section of a module of the ATLAS ID Pixel Detector. Each  
 1889 of these modules consists on a silicon pixel sensor bonded to the front-end  
 1890 electronic chips.

1891 Hits in a pixel are read out if the signal exceeds a tunable threshold. The  
 1892 pulse height is measured using the Time-over-Threshold (ToT) technique.

### 1893 3.3.2.3 Semiconductor Tracker

1894 The SCT consists of 4088 modules tiling four coaxial cylindrical layers  
 1895 in the barrel region and two end-caps each containing nine disk layers, all  
 1896 of this surrounding the Pixel Detector and providing additional precision

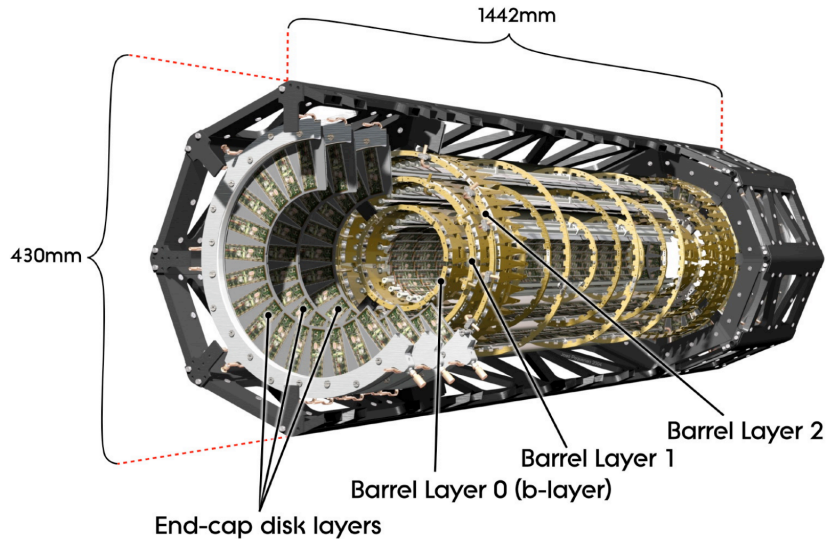


**Figure 3.16:** Schematic view of the ATLAS pixel detector consisting of individual barrel and end-cap layers [119].

tracking. The main difference with the Pixel Detector is that the SCT uses microstrip sensor technology, which is very similar to that of a pixel but being much larger (6 cm). The reason to use microstrips instead of pixels is that the strips are more cost-effective than traditional pixels and a good spatial resolution can be obtained as well if the strips are arranged with an angular offset. Therefore, each SCT detector unit consists on two back-to-back silicon-microstrip planes with a relative angle of 40 mrad. Eight strip layers (i.e. four space points) are crossed by each track in the SCT providing valuable tracking information with resolution of  $17\text{ }\mu\text{m}$  in  $r\text{-}\phi$  and  $580\text{ }\mu\text{m}$  in the  $z$  coordinate. The SCT covers the entire  $\phi$  range and up to 2.5 in  $\eta$ .

Figure 3.18 shows an exploded view of the different components of an SCT module, including the high thermal conductivity spine, the polyimide hybrids and readout chips.

### 3.3.2.4 Transition Radiation Tracker

The TRT is used in conjunction with the Pixel Detector and silicon micro strip (SCT) to extend the  $\eta$  range in which the tracks can be reconstructed to  $|\eta| = 2$ . This part of the ID is formed by a large number of 4 mm straw tubes filled with gas. This part of the ID relies both on the collection of primary ionisation charge and the collection of secondary ionisation charge arising from the transition radiation to measure the track of charged particles. The tube surface functions as a cathode while the wire in the center as a cathode. When a charged particle passes through the gas in the tube, it ionises the

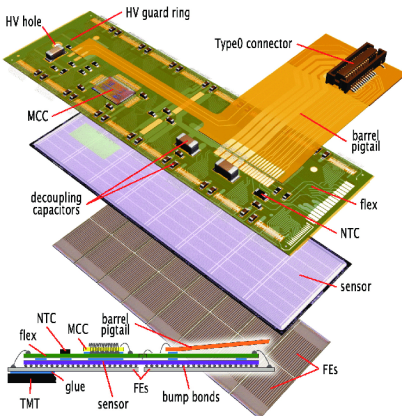


**Figure 3.17:** Pixel Detector module [152].

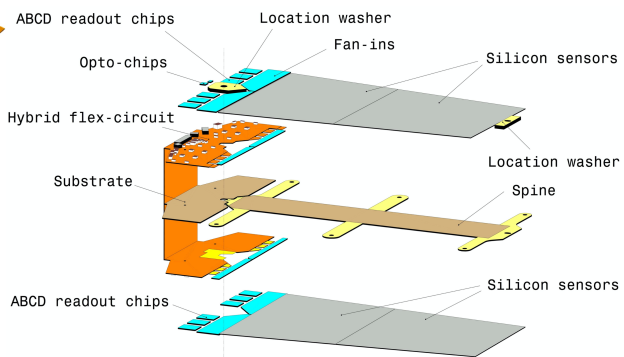


**Figure 3.18:** SCT detector module [119].

gas and the freed electrons drift towards the anode, generating an electrical current. This detector provides a single hit resolution of  $170\text{ }\mu\text{m}$  in  $r\text{-}\phi$  but does not have sensitivity in  $z$ . The TRT also provides discrimination between electrons and pions since the latter generate a much smaller signal than the former. When the electrons pass, they produce x-ray photons that lead to strong avalanches within the tubes and, thus, a great signal.

### 3.3.3 Calorimeters

After the ID, the next layer of detectors in ATLAS correspond to the calorimeters (Figure 3.19) [154]. Their purpose is to measure the energy of the particles (neutral or charged), as well as to help to reconstruct the path followed by them. Most particles initiate a shower (Section 3.3.3.1) when they enter into the calorimeter. Part of the energy of these particles is deposited in the device, then collected and measured by it. Most of calorimeters in particle physics are segmented transversely to provide information about the direction of the particles. Based on how the particle shower develops, the longitudinal segmentation can provide information for identifying the particle (a more detailed discussion of how particles are reconstructed within the ATLAS detector is presented in Chapter 5).

In general, calorimeters can be classified as sampling, when are made of two types of materials, or homogeneous, built with just one type of material. ATLAS uses sampling calorimeters, which consist of alternating layers of different materials:

- **Passive material:** Also known as absorber, it is a denser material to full stop the traversing particles. When a particle interacts with the

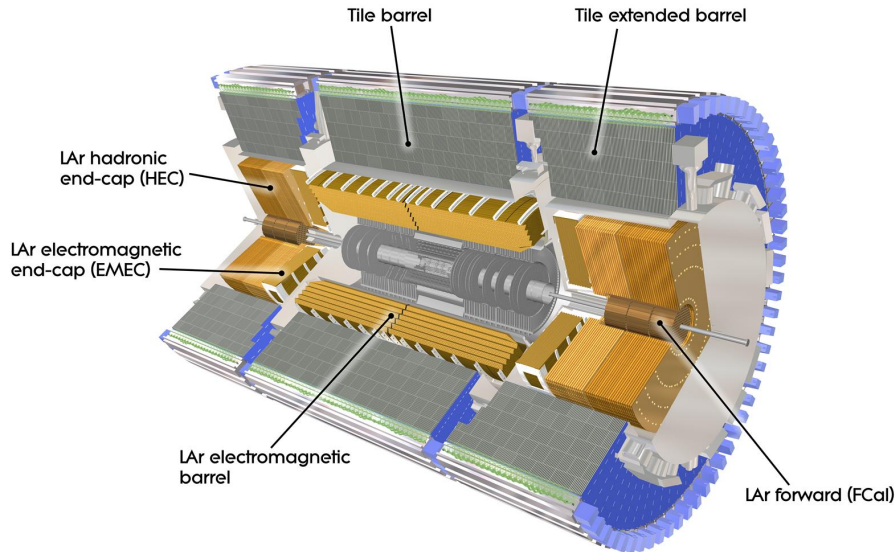


**Figure 3.19:** Computer generated image of the ATLAS calorimeter [153].

1943 passive material it produces the shower (Figures 3.20 and 3.21). For  
 1944 the absorber layers in ATLAS, lead is used for the ECAL and steel  
 1945 for the HCAL.

- 1946 • **Active material:** This material detects the particles from the shower  
 1947 originated in the absorber. The liquid Argon (LAr) is used as active  
 1948 material for ECAL and plastic scintillator for HCAL.

1949 In the homogeneous calorimeters, the material used combines the features  
 1950 of an absorber and a detector, performing both tasks.

1951 Since each type of particle interacts differently, there are two main types  
 1952 of calorimeters: the electromagnetic calorimeter (ECAL), which measures  
 1953 the energy of electrons/positrons and photons, and the hadronic calorimeters  
 1954 (HCAL), which registers the energy of the strongly-interacting particles.  
 1955 Both classes are covered in the next sections.

### 1956 **Scintillator**

1957 The particles from the shower leave some of the molecules of the plastic  
 1958 scintillator in an excited state. The subsequent decay of these molecules  
 1959 produces the emission of photons in the ultraviolet energy region. This  
 1960 light is collected by photomultiplier tubes at the edge of the tiles  
 1961 and converted into a current pulse whose amplitude is proportional to the  
 1962 energy deposited by transversing particle.

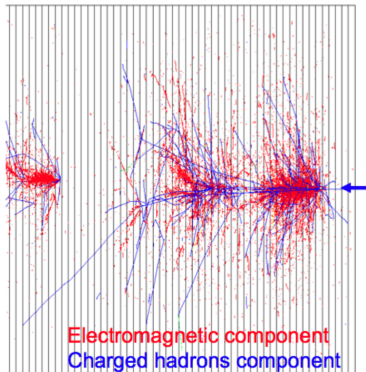


**Figure 3.20:** EM and hadronic cascades.

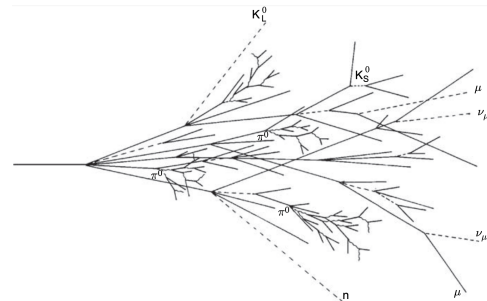


**Figure 3.21:** Sketch of a hadronic cascade [155].

### 1963 3.3.3.1 Particle showering

1964 A particle shower is a cascade of secondary particles produced when  
 1965 a high-energy particle interacts with matter. The first particle interacts  
 1966 with the passive material producing a secondary particle with less energy  
 1967 than the first one. The second particle does the same and, in each step,  
 1968 the particles produced are less and less energetic. For a single incoming  
 1969 particle, this iterative process can continue for thousands of periods [155].  
 1970 An illustration of the EM and hadronic particle cascades is shown in Figure  
 1971 3.20.

#### 1972 Electromagnetic shower

1973 The electromagnetic (EM) shower is initiated by a  $e^-$ ,  $e^+$  or  $\gamma$ , these  
 1974 three particles are the sole components of this type of shower. At energies  
 1975 higher than 100 MeV, the EM showering is based on two main processes:  
 1976 Bremsstrahlung and pair creation. The electrons lose their energy almost  
 1977 exclusively by bremsstrahlung radiation, a process in which the lepton ra-  
 1978 diates thousands of soft photons because of its interaction with another  
 1979 charged particle. The photons lose their energy by the production of an  
 1980  $e^- - e^+$  pair. At lower energy scales, other processes contribute. In the MeV  
 1981 range, the Compton scattering<sup>10</sup> and photoelectric effect<sup>11</sup> are the dominant  
 1982 interactions for energy loss for photons, while the ionisation and excitation  
 1983 are for the charged particles ( $e^-$  and  $e^+$ ).

#### 1984 Hadronic shower

1985 When a hadron interacts with the passive material, this shower is initialised.

<sup>10</sup>Scattering of a photon after interacting with a charged particle, usually an electron.

<sup>11</sup>Emission of photoelectrons when the EM radiation interacts with matter.

Both strong and EM interactions are involved in the development of this type of shower and they present a larger variety of particle components. Therefore, the hadronic showers are significantly more complex than the EM. Figure 3.21 shows the processes leading to a hadronic cascade.

The production of neutral pions represents about a third of the energy loss of hadronic interactions. These pions decay 98.8% of times to two photons [156] that are starting the EM showers. The rest of hadronic interactions consist of the production of charged mesons, nuclear fragments and protons, soft neutrons and photons or unpredictable loss through undetectable processes.

### 3.3.3.2 Electromagnetic calorimeter

The ECAL [154] absorbs the energy of the  $e^-$ ,  $e^+$  or a  $\gamma$  covering a pseudorapidity range of  $|\eta| < 1.475$  in the barrel. It is made of a lead absorber and LAr detector following an accordion shape, as can be seen in Figure 3.22a, where the different layers are clearly visible. The shower originated at the absorber layer ionise the LAr producing a measurable current proportional to the energy of the original particle. The LAr layer operates at 87 K.

The barrel part is split into two identical half-barrels separated by a small gap at  $z = 0$ . Each end-cap calorimeter is composed of two coaxial wheels that cover  $|\eta| < 1.475$ .

The total amount of material in the ECAL corresponds to 25-35 radiation lengths,  $X_0$ , and 2-4 nuclear interaction lengths,  $\lambda$ , over the entire  $\eta$  range. Characteristic of each material, the ration length is the mean distance over which a high-energy electron lose all but  $1/e$  of its energy by bremsstrahlung. The radiation length is the mean free path between interactions required to reduce the number of relativistic charged particles by the factor  $1/e = 0.37$  as they pass through matter.

The energy resolution of a calorimeter can be parametrised as:

$$\frac{\sigma_E}{E} = \frac{a}{\sqrt{E}} \oplus \frac{b}{E} \oplus c = \frac{10\%}{\sqrt{E}} \oplus \frac{170 \text{ MeV}}{E} \oplus 0.7\%$$

Where  $a$  is the stochastic term,  $b$  the electronic noise and  $c$  a constant that includes detector instabilities and increases with  $E$  [157].

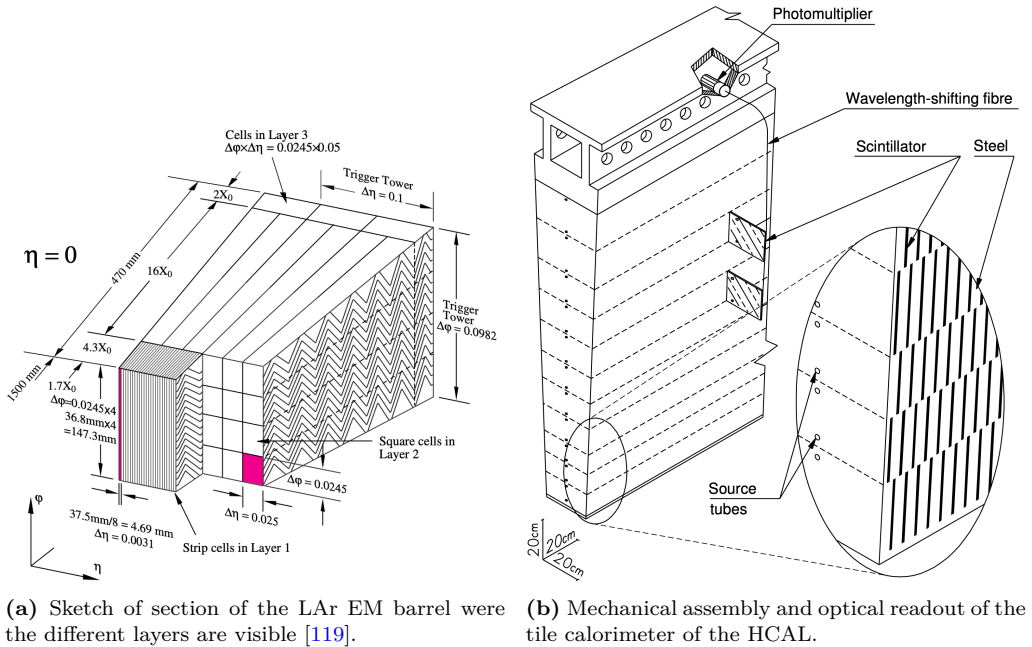


**Figure 3.22:** Sketch of a section of the ATLAS (a) ECAL and (b) HCAL [119].

### 2016 3.3.3.3 Hadronic calorimeter

2017      The ATLAS HCAL [154] is made of a sampling calorimeter of steel and  
 2018 plastic scintillator tiles covering the pseudorapidity region of  $|\eta| < 1.7$  in  
 2019 the barrels. The end-caps are made of copper and LAr, covering  $1.5 < |\eta| <$   
 2020  $3.2$ , and are emended in the end-caps of the ECAL. This calorimeter uses  
 2021 9800 electronic channels in the barrel and 5600 in the end-cap. With 2900  
 2022 tones, the HCAL is the heaviest part of the ATLAS detector. It has 420000  
 2023 scintillator tiles and 9500 photomultiplier tubes [153]. All these elements are  
 2024 shown in Figure 3.22b, where the tiles, the fibres and the photomultipliers  
 2025 are visible.

The contribution of the electronic noise is negligible, therefore, the energy resolution for the tile calorimeter is [154]:

$$\frac{\sigma_E}{E} = \frac{5.9\%}{\sqrt{e}} \oplus 5.7\%$$

### 2026 3.3.3.4 Forward calorimeter

2027      In addition to the ECAL and HCAL, a smaller calorimeter is placed  
 2028 in the end-caps surrounding the beam pipe in order to cover the forward  
 2029 region ( $3.1 < |\eta| < 4.9$ ), the forward calorimeter (FCAL). This coverage is

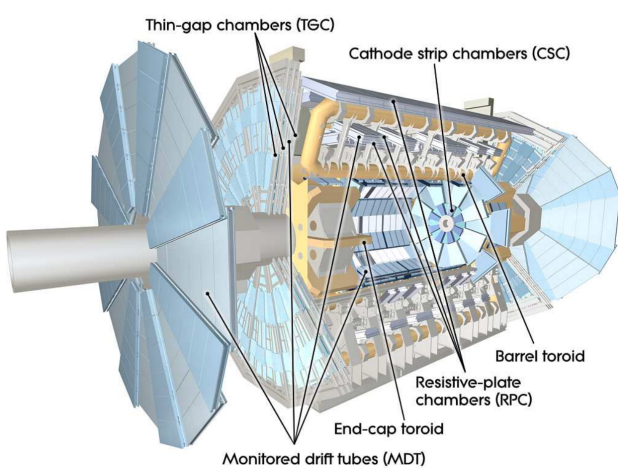


**Figure 3.23:** Conceptual layout of the MS (blue). The magnet system (yellow) is also shown [119].

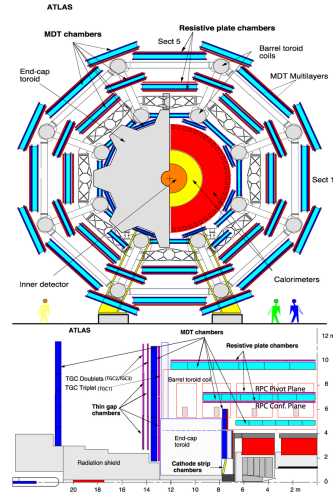


**Figure 3.24:** ATLAS Muon detectors.

2030 required for many physics tasks such as the reconstruction of the  $E_T^{\text{miss}}$  of  
2031 the forward-jet tagging.

2032 This calorimeter is a sampling calorimeter based on LAr as active me-  
2033 dium and copper as absorber. The thickness of the FCAL is optimised to  
2034 achieve high absorption, approximately,  $10 X_0$  [157].

This detector has a resolution of:

$$\frac{\sigma_E}{E} = \frac{100\%}{\sqrt{e}} \oplus 10\%$$

### 2035 3.3.4 Muon Spectrometer

2036 The muons can penetrate through calorimeters and reach the last layer  
2037 of the ATLAS detector, the MS [158]. Figure 3.23 shows a schematic cut-  
2038 away view of the ATLAS muon system.

2039 The MS surrounds the calorimeters and its aim is to measure the traject-  
2040 ories of muons to determine their direction and momentum with excellent  
2041 tracking precision as well as their electric charge in a pseudorapidity cover-  
2042 age of  $|\eta| < 2.7$ . To bend the particle tracks after they exit the HCAL, the  
2043 MS uses eight large superconducting air-core toroid magnets in  $|\eta| < 1.4$   
2044 region. For the  $1.6 < |\eta| < 2.7$ , the tracks are bent by magnets inserted in  
2045 the end-caps. In the transition region,  $1.4 < |\eta| < 1.6$ , the magnetic field  
2046 responsible of bending the particles is provided by both the air-core toroid  
2047 magnets and the smaller end-cap magnets. These fields are perpendicular

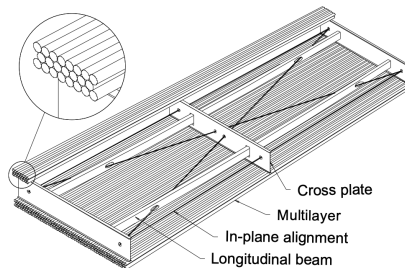
Type	Purpose	Location	Coverage
MDT	Tracking	Barrel + end-cap	$0.0 <  \eta  < 2.7$
CSC	Tracking	End-cap layer 1	$2.0 <  \eta  < 2.7$
RPC	Trigger	Barrel	$0.0 <  \eta  < 1.0$
TGC	Trigger	End-cap	$1.0 <  \eta  < 2.4$

**Table 3.2:** ATLAS MS sub-detectors [159].

2048 to the trajectory of the muons originated in the IP. More details about the  
 2049 magnet systems of the MS can be found in Section 3.3.5.

2050 The MS instrumentation is based, on one hand, on precision chambers  
 2051 for the coordinate measurements in the bending plane: Monitored Drift  
 2052 Tube chambers (MDT) and Cathode-Strip Chambers (CSC), and, on the  
 2053 other hand, on trigger chambers: Resistive Plate Chambers (RPC) and  
 2054 Thin Gap Chambers (TGC). Table 3.2 gives a summary of the MS de-  
 2055 tector components. In Figure 3.24 the distribution of the MS detectors is  
 2056 described.

2057 • **Monitored Drift Tube chambers (MDTs)** [160]: The MDT cham-  
 2058 bers provide precise momentum measurements by determining with  
 2059 high accuracy the curve of the tracks. This part of the MS cover a  
 2060 pseudorapidity range of  $|\eta| < 2$ . The MDTs are designed to have  
 2061 stand-alone measurement capability in order to safeguard against any  
 2062 unanticipated background and to ensure good discovery potential in  
 2063 the scenario of unexpected topologies. In the barrel region, the MDTs  
 2064 are arranged in three cylindrical stations coaxial to the beam axis and  
 2065 in the end-cal, the MDTs are vertically installed in three layers. An  
 2066 MTD chamber consists of six layers of drift tubes (as depicted in Fig-  
 2067 ure 3.25), each of them with 3 cm of diameter, filled with gas. A tube  
 2068 can achieve a single wire resolution of 80  $\mu\text{m}$  [159]. In the entire MDT  
 2069 system, there are 1 171 chambers with a total of 354 240 tubes.

**Figure 3.25:** Schematic view of an MDT chamber.

- **Cathode-Strip Chambers (CSC)**: It is the innermost tracking layer of the MS. Due to its higher rate capability and time resolution, it is located close to the beam axis, where the particle fluxes are higher. This component of the muon detector system covers the  $\eta$  range  $2.0 < |\eta| < 2.7$ . It measures with precision the coordinates at the ends of the detector. With its 70 000 electric channel, provides a resolution around 60  $\mu\text{m}$ .
- **Resistive Plate Chambers (RPC)** [161]: This is the barrel element of the trigger system. These chambers are located on both sides of the central CSC and inside the outermost CSC station. The RPCs are gaseous detectors used for triggering and for measuring the second coordinate in the barrel region. RCPs provide a time-space resolution of  $1\text{ cm} \times 1\text{ ns}$ . The gas gap is of the order of 2 mm and the plate external surfaces are coated by thin layers of graphite painting. This part of the MS is composed of 3 800 electric channels.
- **Thin Gap Chambers (TGC)** [162]: As a first-level trigger, they have to provide high efficiency and excellent time resolution for bunch-crossing tagging in a high-background environment. The particle flux received by the TCG is higher than that of the RPC. The three TGCs are located near the middle end-cap MDT station, in the forward regions. TGCs measure the second coordinate in the non-bending direction with its circa 440 000 electrical channels.

### 3.3.5 Magnet system

The curvature in the track of the particles is fundamental to measure the transverse momentum and the charge of the particles. To bend the path of charged particles, these are immersed in a homogeneous magnetic field which is produced by the both the toroidal and solenoid magnets. The bending power is proportional to  $\int B dl$ , where  $B$  is the magnetic field component orthogonal to the charged direction.

ATLAS magnetic system is divided into three subsystems: the central solenoid magnet, the barrel toroids (BT) and the end-cap toroid (ECT).

#### 3.3.5.1 Central solenoid magnet

The ATLAS solenoid surrounds the ID providing a 2 T magnetic at the centre of the tracking volume. This magnet is very thin, having only 4.5 cm thickness, which minimises the interaction of the particles with the magnet material. It is important to not use a lot of material here because,

2106 otherwise, the interaction of the particles with the solenoid magnet would  
2107 impact negatively in the performance of the calorimeters. To achieve such  
2108 a field within a small thickness, 9 km of niobium-titanium superconductor  
2109 wires into strengthened, pure aluminium strips and cooled down to 4.5 K are  
2110 used. The central solenoid magnet has a cylindrical shape with a diameter  
2111 of 5.6 m and a length of 2.56 m, and it weights 5 tonnes.

2112 **3.3.5.2 Toroid magnets**

2113 Three large air-core toroids (one barrel and two end-caps) generate the  
2114 magnetic field in the MS. Each toroid consists of eight coils assembled with  
2115 cylindrical symmetry (see the yellow elements in Figure 3.23). The coils are  
2116 based on an aluminium stabilised Niobium-Titanium alloy (Al/NbTi/Cu)  
2117 superconductor operating at 4.5 K. The main difference between the barrel  
2118 and end-cap toroids for the cold mass is that the latter has a higher critical  
2119 current and less aluminium than the former [163].

2120 **Barrel Toroid**

2121 The Barrel Toroid magnet is the largest component of the ATLAS magnet  
2122 system. It generates a toroidal magnetic field which, as introduced in Sec-  
2123 tion 3.3.4, is almost completely perpendicular to the track of the particles.  
2124 In order to minimise the impact (i.e. reduce any interaction apart from  
2125 applying magnetic field) of the magnet system with the particles, the barrel  
2126 toroid is designed as an open and light structure. The barrel toroid coils  
2127 are housed in eight individual cryostats, with the linking elements between  
2128 them providing the overall mechanical stability. A view of the coils of the  
2129 barrel toroid in their cryostats is in Figure 3.26.

2130 The magnetic flux density delivered by this magnet is 3.9 T on the su-  
2131 perconductor. For the toroid barrel, the bending power ( $\int B dl$ ) is in the  
2132 interval 1.5 Tm to 5.5 Tm in  $0 < |\eta| < 1.4$ . It is the largest toroidal magnet  
2133 ever built (25.3 m in length), being probably the most iconic and character-  
2134 istic element of ATLAS. It weights 830 tonnes and uses more than 56 km of  
2135 superconducting wire [153].

2136 **End-cap Toroid**

2137 The end-caps extend the magnetic field of the barrel toroid to the beam pipe.  
2138 These magnets are constrained by the inner radius of the barrel toroid and  
2139 the axial length of the experiment.

2140 As well as in the barrel toroid, it has a 4.1 T magnetic field on the  
2141 superconductor. For the end-cap toroid, the  $\int B dl \in [4, 8]$  Tm in the

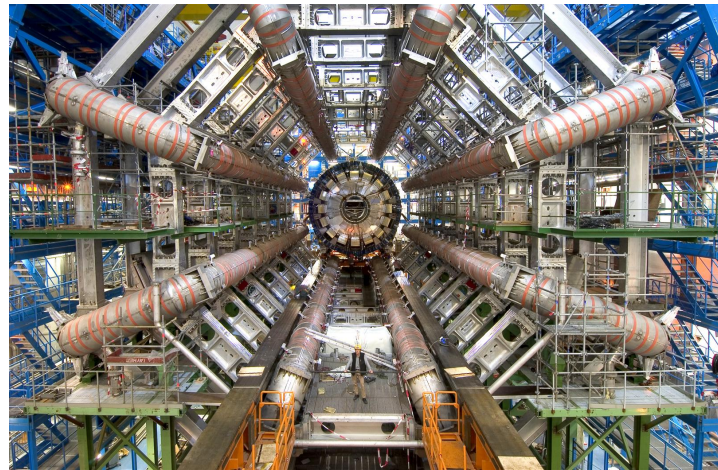


**Figure 3.26:** Very cool picture of the installation ATLAS calorimeters. The eight coils that compose the ATLAS barrel toroid magnets are already installed in the cryostats. Thus view is one of the most iconic of the ATLAS detector.

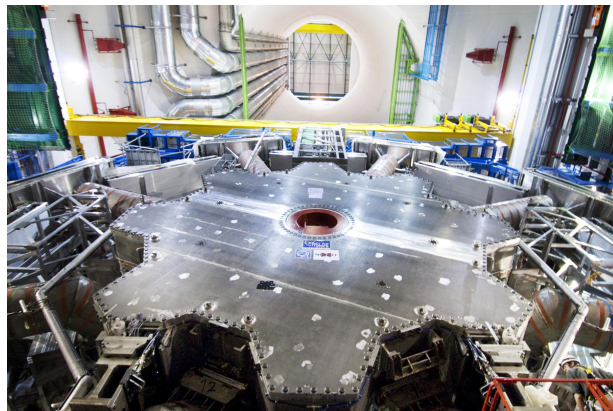


**Figure 3.27:** One of the two end-cap toroidal magnets. Each is made by eight superconducting coils with a magnetic field peaking at 4.1 T.

2142 pseudorapidity range  $1.6 < |\eta| < 2.7$  [163]. In the transition region where  
 2143 the end-cap and barrel toroids overlap ( $1.4 < |\eta| < 1.6$ ), the bending power  
 2144 is lower. Each end-cap magnet (Figure 3.27) has a diameter 10.7 m and  
 2145 weights 240 tonnes [153].

### 2146 3.3.6 Trigger and Data Acquisition System

2147 The proton bunches cross at the center of the ATLAS detector 40 million  
 2148 times per second, resulting in approximately (using Run-2 mean pile-up  
 2149  $\langle\mu\rangle = 33.7$ ) 1 200 million proton collisions per second. Reading out and  
 2150 storing all the information from this interactions is not feasible since it has a  
 2151 combined data volume of more than 60 million megabytes per second. Only

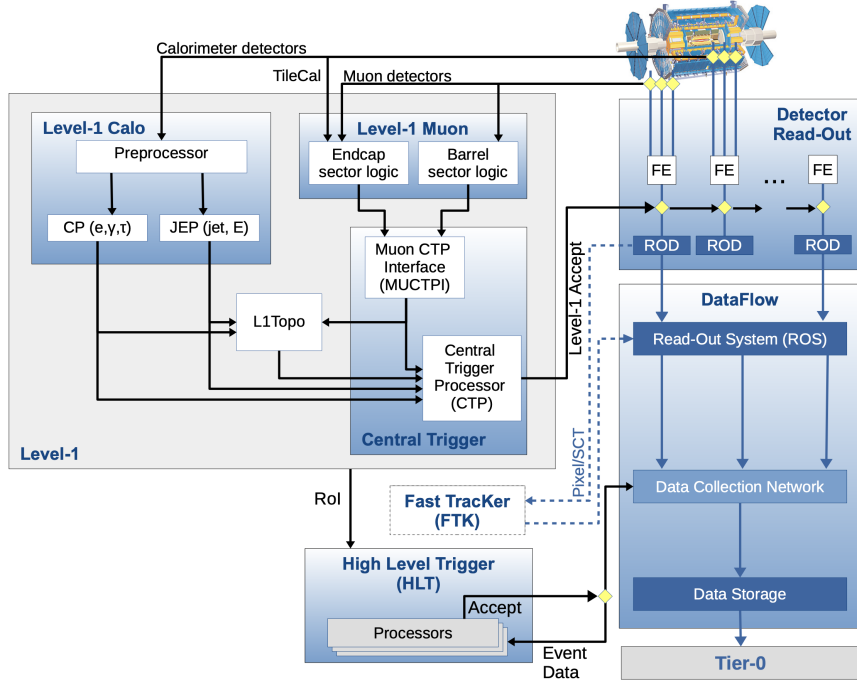


**Figure 3.28:** The ATLAS TDAQ system in Run-2.

some of these events are of interest to physics studies and, consequently, only this subset need to be saved into permanent storage for later analysis. In order to select only interesting data, ATLAS uses a complex and highly distributed Trigger and Data Acquisition System (TDAQ) [164] that reduces the rate of recorded data from the initial 1 200 MHz of interactions to just an average of 1 kHz. The reduction through the trigger is carried in two steps: The electronic performs an initial selection and, afterwards, a large computer farm analyses the data that pass the initial filter.

The TDAQ system is an essential component of ATLAS in charge of processing the events online, selecting the relevant ones and storing them. To do so, the TDAQ verifies for each bunch crossing if at least one among the hundred conditions is satisfied. These conditions, also known as “triggers”, are based on identifying both combinations of candidate physics objects (“signatures”) and global properties of the events [165]. Figure 3.28 shows a diagram of the TDAQ system, in this figure can be seen the different components as well as the detector read-out and data flow.

The first-level trigger (LVL1) is a hardware-based filter performed by ATLAS sub-detectors. The LVL1 uses the information of the Calorimeters and the MS to select events up to the maximum-readout rate of the detector (100 kHz) within a latency of  $2.5 \mu\text{s}$ . Additionally, the LVL1 identify the

2172 regions of interest (RoI), which includes the position and the  $p_T$  of the  
2173 candidate objects.

2174 For each event accepted by the LVL1, the Front-End (FE) detector elec-  
2175 tronics read the detectors data and pass it to the ReadOut Drivers (ROD).  
2176 The ROD performs the initial processing and formatting and the ReadOut  
2177 Systems (ROS) buffers this data.

2178 The data from the different sub-detectors is sent from the ROS to the  
2179 software-based trigger, the so called “High Level Trigger” (HLT), when is  
2180 requested by the HLT. This system is comprised by the second-level trig-  
2181 ger (LVL2) and the Event Filter (EF or third-level), both made of several  
2182 farms of computers (about 40 000 CPU cores) interconnected by Ethernet  
2183 networks. Using modest computing power, LVL2 provides high rejection  
2184 power with fast and limited precision algorithms. With higher computing  
2185 power, the EF features lower rejection power with slower but higher preci-  
2186 sion algorithms [164]. This combination is a cost-effective and flexible way  
2187 of implementing the HLT. The ID, which was not used by the LVL1, is of  
2188 key importance for the HLT because on, one hand, the LVL2 reconstruc-  
2189 tion algorithms are specifically designed to meet strict timing requirements  
2190 and, on the other hand, the track reconstruction on the EF is less time  
2191 constrained. This is done by the ID’s Fast TracKer (FTK) as the Figure  
2192 [3.28](#) shows.

2193 An average 1.2 kHz output rare for Run-2 pass the HLT (with a latency  
2194 of just 200  $\mu$ s) and is sent by the Sub-Farm Output (SFO) to the Tier-0  
2195 facilities for permanent storage and later offline physics analysis. It is im-  
2196 portant to highlight that the decisions performed by trigger about whether  
2197 or not to store an event are irrevocable. If an event does not pass the trigger  
2198 requirements, it is not stored.

## 2199 **3.4 Alignment of the inner detector**

2200 A fundamental part for the correct operation of the ATLAS detector  
2201 is its alignment [166]. The goal of the detector alignment is to determine  
2202 the detector geometry as accurately as possible in order to correct the ef-  
2203 fects of the time-dependent displacements. In this section, the need of an  
2204 adequate alignment is motivated, its principles discussed and my contribu-  
2205 tions presented.

2206 As commented in Section [3.3.2](#), the ID is used to reconstruct the trajec-  
2207 tories of the charged particles by combining into tracks the energy deposits  
2208 (hits) of the particles as well as identifying primary and secondary vertices.

2209 These functionalities are essential for some tasks such as the lepton recon-  
2210 struction or the  $b$ -jet tagging.

2211 To be able to have proper tracking, the full resolution of the ID has to be  
2212 exploited and to do so it is crucial to know the geometry of the detector, i.e.  
2213 the location and orientation of each of its elements. Due to several factors  
2214 such as thermal expansion/contraction, the detector is constantly experien-  
2215 cing small movements that affect to its geometry. With the alignment it is  
2216 possible to account online for this displacements, re-calibrate and correct  
2217 its effects. The alignment algorithm’s accuracy is such that the position of  
2218 the various detector parts may be established with a few microns of accur-  
2219 acy [90]. This accuracy is superior to that attained by directly measuring  
2220 the module placements. Any missalignment of the different elements of the  
2221 ID will degrade the quality of the track reconstruction, which is vital to  
2222 perform any physics analysis. During the development of this thesis, I have  
2223 contributed to the alignment of the ID through the refurbishment of the soft-  
2224 ware package for monitoring the track-based ID alignment results obtained  
2225 at the calibration loop and show them as a web-based service.

2226 **3.4.0.1 Local coordinate frame**

2227 In Section 3.3.1 the global ( $x$ ,  $y$ ,  $z$ ) Cartesian coordinate system of AT-  
2228 LAS was introduced. The local coordinate frame of an individual sensor of  
2229 the detector ( $x'$ ,  $y'$ ,  $z'$ ) is also a Cartesian system. The local system is a  
2230 right-handed frame with the origin placed at the geometrical centre of the  
2231 module. According to the convention, the  $x'$ -axis and  $y'$ -axis are within the  
2232 plane of the component and the  $z'$ -axis points outside of this plane. The  
2233  $x'$ -axis points to the most sensitive direction of the module. For the Pixel  
2234 and IBL modules this is the shorter pitch side and, for the SCT, the perpen-  
2235 dicular to the strip orientation. In the case of the TRT the  $y'$ -axis points  
2236 along the wire while the  $x'$ -axis remains perpendicular to both the wire and  
2237 the radial direction. The local coordinates are represented schematically in  
2238 Figure 3.29.

2239 The hits are reconstructed in the local coordinate frame of the different  
2240 modules.

2241 **3.4.0.2 Track parameters**

2242 The trajectory followed by a charged particle within a magnetic field  
2243  $B$  is a helix that can be fully parametrised by the five track parameters:  
2244  $\tau = (d_0, z_0, \phi_0, \theta_0, q/p)$ , where  $d_0$  and  $z_0$  are the transverse and longitudinal  
2245 impact parameters;  $\phi_0$  and  $\theta_0$  the azimuthal and polar angles of the track.

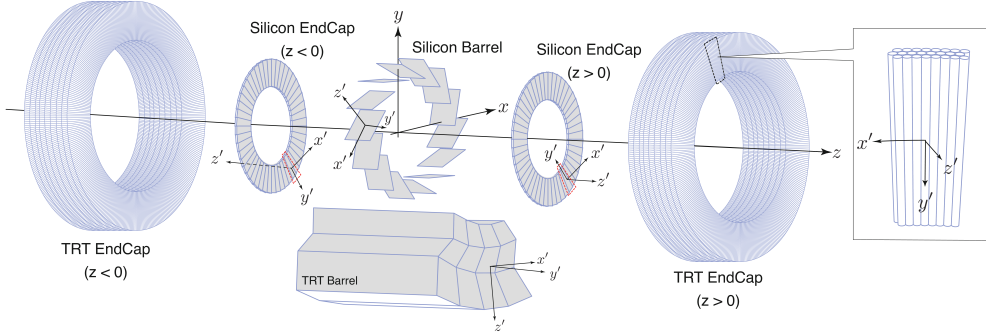


**Figure 3.29:** Schematic representation of the ATLAS global ( $x, y, z$ ) and local ( $x', y', z'$ ) reference frames [166]. The local coordinates are shown for the Pixel, IBL, SCT and TRT.

2246 Lastly, the  $q/p$  is ratio between the particles charge and momentum and it  
2247 measures the curvature of the tracks.

#### 2248 3.4.0.3 Alignment levels and degrees of freedom

2249 The orientation of a rigid body can be described by a total of six degrees  
2250 of freedom. This is translated into what are known as alignment parameters  
2251  $\boldsymbol{\alpha} = (T_x, T_y, T_z, r_x, R_y, R_z)$ . These correspond to the three transitions with  
2252 respect to the origin of the local reference frame ( $T_{x,y,z}$ ) and three rotations  
2253 ( $R_{x,y,z}$ ) around the local Cartesian axes.

#### 2254 3.4.0.4 Residuals

In tracking, a residual is the distance between a hit and the intersection point of the extrapolated track in the sensor. The residual vector ( $\mathbf{r}$ ) is define as:

$$\mathbf{r} = (\mathbf{m} - \mathbf{e}(\boldsymbol{\tau}, \boldsymbol{\alpha}))$$

2255 where  $\mathbf{m}$  is the vector to center of the module and  $\mathbf{e}(\boldsymbol{\tau}, \boldsymbol{\alpha})$  is the vector to  
2256 the track intersection with the surface. For every track and module there  
2257 is a residual, as it is shown in Figure 3.30.

#### 2258 3.4.1 Track based alignment

2259 The distance between the hits and the fitted track should be null if  
2260 the detector were perfectly aligned, and the residual distribution would be

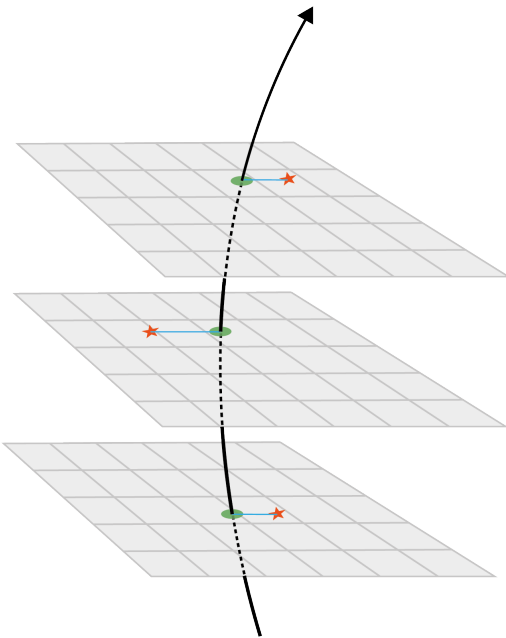


**Figure 3.30:** Schematic representation of a charged particle crossing detector planes [166]. The red star measures represents the measurement in each layer ( $m_i$ ). The black line is the fitted trajectory for a given set of track parameters. The position of the intersection of the fitted track with the surface ( $e_i$ ) on which the  $i^{th}$  measurement is made is indicated with a green ellipse. The residuals ( $r_i$ ) are shown in blue.

2261 centred at zero and have a width that corresponded to the module resolu-  
 2262 tion. Therefore, any deviation from the in the residual distribution would  
 2263 indicate a misalignment of the detector.

2264 A schematic description of the alignment chain is illustrated in the three  
 2265 panels of Figure 3.31. The blue rectangles on the left panel of Figure 3.31  
 2266 represent the true position of the detector modules. A charged particle  
 2267 deposits part of its energy in each module producing the hits, which are  
 2268 marked with red dots. The track of the particle is marked with a red line.  
 2269 The  $x$  distance is the deviation of the module from its apparent position.  
 2270 In the middle panel, the white rectangles represent the apparent position of  
 2271 each module. Here can be seen how the real position and the apparent one  
 2272 is not the same by an unknown distance  $x$ . This deviation leads to a dis-  
 2273 crepancy between the reconstructed tracks and the true ones. The residuals  
 2274 in the middle panel are represented by a green line, which corresponds to  
 2275 the difference between the recorded track (red dots) and the reconstructed  
 2276 one (blue dots). The residual distributions in this panel are displaced from  
 2277 zero, indicating a misalignment. The purpose of the alignment algorithm  
 2278 is to center this distributions in zero by minimising these residuals. As a  
 2279 result of the alignment procedure, the position of the detectors has been  
 2280 updated a distance  $x'$  for each module. After this, the new expected pos-

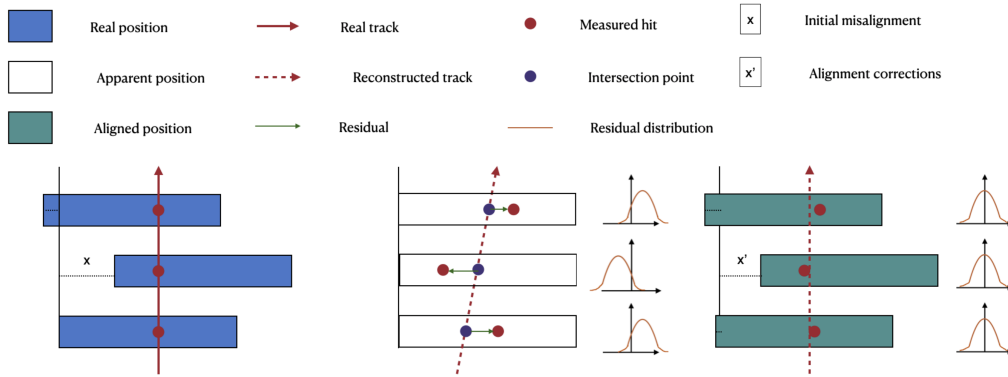


**Figure 3.31:** Alignment procedure scheme where each rectangle is a detector module. The left panel represents the real position of the detector modules and the charged particle track. The middle panel shows the initially-expected position of the modules and the reconstructed track. The right panel exemplifies how the position of the detectors has been updated to resemble the real one. This update is done by the track-based alignment procedure. **I need to vectorise this image**

2281      ition of the modules (green rectangles) is much closer to the real one and,  
 2282      hence, the residuals are more centred at zero. Anyhow, this is not perfect  
 2283      and the different  $x'$  are not all equal to  $x$ . To improve the precision, the  
 2284      alignment procedure is carried iteratively.

### 2285    3.4.1.1 Global $\chi^2$ algorithm

To correct the position of the ID, the alignment constants ( $\boldsymbol{\alpha}$ ) are obtained as result of the minimisation of the  $\chi^2$  function. This function is built from the track-hit residuals:

$$\chi^2 = \sum_t \sum_h \left( \frac{r_{t,h}(\boldsymbol{\tau}, \boldsymbol{\alpha})}{\sigma_h} \right)^2,$$

where the index  $t$  runs over the reconstructed tracks and the  $h$  is the set of hits associated to each track  $t$ . The residual of each hit associated to track  $t$  is  $r_{t,h}$  and  $\sigma_h$  is the hit's uncertainty. In vector notation, the  $\chi^2$  function can be expressed as:

$$\chi^2 = \mathbf{r}^T \Omega^{-1} \mathbf{r},$$

where  $\omega$  is the covariance matrix of the corresponding measurements. The track parameters,  $\boldsymbol{\tau}$ , are those that minimise the  $\chi^2$  and, therefore, first and second derivatives of  $\chi^2$  with respect  $\boldsymbol{\tau}$  are used.

$$\frac{d\chi^2}{d\boldsymbol{\alpha}} = \sum_t \left[ \left( \frac{d\mathbf{r}}{d\boldsymbol{\alpha}} \right)^T \Omega^{-1} \mathbf{r} \right]^T + \sum_t \left[ (\mathbf{r}^T \Omega^{-1} \left( \frac{d\mathbf{r}}{d\boldsymbol{\alpha}} \right)) \right] = 0$$

It is worth to remind that  $\mathbf{r}$  and  $\Omega$  are defined for a single track, so the summary will accumulate the residuals from all considered tracks from all the events in the data sample. The last expresión can be simplified taking into account that  $\Omega^{-1}$  is symmetric and it takes the form:

$$2 \sum_t \left( \frac{d\mathbf{r}}{d\boldsymbol{\alpha}} \right)^T \Omega^{-1} \mathbf{r} = 0 \quad (3.10)$$

Since  $\mathbf{r} = \mathbf{r}(\boldsymbol{\tau}, \boldsymbol{\alpha})$ , the partial derivatives have to be taken into account:

$$\frac{d\mathbf{r}}{d\boldsymbol{\alpha}} = \frac{\partial \mathbf{r}}{\partial \boldsymbol{\tau}} \frac{d\boldsymbol{\tau}}{d\boldsymbol{\alpha}} + \frac{\partial \mathbf{r}}{\partial \boldsymbol{\alpha}}$$

Inserting this into Eq. 3.10, the condition for minimising the  $\chi^2$  turns to be:

$$\sum_t \left( \frac{\partial \mathbf{r}}{\partial \boldsymbol{\tau}} \frac{d\boldsymbol{\tau}}{d\boldsymbol{\alpha}} + \frac{\partial \mathbf{r}}{\partial \boldsymbol{\alpha}} \right)^T \Omega^{-1} \mathbf{r} = 0. \quad (3.11)$$

2286 Here, the term  $d\boldsymbol{\tau}/d\boldsymbol{\alpha}$  is of particular importance since its contains the  
2287 relationship between the track and alignment parameters, and it will determine  
2288 the difference between the *Local* and *Global*  $\chi^2$  algorithms.

2289 If the algorithm assumes that track parameters do not depend on the  
2290 alignment, i.e.  $d\boldsymbol{\tau}/d\boldsymbol{\alpha} = 0$ , it is the so-called *Local*  $\chi^2$  algorithm. On the  
2291 other hand, the *Global*  $\chi^2$  is based on the assumption that the track and  
2292 alignment parameters are dependent.

2293 The track parameters that satisfy the relation in Eq. 3.11 are found by an  
2294 iterative process consisting on evaluating the first and second derivatives of  
2295 the  $\chi^2$  with respect to the current iteration track parameters,  $\boldsymbol{\tau}_0$ . Since the  
2296 derivative terms of Eq. 3.11 depend on  $\boldsymbol{\tau}$  itself, the procedure is repeated  
2297 until a convergence criteria is met.

2298 Additionally, the track fit can be further improved by adding additional  
2299 terms that account for the effects of multiple Coulomb scatterings of the  
2300 particle with the detector.

### 2301 3.4.2 Web-based display for alignment monitoring

2302 The ID Alignment Monitoring Web Display (Figure 3.32) is an applica-  
2303 tion intended for monitoring the track-based alignment results obtained  
2304 at the calibration loop for the ID. It helps to evaluate the computed align-  
2305 ment corrections as well as many graphical distributions related with the  
2306 performance (for example, the detector residuals). **I have not explained**  
2307 **what the calibration loop is :(**

2308     The web application consists in a server, managed by ATLAS Distrib-  
2309     uted Computing, and a collection of scripts to produce distributions, update  
2310     the information and handle the http requests. It is available at Athena<sup>12</sup>,  
2311     the software framework for ATLAS [131].

2312     Part of my personal work has consisted in writing the code for both  
2313     the frontend and backend of the ID Alignment Monitoring Web Display.  
2314     From an outdated set of scripts, the backend of the application has been  
2315     remodelled. In the new version all the code duplicities have been suppressed  
2316     by defining classes, methods and functions. Several new functionalities have  
2317     been added, to name some:

- 2318         • The web uses the standard Athena setup instead of loading a bash  
2319         script in which the Athena version had to be hardcoded.
- 2320         • Debug levels using ATLAS printing style methods have been imple-  
2321         mented.
- 2322         • Now it is possible to update a single run or list of runs while in the  
2323         previous version it was necessary to execute the program over all runs  
2324         again.
- 2325         • It is not necessary to hardcode the year anymore, it is automatically  
2326         now.
- 2327         • Depending on which run was decided to plot, it was necessary to  
2328         hardcode the year in he scripts. Now the web tool allows to do this  
2329         from its interface.
- 2330         • In the new version it is possible to access the ATLAS Metadata In-  
2331         terface<sup>13</sup> information.
- 2332         • The runtime of the code has been speed up by performing the exe-  
2333         cution in a single loop in contrast to the two-loops structure of the  
2334         previous version.

2335     Regarding the frontend, it has been developed from the scratch. The  
2336     aesthetics of the web page is the most visible change in the monitor dis-  
2337     play. The frontend code is based on CherryPy [168], an object-oriented web

---

<sup>12</sup>Athena is a concrete realisation of a component-based architecture (ased on LHCb's Gaudi [167]) which was designed for a wide range of physics data-processing applications.

<sup>13</sup>Known as AMI, it is a generic software ecosystem for retrieving scientific data by metadata criteria. It allows to search for real and simulated data by metadata criteria as well as browse, view, compare and create ATLAS AMI-Tags

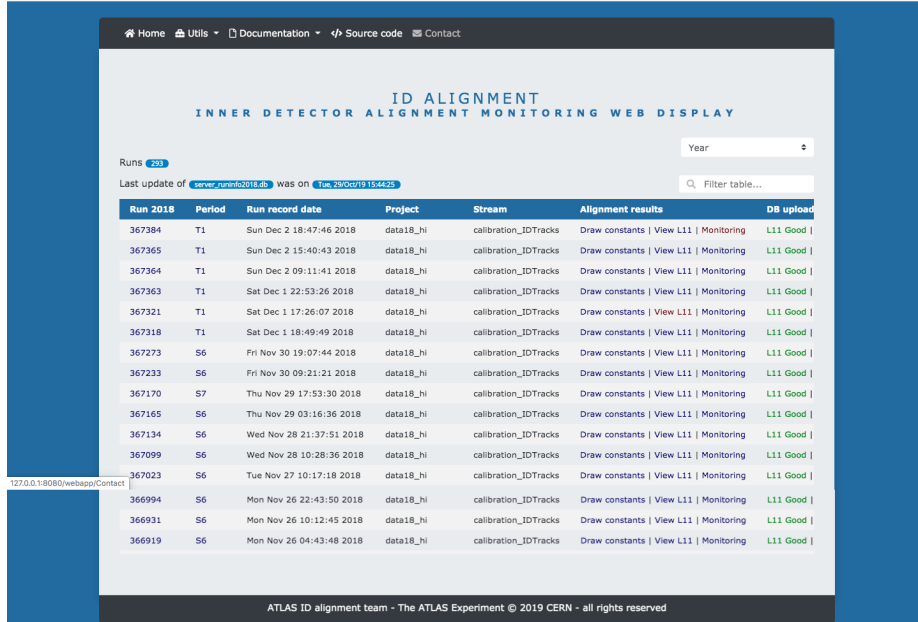


**Figure 3.32:** Main page of the ID Alignment Monitoring Web Display on wide resolution screen. The monitor presents the runs and allows to access the alignment information and plots. Queries can be used to filter the runs presented.

application framework using the Python programming language, and also includes CSS, HTML and Java. The enhanced web display allows to easily choose which information is shown. The web has been designed to adapt to mobile devices, as Figure 3.33 shows. To do so, it uses Bootstrap, a CSS framework directed at responsive, mobile-first frontend web development .

The navigation bar of the web has also being improved, having a better organisation, more option and, if the browser screen is narrowed, it collapses into a desplegable sidebar. A filter has been added that allows to show only the runs that follow the desired specific criteria. A desplegable to select the years has been included, the script reads from the available years in the database. A year selector presentes the possible years via a script that reads the available data. The hoover function highlights the text as the pointer goes over it. The plots are presented in a cleaner way using grid view to select the plot of interest and light boxes to highlight them. The legends of the plots have also been modified to remove duplicated items.

### 3.4.3 Alignment results during Run-2

Here I should find some plot that summarises the results of the alignment and I must highlight the importance of alignment to perform the analysis.

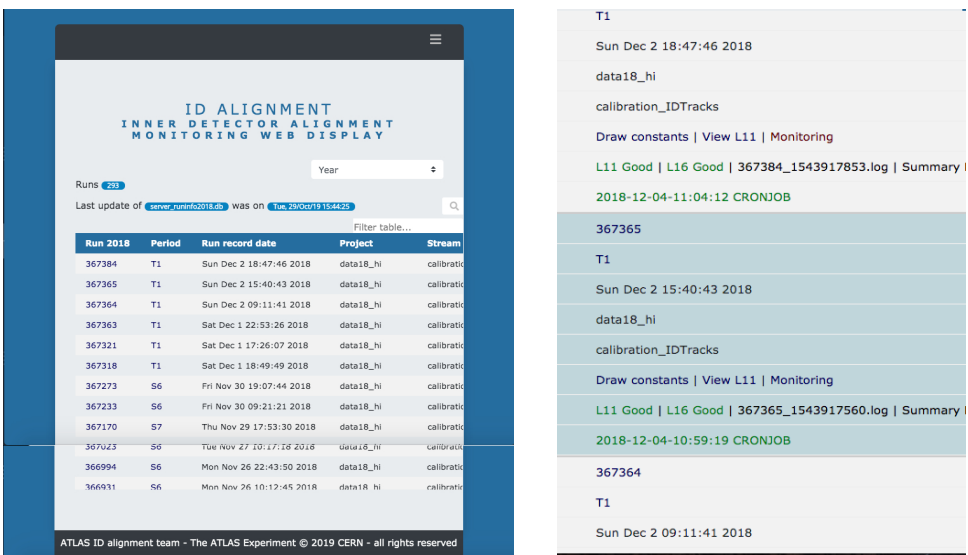


**Figure 3.33:** Main page of the ID Alignment Monitoring Web Display on narrow screens such as the ones of a mobile device.



2357 **Chapter 4**

2358 **Recording data and simulating  
events in ATLAS**  
2359

2360

*In God we trust, all others bring data.*

—WILLIAM EDWARDS DEMING (1900-1993)

2363

2364 The word “event” is one of the most commonly used terms in high  
2365 energy physics. In the context of LHC experiments there are two types  
2366 of events. On side, there are the real events recorded by the detector.  
2367 This event is typically a  $pp$  collision but it could also be a single particle  
2368 such as cosmic ray. On the other side, there the events simulated by the  
2369 MC event generator. In ATLAS, both type of events are precessed by a  
2370 common software, Athena. For real collision data, the detector response is  
2371 evaluated via different algorithms in order to reconstruct the objects in the  
2372 final state. For the simulated processes, the MC generated particles undergo  
2373 a serie of steps replicating the physics of the collisions, the interaction with  
2374 the detector material, the magnetic fields and the response of the detector  
2375 electronics. Once this steps have been applied, the simulated events are  
2376 evaluated using the same algorithms as the ones from real collisions.

2377 This chapter is dived is two sections that discuss both types of events.  
2378 In Section 4.1 the collection of the data in ATLAS is briefly described and  
2379 in Section 4.2 the MC simulation chain is explained.

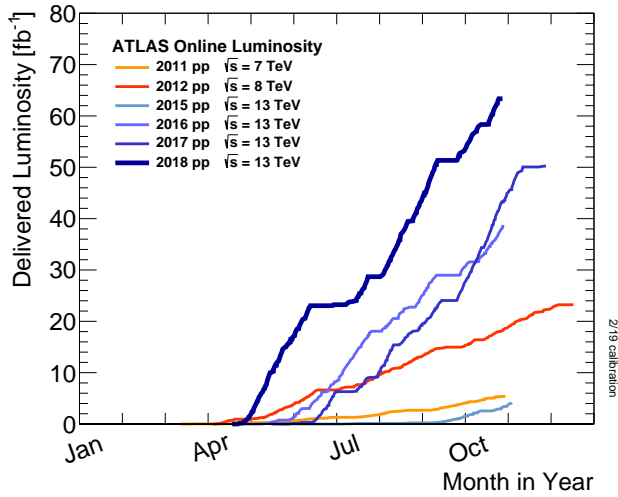


**Figure 4.1:** Cumulative luminosity versus day delivered to ATLAS during stable beams and for high energy  $pp$  collisions. **Maybe it is not a good idea to put an ATLAS plot before introducing ATLAS. Move figure to section 4.2.1.5.**

## 2380 4.1 Data

- 2381 • How is data collected in ATLAS? DAQ
- 2382 • Pileup (differentiate LHC pileup from ATLAS pileup during Run 2)
- 2383 • What are triggers

2384 **This was moved from Chapter 3. Adapt.** The cumulative luminosity delivered by LHC to ATLAS during the Run-2 per year is shown in  
 2385 Figure 4.1. In Figure 4.2, the total Run-2 cumulative luminosity is presented  
 2386 differentiating between the delivered and recorded luminosity and showing  
 2387 that almost all delivered events are considered to be good data quality.  
 2388 The delivered luminosity accounts for the luminosity given from the start  
 2389 of stable beams until the LHC requests ATLAS to put the detector in a  
 2390 safe standby mode to allow a beam dump or beam studies. The recorded  
 2391 luminosity reflects the DAQ inefficiency, as well as the inefficiency of the  
 2392 so-called “warm start”: when the stable beam flag is raised, the tracking  
 2393 detectors undergo a ramp of the high-voltage and, for the pixel system,  
 2394 turning on the preamplifiers. The All Good Data Quality criteria require  
 2395 all reconstructed physics objects to be of good data quality [169].

Year	2015	2016	2017	2018
Peak instantaneous luminosity ( $\times 10^{33} \text{ cm}^2 \text{ s}^{-1}$ )	5	13	16	19
Total delivered integrated luminosity ( $\text{fb}^{-1}$ )	4.0	38.5	50.2	63.4

**Table 4.1:** Peak luminosity and total integrated luminosity delivered by the LHC at  $\sqrt{s} = 13 \text{ TeV}$  in Run-2 per year [170].

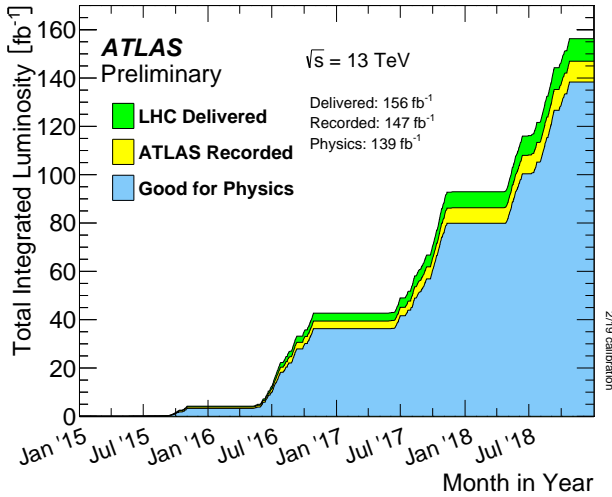


**Figure 4.2:** Total cumulative luminosity versus time delivered to ATLAS (green), recorded by ATLAS (yellow) and certified to be good quality data (blue) during stable beams for  $pp$  collisions at  $\sqrt{s} = 13 \text{ TeV}$ .

### 2397 4.1.1 The Pile-up effect

2398 Pile up is a challenging matter among detectors detector physics, and  
 2399 data acquisition and analysis. Due to the fact that LHC collides bunches of  
 2400 protons instead of single protons, multiple particle interactions occur at a  
 2401 single bunch-crossing<sup>1</sup>. This can result in multiple events at the same time  
 2402 and several interactions with the same detector element, thereby generating  
 2403 overlapping signals which may be difficult to differentiate. This is what is  
 2404 called pile up.

2405 Even though the bunches are composed by  $\sim 10^{11}$  protons, there are  
 2406 only around 30 collisions per crossing with nominal beam currents. The  
 2407 mean number of interactions per bunch crossing is presented in Figure 4.3  
 2408 for each year of Run-2. The mean number of interactions per crossing cor-  
 2409 responds to the mean of the poisson distribution of the number of interactions  
 2410 per crossing calculated for each bunch. It is calculated from the instant-

<sup>1</sup>A bunch crossing can be defined as the instance in which two collections of protons collide at the central region of the detector.

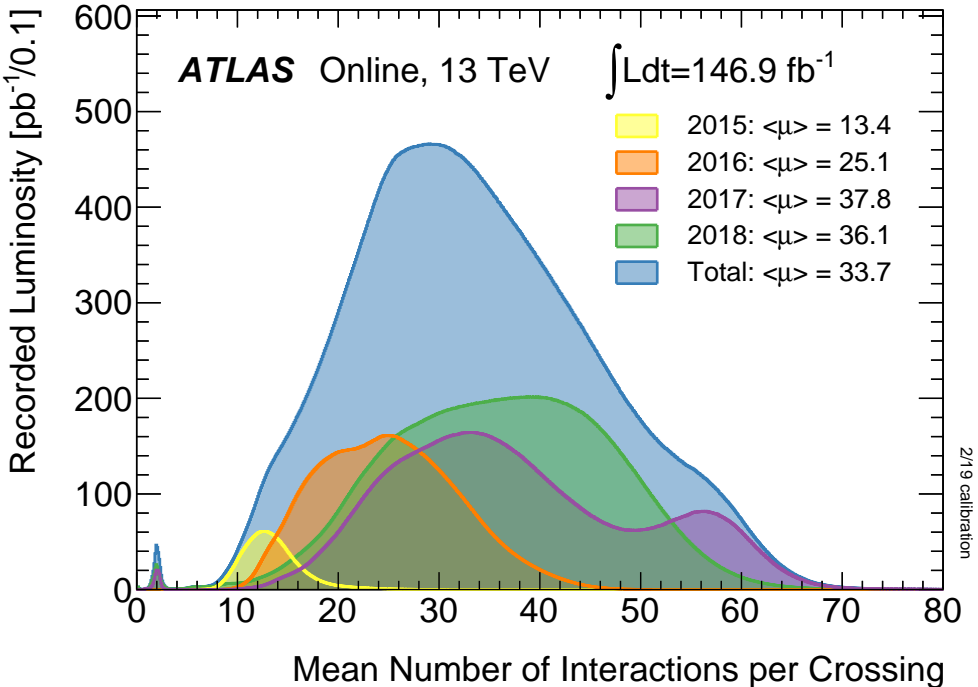


**Figure 4.3:** Luminosity-weighted distribution of the mean number of interactions per crossing  $\langle \mu \rangle$  for Run-2 with  $pp$  collisions data during stable beams at  $\sqrt{s} = 13$  TeV.

2411 aneous per bunch luminosity as  $\langle \mu \rangle = \mathcal{L}_{bunch} \times \sigma_{inel}/f_r$  where  $\mathcal{L}_{bunch}$  is  
 2412 the instantaneous luminosity per bunch,  $\sigma_{inel} = 80$  mb is the inelastic cross  
 2413 section of  $pp$  collisions at 13 TeV and  $f_r = 11.245$  kHz is the LHC revolution  
 2414 frequency.

2415 **Work in progress**

## 2416 4.2 Monte Carlo

2417 In order to study the physics taking place into the ATLAS detector, the  
 2418 signals and backgrounds in the analysis are simulated by Monte Carlo gen-  
 2419 erators according to the cross sections predicted by the SM. The use of the  
 2420 MC simulations is vast and there are many different models generators and  
 2421 techniques. As all MC algorithms, these methods rely on repeated random  
 2422 sampling to obtain numerical results. Since the randomness is intrinsic to  
 2423 the particle collision processes, a large number of events have to be sim-  
 2424 ulated using MC technique and such a collection of events is called a MC  
 2425 sample. In the context of this work, the MC generators provide a detailed

2426 simulation of the precesses from the event generation through to output in  
2427 a format which is identical to that of the true detector.

2428 Typically, the simulation chain is divided into these three steps [171]:

- 2429 1. Generation of the events and immediate decays: An event generator  
2430 produce the result of the collisions in terms of particles created and  
2431 stores any stable particle expected to propagate through the detector.  
2432 At this point, the geometry of the detector is not considered because  
2433 only the immediate decays are taken into account.
- 2434 2. Simulation of the detector and physic interactions: At this point, all  
2435 particles from the previous step are propagated though the full ATLAS  
2436 detector using GEANT4. This part simulates all major components  
2437 and materials as well as the interactions of particles such us ionisation  
2438 in trackers, energy deposition in calorimeters, intermediate decays,  
2439 ration and scattering
- 2440 3. Digitalisation of the energy deposits on the sensitive regions of the  
2441 detector.

2442 The output of the full simulation chain is an object with the exact same  
2443 format as a real event registered by the ATLAS DAQ system. The entire  
2444 simulation chain is shown in Figure 4.4 and compared to the path that the  
2445 data follows when it is originated from an actual collision.

2446 The so called “truth” data is kept for each event and particle in both  
2447 event generation and detector simulation. The truth is a history of the  
2448 interactions from the generator. In the analysis presented in Chapter 6, the  
2449 truth information has several uses such us the determination of fake rates  
2450 or the lepton origin assignment. An important part of the work carried  
2451 during the thesis was the proper implementation of the truth information  
2452 at generator level within ATLAS software framework, Athena.

#### 2453 4.2.1 MC simulations

2454 The generation of the simulated event samples includes the effect of  
2455 multiple  $pp$  interactions per bunch crossing, as well as the effect on the  
2456 detector response due to interactions from bunch crossings before or after  
2457 the one containing the hard interaction.

2458 Every different possible process that can take place during the collision  
2459 has to be simulated separately. To ensure proper description of the entire  
2460 phase-space, the MC samples are not generated proportionally to the cross

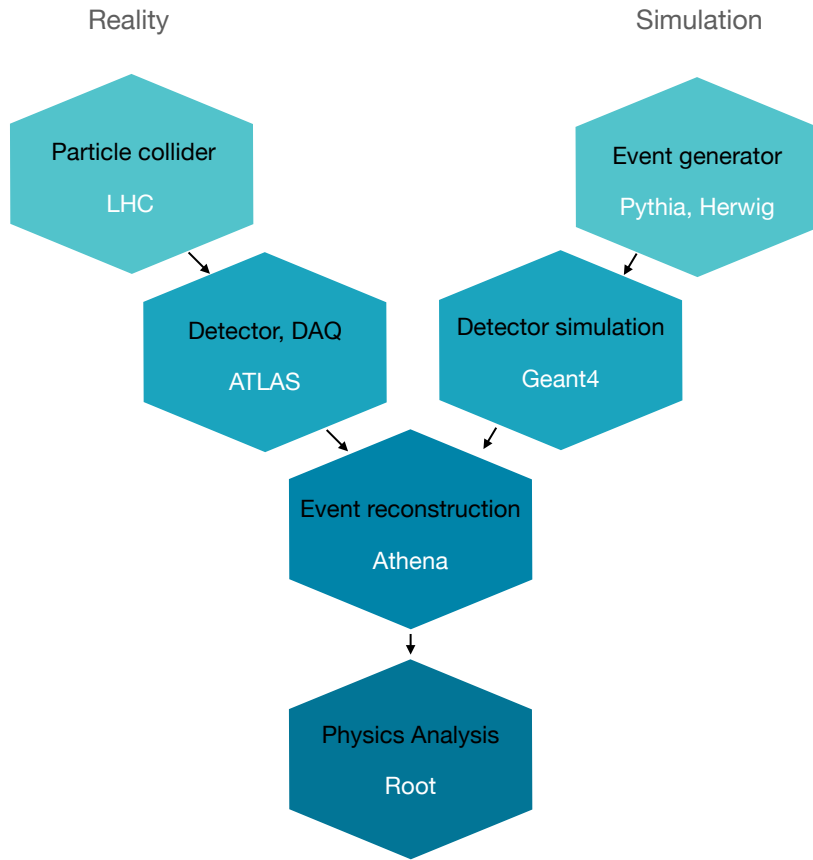


**Figure 4.4:** Comparison of the paths followed by data recorded by the ATLAS detector and the simulated samples. The format of the simulated data is the same as the recorded at each step.

2461 section of each process because that would cause a poor characterisation  
 2462 of the rare processes. Instead, a sufficient large amount of raw events are  
 2463 generated for each process and, afterwards, the all events are reweighted to  
 2464 match their correspondent cross-section. This is the origin of the negative  
 2465 weights in the MC samples. The combination of all these processes provides  
 2466 an accurate description of the collision.

<sup>2467</sup> **4.2.1.1 Parton shower simulation**

<sup>2468</sup> **4.2.1.2 Hadronisation simulation**

<sup>2469</sup> **4.2.1.3 Underlaying decay simulation**

<sup>2470</sup> **4.2.1.4 Hadron decay simulation**

<sup>2471</sup> **4.2.1.5 Pile-up simulation**

<sup>2472</sup> **4.2.2 MC generators**

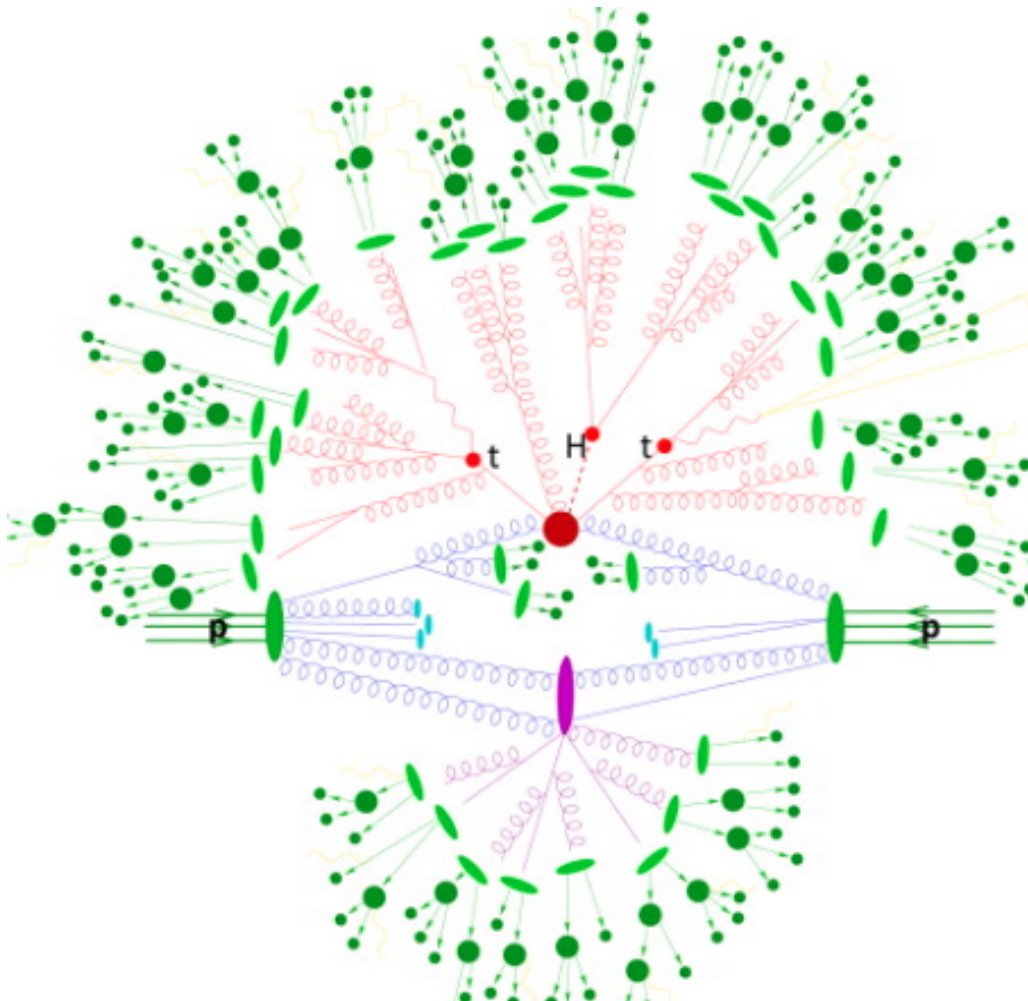


**Figure 4.5:** Representation of a  $t\bar{t}H$  event as produced by an event generator [172]. The big red blob is the hard interaction, which is followed by the decay of the Higgs boson and the two top quarks, represented by the three small red blobs. The additional QCD radiation produced is in red. The secondary interaction, in purple, occurs before the hadronisation of the final-state partons (light green). In darker green, the hadron decay is presented and in the photon radiation appears in yellow.

2473 **Chapter 5**

2474 **Object reconstruction and  
identification**  
2475

2476 **Highlight the importance of alignment for the reconstruction**

2477  
2478 *El dos después del uno.*  
2479 —ISABEL, DEL SERVICIO DE LIMPIEZA  
2480

2481 To reconstruct the physical objects, the information of all the sub-  
2482 detectors and systems of ATLAS is employed. A detailed description of  
2483 all of them is presented in Section 3. After passing the trigger preselection,  
2484 the raw data is analysed to build the physics objects that constitute the  
2485 subject of the physical analyses. The process of constructing these elements  
2486 is known as reconstruction. Figure 3.11 illustrates how each particle inter-  
2487 acts with the different layers of the ATLAS detector. The reconstructed  
2488 objects are the particles tracks and vertices, the leptons, the photons, jets  
2489 (and their flavour tag) and the missing transverse momentum.

2490 **5.1 Tracks and vertices**

2491 The detection and measurement of charged particles momentum is an  
2492 essential aspect of any large particle physics experiment. Regardless of the  
2493 medium through which a charged particle travels, it always leaves a trails

2494 of ionised atoms and liberated electrons. By detecting this it is possible to  
 2495 reconstruct the trajectory of a charged particle. ATLAS does this through  
 2496 its silicon detectors.

2497 The trajectories followed by particles are referred as “tracks”. For  
 2498 charged particles, the tracks are reconstructed using, mainly, the informa-  
 2499 tion of the ID and, in the case of muons, the MS. A charged particle  
 2500 passing through the ID will interact with its active sensors, the pixel detector  
 2501 and SCT (Figures 3.17 and 3.18 respectively) providing a three-dimensional  
 2502 measurement of space-points. While each hit in the pixel detector is directly  
 2503 translated into a space-point, for the SCT two hits are needed to reconstruct  
 2504 one space-point. These space-points can be given by a single pixel activa-  
 2505 tion or by several neighbouring pixels activated simultaneously. Since the  
 2506 ID is submerged in a solenoidal magnetic field, the charged particles have  
 2507 their trajectories curved by the Lorentz force, this allows to calculate its  $p_T$   
 2508 using the sagitta method.

2509 The algorithms described in Section 3.4 are of fundamental importance  
 2510 to reconstruct the tracks. This reconstruction is performed in two stages,  
 2511 the inside-out and the outside-in procedures [173][174]. The first is initiated  
 2512 from the center of the ID and works outwards. This method is also used for  
 2513 the reconstruction of the primary vertex. The inside-out algorithm starts by  
 2514 grouping the hits in the Pixel and SCT and merge them into clusters that are  
 2515 used to define the three-dimensional measurements referred as space-points.  
 2516 Secondly, The space-points are combined in groups of three to form the track  
 2517 seeds. Then, a pattern recognition algorithm named Kalman filter [175] is  
 2518 applied to build track candidates from the seeds. This is accomplished by  
 2519 adding extra clusters from the ID’s remaining layers that are compatible  
 2520 with particle’s estimated trajectory. The Kalman filter provides several  
 2521 track candidates, so an ambiguity-solver algorithm is applied to perform a  
 2522 stringent selection of the candidates. This compares the individual track  
 2523 candidates by simple measurements of the track quality. Finally, the track  
 2524 candidates are then put through a high-resolution global  $\chi^2$  fit, which allows  
 2525 to further reject track candidates with a poor fit.

2526 The inside-out method accounts for the majority of tracks reconstructed  
 2527 in ATLAS but it is complemented by the outside-in, which starts in the  
 2528 TRT and works inwards. This method is used to find small track segments  
 2529 in the ID that were missed.

2530 The identification of the primary vertex is also of crucial importance  
 2531 for the object reconstruction. This vertex identifies the interaction point in  
 2532 which the hard-scattering process takes place. Therefore, the vertices are  
 2533 defined by relating the track’s origin with individual points. The reconstruc-  
 2534 tion of the vertex is done in two complementary steps. First, the tracks

2535 are associated to vertex candidates (vertex finding). Second, iterative  $\chi^2$  fit  
2536 to determine the best final three-dimensional location of the vertex.

### Sagitta method

The linear momentum (or just momentum) of a particle ( $\vec{p}$ ) is one of the most important magnitudes in high energy physics experiments because it provides the information about the energy of that particle. In principle it is not possible to determine the component of  $\vec{p}$  in the direction of the beam. However, it is possible to determine the transverse momentum ( $p_T$ ) of charged particles by measuring the curvature of such particle within a magnetic field. In principle, particles should have a straight trajectory but the magnetic field ( $B$ ) curves its trajectory. The  $p_T$  relates to the bending radius ( $r$ ) by the Lorentz force:

$$m \frac{v^2}{r} = vqB$$

$$p_T = rqB,$$

where  $q$  is the electrical charge of the particle and  $v$  its speed. The  $r$  is determined using the arc length ( $l$ ) and the sagitta ( $s$ ), which is the distance from the center of the arc to the center of its base. Figure 5.1 shows in red the definition of sagitta. The radius is deduced by:

$$r^2 = (l/2)^2 + (r - s)^2 \rightarrow r = \frac{(l/2)^2 + s^2}{2s}.$$

2537 For high  $p_T$  particles  $s \ll r$  and, hence, it is possible to approximate  
2538  $r \sim \frac{l^2}{8s}$ . The main uncertainty on  $p_T$  is the uncertainty on the sagitta and  
2539 it can be modelled with a Gaussian distribution.

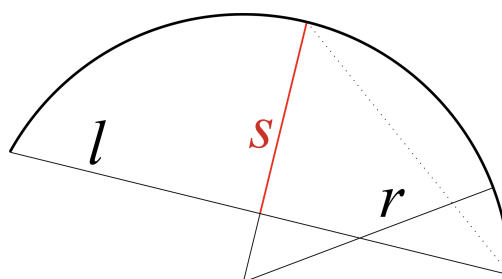


**Figure 5.1:** The arc represents the path of the particle. With the sagitta and the arc length, the radius of curvature can be determined. The more energetic a particle is, the larger is its bending radius.

## 2540 5.2 Electrons and photons

2541 The reconstruction of electrons<sup>1</sup> and photons is accomplished through  
 2542 the identification of energy deposits in the ECAL. For the electrons, particle  
 2543 tracks recorded in the ID are required.

2544 **Electrons**

2545 In the analysis presented at this work, there are two final-state light-leptons  
 2546 that can be electrons. Therefore, accurate and efficient electron identifica-  
 2547 tion is crucial to measure our process of interest. Figure 5.2 presents a  
 2548 schematic representation of the components composing the process of elec-  
 2549 tron reconstruction and identification. When an electron travels through  
 2550 the detector, it leaves traces in the ID and energy deposits in  
 2551 the ECAL. The calorimeter signal activates the LVL1 trigger and electron  
 2552 candidates are selected from an initial match between the ECAL energy  
 2553 clusters and the ID tracks. The clusters must have a value of  $|\eta_{cluster}|$  less  
 2554 than 2.47, excluding the transition region between the barrel and endcap  
 2555 calorimeters. A typical electron candidate is expected to generate 12 hits in  
 2556 the inner tracker system, which includes one hit in the IBL layer, three hits  
 2557 in the silicon pixel layers, and eight hits in the SCT (4 double-sided silicon  
 2558 strips layers). Furthermore, approximately 35 straw hits are produced in  
 2559 the TRT system for an electron of  $p_T$  larger than 500 MeV. Finally, the  
 2560 electron moves to the ECAL, where the majority of its energy is collected  
 2561 by the second layer.

2562 The first step in the electron reconstruction is to build the clusters in the  
 2563 calorimeters. To do so, the space in the ECAL is divided into small elements  
 2564 of dimension  $\Delta\eta \times \Delta\phi = 0.025 \times 0.025$  that combine the subdetector layers.  
 2565 This elements are called towers. A presampler in the  $|\eta| < 1.8$  region also  
 2566 gathers the energy and, along the first three layer of the ECAL, is used  
 2567 to determine the total energy per tower. Cluster seeds by individual towers  
 2568 with energy above 2.5 GeV are searched for within the ECAL middle layer.  
 2569 Once the candidate clusters have been established, the next step is to associate  
 2570 them with the tracks reconstructed in the ID using the tracking algorithms.

2571 When multiple tracks can be linked to a specific electromagnetic calor-  
 2572 imeter cluster, it is necessary to designate a primary electron track. This  
 2573 selection is performed through an algorithm that evaluates the  $\eta - \phi$  distance  
 2574 between the extrapolated tracks and the cluster barycentre, and considers  
 2575 the quantity of hits in the silicon detectors and the number of hits in the  
 2576 innermost silicon layers.

---

<sup>1</sup>Note that the term electrons is used to collectively refer to electrons and positrons.

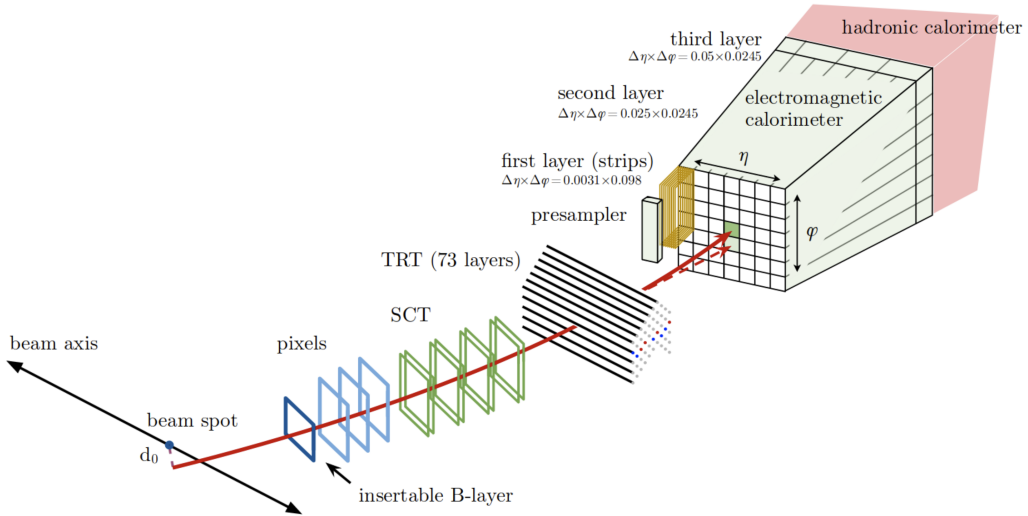


**Figure 5.2:** Trajectory of an electron through the detector. The hypothetical path of the electron is represented by a solid red line, while the trajectory of a bremsstrahlung photon generated in the tracking system material is represented by a dashed red line.

2577 Electrons may arise from either the primary hard-scattering event, such  
 2578 as the decay products of  $W$ ,  $Z$ , and Higgs bosons (referred to as prompt  
 2579 electrons), or as the decay products of secondary particles with relatively  
 2580 long lifetimes, such as  $b$ -hadrons (these are the so called non-prompt elec-  
 2581 trons). An example of non-prompt electron is presented in Figure 5.3. The  
 2582 identification of prompt electrons is achieved through the use of a likelihood  
 2583 discriminant constructed from measurements taken in the ID and ECAL.  
 2584 The measured quantities are selected based on their effectiveness in dis-  
 2585 tinguishing prompt-isolated electrons from energy deposits resulting from  
 2586 hadronic jets, from converted photons and from non-prompt electrons. The  
 2587 discriminant considers the properties of the primary electron track, the lat-  
 2588 eral and longitudinal growth of the electromagnetic shower in the ECAL,  
 2589 and the spatial compatibility of the primary electron track with the cluster.  
 2590 Different operating points, known as working points, can be achieved by  
 2591 setting fixed values for the likelihood discriminant. These are tight, me-  
 2592 dium and loose (in ascending order of signal efficiency). The tight category  
 2593 is the most stringent, while the loose category is much more permissive in  
 2594 terms of accepting something as electron.

## 2595 **Photons**

2596 The process of photon reconstruction closely mirrors that of electron re-  
 2597 construction, with the primary distinction being the absence of tracks in  
 2598 the tracker, unless a photon undergoes conversion into an electron-positron  
 2599 pair, in which case the corresponding tracks must be retrieved.

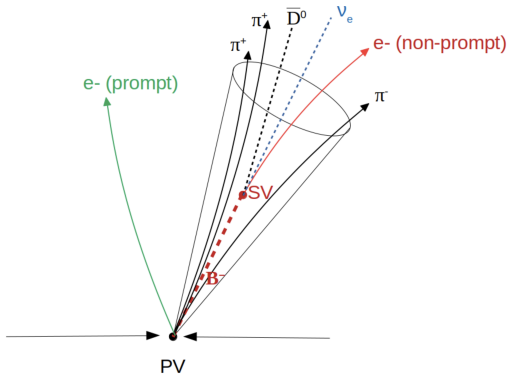


**Figure 5.3:** A prompt electron depicted in green. The cone symbolises a jet containing a several hadrons. The dashed red line corresponds to a  $b$ -hadron ( $B^-$ ), which decays into a  $c$ -hadron ( $\bar{D}^0$ ), a neutrino ( $\nu_e$ ), and a non-prompt electron (red). The non-prompt electron is originated from the secondary vertex while the prompt from the primary vertex.

2600        The identification working points are established with the ECAL information.  
 2601        The distinction between prompt photons and background photons  
 2602        is achieved by applying selections based on quantities that characterise the  
 2603        shape and properties of the corresponding electromagnetic shower, as well  
 2604        as by implementing isolation criteria for the photon candidate.

## 2605        5.3 Muons

## 2606        5.4 Jets

2607        At accelerator based detectors, quarks and gluons are detected by the  
 2608        jets of hadronic particles that they produce in the detector soon after they  
 2609        are created (remember that, as stated in Section 1.1.4, free quarks are sup-  
 2610        pressed due to color confinement). An exception to this rule are the top  
 2611        quarks, whose lifetime is smaller than the hadronisation time by two orders  
 2612        of magnitude and, hence, they are detected by its decay products. For the  
 2613        gluons and the rest of quarks, hadronisation showers (Section 3.3.3.1) take  
 2614        place and jet clustering algorithms merge the clusters and tracks produced  
 2615        by these jets to reconstruct them. In the majority of ATLAS analyses, the  
 2616        “Anti- $k_t$ ” algorithm is used [167] to analyse the data from hadronic col-  
 2617        lisions. Modelling the jet as a cone, the algorithm uses a specific choice  
 2618        of radius parameter ( $R$ ) defining the radial size of the jet. The distance  
 2619        between all pairs of objects  $i$  and  $j$  ( $d_{ij}$ ) and the distance between the  
 2620        objects and beam pipe ( $d_{iB}$ ) are used in:

$$d_{ij} = \min(k_{ti}^{2p}, k_{tj}^{2p}) \frac{\Delta_{ij}^2}{R^2}$$

$$d_{iB} = k_{ti}^{2p}$$

where

$$\Delta_{ij}^2 = (y_i - y_j)^2 - (\phi_i - \phi_j)^2$$

and  $k_{ti}$ ,  $y_i$  and  $\phi_i$  are respectively the transverse momentum, the rapidity and the azimuthal angle of object  $i$ . The parameter  $p$  accounts for the relative power of the energy versus geometrical ( $\Delta_{ij}$ ) scales. For the Anti- $k_t$ ,  $p$  is set to  $-1$ . Other clustering algorithms use different choices of  $p$  such as  $p = 0$  (Cambridge/Aachen algorithm) or  $p = 1$  (inclusive  $k_t$  algorithm).

The algorithm iterates over the topological-cluster (or, simply, top-clusters) objects of the calorimeter as it follows: First it proceeds to identify the smallest distances with among all the combinations of  $d_{ij}$  and  $d_{iB}$ . If the distance is a  $d_{iB}$ , the entity  $i$  is labeled as “jet” and removed from the list of entities. If, on the contrary, it is a  $d_{ij}$ , the objects  $i$  and  $j$  are merged together. This way, before clustering among themselves, soft components (low- $p_T$ ) tend to be merged to the hard ones (high- $p_T$ ). Then the distances are recalculated and the process repeated. This is done iteratively until all entities are assigned to a particular jet.

If a hard particle has no hard neighbours within a  $2R$  distance, all soft particles will be assigned to it, resulting in a perfectly conical jet. But if another hard particle is present in that  $2R$  distance, then there will be two hard jets and it will be impossible for both to be perfectly conical.

### Work in progress

Typically, the cone size  $R$  is selected to be 0.4 or 0.6, though the most standard used in ATLAS is 0.4. If  $R = 1$ , the jet is labeled a Large- $R$  and if  $R = 0.4$  then as Small- $R$  jet.

#### 5.4.1 Jet energy calibration and resolution

The jet calibrations and the associated uncertainties are clearly extremely important in many top analyses. This often makes them the leading experimental uncertainties in Top analyses

**2647 5.4.2 Bottom quark induced jets**

2648 In general, it is impossible to determine which quark flavour was pro-  
2649 duced or even or whether the jet was originated by a quark or a gluon.  
2650 However, if a  $b$  quark is created, the hadronisation will produce a jet of  
2651 hadrons, one of which will be a  $b$ -type hadron (B hadron). The B hadrons  
2652 turn out to be relatively-long-lived particles ( $1.5 \times 10^{-12}$  s). If this larger  
2653 longevity is combined with the Lorentz time-dilation that particles exper-  
2654 ience when produced in high energy collisions, it results in the B hadron  
2655 traveling on average a few mm before disintegrating.

2656 As a result, the experimental signature of a  $b$  quark is a jet of particles  
2657 emerging from the point of collision (primary vertex) and a secondary vertex  
2658 resulting from  $b$ -quark decay that is several mm away from the primary  
2659 vertex. Therefore, the capacity to resolve secondary vertices from the parent  
2660 vertex is crucial for identifying  $b$ -quark jets.

**2661 5.5 Missing transverse energy**

2662 **Chapter 6**

2663 **Search for rare associate  $tHq$   
2664 production**

2665

2666 *Cinquanta quilos pesa el xino.*

2667 —RAFAEL AGULLÓ-IRLES (1941)

2668

2669 **6.1 Introduction**

2670 **Describe the strategy for the  $2\ell + 1\tau_{\text{had}}$  analysis**

2671 The study of the  $tHq$  production can be classified attending to the  
2672 the number of light-flavour leptons ( $\ell$ ), i.e. electrons or muons, and  
2673 hadronically-decaying tau leptons ( $\tau_{\text{had}}$ ). According to this criteria, the  
2674 channels presented in Table 6.1 have been defined. As can be seen in the  
2675 table, the study of the  $1\ell$  channel uses only the  $H \rightarrow b\bar{b}$ , which is the most  
2676 dominant decay mode for the Higgs boson with a 58% BR as is reported in  
2677 Section 2.2.3. However, for the multileptonic channels the  $H \rightarrow W^+ W^-$ ,  
2678  $H \rightarrow \tau^- \tau^+$  and  $H \rightarrow ZZ$  are considered. These three Higgs decay channels  
2679 combined account for a total 21% BR.

2680 Moreover, depending on the relative charge between the light charged  
2681 leptons, the  $2\ell + 1\tau_{\text{had}}$  channel is further subdivided in two sub-channels.  
2682 The so-called  $2\ell \text{SS} + 1\tau_{\text{had}}$  channel is defined by the events in which the

#	0 $\tau_{\text{had}}$	1 $\tau_{\text{had}}$	2 $\tau_{\text{had}}$
1 $\ell$ ( $e/\mu$ )	$tHq (b\bar{b})$ 1 $\ell$		$tHq (WW/ZZ/\tau\tau)$ 1 $\ell + 2\tau_{\text{had}}$
2 $\ell$ ( $e/\mu$ )	$tHq (WW/ZZ/\tau\tau)$ 2 $\ell$ SS	$tHq (WW/ZZ/\tau\tau)$ 2 $\ell + 1\tau_{\text{had}}$	
3 $\ell$ ( $e/\mu$ )	$tHq (WW/ZZ/\tau\tau)$ 3 $\ell$		

**Table 6.1:** Different channels for  $tHq$  production according to the presence of light-flavoured leptons and hadronically-decaying taus in the final state.

2683 two light leptons have the same electric charge. In contrast, the one in  
 2684 which they have opposite electric charge is known as  $2\ell$  OS +  $1\tau_{\text{had}}$  channel.  
 2685 For simplicity, through this document, these two sub-channels are usually  
 2686 referred just as SS and OS respectively.

2687 The work of this thesis is focused in the  $2\ell + 1\tau_{\text{had}}$  channels. To do so,  
 2688 the  $2\ell$  SS +  $1\tau_{\text{had}}$  and  $2\ell$  OS +  $1\tau_{\text{had}}$  are treated separately since they have  
 2689 different background compositions, being the  $2\ell$  SS +  $1\tau_{\text{had}}$  the one with the  
 2690 lower background contribution.

2691 - different MVAs trained for each channel

2692 When assuming that one of the light-flavoured leptons is originated from  
 2693 the Higgs-boson decay and the other one from the top-quark decay, the  
 2694 determination of which lepton comes from which particle is direct for the  
 2695  $2\ell$  OS +  $1\tau_{\text{had}}$  but not for the  $2\ell$  SS +  $1\tau_{\text{had}}$ . Since knowing the origin of the  
 2696 light-flavoured leptons can be very useful to define variables with the power  
 2697 to discriminate the  $tHq$  signal from the background, tools are developed to  
 2698 associate these leptons to its parent particles.

2699 - The fake rate estimates for light leptons and tau leptons are being  
 2700 checked to see if there is anything that has to be treated differently for the  
 2701 two sub-channels.

## 2702 6.2 Data and simulated events

2703 In this section the particularities of the detector real detector data and  
 2704 the MC generated samples are presented. The generalities of the data gath-  
 2705 ering and the MC samples production are described in Chapter 4.

---

2706    **6.2.1 Data event samples**

2707    The real data samples used in this analysis correspond to the events re-  
 2708    corded by the ATLAS detector from  $p\ p$  collisions with 25 ns bunch spacing  
 2709    delivered by the LHC at  $\sqrt{s} = 13$  TeV during Run 2. This corresponds to  
 2710    a total integrated luminosity of  $\mathcal{L}^{\text{Run}2} = 140 \text{ fb}^{-1}$ . The uncertainty corre-  
 2711    sponding to this integrated luminosity has been measured by the LUCID-2  
 2712    detector to be 0.83%. This data-taking period ranges from 2015 to 2018 and  
 2713    for each year ad different luminosity and uncertainty have been measured,  
 2714    as Table 6.2 shows.

Year	Periods	Run numbers	Number of events	Integrated luminosity ( $\text{pb}^{-1}$ )
2015	D–H,J	276262–284484	220.58M	$3244.54 \pm 1.13\%$
2016	A–G,I,K,L	297730–311481	1057.84M	$33402.2 \pm 0.89\%$
2017	B–F,H,I,K	325713–340453	1340.80M	$44630.6 \pm 1.13\%$
2018	B–D,F,I,K,L,M,O,Q	348885–364292	1716.77M	$58791.6 \pm 1.10\%$
2015–2018	All	276262–364292	4335.99M	$140068.94 \pm 0.83\%$

**Table 6.2:** Total integrated luminosity per year with their relative uncertainties for the Run 2. Additionally, the data-taking periods, run numbers and number of events are shown for each year.

2715    The good-runs list (GRL) is an xml file that selects the luminosity blocks  
 2716    that are considered good to be used in an analysis. This is done by demand-  
 2717    ing that the LHC had stable beams and all the detectors and subdetectors  
 2718    were operating correctly. The GRL has been used in order to filter the  
 2719    registered data at the lumiblock<sup>1</sup> level.

2720    **6.2.2 Simulated event samples**

2721    The event samples generated using MC simulators relied on several event  
 2722    generators to produce the different processes.

2723    **6.2.2.1 Simulated  $tHq$  signal events sample**

2724    **6.2.2.2 Simulated background events sample**

2725    **Top quark pairs**

2726

---

<sup>1</sup>A lumiblock corresponds to 1 or 2 minutes of data-taking

**Single boson**

This background corresponds to the  $Z + \text{jets}$  and  $W + \text{jets}$  productions, which were simulated with SHERPA generator.

**Diboson**

2731

**Triboson**

2733

**Top-quark pair + single-boson**

2735

**Top-quark pair + Higgs-boson**

2737

**Single top-quark:  $t$ -channel**

2739

**Single top-quark:  $tW$  associated production**

2741

**Single top-quark:  $s$ -channel**

2743

**Single top-quark + $X$ :  $tZq$** 

2745

**Single top-quark + $X$ :  $tWH$** 

2747

**Single top-quark + $X$ :  $tWZ$** 

2749

**Three top-quark**

2751

2752 **Higgs boson process**

2753

2754 **6.2.3 Single lepton triggers**

2755 Events were selected from a common data stream using unprescaled  
2756 single-lepton triggers

2757 **6.3 Object definition**

2758 **Highlight the importance of alignment**

2759 **6.3.1 Triggers**

2760 **6.3.2 Electrons**

2761 **6.3.3 Muons**

2762 **6.3.4 Taus**

2763 **6.3.5 Jets**

2764 **6.3.6  $b$ -tagged jet identification**

2765 **6.3.7 Missing transverse momentum**

2766 **6.3.8 Overlap removal**

2767 **6.4 Signal**

2768 In this section, it is discussed how it is find what we know as signal.  
2769 In a particular study, the “signal” is the set of events in the dataset that  
2770 correspond to the process of interest. Therefore, in this case, the signal  
2771 is composed by  $tHq$  production events with a  $2\ell + 1\tau_{\text{had}}$  final state. In  
2772 contrast, the background processes are those which, a priori, look like the  
2773 signal process but it is not. A more detailed definition of what a background  
2774 is and how it is classified can be found in Section 6.5.

As mentioned already, the cross-section of  $tHq$  is very small. One of the big challenges of LHC is the wide range of cross sections that of the different process that take place there. When the cross-section is huge, the process is typically uninteresting. When it is large the process is already known. The medium cross-sections corresponds to not-so-well studied process, and when it is low is for process yet to be discovered. This causes that the main backgrounds are much larger than the signal, swamping the interesting physics with known processes. Therefore, in order to produce some small number of signal events, it is necessary to also produce so many of uninteresting ones that they even happen in the same crossing (pile-up).

**Maybe this paragraph can be put somewhere else or removed**

#### 6.4.1 Signal generation and validation

**rivet**

#### 6.4.2 Parton-level truth validation

- > Describe what are truth level and reconstruction level.
- > The truth information is whatever comes from the generator, the physics without taking into account the effects of the detector. The truth level does not include the effects of the interaction with matter. The truth also includes the parton shower and hadronisation information.
- > truth = generator + parton shower + hadronisation
- > The studies I did were done at generator level
- > Particle level is part of truth information
- > Detector level = reconstruction level + calibration +
- > Creo que esto se explica bien en la tesis de florencia
- (**maybe write the calculations of BR\_tHq in the Section 6.4.2**)

#### 6.4.3 Lepton assignment

The two light leptons in the final state of the  $2\ell + 1\tau_{\text{had}}$  channel can originate either from the Higgs boson or the top quark. The ambiguities regarding the origin of these light-flavoured leptons, make the reconstruction of the top quark and Higgs boson systems extremely difficult. Nevertheless,

2806 the electric charge of these leptons could provide us useful information to  
 2807 probe their origins.

2808 To have knowledge of whether the light-flavoured leptons in the final  
 2809 state are originated from the Higgs boson or the top quark is very beneficial  
 2810 in order to both reconstruct the event and design variables at reconstruction  
 2811 level with high discriminant power. As is show in Sections 6.6.4 and 6.6.5,  
 2812 the variables using the lepton assignment information play a relevant role  
 2813 not only in the definition of the signal-enriched section but also the in  
 2814 the determination of the control regions to constrain the most important  
 2815 background processes.

2816 According to the calculations performed by combining the BR of the  
 2817 Higgs boson, the top quark and all its decay products (see Section 6.4.2),  
 2818 in the  $2\ell + 1\tau_{\text{had}}$  channel of  $tHq$  production, the  $\tau_{\text{had}}$  is produced 83.7% of  
 2819 times as a product of the Higgs-boson decay in opposition to the 16% in  
 2820 which it comes from the top-quark disintegration.

### 2821 Opposite-sign Leptons

2822 In the dominant scenario ( $\tau_{\text{had}}$  from Higgs) the association of which light-  
 2823 flavoured lepton comes from the top-quark decay and which one comes  
 2824 from the Higgs-boson decay can be done directly if these two leptons have  
 2825 opposite electric charge, i.e. in the  $2\ell \text{OS} + 1\tau_{\text{had}}$  channel. Since in Higgs  
 2826 boson is neutrally charged, the sum of the charge of its decay products  
 2827 should be zero. Therefore, in the OS channel, while the light lepton with  
 2828 opposite charge to that of the  $\tau_{\text{had}}$  is the one coming from the Higgs, the  
 2829 other lepton, i.e. the one with the same charge as  $\tau_{\text{had}}$ , is the one originated  
 2830 from the top-quark decay.

### 2831 Same-sign Leptons

2832 In contrast to the the  $2\ell \text{OS} + 1\tau_{\text{had}}$  channel, in the case of  $\tau_{\text{had}}$  from Higgs,  
 2833 when the two light leptons have the same electric charge (the so called  
 2834  $2\ell \text{SS} + 1\tau_{\text{had}}$ ) it is not possible to know, a priori, which of the leptons  
 2835 comes from the top-quark system and which from the Higgs-boson decay.

2836 In order to perform this association for the  $2\ell \text{SS} + 1\tau_{\text{had}}$  several methods  
 2837 relying in the truth-level information have been tested. **Describir superficialmente los métodos listados en el ítemize**

- 2839 • First method (Cyrus): Assume that the leading lepton was originated  
 2840 from the top
- 2841 • Second method (Mathias): Cut in two variables

- 2842           – Cut 1:  $m_{vis,H}(lep(t)) - m_{vis,H}(lep(H)) > 57.0 \text{ GeV}$   
 2843           – Cut 2:  $m_{pred,t}(lep(H)) - m_{pred,t}(lep(t)) > 0.0 \text{ GeV}$
- 2844       • BDT based method (me): For accurately assigning the origin of the  
 2845       light lepton in the  $2\ell \text{ SS} + 1\tau_{\text{had}}$ , I developed a BDT based on the  
 2846       TMVA library of ROOT<sup>2</sup>. This method is carefully described in this  
 2847       Section.

2848     **6.4.3.1 Labelling the  $2\ell \text{ SS} + 1\tau_{\text{had}}$  with the reconstruction-level**  
 2849     **and truth-level matching**

2850     Even though at reconstruction level it is not known which are the par-  
 2851     ents of the particles in the final state, at parton level this informations is  
 2852     accesible, in other words, the origin<sup>3</sup> of the light leptons is known. For a  
 2853     given event, it is possible to access to both the particle-level and parton-level  
 2854     information simultaneously. Having the parton-level leptons, whose parents  
 2855     are known, and the reconstruction-level leptons, whose parents need to be  
 2856     identified, it is possible to compare them to create an association. Specific-  
 2857     ally, identify which parton-level lepton correspond to which reconstructed  
 2858     lepton. The aim of this relation is to assign the leading ( $\ell_1$ ) and sub-leading  
 2859     ( $\ell_2$ ) light leptons at reconstruction level to the the “lepton from top-quark-  
 2860     decay chain” ( $\ell_{\text{top}}$ ) and “lepton from Higgs-boson-decay chain” ( $\ell_{\text{Higgs}}$ ) at  
 2861     truth level.

2862     In order to link the reconstruction-level light leptons to the parton-  
 2863     level light leptons, a  $\Delta R < 0.01$  cone around each of the reconstructed  
 2864     leptons is built. When inside that cone there is exactly one truth-level light  
 2865     lepton, there is what is called “a match”. Figure 6.1 presents the possibles  
 2866     scenarios of the association. In order to identify properly determine the  
 2867     lepton origin in an event, it is required that both leptons at reconstruction  
 2868     level have a match. There are two different cases for this. The first situation  
 2869     is that in which the leading-light lepton is  $\ell_{\text{top}}$  and the sub-leading is  $\ell_{\text{tHiggs}}$ .  
 2870     For the sake of simplicity, this configuration is named “Type 1” and it is  
 2871     represented in Figure 6.1a. The second double-matching combination is the  
 2872     other way around, the leading-light lepton is  $\ell_{\text{Higgs}}$  and the sub-leading is  
 2873      $\ell_{\text{top}}$ . Pictured in Figure 6.1b, this type of events are called “Type 2”. On  
 2874     the contrary, if only one of the two reconstructed light leptons is matched  
 2875     (Figure 6.1c), none of the leptons are classified. If a less strict criteria was  
 2876     used, it would be possible requiere only one of the two leptons matching in

---

<sup>2</sup>ROOT is an object-oriented program and library developed by CERN and it was spe-  
cifically designed for particle physics data analysis.

<sup>3</sup>By origin of a light lepton is meant whether it comes from the Higgs-boson-decay chain  
or the top-quark-decay chain.

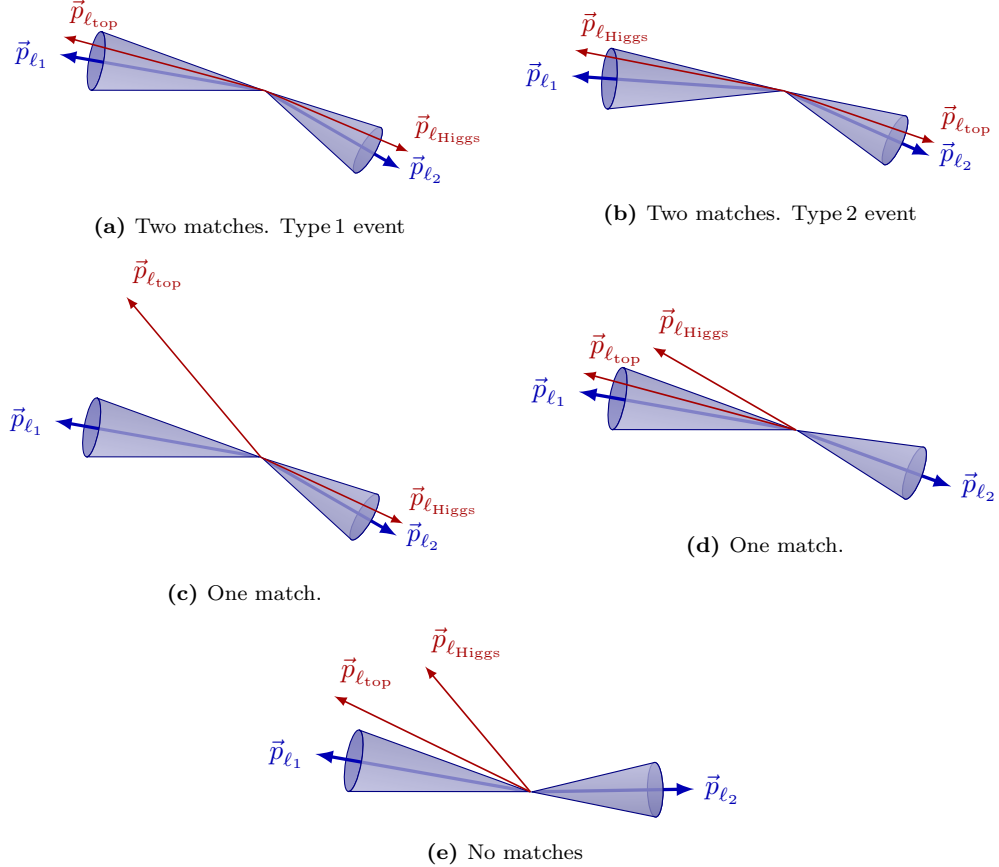


**Figure 6.1:** Association between reconstruction-level (blue) and parton-level (red) light leptons. Note that the labels  $\ell_{\text{top}}$  and  $\ell_{\text{Higgs}}$  are only available for the parton-level particles.

order to classify the event (the unmatched reconstruction-level lepton would be assigned to the unmatched parton-level lepton). The problem of the lax strategy is that while in cases like that on Figure 6.1c it seems clear that unmatched parton correspond to the unmatched reconstructed lepton, for events such as the illustrated in Figure 6.1d the unmatched particle does not necessarily belong to the  $\ell_2$  cone. For this reason, it is mandatory that both reconstructed light leptons have a match. Finally, in the scenario in which none of the parton-level leptons fall into the cones (Figure 6.1e), no assignation takes place.

To perform this labelling, it has been required that the  $\tau_{\text{had}}$  is originated from the Higgs-boson system. This is imposed in order to guarantee that there are both a  $\ell_{\text{top}}$  and a  $\ell_{\text{Higgs}}$ . The Higgs-decay channels used for these studies are the  $H \rightarrow \tau\tau$  (one  $\tau$  decaying letonically and the other hadronically) and the  $H \rightarrow WW$ . The  $H \rightarrow ZZ$  channel has not been included since its impact in the on the  $2\ell + 1\tau_{\text{had}}$  production when the

2892  $\tau_{\text{had}}$  comes from the Higgs is very tiny. If the  $\tau_{\text{had}}$  is originated in the Higgs  
 2893 system, only a 2.0% of the events correspond to the  $H \rightarrow ZZ$  decay channel,  
 2894 contrasting with the 76.5% of the  $H \rightarrow \tau\tau$  and the 21.5% of the  $H \rightarrow WW$ .

2895     **Should add the fraction of events that are labeled from a) the**  
 2896 **total  $2\ell + 1\tau_{\text{had}}$  sample and b) from the total  $2\ell \text{ SS} + 1\tau_{\text{had}}$ .**

2897     

### 6.4.3.2 BDT-based method for lepton association

- 2898     • Describe the idea of using reco-level variables to predict (on unlabelled  
 2899 data) whether it is a “Type 1” or “Type 2” event by means of a BDT  
 2900 trained with labeled data (`isLep1fromTop`).
- 2901     • Describe with a few words what a BDT is and reference appendix  
 2902 **B**. This BDT separates between the categories “Type 1” or “Type 2”  
 2903 similarly to the way signal and background are separated. In this case,  
 2904 the way to identify this categories is via de variable `isLep1fromTop`.  
 2905 Therefore, the two classes are define as:
  - 2906         – **Type 1:** The leading  $e/\mu$  comes from the top-quark decay  
 2907 chain and, hence, the the sub-leading from the Higgs boson  
 2908 (`isLep1fromTop =0`). As expected, this is the most frequent  
 2909 type since the top quark carries more momentum.
  - 2910         – **Type 2:** Just the opposite to the type 1. In this case, the  
 2911 decay chain of the Higgs boson is the source of the leading lepton  
 2912 while the sub-leading comes from the top quark. The lead-  
 2913 ing light lepton is a product from the Higgs-boson-decay chain  
 2914 (`isLep1fromTop =0`).
- 2915     • Using root.TMVA - Advantages: Nowadays most of ML frameworks  
 2916 (`keras`, `pyTorch`, `scikit-learn`, `XGBoost`, etc..) are based on python.  
 2917 These libraries expect numpy arrays or panda data-frames as input, so  
 2918 the first thing to do when using the analysis NTuples is to convert the  
 2919 ROOT data-frame. An advantage of using TMVA library of ROOT  
 2920 is that this data conversion is not necessary. is that
- 2921     • Describe the particularities of this gradient BDT with detail
- 2922     • One way to reap the benefits of a large training set and large test set  
 2923 is to use cross validation: k-folding.
  - 2924             – Programmed in an external-to-tHqLoop script
  - 2925             – Trained only over SS signal events. In contrast to the BDT of  
 2926 SR that trains over all process, this one trains only over signal

- 2927 because its objective is to determine which lepton comes from  
2928 which particle in the signal events and this classification only  
2929 makes sense in signal processes.
- 2930 • Present the feature importance
- 2931 – Present distributions of used variables and a list with the mean-  
2932 ing of this variables
- 2933 – Present correlations between pairs of used variables. Note that  
2934 the correlation maps search for bidimensional correlations (i.e.  
2935 between pairs of two variables) and the BDT uses N-dimensional  
2936 relations. (Page 26 of the TMVA guide)
- 2937 –
- 2938 • Discuss the negative weight strategy: Present used distributions with  
2939 'all weights' and with 'positive weights'
- 2940 – in contrast to XGboost, ROOT.TMVA can deal with negative  
2941 weights
- 2942 • Hyperparameter optimisation
- 2943 • Present BDT response, ROC curve, ¿something else?
- 2944 • Compare to the results using other MVA methods.
- 2945 • The BDT is integrated in tHqLoop (weights.xml) ¿Where do I describe  
2946 what tHqLoop is?
- 2947 • From tHqLoop, the BTD score can be calculated for all the events  
2948 (signal or not) and then the efficiency of the lepton association can be  
2949 calculated depending on the threshold point which is chosen to define  
2950 whether the event is Type 1 or Type 2. Note that this efficiency is  
2951 computed only over signal events. → Table of 'efficiency vs cutpoint'

2952 **6.4.4 Top quark and Higgs boson reconstruction**

2953 **En aras de que esto es extremadamente complicado y no se**  
2954 **logró hacer ¿tiene sentido redactar una sección?**

---

## 2955 6.5 Background estimation

2956     The background can be defined as everything in a subset of the data that  
 2957     simulates the signal processes without truly being a signal event. In other  
 2958     words, in this studies, everything that is not signal, is background. In this  
 2959     case, whatever that mimics the signature of an associated  $tHq$  production  
 2960     with  $2\ell + 1\tau_{\text{had}}$  final state is referred as background.

2961     In order to perform the physics analysis, it is fundamental to subtract  
 2962     the background events from the dataset as much as possible in order to  
 2963     achieve higher signal purity. By doing this, the analysed dataset resembles  
 2964     more to the process that is desired to study. This procedure is the so called  
 2965     “event selection” and its described in Section 6.6

2966     There are two different types of background: “reducible” backgrounds,  
 2967     where particles imitate the particles we are looking for (for instance, a  
 2968     high-energy electron can mimic a high-energy photon), and “irreducible”  
 2969     backgrounds, where particles are the same kind as the ones we are looking  
 2970     for.

2971     The main source of background in the  $2\ell + 1\tau_{\text{had}}$  channel is due to  
 2972     signatures of hadronic tau decays, more specifically, of jets faking  $\tau_{\text{had}}$ .

2973     **Add Oleh pieCharts**

### 2974 6.5.1 Fakes estimation

2975      $\tau^-$  fakes are more important than light lepton fakes

2976     **This is taken from the intNote. I have to reorganise and reph-**  
 2977     **rase this information** The requirements for the objets defined in section  
 2978     (ref ref) provide significant suppression of events with jets wrongly selec-  
 2979     ted as leptons is achieved by asking electrons and muons to pass the tight  
 2980     requirement that combines `tightLH ID` for leptons and `medium` for muons  
 2981     and `PLImprovedTight` isolation working points

2982     Similarly, the hadronic taus are required to pass the `medium` require-  
 2983     ment of the RNN-based discriminator. Even so, the selected data sample  
 2984     is expected to be contaminated with such type of reducible background. It  
 2985     is also expected that the simulation of jets faking leptons (electron, muon,  
 2986     hadronic tau) in ATLAS detector is imprecise or unreliable. Therefore, an  
 2987     important step of the analysis is to estimate this background in data.

2988     **Light-lepton fakes** Particles from the hard scattering process are re-  
 2989     ferred as ‘prompt’ . Acceptance, quality and isolation requirements are ap-

2990 plied to select these leptons Non-prompt leptons and non-leptonic particles  
2991 may satisfy these selection criteria, giving rise to so called ‘non-prompt  
2992 and fake’ lepton backgrounds. Fake electrons/muons will not be explicitly  
2993 distinguished and are referred as fake leptons. The mis-identified lepton  
2994 background arises from leptons from heavy-flavour ( $\ell_{\text{HF}}$ ) hadron decay and  
2995 electrons from  $\gamma$ -conversions. These leptons are mainly produced in  $t\bar{t}$ ,  
2996  $Z + \text{jets}$  and  $tW$  events.

2997 The estimation of the fake/non-prompt lepton background is done with  
2998 the template fit method or via the matrix method

2999 The fake and real lepton efficiencies (fake/real rates) are defined as the  
3000 probabilities of a fake or real electron or muon to pass the nominal elec-  
3001 tron/muon requirements. They are given by the tight over loose ratio

3002 - Get some ideas from here: [https://cds.cern.ch/record/1951336/  
3003 files/ATLAS-CONF-2014-058.pdf](https://cds.cern.ch/record/1951336/files/ATLAS-CONF-2014-058.pdf)

3004 **Tau fakes** In the analysis channels involving hadronic taus, all methods  
3005 used for fake background estimation rely on MC-based templates. These  
3006 are splits of simulation according to a type of object mimicking the lepton  
3007 of interest. Construction of MC templates related to the electron and  
3008 muon fakes is based on **TruthClassificationTool** tool. [Describe the  
3009 TruthClassificationTool](#)

- 3010 • counting method  
3011 • template fit method

3012 The extracted SFs are then applied to the simulated background com-  
3013 ponent in the region with taus passing the preselection requirements.

3014 **6.5.1.1  $t\bar{t}$**

3015 **6.5.1.2  $Z + \text{jets}$**

3016 **6.5.2 Reducible backgrounds**

3017 All the processes whose signature is the same as the process of interest  
3018 are known as reducible backgrounds as in contrast to the fake or irredu-  
3019 cible backgrounds described in Section 6.5.1. The objects in the reducible  
3020 backgrounds are prompt. The main reducible backgrounds are:

3021 **6.5.2.1 Diboson**

3022 **6.5.2.2  $tW$**

3023 **6.5.2.3  $t\bar{t}Z$**

3024 **6.5.2.4  $t\bar{t}H$**

3025 **6.5.2.5  $t\bar{t}W$**

3026 **6.5.2.6  $tZq$**

3027 **6.6 Event selection**

3028 The event selection

3029 As more and more stringent requirements are made to eliminate these  
3030 backgrounds we also lose signal events, so there is a trade off background  
3031 rejection against signal acceptance. Since the data is not only limited but  
3032 also scarce when it refers to the  $tHq$  signal, the event selection is a highly  
3033 non-trivial process that requieres a lot of attention.

3034 The signal selection is done in several steps and using different methods.  
3035 First of all, it is defined a preselection region (PR) where the physical objects  
3036 are selected according to the detector acceptance. The PR is a cut-based  
3037 region. Then, discriminant variables are defined and used as input for a  
3038 BDT. Finally, the BDT outputs are used to define the signal region (SR)  
3039 and control regions (CR).

3040 Two figures of merit are used to simultaneously optimise the fraction of  
3041 signal events in the data and the absolute number of signal events. These  
3042 metrics are the  $S/B$  or purity and the signal significance.

3043 **Purity** : The purity of a process is defined as the ratio between the event  
3044 yields of the target process and the total yields. Usually, for the signal, the  
3045 signal to background ratio ( $S/B$ ) is used instead of the purity.

3046 **Significance** : This metric does not only account to the relative fraction  
3047 of the process of interest but also to the total amount events. Using the  
3048 significance as metric enhances the importance of keeping enough statistics.

Process	SS	OS	SS + OS
$tHq$	0.9	1.2	2.1
$tZq$ (with $Z \rightarrow \ell\ell$ )	6.2	32.9	39.1
$t\bar{t}$	47.9	2965.0	3012.9
$tW$	2.3	118.9	121.2
$W + \text{jets}$	1.9	0.5	2.4
$Z + \text{jets}$	6.7	1956.2	1962.9
VV + jets (V= $W/Z$ )	8.9	121.6	130.5
$t\bar{t}W$	21.0	43.4	64.4
$t\bar{t}Z$	17.5	101.2	118.7
$t\bar{t}H$	17.8	43.2	61.0
$tWZ$ (with $Z \rightarrow \ell\ell$ )	3.1	16.4	19.5
$tWH$	0.6	1.5	2.1
Other	1.9	9.3	11.2
Total	136.7	5411.3	5548.0
S/B (%)	0.6627	0.0222	0.0379
Significance	0.0771	0.0163	0.0282

**Table 6.3:** Event yields at preselection level for SS, OS and SS+OS combination. **The W and Z MC only feature leptonic decays**

The definition of the significance estimator used in this work is the one given in reference [176]

$$\text{Significance} = \sqrt{2[(s + b)\ln(1 + s/b) - s]}, \quad (6.1)$$

where  $s$  is the number of events of the target process and  $b$  is the number of yields for the rest of processes combined. This can be used not only to evaluate the signal significance but also the significance of the background processes in the dedicated CRs.

### 6.6.1 Preselection

Refer to chapter 2 and the geometrical acceptance of the detector to justify the PR cuts

Preselection requirements

3057 **6.6.2 Discriminant variables**

3058 To enhance the capability of discrimination between processes, new vari-  
3059 ables are build out of several others. Some of these are useful to improve  
3060 the separation. The first task in this regard is to substitute the classifica-  
3061 tion of the light leptons from leading ( $\ell_1$ ) and subleading ( $\ell_2$ ) lepton to  $\ell_{\text{top}}$   
3062 and  $\ell_{\text{Higgs}}$ . The variables using the light-lepton origin are more discriminant  
3063 than the ones that classify them by the the  $p_{\text{T}}$ . **Aportar un figura donde**  
3064 **se vea la diferencia entre emplear ( $\ell_1$ ,  $\ell_2$ ) y ( $\ell_{\text{top}}$ ,  $\ell_{\text{Higgs}}$ )**

3065 **6.6.3 BDT**

3066 Since a BDT is going to be used for both the lepton assign-  
3067 ment and region definition, it may be interesting to describe the  
3068 technicalities of the BDT in an appendix

3069 Maybe, it can also be a good idea to explain the generalities of  
3070 the BDT for region definition here and then put the BDT results  
3071 into "Signal Region" and "Control Regions" section.

3072 **6.6.3.1 Performance**

3073 **6.6.3.2 Ranking of variables**

3074 **6.6.3.3 Hyperparameter optimisation**

3075 **Grid search**

3076 **Genetic algorithm**

3077 **6.6.3.4 Negative-weights strategy**

3078 **6.6.3.5 k-Folding**

3079 **6.6.4 Signal Region**

3080 **6.6.4.1 Same Sign channel**

3081 **6.6.4.2 Opposite Sign channel**

3082 Here I shall explain the problem with some variables such us  
3083 MET that, despite having great separation power, produce the  
3084 effect of not differentiating the  $tHq$  signal from the  $t\bar{t}$  contribu-  
3085 tions.

3086 **6.6.5 Control Regions**

3087 **6.6.5.1 Same Sign channel**

3088  $t\bar{t}$

3089  $t\bar{t}W$

3090  $t\bar{t}Z$

3091  $t\bar{t}H$

3092 **6.6.5.2 Opposite Sign channel**

3093  $t\bar{t}$

3094  $Z +\text{jets}$

3095 **Diboson**

3096  $tW$

## 3097 6.7 Systematic uncertainties

3098 Particle collision physics distinguish two types of uncertainties, the statis-  
 3099 tical uncertainty and the systematic uncertainty. The statistical uncer-  
 3100 tainty is the result of stochastic fluctuations in data and is the result of a  
 3101 limited size of analysed dataset. It is fully uncorrelated between subsequent  
 3102 measurements. On the other hand there are the systematic uncertainties,  
 3103 which are defined as everything that is not a statistical error. These are  
 3104 fully correlated between subsequent measurements and are associated with  
 3105 all sort of sources such us the measurement apparatus, the assumptions  
 3106 made, the model used, the MC generator and many others.

3107 While the statistical uncertainty is usually intrinsically added in the  
 3108 inference method, the inclusion of the systematic uncertainties and its  
 3109 propagation through the statistical analysis are not trivial.

3110 Alternative samples are produced to evaluate the systematics: - Herwig7  
 3111 -> parton shower  
 3112 - asdfas. -> modelling  
 3113

### 3114 6.7.1 Theoretical uncertainties

### 3115 6.7.2 Modelling uncertainties

### 3116 6.7.3 Experimental uncertainties

## 3117 6.8 Fit results

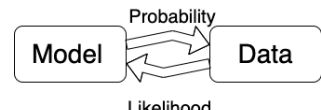
### 3118 6.8.1 Likelihood fit

3119 **Maybe I move the statistics description to an appendix** The  
 3120 likelihood fit....

3121 The likelihood function is defined as the probability of observing a cer-  
 3122 tain set of data ( $\vec{x}$ ) given a model or hypothesis with certain parameter  
 3123 values ( $\vec{\theta}$ ). It is given by

3124

$$L(\vec{\theta}) = \mathcal{P}(\vec{x}|\vec{\theta}) = \prod_i \mathcal{P}(x_i|\vec{\theta})$$



3125 where  $i$  runs over the data points. By maximising the likelihood function,  
 3126 the parameters  $\vec{\theta}$  of the model that better fit the data are obtained.  
 3127 These are known as estimated values. The fit is the parameter estimation  
 3128 via the Likelihood maximisation,  $\vec{\theta}_{estimated} = \text{argmax}_{\vec{\theta}} L(\vec{\theta})$ .

For binned distributions the likelihood function can be written as

$$L(\vec{n}|\vec{\theta}) = \prod_{i \in bins} \mathcal{P}(n_i^{obs}|n_i^{exp}(\vec{\theta})) = \prod_{i \in bins} \mathcal{P}(n_i^{obs}|S_i^{exp}(\vec{\theta}) + B_i^{exp}(\vec{\theta}))$$

3129 Here,  $i$  runs over the bins of the histogram,  $n_i^{obs}$  and  $n_i^{exp}$  are the observed  
 3130 and expected number of entries in the bin  $i$ . The predicted signal and  
 3131 background entries in the bin  $i$  are  $S_i$  and  $B_i$ .

3132 Since particle physics experiments are counting experiments, the dis-  
 3133 tribution follows the poissonian statistics. The Poisson distribution is a  
 3134 discrete probability distribution that expresses the probability of a given  
 3135 number of events occurring in a fixed interval of time or space if these  
 3136 events occur with a known constant mean rate and independently of the  
 3137 time since the last event

From the frequentist point of view the probability is defined as the fraction of times an event occurs, in the limit of very large number ( $N \rightarrow \infty$ ) of repeated trials

$$\mathcal{P} = \lim_{N \rightarrow \infty} \frac{\text{Number of favorable cases}}{N}$$

3138 where  $N$  is the number of trials. Even though this infinity can be concep-  
 3139 tually unpleasant, for LHC experiments, the amount of events is so large  
 3140 that this  $\mathcal{P}$  definition becomes acceptable [177].

3141 In contrast, for the Bayesian (or subjective) probability expresses the  
 3142 degree of belief that a claim is true. Starting from a prior probability,  
 3143 following some observation, the probability can be modified into a posterior  
 3144 probability. The more information an individual receives, the more Bayesian  
 3145 probability is insensitive on prior probability [177].

The Bayes theorem [178] states that considering two events  $A$  and  $B$ , the probability of  $A$  to happen given that  $B$  takes places is

$$\mathcal{P}(A|B) = \frac{\mathcal{P}(B|A)\mathcal{P}(A)}{\mathcal{P}(B)}$$

3146 where  $\mathcal{P}(B|A)$  is the conditional probability of  $B$  given  $A$  and  $\mathcal{P}(B)$  the  
 3147 probability of the event  $B$  to happen. Here,  $\mathcal{P}(A)$  has the role of prior  
 3148 probability while  $\mathcal{P}(A|B)$  is known as posterior probability.

**3149 6.8.2 Strategy****3150 6.8.3 Fit with Asimov data****3151 6.8.3.1 Post-fit****3152 6.8.3.2 Pruning****3153 6.8.3.3 Nuisance Parameters****3154 6.8.3.4 Correlation matrix****3155 6.8.3.5 Ranking****3156 6.8.4 Fit to data****3157 6.8.4.1 Post-fit****3158 6.8.4.2 Pruning****3159 6.8.4.3 Nuisance Parameters****3160 6.8.4.4 Correlation matrix****3161 6.8.4.5 Ranking****3162 6.8.5 Results**

The signal strength  $\mu$  is defined as the ratio of the measured Higgs boson rate to its SM prediction. For the  $tHq$ , the signal strength production is:

$$\mu_{tHq} = \frac{\sigma_{tHq}}{(\sigma_{tHq})_{SM}}.$$

For particular desintegration mode  $f$  the decay signal strength is:

$$\mu^f = \frac{BR^f}{(BR^f)_{SM}},$$

being  $BR^f$  the branching ratio for the  $f$  decay mode. Since cross-section and the BR cannot be separated without further assumptions, only the product can measured experimentally, leading to the combined signal strength:

$$\mu_{tHq}^f = \frac{\sigma_{tHq} \cdot BR^f}{(\sigma_{tHq})_{SM} \cdot (BR^f)_{SM}} = \mu_{tHq} \cdot \mu^f.$$

<sup>3163</sup> In our particular case  $f$  is  $2\ell \text{OS} + 1\tau_{\text{had}}$  or  $2\ell \text{SS} + 1\tau_{\text{had}}$ .

<sup>3164</sup> **6.8.6 Data fit**

<sup>3165</sup> **6.9 Combination results**

<sup>3166</sup> **Discuss results, compare them with CMS, future perspectives**

<sup>3167</sup> ...

<sup>3168</sup> **6.10 Conclusions**



3169 Chapter 7

3170 Conclusion

3171

3172

*Terminamos.*

3173

3174 textsc{Mi ex}

3175



3176 **Appendix A**

3177 **Effect of negative weights**

3178 **A.1 Negative weights uncertainties**

- 3179 • What is a weight in a MC event?
- 3180 • Why are there negatively weighted events?
- 3181 • Why are negative weights problematic?

3182 **A.2 Statistical uncertainty of negative  
3183 weights**

3184 Assume that there is a sample of  $N$  Monte Carlo simulated events. Of  
3185 these, a fraction  $x$  have negative weights and, therefore, a fraction  $(1 - x)$   
3186 has a positive weight. The effective number of events is  $(N_+ - N_-)$ , being  
3187  $N_+ = (1 - x)N$  the amount of positively weighted events and  $N_- = xN$  the  
3188 same for the negative weights.

3189 The statistical fluctuations are calculated in terms of  $x$  and the standard  
3190 deviation ( $\sigma_N = \sqrt{N}$ ). The number of positive and negative events can  
3191 fluctuate randomly between  $\pm\sigma_-$  for the later and  $\pm\sigma_+$  for the former.  
3192 Here,  $\sigma_- = \sqrt{xN} = \sqrt{x}N$  and  $\sigma_+ = \sqrt{1-x}N$

The variance ( $V = \sigma^2$ ) of the sample is then

$$V(N_+ - N_-) = xV(N) + (1 - x)V(N) = V(N)$$

and the fractional uncertainty

$$\frac{\sigma(N_+ - N_-)}{N_+ - N_-} = \frac{\sigma_N}{(1 - x)N - xN} = \frac{1}{1 - 2x} \frac{\sigma_n}{N}$$

3193 When the fraction of negative events is  $x = 0$ ,  $\frac{\sigma(N_+ - N_-)}{N_+ - N_-} = \frac{\sigma_n}{N}$  as expected.  
 3194 In contrast, if  $x = 0.5$  the fractional uncertainty is infinite, as expected.

3195 For the signal  $tHq$   $2\ell + 1\tau_{\text{had}}$  MC signal sample the fraction of negative  
 3196 weights is between 0.3 and 0.4 depending on the production used.

$$3197 \quad \bullet \quad x = 0.3 \rightarrow \frac{\sigma(N_+ - N_-)}{N_+ - N_-} = \frac{1}{0.2} \frac{\sigma_n}{N} = 5.0 \frac{\sigma_n}{N}$$

$$3198 \quad \bullet \quad x = 0.4 \rightarrow \frac{\sigma(N_+ - N_-)}{N_+ - N_-} = \frac{1}{0.4} \frac{\sigma_n}{N} = 2.5 \frac{\sigma_n}{N}$$

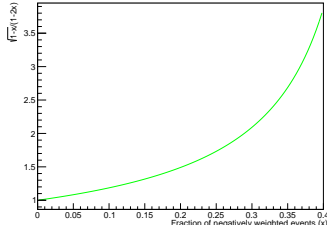
3199 The uncertainty of the effective number of events can be compared to  
 3200 that of using only the positively weighted events. If the two fractional  
 3201 uncertainties are divided:

$$\frac{\frac{\sigma(N_+ - N_-)}{N_+ - N_-}}{\frac{\sigma(N_+)}{N_x}} = \frac{\frac{1}{1-2x} \frac{\sigma_n}{N}}{\frac{1}{\sqrt{(1-x)N}}} = \frac{\sqrt{1-x} \sigma_n}{1-2x} \frac{1}{N} = \frac{\sqrt{1-x}}{1-2x}$$

3202 In the range of  $x$  values for the  $2\ell + 1\tau_{\text{had}}$  simulated signal events.

$$3203 \quad \bullet \quad x = 0.3 \rightarrow \frac{\frac{\sigma(N_+ - N_-)}{N_+ - N_-}}{\frac{\sigma(N_+)}{N_x}} = 2.09$$

$$3204 \quad \bullet \quad x = 0.4 \rightarrow \frac{\frac{\sigma(N_+ - N_-)}{N_+ - N_-}}{\frac{\sigma(N_+)}{N_x}} = 3.87$$



3204 In Figure A.1, several  $\Delta R$  distributions generated using all the events  
 3205 and just the positively weighted ones. As expected, the uncertainty bands  
 3206 are bigger for the 'All events' than for the 'Positive events'. These his-  
 3207 tograms were produced to verify that using only the events with positive  
 3208 weights in the training of the BDT for lepton assignment in the SS scenario  
 3209 (Section 6.4.3) was not biasing the result. The size of the error bands is  
 3210 calculated by ROOT as the square root of the quadratic sum of the weights,  
 3211 as explained below.

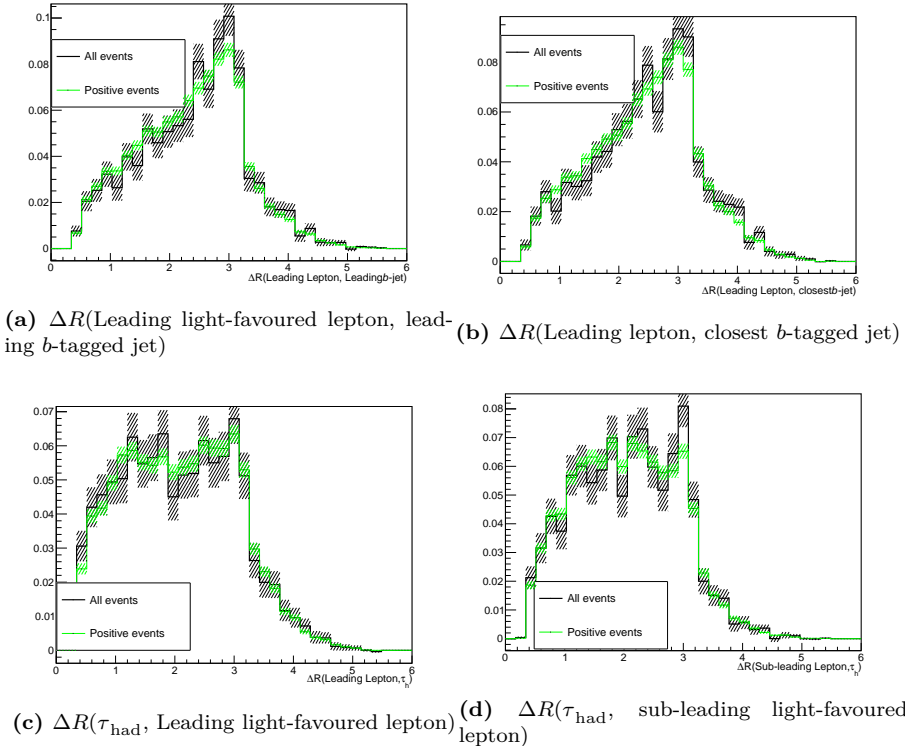


**Figure A.1:** Some normalised distributions for all the signal events in the  $2\ell \text{SS} + 1\tau_{\text{had}}$  (black) and just the positively weighted events (green). For each bin, the error band is calculated as the square root of the quadratic sum of the weights.

### 3212 A.2.1 Errors in binned histograms

If a bin of a histogram has  $n$  entries of weighted events  $w_i$  with  $i = 1, 2, \dots, n$ , the size of the bar is  $\sum_{i=1}^n w_i$ . Therefore, the error of that bar is

$$\sqrt{\sum_{i=1}^n w_i^2} \quad (\text{A.1})$$

This expression for the error of a bin in a histogram is based on error propagation and intrinsic poissonian statistics only. The variance, i.e. the error on the weighted number of events" in that bin, is given by error propagation:

$$V\left(\sum_{i=1}^n w_i\right) = \sqrt{\left(\sum_{i=1}^n w_i^2\right)^2} = \sum_{i=1}^n w_i^2 = \sum_{i=1}^n V(w_i)$$

3213 The variance of the weight  $w_i$ ,  $V(w_i)$ , is determined only by the statistical  
3214 fluctuation of the number of events considered:  $V(w_i) = w_i^2$ .

**3215 A.3 Negative weights in MVA methods**

3216 Events coming from the MC generator can be produced with (unphys-  
3217 ical) negative weights in some phase-space regions. Such occurrences are  
3218 frequently inconvenient to deal with, and whether or not they are handled ef-  
3219 fectively is dependent on the MVA method's actual implementation. Within  
3220 the ROOT TMVA library, probability and multi-dimensional probability  
3221 density estimators, as well as BDTs, are among the methods that correctly  
3222 include occurrences with negative weights. In cases where a method does  
3223 not properly treat events with negative weights, it is advisable to ignore such  
3224 events for the training but to include them in the performance evaluation  
3225 to not bias the results.

3226 **Appendix B**

3227 **Boosted Decision Trees**

3228 A boosted decision tree, typically referred just by its acronym BDT, is  
3229 a supervised<sup>1</sup> machine learning (ML) technique used for classification. The  
3230 analysis presented in this thesis uses several BDTs. Both the light lepton  
3231 origin assignment (Section 6.4.3) and the signal to background separation  
3232 (Section 6.6.3) are based on a BDT. This tool is applied in more scenarios  
3233 within within ATLAS. In the  $b$ -tagging, for instance, a BDT is trained to  
3234 discriminate  $b$ -jets from light-jets [179].

3235 **B.1 How does a BDT work?**

3236 A BDT is an ensamble of decision trees. Each decision tree is a map  
3237 of possible results of related decisions. A decision tree takes a set of input  
3238 features and splits input data recursively based on those features. This  
3239 results in a tree structure that resembles that of a flow charts with a decision  
3240 or split at each node. The last level of the trees are the so called leaves and  
3241 each represents a class. An example of a tree can be seen on Figure B.1,  
3242 where an event is classified in one of the two categories following a set of  
3243 yes-no questions. In this work the BDTs employed are binary, i.e. separates  
3244 into two categories, but multiclassifier BDTs could be used as well<sup>2</sup>.

Boosting is a technique for turning numerous weak classifiers (trees in this case) into a powerful one. Each tree is created iteratively depending on the prior ones. The output of each tree,  $h_t(\mathbf{x})$ , is given a weight,  $w_t$ ,

---

<sup>1</sup>Supervised learning means that the data used in the training is labeled.

<sup>2</sup>For the signal to background discrimination, multiclassifier BDTs were tested but the result was not satisfactory.

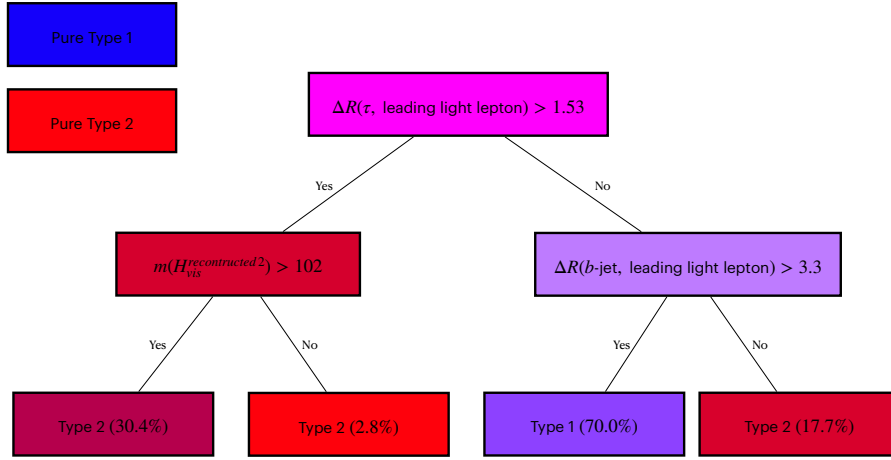


**Figure B.1:** Example of a decision tree with three nodes. This particular example corresponds to one of the trees in the BDT for the light lepton origin assignment (see Section 6.4.3). The color of the boxes represents the purity on Type 1 or Type 2 events that arrive to each node. Repeated left/right (yes/no) decisions are taken on one single variable at a time until the classification takes place.

relative to its accuracy. The ensamble output is the weighted sum

$$\hat{y}(\mathbf{x}) = \sum_t w_t h_t(\mathbf{x})$$

where  $t$  run over the trees. The goal of the boosting is to minimise a regularised objective function

$$L(x) = \sum_i l(\hat{y}_i, y_i) + \sum_t \Omega(f_t) \quad (\text{B.1})$$

3245 where  $l(\hat{y}_i, y_i) = l(f(\mathbf{x}_i|\theta), y_i)$  is a differentiable convex loss function  
 3246 (the distance between the truth and the prediction of the  $i^{th}$  sample) and  
 3247  $\Omega(f_t)$  is the regularisation function (penalises the complexity of the  $t^{th}$  tree,  
 3248  $f_t$ ). The  $\theta$  in  $f(\mathbf{x}_i|\theta)$  are the model parameters for a BDT these would be  
 3249 the weights and biases. The  $\mathbf{x}_i$  are values fo the input variables for the  $i^{th}$   
 3250 sample and  $y_i$  the target variable real value.

3251 The  $\Omega(f_t)$  term helps to smooth the final learnt weights to avoid over-  
 3252 fitting.

The tree ensemble model in Eq. B.1 cannot be optimised using traditional optimisation methods in Euclidean space. The model is trained instead in an additive way so that the the objective function to minimise is:

$$L^{(t)} = \sum_i^n l(y_i, \hat{y}_i^{(t-1)} + f_t(\mathbf{x}_i)) + \Omega(f_t). \quad (\text{B.2})$$

3253 There are several types of boosting for BDTs. Some of the most common  
 3254 are AdaBoost, Gradient Boosting and XGBoost. The later, which stands  
 3255 for “eXtreme Gradient Boosting”, is the used in this work and its details can  
 3256 be found in reference [180]. Boosting can significantly improve performance  
 3257 compared to that of a single tree and stabilise the response of the decision  
 3258 trees to fluctuations in the training sample.

### 3259 **B.1.1 Training**

3260 For a ML algorithm, to train means to learn or determine good values  
 3261 for all the weights within that model. To do so, the algorithm takes the  
 3262 labelled data and fits the model. For instance, for the signal discrimination,  
 3263 the ML model takes the MC samples, where all the events are labeled either  
 3264 as signal or background events. A renormalisation can take place if needed.  
 3265 With the data, the model also needs a set of variables that have some power  
 3266 to discriminate between our categories. A condition on one discriminant  
 3267 variable is set on each node of the BDT to split the phase space into two  
 3268 parts. The aim of the training is to find the optimal cut in each node so that  
 3269 after it the separation between the categories is maximised, in our example  
 3270 one category is enriched in background and the other in signal. This is  
 3271 done in a loop over all discriminating variables and trying to test as many  
 3272 as possible values for each cut (the default in TMVA is trying 20 values for  
 3273 each variable). The best splitting is defined on the basis of the splitting  
 3274 index, which works as a measure of inequality because we want to measure the  
 3275 inequality between the two categories in each split node. A low splitting  
 3276 index value means a high inequality between the classes, i.e. high purity.  
 3277 The best cut is defined as the one the one that yields the highest splitting  
 3278 index difference between the parent node and the two children node (each  
 3279 weighted by the total number of events in the corresponding block). Then  
 3280 it is possible keep splitting blocks until a stopping requirement is satisfied.

#### 3281 **Internal reweight of events in training sample**

3282 Sometimes, MC generators may provide event weights which may turn out  
 3283 to be extremely small or very high. To avoid artefacts, TMVA can renor-  
 3284 malise the signal and background training weights internally so that their  
 3285 respective sums of effective (weighted) events are equal. By doing this,  
 3286 the performance of the BDT can be improved since some classifiers are  
 3287 sensitive to the relative amount of each category (Type1/Type2 or sig-  
 3288 nal/background) in the training data. While for the lepton assignment  
 3289 this renormalisation does not play an important role (the amount of Type1

3290 and Type2 signal events is similar), for the the  $tHq$  signal discrimination  
 3291 the signal sample in the training test has to be reweighted.

3292 **B.1.1.1 Loss function**

3293 Sometimes called error function, the loss function is used to define what  
 3294 is a good prediction and what is not by assessing how far an estimated value  
 3295 is from its true value for a particular model iteration and penalising errors  
 3296 in the prediction. Therefore, it is crucial to any supervised ML model.  
 3297 Depending on whether the model is for a regression or for classification, the  
 3298 way  $l(y_n, f(\mathbf{x}_n|\theta))$  is defined may vary and, for the analysis, only binary  
 3299 classification BDTs have been used.

3300 Classification problems include foreseeing a discrete class output. It  
 3301 entails categorising the dataset into distinct categories based on various  
 3302 factors (variables) so that when new and unseen data appears it can be  
 3303 classified as well.

3304 **XGBoost loss functions**

3305 The loss function that have been used for predicting probabilities for the  
 3306 binary classification in the signal selection is “binary:logistic” but there are  
 3307 other available options such as “binary:logitraw” and “binary:hinge”. Some  
 3308 tests were carried using a multiclass BDT, for those the “multi:softprob”  
 3309 loss function was used.

When using the binary logistic loss function of XGBoost, the  $l$  in Eq B.2 is the logarithmic likelihood of the Bernoulli distribution and it takes the form

$$l = y_i \log[\text{logistic}(\hat{y}_i^{(t-1)} + f_t(\mathbf{x}_i))] + (1 - y_i) \log[1 - \text{logistic}(\hat{y}_i^{(t-1)} + f_t(\mathbf{x}_i))] \quad (\text{B.3})$$

where  $\text{logistic}(\hat{y}_i^{(t-1)} + f_t(\mathbf{x}_i))$  is the probability. In an algebraically equivalent manner, it can be written as:

$$l = y_i[\hat{y}_i^{t-1} + f_t(\mathbf{x}_i)] - \log(1 + \exp(\hat{y}_i^{t-1} + f_t(\mathbf{x}_i))) \quad (\text{B.4})$$

3310 Other loss functions

- 3311 • **binary:logistic:** Logistic regression for binary classification, output  
 3312 probability
- 3313 • **binary:logitraw:** Logistic regression for binary classification, output  
 3314 score before logistic transformation

- **binary:hinge:** Hinge loss for binary classification. This makes predictions of 0 or 1, rather than producing probabilities.

$$l(f(x_i|\theta), y_i) = \max(0, 1 - f(x_i|\theta)y_i) \quad (\text{B.5})$$

3315 **B.1.1.2 Overtraining**

3316 Let's consider a ML model  $f(\mathbf{x}|\theta)$ , where  $x$  are the data points used as  
3317 input and  $\theta$  the tuneable parameters of the model. The function  $f(\mathbf{x}|\theta)$   
3318 outputs the prediction of the model. The parameters  $\theta$  of the model are  
3319 tuned during the training process using a training set ( $\mathcal{T}$ ). The true output  
3320 ( $y$ ) of the elements in  $\mathcal{T}$ . When successful, the training finds the  $\theta$  that  
3321 performs as good as possible on new, unseen, data.

For a given  $f(\mathbf{x}|\theta)$  model, the training error,  $\text{err}(\mathcal{T})$ , is defined by [181]:

$$\text{err}(\mathcal{T}) = \frac{1}{N_t} \sum_{n=1}^{N_t} l(y_n, f(\mathbf{x}_n|\theta)) \quad (\text{B.6})$$

3322 where  $N_t$  is the number of events used for the training and  $l$  the chosen loss  
3323 function and  $\mathbf{x}_n$  and  $y_n$  the points in the training set. So, the error function  
3324 measures the model's error on a group of objects, whereas the loss function  
3325 deals with a single data instance.

3326 The  $\text{err}(\mathcal{T})$  is a poor estimator of the model's performance on new data.  
3327 It usually decreases as the number of training cycles increases, and it can  
3328 begin to adapt to noise in the training data. When this happens the training  
3329 error continues to decrease but the error on the data outside of the training  
3330 set starts increasing, jeopardising the general performance of the model.  
3331 This effect is the so called overfitting or overtraining.

3332 Overtraining occurs when a ML model can accurately predict training  
3333 examples but is unable to generalise<sup>3</sup> to new data. When overtraining takes  
3334 place, the ML model has learnt the details of the training data to an extent  
3335 in which these knowledge do not reflect the behaviour of the test sample.  
3336 This results in poor field performance.

3337 Figure B.2 shows how an overtrained BDT evolves. In Figure B.2a can  
3338 be seen that as the training of the BDT continues, the ability of the model  
3339 to classify the events in  $\mathcal{T}$  (blue) improves while for the data in the test  
3340 sample (orange) it doesn't. This means that the model is not generalising  
3341 properly. With the plot of the loss function (Figure B.2b) can be seen how  
3342 the error of the test data slightly increases while for the training samples is  
3343 strongly reduced.

---

<sup>3</sup>By generalise is meant that the model recognises only those characteristics of the data that are general enough to also apply to some unseen data.

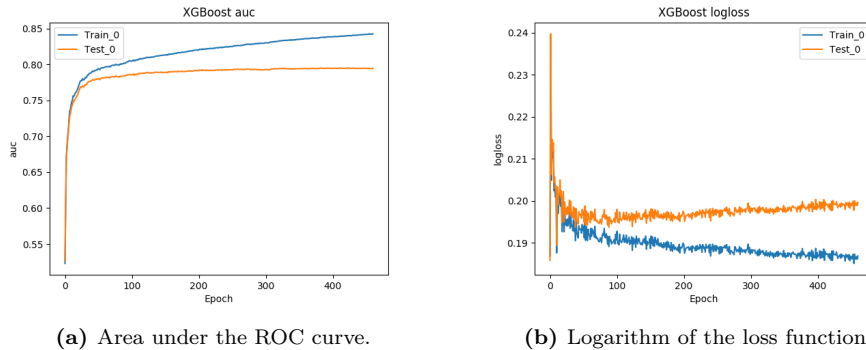


**Figure B.2:** Example of the evolution of the BDT metrics when overtraining occurs. The x-axis shows the training iteration.

When tested on the training sample, overtraining results in an apparent improvement in classification or regression performance over the objectively achievable one, but an effective performance loss when measured on an independent test sample (even though, there is a risk that it can still happen even if we use separate test data). Until deployed to real unseen data, there is a danger that overtraining will go unnoticed. This makes of overtraining one of the greatest dangers in ML. Other names for this phenomenon are overfitting and type III error.

Usually, this is a result of too little data or data that is too homogenous. Overtraining arises when there are too few degrees of freedom, because too many model parameters of an algorithm were adjusted to too few data points. Not all MVA methods are equally sensible to overtraining. While Fisher discriminant hardly suffers from it, BDTs usually suffer from at least partial overtraining, owing to their large number of nodes. Nevertheless, for the BDTs some countermeasures can be applied to preserve the ability to generalise:

- Never test the model on the data used for the training.
- The number of nodes in boosted decision trees can be reduced by removing insignificant ones (“tree pruning”). There are two types, pre-pruning and post-pruning
  - Pre-pruning: Refers to the early stopping of the growth of the decision tree
  - Post-pruning: Allows the decision tree model to grow to its full depth, then removes the tree branches to prevent the model from overfitting

- 3369     • Cross validation is a powerful technique to use all the data for training  
3370       at the same time that all the data for testing is employed while  
3371       avoiding overfitting. This method is based in cleverly iterating the  
3372       test and training split around and it is described in Section B.3.

3373   **B.1.2 Evaluation / Validation**

3374   **B.1.3 Application**

3375   **B.2 Treatment of negative weights**

3376   **B.2.1 BDT for Lepton origin assignment**

3377       The ROOT.TMVA library offers several possibilities to deal with the  
3378       negatively weighted events. These are:

- 3379     • InverseBoostNegWeights: It boosts with inverse boostweight. This  
3380       option is not available for gradient boosting.
- 3381     • IgnoreNegWeightsInTraining: This offers
- 3382     • Pray: This option allows to use negative weights in the training but  
3383       might cause problems with small node sizes or with the boosting. It  
3384       was tested and the model could not achieve stability.
- 3385     • PairNegWeightsGlobal: This option is still experimental. It takes the  
3386       negatively weighted events and pairs them with the events with pos-  
3387       itive weights, annihilating both. When using this option the gradient  
3388       BDT was not able to converge.

3389       In the BDT for determining the light-lepton origin, the selected treatment  
3390       is ignoring the negative weights in the training. When testing the model,  
3391       these weights are taken into account.

3392   **B.3 Cross validation and  $k$ -folding**

3393       Cross validation is a technique consisting in training several ML models  
3394       on different subsets of the input data and evaluated on the complementary  
3395       subset of the data. The goal cross validation is to estimate the performance

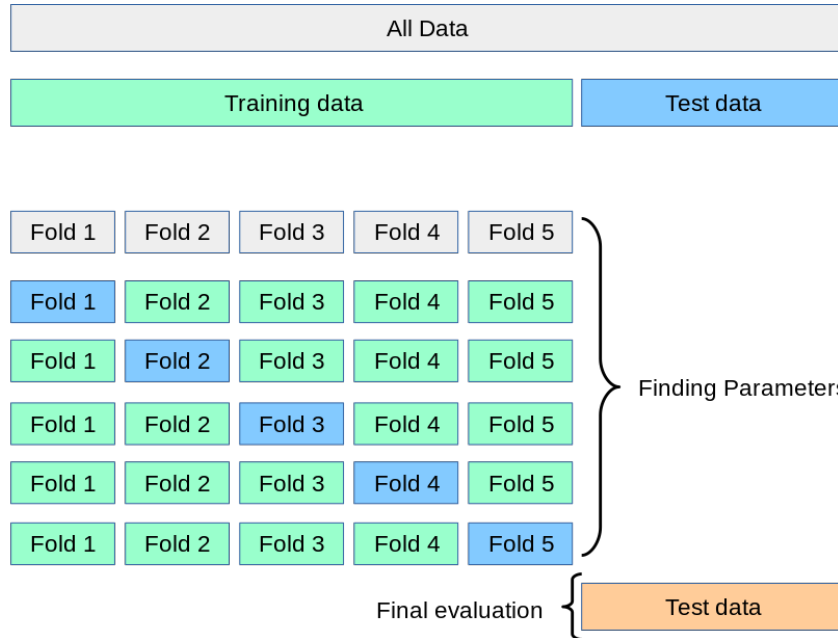


**Figure B.3:** Illustration of  $k$ -folding cross validation using 5 folds.

3396 of a machine learning model. It can identify overfitting or recognise the  
 3397 failure of the model to generalise a pattern.

3398 One particular method to do this is the  $k$ -folding. It consists on splitting  
 3399 the input data into  $k \in \mathcal{N}$  equally-sized subsets. Each of these is known  
 3400 as fold. With this procedure the ML model is trained  $k$  times. For each  
 3401 train  $k - 1$  folds are used as training set and the non-used fold is the subset  
 3402 of date where the evaluation takes place. All folds are used once as test  
 3403 sample and  $k - 1$  times in the train sample.

3404  $k$ -folding cross validation resample is of particular interest when the data  
 3405 available is limited because, by using it, all events are used in the training  
 3406 phase. It generally results in a less biased or less optimistic estimate of the  
 3407 model skill than other methods, such as a simple train/test split.

3408 Note that when the score of the model is applied, each event gets the  
 3409 score that was assigned when it was used as test event. Not doing this  
 3410 would bias the model.

The expected error for a  $f(x|\theta)$  trained using  $k$ -folding is:

$$\text{err}(\mathcal{T}) = \frac{1}{k} \sum_k \text{err}(\mathcal{T}_k), \quad (\text{B.7})$$

3411 where  $\text{err}(\mathcal{T}_k)$  is the error as described in Eq. B.6 for each splits test. As  
 3412 Eq. B.7 shows, an increase on the number of folds would imply more models  
 3413 to average over and, hence, implying an improvement on the confidence of

3414 how consistent the  $f(x|\theta)$  achieves a given level of performance. However,  
3415 a larger  $k$  would also reduce the statistical strength of each fold.

3416 **Should I comment that the event number is the variable used  
3417 to split the samples into different folds so that we can later assign  
3418 the score properly?**

## 3419 **B.4 Other considerations about BDTs**

### 3420 **Binary splits**

3421 Rather than splitting into two groups at each node, one could consider  
3422 several splits at each stage. Although this has its benefits, it is not a wise  
3423 general course of action. Multiway splits cause the data to fragment too  
3424 quickly, leaving the next level below with insufficient data. At the end,  
3425 binary splits are favoured because they can also be used to create multiclass  
3426 divides.

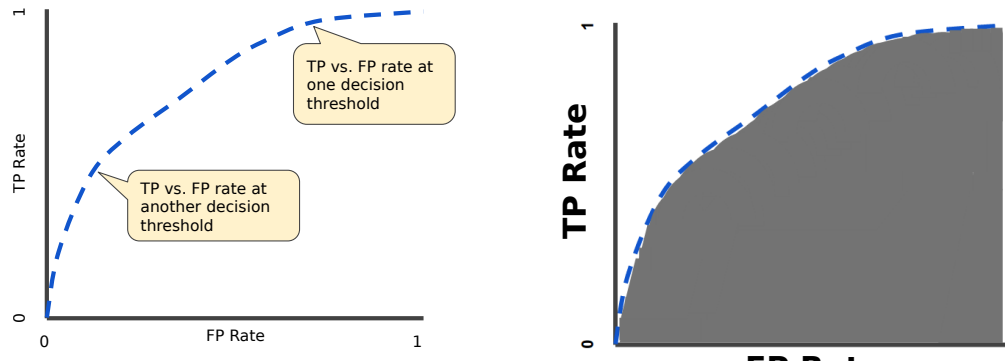
### 3427 **Instability of trees**

3428 The large variance of trees is one of their main issues. A little modification  
3429 in the data can frequently lead to very different results. This is mainly  
3430 caused by the hierarchical structure of the trees, which causes errors in  
3431 the top split to cascade down to all splits below it. By attempting to  
3432 employ a more stable split criterion, this can be somewhat mitigated, but  
3433 the fundamental instability remains. It is the cost of using the data to infer  
3434 a straightforward, tree-based structure.

### 3435 **Receiver operating characteristic curve**

3436 The receiver operating characteristic curve (ROC) is graphical plot used  
3437 that is used to illustrate the ability of a binary classifier. It assesses the  
3438 tradeoff between true positive (TP) and false negative (FP) rates as the  
3439 parameters of the classification vary. This is depicted in Figure B.4a.

- 3440 • **True positive rate:** Also known as sensitivity. It is the possibility of  
3441 a positive test conditioned on truly being positive. For instance, it's  
3442 the probability for the BDT in Section 6.6.3 to identify a  $tHq$  event  
3443 as such.
- 3444 • **False positivity rate:** It can be calculated as 1 - sensitivity. It refers  
3445 to the possibility of a negative test given that it's truly positive. In  
3446 the Section 6.6.3 BDT scenario it would be the ability to classify a  
3447 background event as if it was  $tHq$  signal event.



(a) Typical ROC curve. It shows that as the classification threshold decreases, more events are classified as positive, causing both the FP and FN rates to increase.

(b) The AUC varies from 0 to 1. While 0.0 corresponds to a model that always fails, a 1.0 means that the model is right a 100% of times.

**Figure B.4:** The ROC presents the TP vs the FN rate. The ROC analysis is related to cost/benefit interpretation of decision making.

3448        The area under the curve (AUC) is a commonly used quantitative sum-  
 3449        mary, it measures the bidimensional area under the ROC from (0,0) to (1,1)  
 3450        as Figure B.4b shows. The use of the AUC is convenient for several two  
 3451        reasons. Firstly, it is invariant with the scale because it does not meas-  
 3452        ure absolute values but rates. Secondly, it is invariant with respect to the  
 3453        classification threshold and, hence, it evaluates quality of the classification  
 3454        model.

### 3455        Precision-Recall curves

3456        While the ROC shows the summarises the trade-off between the true pos-  
 3457        itive rate and false positive rate for a predictive for different probability  
 3458        thresholds, there is other plot that helps with the diagnosis of the binary  
 3459        classification models; the Precision-Recall curves. These summarise the  
 3460        equilibrium between the true positive rate and the positive predictive value  
 3461        for a predictive model using different probability thresholds.

3462        Typically, the use of ROC and precession-recall curves is such that the  
 3463        first type is used when there are roughly equal numbers of observations for  
 3464        each class and the second should be used when there is a moderate to large  
 3465        class imbalance.

3466        For both the ROC and the precision-recall curves, the larger the area  
 3467        under the curve, the better. Figure B.5 shows that the optimal classifier is  
 3468        the one in which the curve in the precision-recall plot is close to (1,1).

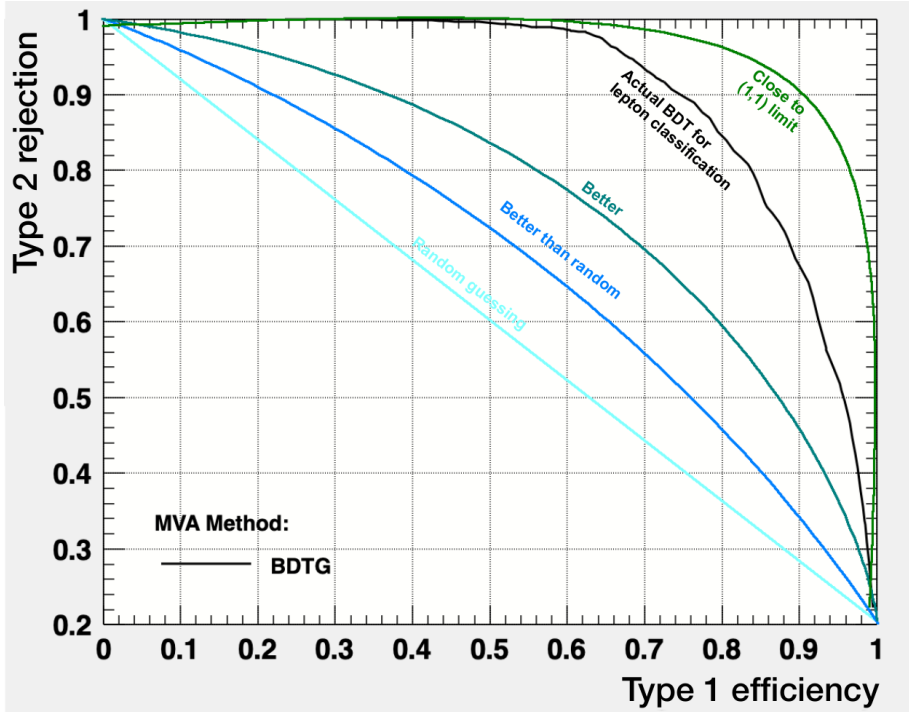


**Figure B.5:** Precision-recall curves for different models. The one in black corresponds to the model used for the light-lepton-origin assignment.

### 3469 Kolmogorov-Smirnov test

3470 In statistics, the Kolmogorov-Smirnov (KS) test is a non-parametric method  
 3471 for comparing the equality of one-dimensional probability distributions. It  
 3472 is used to assess the similarity between a sample distribution and a reference  
 3473 probability distribution.

3474 In the context of multivariate analysis, the distributions tested by the  
 3475 KS are the scores of the test and train. In other words, the test sample. If  
 3476 the score is close to zero, it may imply that the classifier is overtrained. In  
 3477 the way it is implemented in ROOT.TMVA, the ideal value is 0.5, although  
 3478 being above 0.01 is considered enough.

3479 Some sources argue that KS test requires a large sample to be effective.  
 3480 This may explain the low values in for all folds in the ROOT.TMVA gradient  
 3481 BDT used for the lepton-origin assignment.

---

### 3482 B.4.1 Hyperparameters

3483     Hyperparameters is the term used to refer to the specifications that  
 3484     control<sup>4</sup> the learning process of a ML algorithm.

3485     A ML model is defined by its model parameters, which are set by the  
 3486     process of training. In order to reach some level of intelligence, the process  
 3487     of training a model involves selecting the optimal hyperparameters that  
 3488     the learning algorithm will use to learn the ideal model parameters that  
 3489     accurately map the input variables ( $\mathbf{x}$ ) to the labels ( $y$ ). The learning  
 3490     algorithm uses hyperparameters when learning, but these are not included  
 3491     in the resulting model.

#### 3492 B.4.1.1 XGBoost

3493     In XGBoost, the hyperparameters are classified in three categories: general,  
 3494     booster and task hyperparameters. For the work developed in this  
 3495     thesis, the parameters related to the boosting of the trees are the ones that  
 3496     have been optimised. The process of finding the optimal set of hyperpara-  
 3497     meters for each model is crucial to achieve success.

- 3498     • General parameters: Refers to which booster it's been used (typically  
 3499        a tree or linear model) are the number of parallel threads to be used  
 3500        (set to the maximum in our case).
- 3501     • Booster parameters: Control the performance of the selected booster.  
 3502        For trees, the most relevant are:
  - 3503           – **Learning rate:** This tuning parameter in an optimisation al-  
 3504           gorithm determines the step size at each iteration while moving  
 3505           toward a minimum of a loss function. Figure B.6 shows the evolu-  
 3506           tion per epoch for the loss function depending on the learning  
 3507           rate. This hyperparameter is also known as eta and ranges from  
 3508           0 to 1.
  - 3509           – **Minimum split loss:** Also known as gamma or Lagrangian mul-  
 3510           tiplier. It is the A node is split only when the resulting split gives  
 3511           a positive reduction in the loss function and the gamma gives the  
 3512           minimum loss reduction required to make a further partition on  
 3513           a leaf node of the tree. Therefore, the higher the gamma, the  
 3514           more conservative the algorithm will be. The minimum split loss

---

<sup>4</sup>The prefix “hyper” suggest that these parameters are on a higher level that modulates the training process.

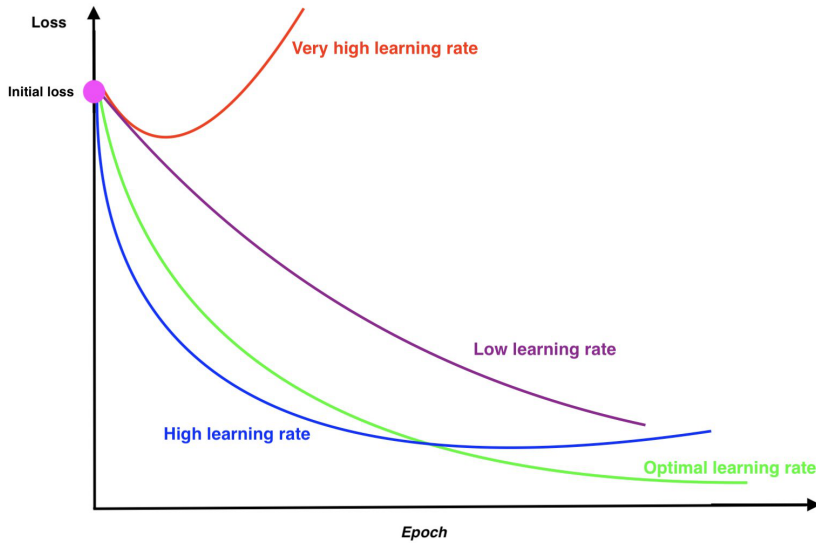


**Figure B.6:** Different loss-function curves versus iteration. Learning rate is one of the most important hyperparameters to adjust well during the ML model training. If it's high, it can cause the model to diverge. If it's too low it can slow down the training.

3515                   rages from 0 to inf. **We are not optimising this parameter**  
 3516                   **but using the default (not constrained).** Nevertheless,  
 3517                   **values between 1 and 10 have been tested.**

- 3518                   – **Minimum child weight:** It defines the minimum sum of  
 3519                   weights of all observations required in a child. When the tree par-  
 3520                   tition results in a leaf node with the sum of instance weight less  
 3521                   than the value of this hyperparameter, the tree stops partition-  
 3522                   ing. Higher min\_child\_weight prevent the model from learning  
 3523                   too specific relation. So, this is done to prevent overfitting. This  
 3524                   tunable parameter ranges from 0 to inf.
- 3525                   – **Maximum depth:** It refers to the number of splits in each tree,  
 3526                   which controls the complexity of the boosted ensamble. The  
 3527                   maximum depth of a tree is an integer ranging from 1 to inf but  
 3528                   is rare to have trees with depth higher than 10 since XGBoost  
 3529                   aggressively consumes memory when training a deep tree. In our  
 3530                   trees this hyperparameter is 4 or 5.
- 3531                   – **Scale of positive weight:** When the categories are imbalanced  
 3532                   as it is the case for the signal and background categories in this  
 3533                   analysis, the signal sample can be reweighted by this value to  
 3534                   have a larger impact. The typical value to consider is the frac-  
 3535                   tion between positive instances (signal) and negative instances  
 3536                   (background). When the BDT is targeting the identification of  
 3537                   background processes this hyperparameter is also used although  
 3538                   it does not take such extreme values.

- 3539 – Maximum delta step:
- 3540 – **Tree method:** It alludes to the tree construction algorithm
- 3541 used in XGBoost. Since the training of the BDTs takes place
- 3542 in ARTEMISA<sup>5</sup> facility [182], the method used here is the GPU
- 3543 implementation of the faster histogram optimised approximate
- 3544 greedy algorithm.
- 3545 • Learning task parameters: Decide on the learning scenario. Specify
- 3546 the learning task and the corresponding learning objective.

#### 3547 B.4.1.2 TMVA ROOT

3548 The hyperparameters that we configure are:

- 3549 • **Number of trees:** Number of trees in the forest.
- 3550 • **Maximum tree depth:** Maximum depth allowed for each decision
- 3551 tree.
- 3552 • **Minimum size for each node:** Minimum percentage of training
- 3553 events required in a leaf node. The default for classification: 5%.
- 3554 • **Number of cuts:** Control the number of cuts tested within a variable
- 3555 in order to find the optimal cut value for a node splitting.
- 3556 • **Negative weight treatment:**
- 3557 • **BoostType:** Type of boosting algorithm. The options are
  - 3558 – **AdaBoost:** This is the most popular type of boosting algorithm
  - 3559 and it uses an exponential loss function. Its name comes from
  - 3560 “adaptative boosting”. It consists on creating several weak trees,
  - 3561 each of them adjusting what the previous one could not. This
  - 3562 algorithm lacks robustness in presence of outliers or mislabelled
  - 3563 data points, which can happen in the lepton-origin-assignment
  - 3564 scenario.
  - 3565 – **Gradient boosting:** The ROOT.TMVA implementation of the
  - 3566 gradient boost uses the binomial log-likelihood loss function for
  - 3567 classification. This algorithm attempts to overcome the problem
  - 3568 presented by AdaBoost regarding the outliers or mislabeled data.

---

<sup>5</sup>ARTEMISA (ARTificial Environment for Machine learning and Innovation in Scientific Advanced computing) is a ML dedicated facility at IFIC. It is composed of several Intel Xeon Platinum CPUs and Tesla Volta GPUs that help to find the optimal configuration for ML algorithms.

- 3569     • **Learning rate:** Also called shrinkage, it is the learning rate of the  
3570       GradientBoost algorithm. A small shrinkage demands the use of more  
3571       trees in the BDT but can significantly improve the accuracy of the  
3572       prediction.
- 3573     • **Use Bagged Boost:** If used, only a random subsample of the events  
3574       is used for creating the trees at each iteration. The “bagged sample  
3575       fraction” is the relative size of bagged sample to the original size of  
3576       the data sample.
- 3577     • **BaggedSampleFraction:**
- 3578     • **Pruning:** Method used for removing statistically insignificant  
3579       branches For BDTs, rather than pruning it is suggested to small trees  
3580       (max. depth  $\simeq 3$ ) and use “NoPruning”.





# <sup>3581</sup> Abbreviations

<sup>3582</sup>

Acronym	Meaning
AD	Antiproton Decelerator
ALICE	A Large Ion Collider Experiment
ATLAS	A Toroidal LArge AparatuS
AWAKE	Advanced Proton Driven Plasma Wakefield Acceleration Experiment
CERN	European Organization for Nuclear Research
CMS	Compact Muon Solenoid
CP	Charge conjugation Parity
CSC	Cathode-Strip Chambers
DAQ	Data Acquisition
ECAL	Electromagnetic Calorimeter
EF	Event Filter
EM	Electromagnetic
EW	Electro Weak
EWSB	Electroweak Symmetry Breaking
FASER	ForwArd Search ExpeRiment
FCAL	Forward calorimeter
FTK	Fast TracKer
GR	General Relativity
HCAL	Hadronic Calorimeter
HLT	High Level Trigger
IBL	Insertable B-Layer
IP	Interaction Point

Acronym	Meaning
IR	Insertion Regions
ISOLDE	On-Line Isotope Mass Separator
ITk	Inner Tracker
LAr	Liquid Argon
LCG	LHC Computing Grid
LEIR	Low Energy Ion Ring
LEP	Large Electron-Positron
LHC	Large Hadron Collider
LHCb	The Large Hadron Collider Beauty
LHCf	Large Hadron Collider forward
LINAC2	Linear Accelerator 2
LINAC3	Linear Accelerator 3
LINAC4	Linear Accelerator 4
3583	LO
	Leading Order
	LVL1
	Level-1 Trigger
	LVL2
	Level-2 Trigger
MATHUSLA	Massive Timing Hodoscope for Ultra Stable neutrAL pArticles
MDT	Monitored Drift Tube
MoEDAL	Monopole and exotic particle detector at the LHC
MS	Muon Spectrometer
NLO	Next-to-Leading Order
NNLO	Next-to-Next-to-Leading Order
PDF	Parton Distribution Function
PS	Proton Synchrotron
PSB	Proton Synchrotron Booster
QCD	Quantum Chromodynamics
QED	Quantum Electrodynamics
QFT	Quantum Field Theory

3584

Acronym	Meaning
RF	Radio Frequency
ROD	ReadOut Drivers
RoI	Regions of interest
ROS	ReadOut Systems
RPC	Resistive Plate Chambers
SCT	Semiconductor Tracker
SFO	Sub-Farm Output
SM	Standar Model
SPS	Super Proton Synchrotron
SSB	Spontaneus Symmetry Breakin
SSC	Superconducting Super Collider
SUSY	Supersimmetry
TGC	Thin Gap Chambers
TI	Transfer Injection

3585    

# Bibliography

- 3586    <sup>1</sup>G. Aad et al., *Observation of a new particle in the search for the*  
3587    *Standard Model Higgs boson with the ATLAS detector at the LHC,*  
3588    *Phys. Lett. B* **716** (2012) 1–29 (2012) (cit. on pp. v, 48, 64).
- 3589    <sup>2</sup>S. Chatrchyan et al., *Observation of a New Boson at a Mass of 125*  
3590    *GeV with the CMS Experiment at the LHC,*  
3591    *Phys. Lett. B* **716** (2012) 30–61 (2012) (cit. on pp. v, 48, 64).
- 3592    <sup>3</sup>F. Demartin, F. Maltoni, K. Mawatari and M. Zaro,  
3593    *Higgs production in association with a single top quark at the LHC,*  
3594    *Eur. Phys. J. C* **75** (2015) 267 (2015) (cit. on pp. v, 54, 58, 60).
- 3595    <sup>4</sup>D. de Florian et al., *Handbook of LHC Higgs Cross Sections: 4.*  
3596    *Deciphering the Nature of the Higgs Sector*, **2/2017** (2016) (2016)  
3597    (cit. on pp. vi, 50–52).
- 3598    <sup>5</sup>Online Etymology Dictionary, "Physics", (2022)  
3599    <https://www.etymonline.com/word/physics> (visited on 20/01/2022)  
3600    (cit. on p. 1).
- 3601    <sup>6</sup>Perseus Digital Library, "fusiko", (2022)  
3602    <https://www.perseus.tufts.edu/hopper/text?doc=Perseus:text:1999.04.0057:entry=fusiko/s> (visited on 20/01/2022) (cit. on p. 1).
- 3604    <sup>7</sup>C Singer, *A Short History of Science to the Nineteenth Century*, p. 35.  
3605    (Streeter Press, 2008) (cit. on p. 1).
- 3606    <sup>8</sup>C. C. W. Taylor et al., *The atomists, leucippus and democritus:*  
3607    *fragments: a text and translation with a commentary*, Vol. 5  
3608    (University of Toronto Press, 2010) (cit. on p. 1).
- 3609    <sup>9</sup>O. Leaman, *Key concepts in eastern philosophy* (Routledge, 2002)  
3610    (cit. on p. 1).
- 3611    <sup>10</sup>A. Purcell, *Go on a particle quest at the first CERN webfest. Le premier*  
3612    *webfest du CERN se lance à la conquête des particules*, (2012) 10 (2012)  
3613    (cit. on p. 3).

- <sup>3614</sup><sup>11</sup>A. Einstein, *The Foundation of the General Theory of Relativity*,  
<sup>3615</sup>*Annalen Phys.* **49** (1916) 769–822, edited by J.-P. Hsu and D. Fine  
<sup>3616</sup>(1916) (cit. on p. 2).
- <sup>3617</sup><sup>12</sup>M. Aaboud et al., *Measurement of the  $W$ -boson mass in  $pp$  collisions at*  
<sup>3618</sup> $\sqrt{s} = 7 \text{ TeV}$  *with the ATLAS detector*,  
<sup>3619</sup>*Eur. Phys. J. C* **78** (2018) 110, [Erratum: *Eur.Phys.J.C* 78, 898 (2018)]  
<sup>3620</sup>(2018) (cit. on p. 2).
- <sup>3621</sup><sup>13</sup>S. Schael et al.,  
<sup>3622</sup>*Precision electroweak measurements on the  $Z$  resonance*,  
<sup>3623</sup>*Phys. Rept.* **427** (2006) 257–454 (2006) (cit. on p. 2).
- <sup>3624</sup><sup>14</sup>F. Englert and R. Brout,  
<sup>3625</sup>*Broken Symmetry and the Mass of Gauge Vector Mesons*,  
<sup>3626</sup>*Phys. Rev. Lett.* **13** (1964) 321–323, edited by J. C. Taylor (1964)  
<sup>3627</sup>(cit. on p. 3).
- <sup>3628</sup><sup>15</sup>P. W. Higgs, *Broken Symmetries and the Masses of Gauge Bosons*,  
<sup>3629</sup>*Phys. Rev. Lett.* **13** (1964) 508–509, edited by J. C. Taylor (1964)  
<sup>3630</sup>(cit. on p. 3).
- <sup>3631</sup><sup>16</sup>P. A. M. Dirac, *On the theory of quantum mechanics*,  
<sup>3632</sup>*Proceedings of the Royal Society of London. Series A, Containing*  
<sup>3633</sup>*Papers of a Mathematical and Physical Character* **112** (1926) 661–677  
<sup>3634</sup>(1926) (cit. on p. 4).
- <sup>3635</sup><sup>17</sup>R. Aaij et al., *Observation of a narrow pentaquark state,  $P_c(4312)^+$ , and*  
<sup>3636</sup>*of two-peak structure of the  $P_c(4450)^+$* ,  
<sup>3637</sup>*Phys. Rev. Lett.* **122** (2019) 222001 (2019) (cit. on p. 4).
- <sup>3638</sup><sup>18</sup>A. Pich, ‘The Standard model of electroweak interactions’,  
<sup>3639</sup>2006 European School of High-Energy Physics (2007) 1  
<sup>3640</sup>(cit. on pp. 4, 16).
- <sup>3641</sup><sup>19</sup>E. Noether, *Invariante variationsprobleme*, ger,  
<sup>3642</sup>*Nachrichten von der Gesellschaft der Wissenschaften zu Göttingen*,  
<sup>3643</sup>*Mathematisch-Physikalische Klasse* **1918** (1918) 235–257 (1918)  
<sup>3644</sup>(cit. on p. 6).
- <sup>3645</sup><sup>20</sup>C. A. Moura and F. Rossi-Torres, *Searches for Violation of CPT*  
<sup>3646</sup>*Symmetry and Lorentz Invariance with Astrophysical Neutrinos*,  
<sup>3647</sup>*Universe* **8** (2022) 42 (2022) (cit. on p. 9).
- <sup>3648</sup><sup>21</sup>J. S. Bell, *Time reversal in field theory*,  
<sup>3649</sup>*Proc. Roy. Soc. Lond. A* **231** (1955) 479–495 (1955) (cit. on p. 9).
- <sup>3650</sup><sup>22</sup>R. F. Streater and A. S. Wightman,  
<sup>3651</sup>*PCT, spin and statistics, and all that* (1989) (cit. on p. 9).

- <sup>3652</sup><sup>23</sup>T. D. Lee and C.-N. Yang,  
*Question of Parity Conservation in Weak Interactions*,  
Phys. Rev. **104** (1956) 254–258 (1956) (cit. on p. 10).
- <sup>3653</sup><sup>24</sup>C. S. Wu, E. Ambler, R. W. Hayward, D. D. Hoppes and R. P. Hudson,  
*Experimental Test of Parity Conservation in  $\beta$  Decay*,  
Phys. Rev. **105** (1957) 1413–1414 (1957) (cit. on p. 10).
- <sup>3654</sup><sup>25</sup>J. H. Christenson, J. W. Cronin, V. L. Fitch and R. Turlay,  
*Evidence for the  $2\pi$  Decay of the  $K_2^0$  Meson*,  
Phys. Rev. Lett. **13** (1964) 138–140 (1964) (cit. on p. 10).
- <sup>3655</sup><sup>26</sup>L.-L. Chau and W.-Y. Keung,  
*Comments on the Parametrization of the Kobayashi-Maskawa Matrix*,  
Phys. Rev. Lett. **53** (1984) 1802 (1984) (cit. on p. 11).
- <sup>3656</sup><sup>27</sup>P. A. Zyla et al., *Review of Particle Physics*,  
PTEP **2020** (2020) 083C01 (2020) (cit. on p. 12).
- <sup>3657</sup><sup>28</sup>A. M. Sirunyan et al.,  
*Measurement of the weak mixing angle using the forward-backward  
asymmetry of Drell-Yan events in pp collisions at 8 TeV*,  
Eur. Phys. J. C **78** (2018) 701 (2018) (cit. on p. 14).
- <sup>3658</sup><sup>29</sup>O. W. Greenberg, *Spin and Unitary Spin Independence in a Paraquark  
Model of Baryons and Mesons*, Phys. Rev. Lett. **13** (1964) 598–602  
(1964) (cit. on p. 15).
- <sup>3659</sup><sup>30</sup>D. D. Ryutov, *Using Plasma Physics to Weigh the Photon*,  
Plasma Phys. Control. Fusion **49** (2007) B429 (2007) (cit. on p. 19).
- <sup>3660</sup><sup>31</sup>F. J. Yndurain, *Limits on the mass of the gluon*,  
Phys. Lett. B **345** (1995) 524–526 (1995) (cit. on p. 19).
- <sup>3661</sup><sup>32</sup>J. Goldstone, A. Salam and S. Weinberg, *Broken Symmetries*,  
Phys. Rev. **127** (1962) 965–970 (1962) (cit. on p. 21).
- <sup>3662</sup><sup>33</sup>D. M. Webber et al., *Measurement of the Positive Muon Lifetime and  
Determination of the Fermi Constant to Part-per-Million Precision*,  
Phys. Rev. Lett. **106** (2011) 041803 (2011) (cit. on p. 25).
- <sup>3663</sup><sup>34</sup>M. Aker et al.,  
*Direct neutrino-mass measurement with sub-electronvolt sensitivity*,  
Nature Phys. **18** (2022) 160–166 (2022) (cit. on p. 26).
- <sup>3664</sup><sup>35</sup>N. Aghanim et al., *Planck 2018 results. VI. Cosmological parameters*,  
Astron. Astrophys. **641** (2020) A6, [Erratum: Astron. Astrophys. 652,  
C4 (2021)] (2020) (cit. on p. 28).
- <sup>3665</sup><sup>36</sup>S. Weinberg, *A New Light Boson?*, Phys. Rev. Lett. **40** (1978) 223–226  
(1978) (cit. on p. 29).

- <sup>3690</sup><sup>37</sup>F. Wilczek,  
<sup>3691</sup>*Problem of Strong P and T Invariance in the Presence of Instantons,*  
<sup>3692</sup>*Phys. Rev. Lett.* **40** (1978) 279–282 (1978) (cit. on p. 29).
- <sup>3693</sup><sup>38</sup>V. C. Rubin and W. K. Ford Jr., *Rotation of the Andromeda Nebula*  
<sup>3694</sup>*from a Spectroscopic Survey of Emission Regions,*  
<sup>3695</sup>*Astrophys. J.* **159** (1970) 379–403 (1970) (cit. on p. 29).
- <sup>3696</sup><sup>39</sup>A. N. Taylor, S. Dye, T. J. Broadhurst, N. Benitez and E. van Kampen,  
<sup>3697</sup>*Gravitational lens magnification and the mass of abell 1689,*  
<sup>3698</sup>*Astrophys. J.* **501** (1998) 539 (1998) (cit. on pp. 29, 33).
- <sup>3699</sup><sup>40</sup>P. A. R. Ade et al., *Planck 2015 results. XIII. Cosmological parameters,*  
<sup>3700</sup>*Astron. Astrophys.* **594** (2016) A13 (2016) (cit. on p. 29).
- <sup>3701</sup><sup>41</sup>M. Banner et al., *Observation of Single Isolated Electrons of High*  
<sup>3702</sup>*Transverse Momentum in Events with Missing Transverse Energy at the*  
<sup>3703</sup>*CERN anti-p p Collider*, *Phys. Lett. B* **122** (1983) 476–485 (1983)  
<sup>3704</sup>(cit. on p. 30).
- <sup>3705</sup><sup>42</sup>G. Arnison et al., *Experimental Observation of Lepton Pairs of*  
<sup>3706</sup>*Invariant Mass Around 95-GeV/c\*\*2 at the CERN SPS Collider,*  
<sup>3707</sup>*Phys. Lett. B* **126** (1983) 398–410 (1983) (cit. on p. 30).
- <sup>3708</sup><sup>43</sup>I. Zurbano Fernandez et al., *High-Luminosity Large Hadron Collider*  
<sup>3709</sup>*(HL-LHC): Technical design report,*  
<sup>3710</sup>*10/2020* (2020), edited by I. Béjar Alonso et al. (2020) (cit. on p. 30).
- <sup>3711</sup><sup>44</sup>G. Mahlon and S. J. Parke,  
<sup>3712</sup>*Spin Correlation Effects in Top Quark Pair Production at the LHC,*  
<sup>3713</sup>*Phys. Rev. D* **81** (2010) 074024 (2010) (cit. on p. 33).
- <sup>3714</sup><sup>45</sup>M. Kobayashi and T. Maskawa,  
<sup>3715</sup>*CP Violation in the Renormalizable Theory of Weak Interaction,*  
<sup>3716</sup>*Prog. Theor. Phys.* **49** (1973) 652–657 (1973) (cit. on p. 34).
- <sup>3717</sup><sup>46</sup>S. L. Glashow, J. Iliopoulos and L. Maiani,  
<sup>3718</sup>*Weak Interactions with Lepton-Hadron Symmetry,*  
<sup>3719</sup>*Phys. Rev. D* **2** (1970) 1285–1292 (1970) (cit. on p. 34).
- <sup>3720</sup><sup>47</sup>J. E. Augustin et al.,  
<sup>3721</sup>*Discovery of a Narrow Resonance in  $e^+e^-$  Annihilation,*  
<sup>3722</sup>*Phys. Rev. Lett.* **33** (1974) 1406–1408 (1974) (cit. on p. 34).
- <sup>3723</sup><sup>48</sup>S. W. Herb et al., *Observation of a Dimuon Resonance at 9.5-GeV in*  
<sup>3724</sup>*400-GeV Proton-Nucleus Collisions,*  
<sup>3725</sup>*Phys. Rev. Lett.* **39** (1977) 252–255 (1977) (cit. on p. 34).
- <sup>3726</sup><sup>49</sup>F. Abe et al., *Observation of top quark production in  $\bar{p}p$  collisions,*  
<sup>3727</sup>*Phys. Rev. Lett.* **74** (1995) 2626–2631 (1995) (cit. on p. 34).

- <sup>3728</sup><sup>50</sup>S. Abachi et al., *Observation of the top quark*,  
<sup>3729</sup>*Phys. Rev. Lett.* **74** (1995) 2632–2637 (1995) (cit. on p. 34).
- <sup>3730</sup><sup>51</sup>S. Amoroso et al.,  
<sup>3731</sup>*Strategy for ATLAS top quark mass measurements: 2021-2023*,  
<sup>3732</sup>tech. rep., CERN, 2020 (cit. on pp. 34, 35).
- <sup>3733</sup><sup>52</sup>*Top quark mass and properties summary plots November 2022*, (2022)  
<sup>3734</sup>(2022) (cit. on p. 35).
- <sup>3735</sup><sup>53</sup>Particle Data Group Web Page, *top-quark Mass (Direct Measurements)*,  
<sup>3736</sup>(2022) <https://pdglive.lbl.gov/DataBlock.action?node=Q007TP>  
<sup>3737</sup>(visited on 22/01/2022) (cit. on p. 35).
- <sup>3738</sup><sup>54</sup>M. Aaboud et al.,  
<sup>3739</sup>*Measurement of the top quark mass in the  $t\bar{t} \rightarrow \text{lepton+jets}$  channel*  
<sup>3740</sup>*from  $\sqrt{s} = 8$  TeV ATLAS data and combination with previous results*,  
<sup>3741</sup>*Eur. Phys. J. C* **79** (2019) 290 (2019) (cit. on p. 35).
- <sup>3742</sup><sup>55</sup>A. M. Sirunyan et al.,  
<sup>3743</sup>*Measurement of the Jet Mass Distribution and Top Quark Mass in*  
<sup>3744</sup>*Hadronic Decays of Boosted Top Quarks in  $pp$  Collisions at  $\sqrt{s} = \text{TeV}$* ,  
<sup>3745</sup>*Phys. Rev. Lett.* **124** (2020) 202001 (2020) (cit. on p. 35).
- <sup>3746</sup><sup>56</sup>*Combination of CDF and D0 results on the mass of the top quark using*  
<sup>3747</sup>*up 9.7  $\text{fb}^{-1}$  at the Tevatron*, (2016) (2016) (cit. on p. 36).
- <sup>3748</sup><sup>57</sup>M. Czakon and A. Ferroglia, *Top quark pair production at complete*  
<sup>3749</sup>*NLO accuracy with NNLO +NNLL corrections in QCD*,  
<sup>3750</sup>*Chinese Physics C* **44** (2020) 083104 (2020) (cit. on p. 36).
- <sup>3751</sup><sup>58</sup>*Top working group cross-section summary plots, November 2022*, (2022)  
<sup>3752</sup>(2022) (cit. on pp. 38, 39).
- <sup>3753</sup><sup>59</sup>A. M. Sirunyan et al., *Measurement of the single top quark and*  
<sup>3754</sup>*antiquark production cross sections in the  $t$  channel and their ratio in*  
<sup>3755</sup>*proton-proton collisions at  $\sqrt{s} = 13$  TeV*,  
<sup>3756</sup>*Phys. Lett. B* **800** (2020) 135042 (2020) (cit. on p. 39).
- <sup>3757</sup><sup>60</sup>P. Kant et al., *HatHor for single top-quark production: Updated*  
<sup>3758</sup>*predictions and uncertainty estimates for single top-quark production in*  
<sup>3759</sup>*hadronic collisions*, *Comput. Phys. Commun.* **191** (2015) 74–89 (2015)  
<sup>3760</sup>(cit. on pp. 39, 41).
- <sup>3761</sup><sup>61</sup>M. Aliev et al.,  
<sup>3762</sup>*HATHOR – HAdronic Top and Heavy quarks crOss section calculatoR*,  
<sup>3763</sup>*Comput. Phys. Commun.* **182** (2011) 1034–1046 (2011) (cit. on p. 39).
- <sup>3764</sup><sup>62</sup>J. A. Aguilar-Saavedra,  
<sup>3765</sup>*Single top quark production at LHC with anomalous  $Wtb$  couplings*,  
<sup>3766</sup>*Nucl. Phys. B* **804** (2008) 160–192 (2008) (cit. on p. 40).

- <sup>3767</sup><sup>63</sup>R. Frederix, D. Pagani and M. Zaro, *Large NLO corrections in  $t\bar{t}W^\pm$  and  $t\bar{t}\bar{t}\bar{t}$  hadroproduction from supposedly subleading EW contributions*, JHEP **02** (2018) 031 (2018) (cit. on p. 42).
- <sup>3770</sup><sup>64</sup>M. Komm, ‘Measurement of Top-Quark Polarization in t-channel Single-Top Production’, 7th International Workshop on Top Quark Physics (2014) (cit. on p. 45).
- <sup>3774</sup><sup>65</sup>P. Martínez-Agulló, *Optimisation of selection criteria of t-channel single-top-quark events at  $\sqrt{s}=13$  TeV for studies of anomalous couplings in the  $Wtb$  vertex*, MA thesis: Valencia U., 2017 (cit. on p. 45).
- <sup>3778</sup><sup>66</sup>G. Aad et al., *Measurement of the polarisation of single top quarks and antiquarks produced in the t-channel at  $\sqrt{s} = 13$  TeV and bounds on the  $tWb$  dipole operator from the ATLAS experiment*, JHEP **11** (2022) 040 (2022) (cit. on p. 45).
- <sup>3782</sup><sup>67</sup>Particle Data Group Web Page, *Higgs-boson Mass*, (2022) <https://pdglive.lbl.gov/DataBlock.action?node=S126M> (visited on 22/01/2022) (cit. on p. 47).
- <sup>3785</sup><sup>68</sup>M. Aaboud et al., *Measurement of the Higgs boson mass in the  $H \rightarrow ZZ^* \rightarrow 4\ell$  and  $H \rightarrow \gamma\gamma$  channels with  $\sqrt{s} = 13$  TeV pp collisions using the ATLAS detector*, Phys. Lett. B **784** (2018) 345–366 (2018) (cit. on p. 47).
- <sup>3789</sup><sup>69</sup>A. M. Sirunyan et al., *A measurement of the Higgs boson mass in the diphoton decay channel*, Phys. Lett. B **805** (2020) 135425 (2020) (cit. on p. 47).
- <sup>3792</sup><sup>70</sup>F. Englert and R. Brout, *Broken symmetry and the mass of gauge vector mesons*, Phys. Rev. Lett. **13** (9 1964) 321–323 (1964) (cit. on p. 47).
- <sup>3795</sup><sup>71</sup>P. W. Higgs, *Broken symmetries and the masses of gauge bosons*, Phys. Rev. Lett. **13** (16 1964) 508–509 (1964) (cit. on p. 47).
- <sup>3797</sup><sup>72</sup>G. S. Guralnik, C. R. Hagen and T. W. B. Kibble, *Global conservation laws and massless particles*, Phys. Rev. Lett. **13** (20 1964) 585–587 (1964) (cit. on p. 47).
- <sup>3800</sup><sup>73</sup>T. Aaltonen et al., *Combined search for the standard model Higgs boson decaying to a  $bb$  pair using the full CDF data set*, Phys. Rev. Lett. **109** (2012) 111802 (2012) (cit. on p. 48).
- <sup>3803</sup><sup>74</sup>V. M. Abazov et al., *Combined Search for the Standard Model Higgs Boson Decaying to  $bb$  Using the D0 Run II Data Set*, Phys. Rev. Lett. **109** (2012) 121802 (2012) (cit. on p. 48).

- 3806   <sup>75</sup>B. Mellado Garcia, P. Musella, M. Grazzini and R. Harlander,  
3807   *CERN Report 4: Part I Standard Model Predictions*, (2016) (2016)  
3808   (cit. on p. 51).
- 3809   <sup>76</sup>M. Farina, C. Grojean, F. Maltoni, E. Salvioni and A. Thamm,  
3810   *Lifting degeneracies in Higgs couplings using single top production in*  
3811   *association with a Higgs boson*, *JHEP* **05** (2013) 022 (2013)  
3812   (cit. on p. 53).
- 3813   <sup>77</sup>S. Biswas, E. Gabrielli and B. Mele, *Single top and Higgs associated*  
3814   *production as a probe of the Htt coupling sign at the LHC*,  
3815   *JHEP* **01** (2013) 088 (2013) (cit. on p. 53).
- 3816   <sup>78</sup>T. Appelquist and M. S. Chanowitz,  
3817   *Unitarity Bound on the Scale of Fermion Mass Generation*, *Phys. Rev.*  
3818   *Lett.* **59** (1987) 2405, [Erratum: *Phys.Rev.Lett.* 60, 1589 (1988)] (1987)  
3819   (cit. on p. 53).
- 3820   <sup>79</sup>B. Grzadkowski, M. Iskrzynski, M. Misiak and J. Rosiek,  
3821   *Dimension-Six Terms in the Standard Model Lagrangian*,  
3822   *JHEP* **10** (2010) 085 (2010) (cit. on p. 54).
- 3823   <sup>80</sup>A. Broggio, A. Ferroglio, B. D. Pecjak and L. L. Yang,  
3824   *NNLL resummation for the associated production of a top pair and a*  
3825   *Higgs boson at the LHC*, *JHEP* **02** (2017) 126 (2017) (cit. on p. 55).
- 3826   <sup>81</sup>M. Aaboud et al., *Observation of Higgs boson production in association*  
3827   *with a top quark pair at the LHC with the ATLAS detector*,  
3828   *Phys. Lett. B* **784** (2018) 173–191 (2018) (cit. on pp. 56, 57).
- 3829   <sup>82</sup>K. Skovpen, ‘First observation of the  $t\bar{t}H$  process at CMS’,  
3830   11th International Workshop on Top Quark Physics (2018)  
3831   (cit. on p. 56).
- 3832   <sup>83</sup>G. Aad et al.,  
3833   *Search for  $H \rightarrow \gamma\gamma$  produced in association with top quarks and*  
3834   *constraints on the Yukawa coupling between the top quark and the Higgs*  
3835   *boson using data taken at 7 TeV and 8 TeV with the ATLAS detector*,  
3836   *Phys. Lett. B* **740** (2015) 222–242 (2015) (cit. on p. 56).
- 3837   <sup>84</sup>V. Khachatryan et al., *Search for the associated production of the Higgs*  
3838   *boson with a top-quark pair*,  
3839   *JHEP* **09** (2014) 087, [Erratum: *JHEP* 10, 106 (2014)] (2014)  
3840   (cit. on p. 56).
- 3841   <sup>85</sup>A. Giraldi, ‘ $t\bar{t}H/tH$  production at CMS’,  
3842   10th Large Hadron Collider Physics Conference (2022) (cit. on p. 56).
- 3843   <sup>86</sup>F. Demartin, B. Maier, F. Maltoni, K. Mawatari and M. Zaro,  
3844   *tWH associated production at the LHC*, *Eur. Phys. J. C* **77** (2017) 34  
3845   (2017) (cit. on p. 61).

- <sup>3846</sup><sup>87</sup>T. M. P. Tait and C. P. Yuan, *Single top quark production as a window*  
<sup>3847</sup>*to physics beyond the standard model*, Phys. Rev. D **63** (2000) 014018  
<sup>3848</sup>(2000) (cit. on p. 62).
- <sup>3849</sup><sup>88</sup>S. Biswas, E. Gabrielli, F. Margaroli and B. Mele,  
<sup>3850</sup>*Direct constraints on the top-Higgs coupling from the 8 TeV LHC data*,  
<sup>3851</sup>JHEP **07** (2013) 073 (2013) (cit. on p. 62).
- <sup>3852</sup><sup>89</sup>V. Khachatryan et al., *Search for the associated production of a Higgs*  
<sup>3853</sup>*boson with a single top quark in proton-proton collisions at  $\sqrt{s} = 8$  TeV*,  
<sup>3854</sup>JHEP **06** (2016) 177 (2016) (cit. on p. 62).
- <sup>3855</sup><sup>90</sup>A. Airapetian et al., *ATLAS: Detector and physics performance*  
<sup>3856</sup>*technical design report. Volume 2*, (1999) (1999) (cit. on pp. 63, 100).
- <sup>3857</sup><sup>91</sup>CERN Web Page, *Our Member States*, (2022)  
<sup>3858</sup>[https://home.web.cern.ch/about/who-we-are/our-](https://home.web.cern.ch/about/who-we-are/our-governance/member-states)  
<sup>3859</sup>[governance/member-states](https://home.web.cern.ch/about/who-we-are/our-governance/member-states) (visited on 11/01/2022) (cit. on p. 64).
- <sup>3860</sup><sup>92</sup>T. Fazzini, G. Fidecaro, A. W. Merrison, H. Paul and A. V. Tollestrup,  
<sup>3861</sup>*Electron decay of the pion*, Phys. Rev. Lett. **1** (7 1958) 247–249 (1958)  
<sup>3862</sup>(cit. on p. 64).
- <sup>3863</sup><sup>93</sup>F. J. Hasert et al., *Observation of Neutrino Like Interactions Without*  
<sup>3864</sup>*Muon Or Electron in the Gargamelle Neutrino Experiment*,  
<sup>3865</sup>Phys. Lett. B **46** (1973) 138–140 (1973) (cit. on p. 64).
- <sup>3866</sup><sup>94</sup>P. M. Watkins, *Discovery of the w and 2 bosons*,  
<sup>3867</sup>Contemporary Physics **27** (1986) 291–324 (1986) (cit. on p. 64).
- <sup>3868</sup><sup>95</sup>D. Decamp et al.,  
<sup>3869</sup>*Determination of the Number of Light Neutrino Species*,  
<sup>3870</sup>Phys. Lett. B **231** (1989) 519–529 (1989) (cit. on p. 64).
- <sup>3871</sup><sup>96</sup>G. Baur et al., *Production of anti-hydrogen*,  
<sup>3872</sup>Phys. Lett. B **368** (1996) 251–258 (1996) (cit. on p. 64).
- <sup>3873</sup><sup>97</sup>G. D. Barr et al.,  
<sup>3874</sup>*A New measurement of direct CP violation in the neutral kaon system*,  
<sup>3875</sup>Phys. Lett. B **317** (1993) 233–242 (1993) (cit. on p. 64).
- <sup>3876</sup><sup>98</sup>V. Fanti et al., *A New measurement of direct CP violation in two pion*  
<sup>3877</sup>*decays of the neutral kaon*, Phys. Lett. B **465** (1999) 335–348 (1999)  
<sup>3878</sup>(cit. on p. 64).
- <sup>3879</sup><sup>99</sup>R. Aaij et al., *Observation of  $J/\psi p$  Resonances Consistent with*  
<sup>3880</sup>*Pentaquark States in  $\Lambda_b^0 \rightarrow J/\psi K^- p$  Decays*,  
<sup>3881</sup>Phys. Rev. Lett. **115** (2015) 072001 (2015) (cit. on p. 64).
- <sup>3882</sup><sup>100</sup>S. Maury, *The Antiproton Decelerator: AD*,  
<sup>3883</sup>Hyperfine Interact. **109** (1997) 43–52 (1997) (cit. on p. 65).

- 3884 <sup>101</sup>R. Alemany et al.,  
3885   *Summary Report of Physics Beyond Colliders at CERN*,  
3886   (2019), edited by J. Jaeckel, M. Lamont and C. Vallée (2019)  
3887   (cit. on p. 65).
- 3888 <sup>102</sup>R. Catherall et al., *The ISOLDE facility*, *J. Phys. G* **44** (2017) 094002  
3889   (2017) (cit. on p. 65).
- 3890 <sup>103</sup>E. Gschwendtner et al., *AWAKE, The Advanced Proton Driven Plasma*  
3891   *Wakefield Acceleration Experiment at CERN*,  
3892   *Nucl. Instrum. Meth. A* **829** (2016) 76–82, edited by U. Dorda et al.  
3893   (2016) (cit. on p. 65).
- 3894 <sup>104</sup>M. Aguilar et al.,  
3895   *The Alpha Magnetic Spectrometer (AMS) on the International Space*  
3896   *Station. I: Results from the test flight on the space shuttle*, *Phys. Rept.*  
3897   **366** (2002) 331–405, [Erratum: *Phys.Rept.* **380**, 97–98 (2003)] (2002)  
3898   (cit. on p. 65).
- 3899 <sup>105</sup>*CERN Council holds special session on the Large Hadron Collider*  
3900   *project*, (1991) 3 p, Issued on 19 December 1991 (1991) (cit. on p. 65).
- 3901 <sup>106</sup>T. S. Pettersson and P Lefèvre,  
3902   *The Large Hadron Collider: conceptual design*, tech. rep., 1995  
3903   (cit. on pp. 65, 70).
- 3904 <sup>107</sup>W. Herr and B Muratori, *Concept of luminosity*, (2006) (2006)  
3905   (cit. on p. 67).
- 3906 <sup>108</sup>A. Hoecker, ‘Physics at the LHC Run-2 and Beyond’,  
3907   2016 European School of High-Energy Physics (2016)  
3908   (cit. on pp. 67, 68, 79).
- 3909 <sup>109</sup>M. Aaboud et al., *Luminosity determination in pp collisions at  $\sqrt{s} = 8$*   
3910   *TeV using the ATLAS detector at the LHC*,  
3911   *Eur. Phys. J. C* **76** (2016) 653 (2016) (cit. on p. 67).
- 3912 <sup>110</sup>S. Myers,  
3913   *The LEP Collider, from design to approval and commissioning*,  
3914   John Adams’ memorial lecture, Delivered at CERN, 26 Nov 1990  
3915   (CERN, Geneva, 1991) (cit. on p. 68).
- 3916 <sup>111</sup>B. Müller, J. Schukraft and B. Wysłouch,  
3917   *First Results from Pb+Pb Collisions at the LHC*,  
3918   *Annual Review of Nuclear and Particle Science* **62** (2012) 361–386  
3919   (2012) (cit. on p. 69).
- 3920 <sup>112</sup>CERN Web Page, *The Large Hadron Collider*, (2022)  
3921   [https://home.cern/science/accelerators/large-hadron-](https://home.cern/science/accelerators/large-hadron-collider)  
3922   [collider](https://home.cern/science/accelerators/large-hadron-collider) (visited on 11/01/2022) (cit. on p. 69).

- 3923   <sup>113</sup>R. Steerenberg et al., ‘Operation and performance of the cern large  
3924   hadron collider during proton run 2’,  
3925   [10th international particle accelerator conference](#) (2019) MOPMP031  
3926   (cit. on p. 69).
- 3927   <sup>114</sup>by Rende Steerenberg and A. Schaeffer, *LHC Report: The LHC is full!*,  
3928   [\(2018\)](#) (2018) (cit. on p. 69).
- 3929   <sup>115</sup>*8th International Conference on High-Energy Accelerators*,  
3930   CERN (CERN, Geneva, 1971) (cit. on p. 69).
- 3931   <sup>116</sup>*LHC Machine*,  
3932   [JINST 3 \(2008\) S08001](#), edited by L. Evans and P. Bryant (2008)  
3933   (cit. on pp. 69, 71).
- 3934   <sup>117</sup>*Radiofrequency cavities*, [\(2012\)](#) (2012) (cit. on p. 70).
- 3935   <sup>118</sup>L Lari, H Gaillard and V Mertens,  
3936   [Scheduling the installation of the LHC injection lines](#), tech. rep.,  
3937   CERN, 2004 (cit. on p. 71).
- 3938   <sup>119</sup>G. Aad et al.,  
3939   [The ATLAS Experiment at the CERN Large Hadron Collider](#),  
3940   [JINST 3 \(2008\) S08003](#) (2008) (cit. on pp. 71, 83, 87, 88, 92, 93).
- 3941   <sup>120</sup>S. Chatrchyan et al., *The CMS Experiment at the CERN LHC*,  
3942   [JINST 3 \(2008\) S08004](#) (2008) (cit. on p. 72).
- 3943   <sup>121</sup>A. A. Alves Jr. et al., *The LHCb Detector at the LHC*,  
3944   [JINST 3 \(2008\) S08005](#) (2008) (cit. on p. 73).
- 3945   <sup>122</sup>K. Aamodt et al., *The ALICE experiment at the CERN LHC*,  
3946   [JINST 3 \(2008\) S08002](#) (2008) (cit. on p. 73).
- 3947   <sup>123</sup>O. Adriani et al.,  
3948   [The LHCf detector at the CERN Large Hadron Collider](#),  
3949   [JINST 3 \(2008\) S08006](#) (2008) (cit. on p. 73).
- 3950   <sup>124</sup>C. Alpigiani et al., *A Letter of Intent for MATHUSLA: A Dedicated*  
3951   *Displaced Vertex Detector above ATLAS or CMS.*, (2018) (2018)  
3952   (cit. on p. 73).
- 3953   <sup>125</sup>J. H. Yoo, *The milliQan Experiment: Search for milli-charged Particles*  
3954   *at the LHC*, [PoS ICHEP2018](#) (2018) 520. 4 p, proceeding for ICHEP  
3955   2018 SEOUL, International Conference on High Energy Physics, 4-11  
3956   July 2018, SEOUL, KOREA (2018) (cit. on p. 73).
- 3957   <sup>126</sup>V. A. Mitsou, *The MoEDAL experiment at the LHC: status and results*,  
3958   [J. Phys. Conf. Ser. 873](#) (2017) 012010, edited by B. Grzadkowski,  
3959   J. Kalinowski and M. Krawczyk (2017) (cit. on p. 73).

- 3960 <sup>127</sup>G. Anelli et al.,  
3961 *The TOTEM experiment at the CERN Large Hadron Collider,*  
3962 *JINST* **3** (2008) S08007 (2008) (cit. on p. 73).
- 3963 <sup>128</sup>A. Ariga et al.,  
3964 *Letter of Intent for FASER: ForwArd Search ExpeRiment at the LHC,*  
3965 (2018) (2018) (cit. on p. 73).
- 3966 <sup>129</sup>*LHC computing Grid. Technical design report,*  
3967 (2005), edited by I. Bird et al. (2005) (cit. on p. 74).
- 3968 <sup>130</sup>WLCG Web Page, *Resources*, (2022)  
3969 <https://wlcg-public.web.cern.ch/resources> (visited on  
3970 31/01/2022) (cit. on p. 75).
- 3971 <sup>131</sup>*ATLAS computing: Technical design report,*  
3972 (2005), edited by G. Duckeck et al. (2005) (cit. on pp. 74, 105).
- 3973 <sup>132</sup>WLCG Web Page, *Tier centres*, (2022)  
3974 <https://wlcg-public.web.cern.ch/tier-centres> (visited on  
3975 31/01/2022) (cit. on pp. 74, 76).
- 3976 <sup>133</sup>F. S. Cafagna, *Latest results for Proton-proton Cross Section*  
3977 *Measurements with the TOTEM experiment at LHC,*  
3978 *PoS ICRC2019* (2021) 207 (2021) (cit. on p. 75).
- 3979 <sup>134</sup>Particle Data Group Web Page,  
3980 *Data files and plots of cross-sections and related quantities for hadrons*,  
3981 (2022) <https://pdg.lbl.gov/2021/hadronic-xsections/> (visited on  
3982 08/02/2022) (cit. on p. 77).
- 3983 <sup>135</sup>J. Butterworth et al., *PDF4LHC recommendations for LHC Run II*,  
3984 *J. Phys. G* **43** (2016) 023001 (2016) (cit. on p. 77).
- 3985 <sup>136</sup>A. D. Martin, W. J. Stirling, R. S. Thorne and G. Watt,  
3986 *Parton distributions for the LHC*, *Eur. Phys. J. C* **63** (2009) 189 (2009)  
3987 (cit. on p. 78).
- 3988 <sup>137</sup>G. Aad et al., *Measurements of the Higgs boson production and decay*  
3989 *rates and constraints on its couplings from a combined ATLAS and*  
3990 *CMS analysis of the LHC pp collision data at  $\sqrt{s} = 7$  and 8 TeV*,  
3991 *JHEP* **08** (2016) 045 (2016) (cit. on p. 81).
- 3992 <sup>138</sup>G. Aad et al., *Measurement of the top quark-pair production cross*  
3993 *section with ATLAS in pp collisions at  $\sqrt{s} = 7$  TeV*,  
3994 *Eur. Phys. J. C* **71** (2011) 1577 (2011) (cit. on p. 81).
- 3995 <sup>139</sup>G. Aad et al., *Evidence for Electroweak Production of  $W^\pm W^\pm jj$  in pp*  
3996 *Collisions at  $\sqrt{s} = 8$  TeV with the ATLAS Detector*,  
3997 *Phys. Rev. Lett.* **113** (2014) 141803 (2014) (cit. on p. 81).

- 3998 <sup>140</sup>M. Aaboud et al., *Evidence for light-by-light scattering in heavy-ion*
- 3999     *collisions with the ATLAS detector at the LHC,*
- 4000     *Nature Phys.* **13** (2017) 852–858 (2017) (cit. on p. 81).
- 4001 <sup>141</sup>M. Aaboud et al., *Search for the standard model Higgs boson produced*
- 4002     *in association with top quarks and decaying into a  $b\bar{b}$  pair in  $pp$*
- 4003     *collisions at  $\sqrt{s} = 13$  TeV with the ATLAS detector,*
- 4004     *Phys. Rev. D* **97** (2018) 072016 (2018) (cit. on p. 81).
- 4005 <sup>142</sup>M. Aaboud et al., *Observation of  $H \rightarrow b\bar{b}$  decays and  $VH$  production*
- 4006     *with the ATLAS detector, Phys. Lett. B* **786** (2018) 59–86 (2018)
- 4007     (cit. on p. 81).
- 4008 <sup>143</sup>S. Amoroso, *Precision measurements at the LHC*, tech. rep.,
- 4009     CERN, 2020 (cit. on p. 81).
- 4010 <sup>144</sup>H. Pacey, *EW SUSY Production at the LHC*, tech. rep., CERN, 2021
- 4011     (cit. on p. 81).
- 4012 <sup>145</sup>S. Das Bakshi, J. Chakrabortty, C. Englert, M. Spannowsky and
- 4013     P. Stylianou, *CP Violation at atlas in effective field theory,*
- 4014     *Phys. Rev. D* **103** (5 2021) 055008 (2021) (cit. on p. 81).
- 4015 <sup>146</sup>B. T. Carlson, *Dark Matter searches with the ATLAS detector*, (2020)
- 4016     (2020) (cit. on p. 81).
- 4017 <sup>147</sup>J. L. Pinfold, *ATLAS and astroparticle physics*, *Nucl. Phys. B Proc.*
- 4018     *Suppl.* **175-176** (2008) 25–32, edited by K. S. Cheng et al. (2008)
- 4019     (cit. on p. 81).
- 4020 <sup>148</sup>N. D. Brett et al., *Discovery Reach for Black Hole Production*, (2009)
- 4021     (2009) (cit. on p. 81).
- 4022 <sup>149</sup>*ATLAS inner detector: Technical Design Report*, 1,
- 4023     Technical design report. ATLAS (CERN, Geneva, 1997) (cit. on p. 83).
- 4024 <sup>150</sup>G. Aad et al.,
- 4025     *The ATLAS Inner Detector commissioning and calibration,*
- 4026     *Eur. Phys. J. C* **70** (2010) 787–821 (2010) (cit. on p. 83).
- 4027 <sup>151</sup>M Capeans et al., *ATLAS Insertable B-Layer Technical Design Report*,
- 4028     tech. rep., 2010 (cit. on pp. 85, 86).
- 4029 <sup>152</sup>*Technical Design Report for the ATLAS Inner Tracker Pixel Detector*,
- 4030     tech. rep., CERN, 2017 (cit. on pp. 86, 88).
- 4031 <sup>153</sup>ATLAS Experiment Web Page, *Detector and Technology*, (2022)
- 4032     <https://atlas.cern/discover/detector> (visited on 02/02/2022)
- 4033     (cit. on pp. 86, 89, 92, 96, 97).
- 4034 <sup>154</sup>F. Cavallari, *Performance of calorimeters at the LHC*,
- 4035     *Journal of Physics: Conference Series* **293** (2011) 012001 (2011)
- 4036     (cit. on pp. 88, 91, 92).

- 4037   <sup>155</sup>C. Grupen and B. Shwartz, ‘Calorimetry’, *Particle detectors*, 2nd ed.,  
4038   Cambridge Monographs on Particle Physics, Nuclear Physics and  
4039   Cosmology (Cambridge University Press, 2008) 230–272 (cit. on p. 90).
- 4040   <sup>156</sup>Particle Data Group Web Page,  $\pi^0$  Decay Modes, (2022)  
4041   <https://pdglive.lbl.gov/DataBlock.action?node=Q007TP> (visited  
4042   on 02/02/2022) (cit. on p. 91).
- 4043   <sup>157</sup>A. Tarek Abouelfadl Mohamed, ‘The lhc and the atlas experiment’,  
4044   *Measurement of higgs boson production cross sections in the diphoton*  
4045   *channel: with the full atlas run-2 data and constraints on anomalous*  
4046   *higgs boson interactions*  
4047   (Springer International Publishing, Cham, 2020) 61 (cit. on pp. 91, 93).
- 4048   <sup>158</sup>*ATLAS muon spectrometer: Technical design report*, (1997) (1997)  
4049   (cit. on p. 93).
- 4050   <sup>159</sup>K. Ishii, *The ATLAS muon spectrometer*, PoS **HEP2001** (2001) 253,  
4051   edited by D. o. Horváth, P. Lévai and A. Patkós (2001) (cit. on p. 94).
- 4052   <sup>160</sup>M Livan, *Monitored drift tubes in ATLAS*, tech. rep., CERN, 1996  
4053   (cit. on p. 94).
- 4054   <sup>161</sup>G. Cattani, *The resistive plate chambers of the ATLAS experiment: performance studies*,  
4055   *Journal of Physics: Conference Series* **280** (2011) 012001 (2011)  
4056   (cit. on p. 95).
- 4058   <sup>162</sup>K. Nagai, *Thin gap chambers in ATLAS*, Nucl. Instrum. Meth. A **384**  
4059   (1996) 219–221, edited by F. Ferroni and P. Schlein (1996)  
4060   (cit. on p. 95).
- 4061   <sup>163</sup>*ATLAS magnet system: Technical Design Report*, 1,  
4062   Technical design report. ATLAS (CERN, Geneva, 1997)  
4063   (cit. on pp. 96, 97).
- 4064   <sup>164</sup>*ATLAS high-level trigger, data acquisition and controls: Technical design report*, (2003) (2003) (cit. on pp. 98, 99).
- 4066   <sup>165</sup>G. Aad et al., *Performance of the ATLAS Trigger System in 2010*,  
4067   Eur. Phys. J. C **72** (2012) 1849 (2012) (cit. on p. 98).
- 4068   <sup>166</sup>G. Aad et al., *Alignment of the ATLAS Inner Detector in Run-2*,  
4069   Eur. Phys. J. C **80** (2020) 1194 (2020) (cit. on pp. 99, 101, 102).
- 4070   <sup>167</sup>P. Mato, *GAUDI-Architecture design document*, (1998) (1998)  
4071   (cit. on pp. 105, 122).
- 4072   <sup>168</sup>CherryPy Team, *CherryPy Documentation* (2'17) (cit. on p. 105).
- 4073   <sup>169</sup>G. Aad et al., *ATLAS data quality operations and performance for 2015–2018 data-taking*, JINST **15** (2020) P04003 (2020) (cit. on p. 110).

- 4075 <sup>170</sup>*Luminosity determination in pp collisions at  $\sqrt{s} = 13$  TeV using the*  
 4076 *ATLAS detector at the LHC*, tech. rep., CERN, 2019 (cit. on p. 111).
- 4077 <sup>171</sup>G. Aad et al., *The ATLAS Simulation Infrastructure*,  
 4078 *Eur. Phys. J. C* **70** (2010) 823–874 (2010) (cit. on p. 113).
- 4079 <sup>172</sup>T. Gleisberg et al., *Event generation with SHERPA 1.1*,  
 4080 *JHEP* **02** (2009) 007 (2009) (cit. on p. 116).
- 4081 <sup>173</sup>M. Aaboud et al., *Performance of the ATLAS Track Reconstruction*  
 4082 *Algorithms in Dense Environments in LHC Run 2*,  
 4083 *Eur. Phys. J. C* **77** (2017) 673 (2017) (cit. on p. 118).
- 4084 <sup>174</sup>T. Cornelissen et al., *The new ATLAS track reconstruction (NEWT)*,  
 4085 *J. Phys. Conf. Ser.* **119** (2008) 032014, edited by R. Sobie, R. Tafirout  
 4086 and J. Thomson (2008) (cit. on p. 118).
- 4087 <sup>175</sup>R. Fruhwirth, *Application of Kalman filtering to track and vertex fitting*,  
 4088 *Nucl. Instrum. Meth. A* **262** (1987) 444–450 (1987) (cit. on p. 118).
- 4089 <sup>176</sup>G. Cowan, K. Cranmer, E. Gross and O. Vitells,  
 4090 *Asymptotic formulae for likelihood-based tests of new physics*,  
 4091 *Eur. Phys. J. C* **71** (2011) 1554 (2011) (cit. on p. 139).
- 4092 <sup>177</sup>L. Lista, ‘Practical Statistics for Particle Physicists’,  
 4093 *2016 European School of High-Energy Physics* (2017) 213  
 4094 (cit. on p. 143).
- 4095 <sup>178</sup>T. Bayes Rev.,  
 4096 *An essay toward solving a problem in the doctrine of chances*,  
 4097 *Phil. Trans. Roy. Soc. Lond.* **53** (1764) 370–418 (1764) (cit. on p. 143).
- 4098 <sup>179</sup>I. Connelly, *Performance and calibration of b-tagging with the ATLAS*  
 4099 *experiment at LHC Run-2*, *EPJ Web Conf.* **164** (2017) 07025, edited by  
 4100 L. Bravina, Y. Foka and S. Kabana (2017) (cit. on p. 153).
- 4101 <sup>180</sup>T. Chen and C. Guestrin, ‘XGBoost’,  
 4102 *Proceedings of the 22nd ACM SIGKDD international conference on*  
 4103 *knowledge discovery and data mining* (2016) (cit. on p. 155).
- 4104 <sup>181</sup>J Zimmermann,  
 4105 *Statistical learning methods: basics, control and performance*,  
 4106 Nuclear Instruments and Methods in Physics Research Section A:  
 4107 Accelerators, Spectrometers, Detectors and Associated Equipment **559**  
 4108 (2006) 106–114 (2006) (cit. on p. 157).
- 4109 <sup>182</sup>Artemisa, *ARTificial Environment for ML and Innovation in Scientific*  
 4110 *Advanced Computing*, (2023)  
 4111 <https://artemisa.ific.uv.es/web/> (visited on 03/01/2023)  
 4112 (cit. on p. 166).

<sup>4113</sup> Summary of the results



4114 **Búsqueda de la producción  
4115 asociada de un bosón de Higgs  
4116 y un quark top en el estado  
4117 final con un tau hadrónico**

4118 **1 Marco teórico**

4119 **1.1 El Model Estándar**

4120 El Modelo Estándar de Física de Partículas (SM, por sus siglas en inglés)  
4121 es un marco teórico que describe los constituyentes básicos de la materia  
4122 y sus interacciones. Es el modelo más ampliamente aceptado y confirmado  
4123 experimentalmente en la física de partículas.

4124 El SM incluye dos tipos de partículas elementales, los fermiones y bo-  
4125 sones. Los fermiones son partículas subatómicas que obedecen las reglas de  
4126 la mecánica cuántica estadística de Fermi-Dirac. Este tipo de partícula se  
4127 caracteriza por tener un spin semientero y obedecer el principio de exclusión  
4128 de Pauli, el cual establece que dos fermiones no pueden ocupar el mismo  
4129 estado cuántico al mismo tiempo. Los fermiones se dividen en quarks y  
4130 leptones. Ambos tipos de fermiones son los constituyentes básicos de la  
4131 materia pero son distintos entre sí.

4132 Por un lado, los quarks son partículas que tienen carga eléctrica frac-  
4133 cionaria y son la unidad fundamental de los protones y los neutrones. Estas  
4134 partículas se combinan en grupos para formar hadrones (mesones y ba-  
4135 riones). Los bariones incluyen los protones y los neutrones, que son las  
4136 partículas subatómicas más abundantes en la materia. Los mesones tienen  
4137 un número par de quarks, lo que hace que tengan spin entero y sean bo-  
4138 sones. Los quarks se dividen en seis *sabores* (no confundir con la sensación  
4139 que producen las sustancias con gusto) diferentes: arriba, abajo, encanto,

extraño, arriba y abajo. La forma más habitual de referirse a estos es por sus nombres en inglés: up, down, charm, strange, top y bottom.

Por otro lado, los leptones son partículas elementales que no interactúan fuertemente. Los leptones están divididos en dos clases: neutrinos y leptones cargados. Los neutrinos son partículas muy ligeras y se les conoce por su interacción débil con la materia. Los leptones cargados (electrón, muón y tauón) tienen carga eléctrica entera. A diferencia de los quarks, este tipo de partículas no se combinan entre sí para formar otras aunque, sí que lo hacen con hadrones para formar, por ejemplo, los átomos.

Los otros elementos que componen el SM son los bosones, partículas de spin entero que median las interacciones fundamentales de la física. Los bosones de gauge (spin 1) son responsables de describir tres de las cuatro fuerzas fundamentales de la naturaleza<sup>6</sup>:

- Interacción electromagnética: Mediada por el fotón ( $\gamma$ ), es la teoría que estudia los fenómenos eléctricos y magnéticos. Todas las partículas cargadas interactúan entre sí a través de esta fuerza. Las principales características de la interacción electromagnética son su infinito alcance y la ausencia de masa para sus portadores. Es responsable de la estabilidad de los átomos, ya que mantiene unidos a los electrones en su órbita alrededor del núcleo, y de la transmisión de la luz y otras formas de radiación electromagnética. La teoría que describe esta interacción se denomina electrodinámica cuántica.
- Interacción nuclear débil: Medida por dos bosones  $W$  ( $W^+$  y  $W^-$ ) y el bosón  $Z$ . Esta es responsable de la radioactividad beta, en la que un neutrón se descompone en un protón, un electrón y un antineutrino. También es la fuerza que media la desintegración del quark top a un quark  $b$  y un bosón  $W$ . Además, la interacción nuclear débil es crucial en el proceso de fusión en las estrellas, donde se combinan protones para formar elementos más pesados. Las fuerzas nuclear débil y electromagnéticas son descritas simultáneamente por la teoría electrodébil.
- Interacción nuclear fuerte: Mediada por el gluón, es responsable de mantener unidos los protones y neutrones en el núcleo atómico. Es la interacción más fuerte de la naturaleza pero su rango de acción está limitado a distancias subatómicas. Debido al confinamiento por color de la teoría nuclear fuerte ni los gluones ni los quarks aparecen aislados (salvo a altas energías). La teoría que describe esta interacción se

---

<sup>6</sup>La gravedad queda fuera del SM.

4177 llama cromodinámica cuántica. Esta teoría, al igual que la electrod-  
4178 inámica cuántica y la teoría electrodébil, está basada en el formalismo  
4179 de la teoría cuántica de campos.

4180 **1.2 La física del quark top**

4181 **1.3 La física del bosón de Higgs**

4182 **2 Dispositivo experimental**

4183 **2.1 El gran colisionador de hadrones**

4184 El Gran Colisionador de Hadrones (LHC, por sus siglas en inglés) es  
4185 un acelerador de partículas que se encuentra en el CERN (Centro Europeo  
4186 para la Investigación Nuclear o Laboratorio Europeo de Física de Partículas  
4187 Elementales), en Ginebra, Suiza. Fue diseñado para colisionar protones y  
4188 iones pesados con alta energía, lo que permite a los científicos estudiar la  
4189 estructura subatómica de la materia y buscar nuevas partículas.

4190 El LHC es una máquina de vanguardia que utiliza tecnología avanzada  
4191 para acelerar partículas hasta velocidades cercanas a las de la luz antes de  
4192 chocarlas entre sí. Estos choques generan partículas secundarias que se de-  
4193 tectan mediante una red de detectores situados en su interior. Los datos  
4194 recopilados de estas colisiones se utilizan para investigar la física de partícu-  
4195 las. Llegando a energías de  $\sqrt{s} = 13 \text{ TeV}$ , el LHC es el mayor acelerador de  
4196 partículas construido y constituye una herramienta clave para el avance de  
4197 la ciencia.

4198 Los cuatro principales detectores que rodean el LHC son: ATLAS, CMS,  
4199 LHCb y ALICE. El primero de estos es el experimento en el cual se desarrolla  
4200 esta tesis.

4201 **2.2 El detector ATLAS**

4202 ATLAS es uno de los principales detectores del LHC y se utiliza para  
4203 medir las propiedades de las partículas resultantes de las colisiones de had-  
4204 rones. ATLAS tiene una estructura cilíndrica y es uno de los más grandes  
4205 detectores de partículas del mundo, midiendo aproximadamente 46 metros  
4206 de largo y 25 metros de diámetro. Está compuesto por varios componentes  
4207 y subcomponentes. Cada uno de estos sistemas se encarga de registrar un

4208 tipo de información diferente. En orden dentro hacia fuera, ATLAS está  
4209 compuesto por:

- 4210 • Detector interno (Inner Detector, ID)  
4211     – Pixel  
4212     – SCT  
4213     – TRT  
4214 • Imán solenoidal:  
4215 • Calorímetro electromagnético (ECAL):  
4216 • Calorímetro hadrónico (HCAL):  
4217 • Muon Spectrometer (MS):

4218 **3 Búsqueda de procesos  $tH$  con un con final  
4219  $2\ell + 1\tau_{\text{had}}$**

4220 **3.1 Selección de eventos**

4221 **3.2 Estimación del fondo**

4222 **3.3 Fontes de incertidumbre**

4223 **3.4 Resultados**

4224 **4 Conclusiones**

4225



# 4226 Contraportada

4227 The discovery of a Higgs boson by the ATLAS and CMS experiments  
4228 in 2012 opened a new field for exploration in the realm of particle physics.  
4229 In order to better understand the Standard Model (SM) of particle physics,  
4230 it is imperative to study the Yukawa coupling between this new particle  
4231 and the rest of the SM components. Among these, of prominent interest is  
4232 the coupling of the Higgs boson to the top quark ( $y_t$ ), which is the most  
4233 massive fundamental particle and, consequently, the one with the strongest  
4234 coupling to the Higgs

4235 The direct measurement of  $y_t$  is only possible at LHC via two associated  
4236 Higgs productions; with a pair of top quarks ( $t\bar{t}H$ ) and with single-top  
4237 quark ( $tHq$ ). While the  $t\bar{t}H$  permits a model-independent determination of  
4238 the magnitude of  $y_t$ , the only way of directly measuring its sign is through  
4239 the  $tHq$  production. This is due to the fact that the two leading-order  
4240 Feynman diagrams for  $tHq$  production interfere with each other depending  
4241 on  $y_t$  sign. Current experimental constraints on  $y_t$  favour the SM predictions,  
4242 even though an opposite sign with respect to the SM expectations is not  
4243 completely excluded yet.

4244 In this work it is presented a search for the production of a Higgs boson in  
4245 association with a single-top quark in a final state with two light-floavoured-  
4246 charged leptons and one hadronically decaying tau lepton (named  $2\ell + 1\tau_{\text{had}}$   
4247 channel). This analysis uses an integrated luminosity of  $139 \text{ fb}^{-1}$  of proton-  
4248 proton collision data at centre-of-mass energy of  $13 \text{ TeV}$  collected by ATLAS  
4249 during LHC Run 2.

4250 This search is exceptionally challenging due to the extremely small cross  
4251 section of the  $tHq$  process ( $70 \text{ fb}^{-1}$ ) in general and, more particularly, the  
4252 the  $2\ell + 1\tau_{\text{had}}$  final-state channel, which only accounts for a 3.5% of the  
4253 total  $tHq$  production.

4254 Because of this, the separation of the  $tHq$  signal events from background  
4255 events is done by means of machine-learning (ML) techniques using boosted-  
4256 decision trees (BDT) to define both signal and control regions. The most  
4257 most relevant background processes are those related to top-pairs produc-

4258 tion (such as  $t\bar{t}$ ,  $t\bar{t}H$ ,  $t\bar{t}Z$  and  $t\bar{t}W$ ),  $Z$ -boson plus jets and single-top  
4259 processes.

4260 Significant suppression of the background events with jets wrongly selected  
4261 as leptons is achieved by demanding electrons and muons to pass strict  
4262 isolation requirements. Simultaneously, hadronic-tau leptons are demanded  
4263 to pass the requirement of the recurrent-neural-network-based discriminator  
4264 to reduce misidentifications from jets.

4265 The reconstruction of the events is also enhanced by similar ML methods  
4266 since in the scenario in which the light-flavour leptons have the same sign,  
4267 in principle, it is not possible to determine which lepton is originated from  
4268 the Higgs boson and which from the top quark.

4269 The possible observation of an excess of signal events with respect to  
4270 the SM predictions, would be a clear evidence of new physics in terms of  
4271  $\mathcal{CP}$ -violating  $y_t$  coupling.

4272 Additionally, the contribution to the single-top-quark polarisation first  
4273 measurement is presented as well. In this other analysis the components of  
4274 the full polarisation vector of the top quark are measured taking advantage  
4275 of the peculiarities of the single-top-quark decay. Benefitting from the fact  
4276 that the top quark lifetime is smaller than the depolarisation timescale, the  
4277 decay products preserve the spin information of the top quark. Via angular  
4278 distributions, it is measured in the top-quark rest frame.